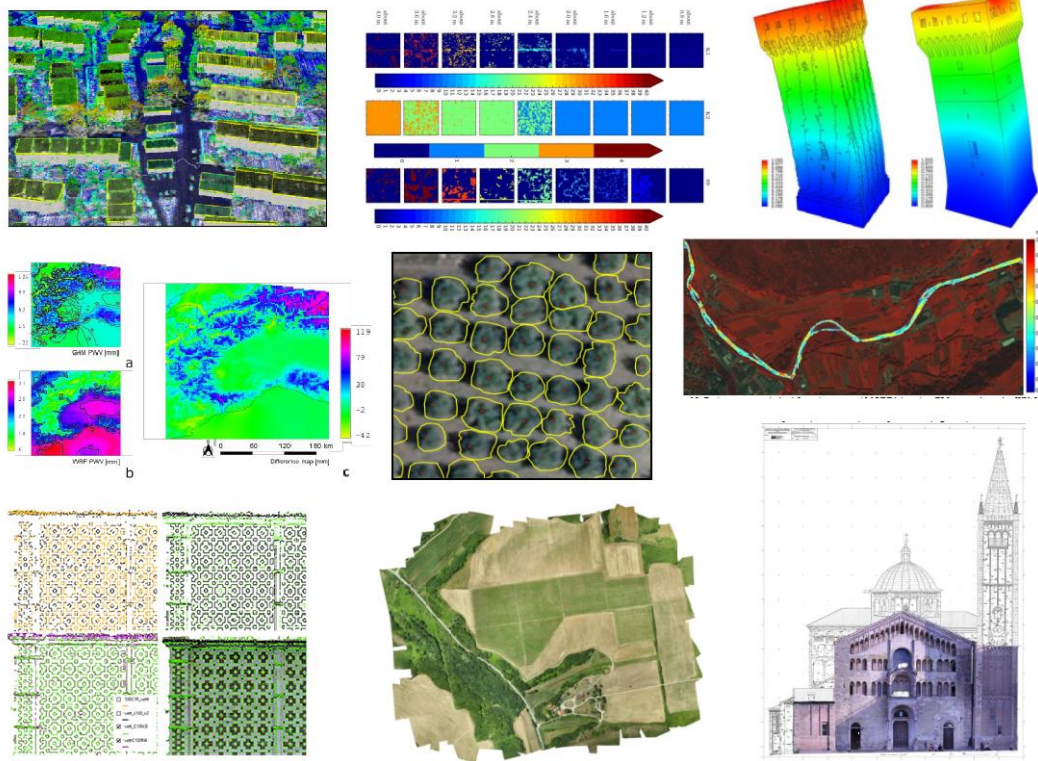


Antonio Vettore editor

RICERCHE DI GEOMATICA 2018



GEOMATICS RESEARCH 2018



**STUDI PRESENTATI ALLA QUATTORDICESIMA EDIZIONE DEL PREMIO AUTeC
STUDIES PRESENTED TO THE FOURTEENTH EDITION OF THE AUTeC AWARD**

Associazione **U**niversitari di **T**opografia e **C**artografia



Associazione **U**niversitari di **T**opografia e **C**artografia

RICERCHE DI GEOMATICA 2018

*

GEOMATICS RESEARCH 2018

*STUDI PRESENTATI ALLA DODICESIMA EDIZIONE DEL PREMIO AUTEc
STUDIES PRESENTED AT THE TWELFTH EDITION OF AUTEc AWARD*

Questo volume raccoglie gli articoli che hanno partecipato al **Premio AUTEc 2018**. Il premio è stato istituito nel 2005 e, fino al 2015, veniva conferito ogni anno ad una tesi di Dottorato giudicata particolarmente significativa sui temi di pertinenza del SSD ICAR/06 (Topografia e Cartografia) nei diversi Dottorati di Ricerca attivi in Italia.

A partire dal 2016 si è deciso di differenziare la competizione sulla base dell'affinità tra gli argomenti sviluppati e di attribuire fino a tre premi uno per ciascuna delle tre sezioni tematiche proprie del settore:

1. Geodesia, GNSS, Navigazione
2. Fotogrammetria e Laser Scanner
3. GIS, Remote Sensing

Ciascun candidato riassume in un articolo i punti salienti della propria tesi. Gli articoli vengono sottoposti al giudizio di una Commissione giudicatrice costituita dai membri della Giunta AUTEc vigente nell'anno in cui si conferisce il premio e eventualmente altri esperti del settore. In questa edizione, la Commissione è risultata composta dai professori Caterina Balletti Università IUAV di Venezia, Donatella Dominici dell'Università dell'Aquila, Eva Savina Malinverni dell'Università Politecnica delle Marche, Domenico Visintini dell'Università di Udine, Luca Vittuari dell'Università di Bologna, Ambrogio Manzino del Politecnico di Torino e Fabio Radicioni dell'Università degli Studi di Perugia.

Il premio AUTEc 2018 è stato assegnato al Dott. Fabrizio Banfi, che ha conseguito il Dottorato di Ricerca presso il Politecnico di Milano, per la tesi dal titolo: "HOLISTIC GENERATIVE MODELING PROCESS FOR HBIM";

Il premio e la pubblicazione degli articoli in un volume e-book vogliono essere un riconoscimento degli Universitari del SSD ICAR/06 per il lavoro di questi giovani ricercatori e una motivazione per continuare le loro ricerche.

Prof. Antonio Vettore
Coordinatore AUTEc 2018-2019



*The volume contains the papers submitted for applying to the **AUTEc Award 2018**. The award was established in 2005 and until 2015 it has been assigned annually to the most scientifically-sound Ph.D. thesis realized in one of the Italian Doctoral Courses pertaining to the scientific sector ICAR/06 (Surveying and Mapping). Since 2016, up to three awards have been established, each one related to one of the following thematic sections:*

- *Geodesy, GNSS, Navigation*
- *Photogrammetry and Laser Scanner*
- *GIS, Remote Sensing*

Candidates are invited to summarize the main outcomes of their research in a paper. Then, articles are examined by a Commission composed by current members of the AUTEc Executive Board. In this edition, the Commission was composed by Professors Caterina Balletti from the University IUAV of Venice, Donatella Dominici from University of l'Aquila, Eva Savina Malinverni from the Polytechnic of Marche, Domenico Visintini from University of Udine, Luca Vittuari from the University of Bologna, Ambrogio Manzino from the Polytechnic of Turin and Fabio Radicioni from the University of Perugia.

The winner of the AUTEc Award 2018 is Fabrizio Banfi. Fabrizio received his PhD from the Polytechnic University of Milan with a thesis entitled "Holistic generative modeling process for HBIM"

AUTEc Awards and "Ricerche di Geomatica" e-book, which are both promoted by ICAR/06 academics and AUTEc associates, aim at rewarding young researchers for their efforts in challenging studies and stimulating their future works.

*Prof. Antonio Vettore
AUTEc Coordinator 2018-2019*



Associazione Universitari di Topografia e Cartografia

AUTEc (Associazione Universitari di Topografia e Cartografia) si è costituita a Bologna il 9 febbraio 1998. Possono iscriversi a questa Associazione i docenti universitari inquadrati nel Settore Scientifico Disciplinare ICAR/06 - Topografia e Cartografia (Settore Concorsuale 08/A4 - Geomatica).

L' **AUTEc** si propone i seguenti obiettivi:

- creare un luogo di incontro per discutere problemi di sviluppo della ricerca, di allocazione delle risorse e di promozione di iniziative didattiche di formazione;
- coordinare le iniziative nei riguardi di Enti ed Organismi nazionali ed internazionali, comunitari e non, con i quali intercorrono rapporti, per sviluppare e promuovere una politica di richieste e di scelte coordinata;
- promuovere quanto necessario per migliorare la qualità dell'insegnamento delle discipline del settore e il loro impatto sulla realtà produttiva del Paese;
- diffondere in maniera sistematica le informazioni che riguardano il settore.

AUTEc è retta da un Coordinatore nazionale coadiuvato dalla Giunta. Le cariche si rinnovano ogni biennio.

Hanno rivestito la carica di Coordinatore **AUTEc** i professori:

Riccardo Galetto, ordinario dell'Università degli Studi di Pavia, nel biennio 1998-1999;

Giorgio Bezoari, ordinario del Politecnico di Milano, nel biennio 2000-2001;

Bruno Astori, ordinario del Politecnico di Torino, nel biennio 2002-2003;

Anna Spalla, ordinario dell'Università degli Studi di Pavia, nei bienni 2004-2005 e 2006-2007;

Benedetto Villa, ordinario dell'Università degli Studi di Palermo, nei bienni 2008-2009 e 2010-2011;

Gabriele Bitelli, ordinario dell'Università degli Studi di Bologna, nei bienni 2012-2013 e 2014-2015.

Dal 2016 riveste la carica di Coordinatore il prof. Antonio Vettore, ordinario dell'Università degli Studi di Padova.

***AUTEc** is the Italian Association of the academics (University Professors and Researchers) belonging to the Scientific Sector ICAR/06 - Surveying and Mapping. It was founded in Bologna, February 9, 1998.*

***AUTEc** has the following objectives:*

- *to create a meeting place to discuss issues related to research development, resource allocation and promotion of educational training in the scientific sector;*
- *to co-ordinate actions and to promote a common policy towards national and international entities and organizations;*
- *to promote what is necessary to improve both the quality of teaching of the disciplines of the scientific sector and their impact on the national productive reality;*
- *to disseminate information related to the scientific sector in a systematic manner.*

***AUTEc** is governed by a National Coordinator assisted by an Executive Board. The positions are renewed every two years.*

*The position of **AUTEc** Coordinator was covered by:*

Riccardo Galetto, Full Professor at the University of Pavia, in the period 1998-1999;

Giorgio Bezoari, Full Professor at the Polytechnic of Milan in 2000-2001;

Bruno Astori, Full Professor at the Polytechnic of Turin in 2002-2003;

Anna Spalla, Full Professor at the University of Pavia, in the two-year periods 2004-2005 and 2006-2007;

Benedetto Villa, Full Professor at the University of Palermo, in the two-year periods 2008-2009 and 2010-2011;

Gabriele Bitelli, Full Professor at the University of Bologna, in the two-year periods 2012-2013 and 2014-2015;

Since 2016, the position of Coordinator is held by Antonio Vettore, Full Professor at the University of Padova.



Indice

*

Index

	Sezione Tematica 1 Geodesia, GNSS, Navigazione * <i>Thematic Section 1</i> <i>Geodesy, GNSS, Navigation</i>	p. 9
CAPPONI Martina	AN INNOVATIVE APPROACH TO PROCESS AEROGRAVIMETRIC DATA	p. 11
SAVASTANO Giorgio	NEW APPLICATIONS AND CHALLENGES OF GNSS VARIOMETRIC APPROACH	p. 23
	Sezione Tematica 2 Fotogrammetria e Laser Scanner * <i>Thematic Section 2</i> <i>Photogrammetry and Laser Scanner</i>	p. 35
BANFI Fabrizio	HOLISTIC GENERATIVE MODELING PROCESS FOR HBIM	p. 37
MASET Eleonora	ADVANCED METHODS FOR LIDAR AND PHOTOGRAMMETRIC DATA PROCESSING: FROM PROCRUSTES ANALYSIS TO DEEP LEARNING	p. 49
SAMMARTANO Giulia	RAPID MAPPING STRATEGIES TOWARD BUILT HERITAGE 3D DENSE MODELING. SUITABILITY AND VALIDATION OF INFORMATION EXTRACTION FROM INTEGRATED SOLUTIONS	p. 61
	Sezione Tematica 3 GIS e Remote Sensing * <i>Thematic Section 3</i> <i>GIS and Remote Sensing</i>	p. 75



Associazione **U**niversitari di **T**opografia e **C**artografia

GRASSO Nives	VISIBILITY ANALYSES USING 3D URBAN MODELS GENERATED BY LOW-COST MULTI-SENSOR APPROACHES	p. 77
------------------------	--	-------



AUTEc

Associazione Universitari di Topografia e Cartografia

Sezione Tematica 1 Geodesia, GNSS, Navigazione

*

*Thematic Section 1
Geodesy, GNSS, Navigation*

AN INNOVATIVE APPROACH TO PROCESS AEROGRAVIMETRIC DATA

M. Capponi^{1,2*}

¹ DICEA, University of Rome “La Sapienza”, Rome, Italy

² DICA, Politecnico di Milano, Milan, Italy - martina.capponi@polimi.it

KEY WORDS: Gravity, Airborne gravimetry, GNSS Variometric Approach, Remove-Compute-Restore Procedure, Covariance Modelling, Space-Wise Approach

ABSTRACT:

The regional gravity field modeling is nowadays widely used in different contexts: from geodetic applications for the regional geoid determination to exploration geophysics applications aimed to understand and map geological structures in a specific region. The accuracies and resolutions necessary for such activities, generally requires the combination of satellite-only gravity field data with observation acquired at lower altitude. Thanks to the development of Global Navigation Satellite Systems (GNSS), the airborne gravimetry technique started to spread worldwide, becoming one of the most efficient techniques to collect gravity observations in a fast and cost-effective way. However due to the dynamic acquisition conditions the data acquired with this technique require to be filtered with a proper procedure in order to recover valuable information. In this work a new methodology to process airborne gravity measurements is presented. It allows to pre-process the raw observations coming from both the onboard GNSS receiver and gravimeter, with the aim to optimally combine them to compute the raw gravity anomalies/disturbances. Furthermore, it consents to process by means of a filtering and gridding procedure these latter raw gravity disturbances to predict the signal on other points. The algorithms used to pre-process raw GNSS acquired data are based on the application of the variometric approach. While the filtering and gridding phase is basically an adaptation to airborne gravimetry of the Space-Wise approach, developed by Politecnico di Milano, to process data coming from the ESA satellite mission GOCE. Within the whole research project, a software in parallel C language has been developed and used to perform numerical tests on a real aerogravimetric dataset. The obtained result in term of accuracy (1.3 mGal) is in line with the expectations derived from the specific survey characteristics.

1. INTRODUCTION

1.1 Overview

The Earth's gravitational field has always been a matter of interest for the scientific community because its knowledge can be helpful to various geosciences, such as those involved with the study of the real Earth's shape, of the mass transport in the Earth's system or of the geological composition of the Earth's interior. The rapid technological development of the last decades has noticeably improved the instrumentation used to measure the gravitational field both at global and local scale. The successful satellite missions like CHAMP (2000), GRACE (2002) and GOCE (2009), dedicated to the Earth's gravity field measurement, for example, have revolutionized the mapping of this field on a global scale reaching accuracies never reached before. These improvements have paved the way for important scientific applications such as the precise determination of the actual shape of the Earth, i.e. the geoid, the identification of the crust-mantle boundary surface or the modeling of geostrophic currents (Sansó et al., 2013). At regional and local level, the development in the late eighties and early nineties of Global Navigation Satellite Systems (GNSS) and the consequent availability of accurate navigational data, has led to the spread of techniques such as airborne or shipborne gravimetry. These type of gravity measurements are capable of providing accurate data at a much higher resolution than the one obtained from satellite observations. Local gravity data can be used for scientific applications, like the regional gravity field modeling or geophysical studies, but can also be used for commercial applications such as resources exploration.

Nowadays airborne gravimetry results to be one of the most efficient techniques ideal to collect gravity observations close to the Earth's surface in a fast and cost-effective way. One of the main reasons of its wide spread is the capability of providing gravity measurements also in challenging environments, which can be difficult to access otherwise, such as mountainous areas, rain forests and polar regions. To measure gravity with this technique, several components are required: an accelerometer for measuring the specific force (gravimeter), a system to compute the accelerometer attitude and a system that measures the inertial acceleration of the aircraft. This latter is derived from GNSS observations and by combining it with the measurements of the gravimeter it is possible to obtain the gravity observations. A negative aspect of this technique is that, in general, the acquired data are characterized by extremely large noise, due to the fact that measurements are taken in a complex and dynamic environment. This noise has both a high frequency component caused by aircraft vibrations, and a low frequency one, due to drifts and systematic errors which affect the accelerometers and the attitude measurements (typical values for noise-to-signal ratio are of the order of 1000). Another critical issue is the processing of GNSS raw data to compute accelerations, which can lead to an increase of the high frequency noise which is reflected in a degradation of the derived gravity observations.

The present research is focused on the description of an innovative methodology for processing gravity data acquired with this airborne technique.

1.2 The main contributions of the present research

This research project aims to improve performances of airborne gravimetry in terms of both accuracy and spatial resolution of

*Corresponding author

the retrieved local gravity field, with the exploitation of current state of the art satellite technology and innovative processing capabilities.

It is worth to highlight that within this work it is made a distinction between pre-processing and processing of airborne observations. The former deals with the manipulation of data acquired from the onboard gravimeter and GNSS receiver to correct biases and to combine them optimally to derive gravity accelerations; the latter regards the procedure to filter and grid the gravity accelerations data to obtain gravity anomalies/disturbances maps.

The method used for the pre-processing of raw GNSS observations is based on the application of the variometric approach (Colosimo, 2012) which consists in the manipulation of the classical GNSS observation equation in such a way that a new observable is derived (sensitive to the antenna acceleration but almost insensitive to the actual antenna position). Regarding the pre-processing of the gravimeter data, the two principal objectives are the computation of all the corrections to properly combine gravimeter observations with GNSS observations and the “effective” sampling of gravimeter data, characterized by a very high observation rate, so that there is no loss of valuable information in terms of gravity accelerations. The first issue is related to the geometry of the instruments onboard and if not properly treated can cause the two instruments to sense different accelerations.

About the procedure to process (filter and grid) airborne observations, it consists in a combination of an along-track Wiener filter with a classical Least Squares Collocation adjustment (Sampietro et al., 2017). This algorithm is similar to the GOCE space-wise approach, developed by Politecnico di Milano for one of the ESA official solution for the GOCE mission. Among the main differences with respect to the GOCE space-wise solution it has to be mentioned the fact that, when dealing with airborne observations, the stochastic properties of the observation error are in general unknown and should be therefore estimated by the dataset itself. This last issue has been solved using the crossover analysis in an innovative way, i.e. to sample the airborne system observation error, as described in the following.

2. AIRBORNE GRAVIMETRY: STATE OF THE ART

2.1 The principle of airborne gravimetry

To measure the gravity field, different measurement systems can be generally adopted for an airborne survey. The principal instrument remains the gravimeter, which in principle is a highly sensitive accelerometer. Depending on the airborne instruments setting we distinguish scalar gravimetry, vector gravimetry and gradiometry. In the first case, the component of interest is the magnitude of the gravity vector and the measurement system can be the stabilized platform or the strapdown system. In vector gravimetry, all the components of the gravity vector are measured using in general a strapdown system with a triad of accelerometers and of gyroscopes. While in airborne gradiometry, the observables are the second derivatives of the gravity field. In this latter case the designed system consists in opposite pairs of accelerometers on a rotating platform (Schwartz et al., 1997). In this work we focused just on classical scalar gravimetry by means of stabilized platform systems, which remains the standard measurement technique for industrial (i.e. oil&gas) applications; however, some of the proposed procedures can be easily adapted to other

measurement principles.

The three fundamental laws of physics, valid in an inertial reference frame, which govern airborne gravimetry are: the Newton’s second law of motion, the Newton’s law of gravitation and Einstein’s equivalence principle.

The Newton’s second law of motion considering the presence of the Earth’s gravitational field, becomes:

$$m_i \ddot{\underline{x}} = \underline{F} + \underline{F}_g \quad (1)$$

where m_i is the proof mass, $\ddot{\underline{x}}$ represents the second derivative in time of the position vector \underline{x} , \underline{F} is the force acting upon the mass and \underline{F}_g is the gravitational force ideally due to the field generated by all masses in the universe (according to the Newton’s law of gravitation).

The Einstein’s equivalence principle, formulated within his theory of relativity in early 1990s, states that “we [...] assume the complete physical equivalence of a gravitational field and a corresponding acceleration of the reference system.”, which means that no experiment or exploitation of the laws of physics performed in a closed system can distinguish between a reference frame in a gravitational field and an accelerated reference frame. As a consequence of this principle the inertial mass is considered equivalent to a gravitational mass and the complete equation of motion, into an inertial reference frame, can be expressed as follows:

$$\ddot{\underline{x}} = \frac{\underline{F}}{m} + \underline{g} = \underline{f} + \underline{g} \quad (2)$$

where $\ddot{\underline{x}}$ is the total kinematic acceleration, \underline{f} is the specific force or the acceleration resulting from an active force applied to the body; \underline{g} is the gravitational specific force. Among these accelerations the one sensed by the accelerometer is \underline{f} , i.e. the one generated by the action forces and not the gravitational one. The only case in which it is possible to directly measure the gravitational acceleration \underline{g} is in case of $\ddot{\underline{x}} = 0$, which means if the measurement is conducted in static conditions on the Earth’s surface, with the gravimeter properly oriented along the direction of the gravity vector (with sensitive axis along the plumb line). To measure the kinematic acceleration another instrument has to be used and with the advent of GNSS, all airborne systems use a GNSS receiver to track the vehicle movements and determine the motion.

Actually the equation for airborne gravimetry is more complicated than Eq.2 because of the dynamic conditions in which the measurement is done. First of all, different reference frames require to be considered as shown in Fig.1, which are:

- the *body frame* where the axes are defined by principal the axes of the vehicle: forward, to-the-left and up;
- the *navigation reference frame* in which the navigation equation are formulated; this frame is a local Cartesian reference frame with origin in a point P with known coordinates with respect to the reference ellipsoid, z-axis aligned with the normal to the ellipsoid, the x-axis pointing toward east and y-axis toward north, forming North-East-Up frame (l-frame);
- *Earth-centered Earth-fixed reference frame* with origin in the Earth’s center of mass and axes defined by conventional pole and Greenwich meridian (e-frame).

In the navigational frame (*l-frame*) the general equation to obtain the gravity vector from airborne gravity measurements

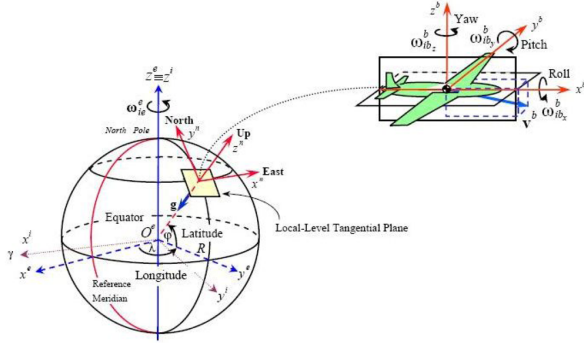


Figure 1. Reference frames adopted in airborne gravimetry (from (12))

can be written in the following way (21):

$$\underline{g}^l = \underline{\ddot{x}}^l - \underline{f}^l + (2\Omega_{ie}^l + \Omega_{el}^l)\underline{\dot{x}}^l \quad (3)$$

where the superscript l stand for l -frame. In Eq.3 $\underline{\ddot{x}}$ is the aircraft acceleration vector, \underline{f} is the specific force measured by the gravimeter, Ω_{ie} and Ω_{el} are the skew-symmetric matrices of the angular velocities due to the Earth-rate and aircraft-rate over the ellipsoid, $\underline{\dot{x}}$ is the vehicle velocity vector. The third right-hand term of this expression represents the Coriolis acceleration vector.

Moving from the vector form to the scalar one, considering just the vertical component of interest, Eq.3 becomes:

$$g_U^l = \ddot{x}_U^l - f_U^l - \left(\frac{v_E^2}{R_1 + h} - 2\omega_{ie}v_E \cos\varphi - \frac{v_N^2}{R_2 + h} \right) \quad (4)$$

with \ddot{x}_U the acceleration component in the Up axis, v_E , v_N the velocity components in the East, North axis of the navigational frame, R_1 and R_2 the prime vertical and the meridian radii of curvature. The third term in parenthesis represents the so called Eötvös correction term to consider the centripetal acceleration generated by the movement of the aircraft over a curved and rotating Earth (Schwartz et al., 1997).

To complete the general equation of airborne gravimetry, at least another correction term need to be considered: the one to remove the lever-arm effect. This effect is a consequence of the fact that the gravimeter and the GNSS receiver observations are referred to two different physical points so the vertical accelerations sensed by the two instruments can differ due to the aircraft attitude variations (i.e. its orientation relative to Earth's horizon). It can be modeled if the aircraft orientation and the onboard instruments geometry are available or may be neglected if the offset between the GNSS antenna and the gravimeter is small. A stable and accurate formula to compute it is given in (Jekely, 1998), assuming to know the lever-arm position (\underline{b}^b) in the inertial reference frame:

$$\underline{LA} = \frac{d^2}{dt^2} \left(\mathbf{R}_b^i \underline{b}^b \right) \quad (5)$$

where \underline{LA} is the lever-arm effect, \mathbf{R}_b^i is the rotation matrix to transform the lever-arm coordinates from the body frame, \underline{b}^b , to the inertial one. To be precise, also the tilt effect should be considered (namely the effect due to a misalignment of the stabilized platform), however in airborne gravimetric surveys it is automatically corrected and it will not be introduced in the following equations. At this point, the general equation for

gravity at a certain altitude results to be:

$$\underline{g} = \underline{\ddot{x}} - \underline{f} - \underline{E\ddot{o}} - \underline{LA} \quad (6)$$

with $\underline{\ddot{x}}$ the result of GNSS data processing, \underline{f} the output of the gravimeter, $\underline{E\ddot{o}}$ the Eötvös correction term, \underline{LA} the lever arm term.

In the end, it is worth to be mentioned that in a real aerogravimetric survey the gravimeter does not measure \underline{f} but its variations with respect to the value measured at a certain calibration point. The instrument calibration is generally done in static conditions at the airport before the departure and the measured value is assumed as a reference for all the following data acquired during the survey. The standard quantity used as reference is the gravity disturbance, obtained as the difference between the gravity acceleration \underline{g} at a certain point P and the normal gravity $\underline{\gamma}$ at the same point. This means that Eq.6 in classical airborne gravimetry is modified in:

$$\underline{\delta g} = \underline{\ddot{x}} - \underline{f} - \underline{E\ddot{o}} - \underline{LA} - \underline{\gamma} - \underline{\delta g_0} \quad (7)$$

with $\underline{\delta g}$ the gravity disturbance, $\underline{\gamma}$ the normal gravity and $\underline{\delta g_0} = g_0 - \gamma_0$ the gravity disturbance measured at the calibration point.

2.2 Classical pre-processing of airborne gravity data

The standard procedure to pre-process raw aerogravimetric data acquired with the GNSS receiver and the gravimeter is here presented. With the term "raw" data we refer to the direct output of the onboard instrumentation without any processing.

The GNSS data are used for navigational purposes to derive the aircraft trajectory, velocity and acceleration. For airborne gravimetry, the observable commonly used is the carrier phase, obtained from the difference between the incoming carrier wave and the phase of a signal generated internally by the receiver. The general expression of the GNSS signal traveling in the Earth's atmosphere is:

$$L_{r,i}^s(t_r) = \rho_r^s(t^s) + \lambda_i N_{r,i}^s + c(\delta t_r - \delta t^s) + T_r^s(t_r) - I_r^s(t_r) + m_r^s(t_r) + \epsilon_{r,i,L}^s \quad (8)$$

where ρ is the geometric distance between the receiver position at epoch t_r and the satellite position at t^s , λ is the wavelength of the carrier phase i , N is the integer ambiguity, c is the speed of light, δt_r and δt^s are the receiver and satellite clock errors, T_r^s is the tropospheric delay due to the neutral part of the Earth's atmosphere, I_r^s is the ionospheric delay and depends on the free electrons content in the ionosphere, m_r^s is the multipath effect, caused by the signals that reach the receiver after being reflected and not from the direct path and finally ϵ_r^s is the observation error. To estimate the receiver position, reducing as much as possible these errors which affect the observations, the double differences of carrier phase are commonly used. Given two receivers r and l , observing simultaneously two satellites s and u , it is possible to combine the carrier phase observable (L_i) to form a new observable, called double difference of carrier phase, which displays as follows:

$$L_{rl,i}^{su}(t) = L_{rl,i}^s(t) - L_{rl,i}^u(t) = \rho_{rl,i}^{su}(t^s) + \lambda_i N_{rl,i}^{su} + T_{rl}^{su} - I_{rl,i}^{su}(t) + m_{rl,i}^{su}(t) + \epsilon_{rl,i}^{su} \quad (9)$$

where the notation stands for:

$$\cdot_{rl}^{su} = (\cdot_i^s(t) - \cdot_r^s(t)) - (\cdot_i^u(t) - \cdot_r^u(t)). \quad (10)$$

The use of this differentiated observable prevents the estimation of the absolute position of the receiver and consents only to determine its relative position with respect to another station. Generally the reference station is chosen among the ground permanent stations (continuously operating network). In case this is not possible, a ground point is used as reference station, measured in static conditions and post-processed in Precise Point Positioning (PPP - an absolute positioning method). Despite this aspect of relative position, the double difference of carrier phase remains nowadays the fundamental observable used for positioning because it brings some important benefits in the reduction of the unknown terms and of the errors afflicting the signal (i.e. the receiver clock unknowns, the fractional part of the initial ambiguity).

In practice, the GNSS observations acquired during an aerogravimetric survey are processed using commercial software which provide to detect and repair cycle slips, model and remove tropospheric and ionospheric errors, fix initial ambiguities and determine the double differences estimates for each flight line. Once estimated the positions, the aircraft accelerations are obtained with two numerical differentiations. The inertial accelerations measured by the gravimeter instead, before the combination with GNSS accelerations, are processed with the principal aim of reducing the observation noise. The gravimeter's recording rate, in fact, is usually extremely higher than the GNSS one so data have to be filtered and downsampled to match GNSS measurements. The filters have to be carefully chosen to avoid and reduce at minimum biasing the data. In general the standard filtering procedures for gravimeter data are based on the a-priori knowledge of the error spectrum. Before computing gravity, these gravimeter accelerations are corrected for the Eötvös effect and for normal gravity. In the end, gravity is calculated by subtracting the GNSS derived aircraft accelerations from the inertial accelerations, according to Eq.7.

3. METHODOLOGY TO PRE-PROCESS THE DATA

3.1 The variometric approach for GNSS processing

In this section the objective is to recall the theory behind the estimation of GNSS accelerations within the variometric approach (Colosimo, 2012). The basic idea is the definition of a new observation equation directly sensitive to the antenna acceleration. This new observable is obtained from the manipulation of the classical GNSS phase observation (Eq. 8) which instead is sensitive to the actual antenna position. Before introducing the equations it has to be underlined that the proposed methodology has been expressly thought for airborne gravimetry applied to resources exploration geophysics. This means that the final target of GNSS pre-processing is the estimation of the aircraft accelerations over a region with a maximum extension of $100 \times 100 \text{ km}^2$ and acquired close to the ground (at heights of about 150 m over the topography) with accuracies possibly better than 1 mGal at a spatial resolution of about 500 m . For a complete description of typical characteristics of such airborne acquisition the interest reader can refer to (Schwartz et al., 1997). To reach this accuracy level, four main assumptions have to be done:

- an approximated trajectory \tilde{x} of the aircraft flight is known; being x the real trajectory (see Fig.2), the error of the approximated track for each epoch t , $\xi_t = x_t - \tilde{x}_t$, is supposed to be smaller than 10 cm ;

- the aircraft is flying at an almost constant velocity of 50 ms^{-1} ; this means that, considering for example as final target an acceleration at a spatial resolution of about 500 m , the vehicle acceleration can be modeled in principle with a temporal resolution of 10 s ;
- several GNSS constellations are available and used, exploiting the largest number of satellites;
- GNSS observations are cycle-slip free; this is satisfied adopting specific algorithms to detect and fix the cycle-slips in the acquired data.

The geometry of the GNSS problem is schematically presented in Fig.2.

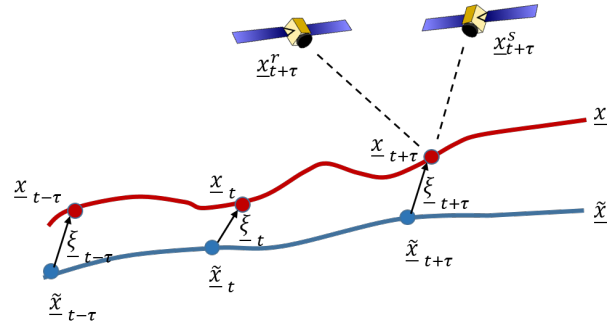


Figure 2. Schematic representation of the GNSS problem

According to the notation used in this figure the classical GNSS observation equation can be written as:

$$L_{t+\tau}^s = \rho_{t+\tau}^s + \sigma_{t+\tau}^s - \sigma_{t+\tau} - N^s \lambda + T_{t+\tau}^s - I_{t+\tau}^s + \nu_{t+\tau}^s \quad (11)$$

where $L_{t+\tau}^s$ is the GNSS phase observation for satellite s at epoch $t + \tau$, $\rho_{t+\tau}^s = \|x_{t+\tau}^s - x_{t+\tau}\|$ the geometric distance between receiver and satellite, $\sigma_{t+\tau}^s$ and $\sigma_{t+\tau}$ are the satellite and the receiver clock offsets respectively, N^s is the (integer) initial ambiguity for satellite s , λ is the wavelength for the considered GNSS signal, $T_{t+\tau}^s$ and $I_{t+\tau}^s$ are the tropospheric and ionospheric delays and $\nu_{t+\tau}^s$ is the observation error due to the receiver circuitry.

Taking in consideration two different satellites (s and r) as represented in Fig.2, it is possible to compute the difference between these two GNSS phase observations at the same receiver:

$$L_{t+\tau}^{sr} = L_{t+\tau}^s - L_{t+\tau}^r \quad (12)$$

(denoting with the superscript \cdot^{sr} the difference between \cdot^s and \cdot^r). Now, considering two epochs t and $t + \tau$, it is also possible to compute another difference of these quantities. The full expression of the new observable is:

$$L_{t+\tau,t}^{sr} = \rho_{t+\tau,t}^{sr} + \sigma_{t+\tau,t}^{sr} + T_{t+\tau,t}^{sr} - I_{t+\tau,t}^{sr} + \nu_{t+\tau,t}^{sr} \quad (13)$$

This observable is sensitive to the aircraft velocity, so to obtain the final expression relative to the acceleration another epoch has to be taken into account, e.g. $t - \tau$, and the observable becomes:

$$\begin{aligned} L_{t+\tau,t}^{sr} - L_{t,t-\tau}^{sr} &= \rho_{t+\tau,t}^{sr} - \rho_{t,t-\tau}^{sr} + \sigma_{t+\tau,t}^{sr} - \sigma_{t,t-\tau}^{sr} + \\ &+ T_{t+\tau,t}^{sr} - T_{t,t-\tau}^{sr} + I_{t+\tau,t}^{sr} - I_{t,t-\tau}^{sr} + \\ &+ \nu_{t+\tau,t}^{sr} - \nu_{t,t-\tau}^{sr}. \end{aligned} \quad (14)$$

To make this quantity dimensionally homogeneous to an acceleration one can divide it by τ^2 . Now it is possible to prove that, once properly chosen the time step τ (e.g. equal to 5 s) all the right terms of the above equation, except from the first one ($\rho_{t+\tau,t}^{sr} - \rho_{t,t-\tau}^{sr}$), have errors in the range of few tenths of a *mGal* (Capponi, 2018), so it is possible to proceed with the linearization with respect to the unknown acceleration of the GNSS receiver.

Lets recall that, the term $\rho_{t+\tau,t}^{sr} - \rho_{t,t-\tau}^{sr}$, is related to geometric distances between the receiver and satellites, containing the unknown receiver position coordinates that can be re-conducted to the sensed accelerations. Recalling that:

$$\rho_{t+\tau}^s = \left\| \underline{x}_{t+\tau}^s - \underline{\tilde{x}}_{t+\tau} - \underline{\xi}_{t+\tau} \right\| \quad (15)$$

so the term $\rho_{t+\tau}^s$ can also be rewritten as:

$$\rho_{t+\tau}^s \approx \tilde{\rho}_{t+\tau}^s - \underline{\tilde{e}}_{t+\tau}^s \cdot \underline{\xi}_{t+\tau} \quad (16)$$

where the $\underline{\tilde{e}}_{t+\tau}^s$ corresponds to the unit vector centered at the receiver with direction toward the satellite s . If $\delta\rho_{t+\tau}^s$ is the difference $\rho_{t+\tau}^s - \tilde{\rho}_{t+\tau}^s$, considering two different epochs $t + \tau$ and t , we have:

$$\delta\rho_{t+\tau,t}^s = -\underline{\tilde{e}}_{t+\tau}^s \cdot \underline{\xi}_{t+\tau} + \underline{\tilde{e}}_t^s \cdot \underline{\xi}_t. \quad (17)$$

By subtracting the term relative to the interval $(t, t - \tau)$ and by manipulating the equations we get:

$$\delta\rho_{t+\tau,t}^{sr} - \delta\rho_{t,t-\tau}^{sr} = -\frac{\underline{\tilde{e}}_{t+\tau}^{sr} + \underline{\tilde{e}}_{t-\tau}^{sr}}{2} \cdot \left(\underline{\xi}_{t+\tau} - 2\underline{\xi}_t + \underline{\xi}_{t-\tau} \right). \quad (18)$$

Note that, apart for a constant equal to the inverse of the squared time variation, this term is proportional to the correction to be applied to the approximated acceleration (obtained from the approximated position $\underline{\tilde{x}}$) to compute the actual acceleration. The final linearized observation equation reads:

$$\begin{aligned} L_{t+\tau,t}^{sr} - L_{t,t-\tau}^{sr} &= \tilde{\rho}_{t+\tau,t}^{sr} - \tilde{\rho}_{t,t-\tau}^{sr} + \\ &- \frac{\underline{\tilde{e}}_{t+\tau}^{sr} + \underline{\tilde{e}}_{t-\tau}^{sr}}{2} \cdot \left(\underline{\xi}_{t+\tau} - 2\underline{\xi}_t + \underline{\xi}_{t-\tau} \right). \end{aligned} \quad (19)$$

Looking at Eq.19 to estimate the unknown values of the correction for aircraft approximated accelerations, the procedure requires:

- approximated values of the aircraft trajectory and satellite positions to compute the $\underline{\tilde{e}}_{t\pm\tau}^{sr}$ term and $\tilde{\rho}_{t+\tau,t}^{sr}$ and $\tilde{\rho}_{t,t-\tau}^{sr}$;
- GNSS observations without cycle-slips.

Regarding the first point, once computed the satellites positions from the ephemerids, the approximated aircraft trajectory can be estimated in different ways: if a ground infrastructure is available, it can be derived by using a differential approach (classical double differences) or, if the infrastructure is not available, it can be estimated by means of a classical stand-alone GNSS positioning by means of code and phase observations (Colon, 1999).

About the cycle-slips detection, within the proposed methodology, it is performed by means of four different techniques, standardly used in GNSS processing (Karaim et al., 2014): a comparison between phase and code observations

(CODE), a comparison between phase and Doppler shift observations (DOPPLER), an analysis of time variation of phase observations (TIME) and analysis of geometry free combination (GEO-FREE). In case of absence of cycle-slips the first two quantities, namely $CODE_t$ and $DOPPLER_t$ are expected to be zero, while the last two are expected to be a smooth signal. On the contrary if a cycle-slip is present in the phase observations a jump appears in all the above observables. In order to detect a cycle-slip the four observables are computed for all the available epochs, after that they are ordered by their smoothness thus selecting the two methods with the smallest standard deviation. Finally a certain epoch is flagged as cycle-slip, if a jump larger than a certain threshold occurs in both the two selected observables. Once the potential cycle-slip is detected, by means of a Grubbs test (Grubbs, 1950), the integer number of cycles slipped is estimated and the phase observation is corrected accordingly.

Once detected and repaired the cycle slips from the observations, estimated the satellites positions and the approximated aircraft tracks, the linearized Eq.19 is solved in term of the unknown accelerations corrections by means of a Least Square adjustment. It is important to highlight that the well known biases and drifts typical of the variometric approach (Colosimo, 2012) can be here safely disregarded due to the application in the consequent steps of the processing procedure of a Wiener filter.

3.2 The gravimeter processing

The theoretical aspects related to the processing of the accelerations sensed by the gravimeter, before their combination with GNSS derived accelerations, are here recalled. The gravimeter data require to be corrected for all the errors affecting the onboard instrumentation of the aircraft; moreover, being acquired with a very high sampling rate (up to 128 Hz), they are characterized by large noise which is the sum of the accelerometer errors and the high frequency signal (e.g. accelerations with frequencies higher than 0.2 Hz which are not sensed by the GNSS receiver). Consequently, these data need to be filtered and downsampled without losing information on the real gravity signal.

The first correction to be applied is related to the geometry of the onboard instruments and it is necessary due to the fact that the gravimeter center of mass does not coincide with the GNSS antenna phase center. This effect is referred to as the lever-arm effect (Saint Jean, 2007) and, if not properly accounted for, it causes the two instruments to measure accelerations at different points. In order to compute it, the coordinates of the gravimeter center of mass and GNSS antenna phase center should be known in the aircraft reference frame (*b-frame*) to measure the precise distance between them, also called the arm. The three dimensional position of the arm, for each observation epoch t , can be determined by multiplying the current arm by the rotation matrix \mathbf{R} computed from the roll (r) and pitch (p) angles (Fig.3). Now, by applying a double differentiation in time (Jekely, 1998) the correction term can be estimated and removed from the gravimeter raw observations. The second effect that can not be neglected is the so called Eötös effect. This correction term needs to be added to gravimeter observations to compensate for horizontal motion over the Earth's surface, which causes a change in the perceived gravitational force due to the change in centrifugal acceleration. To compute this effect it is necessary to know the aircraft velocities in the navigational frame (*l-frame*) and the East-West and North-South direction, v_e and v_n respectively,

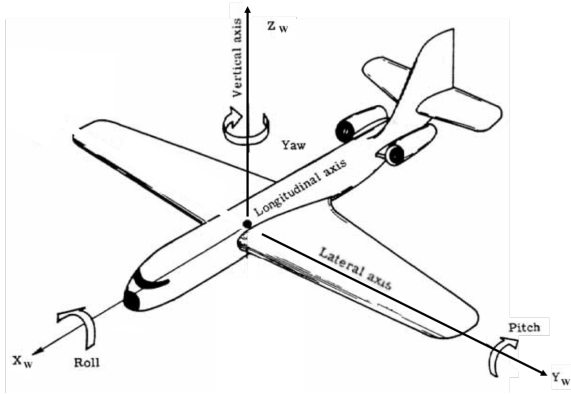


Figure 3. Roll, pitch and yaw rotation angles

as well as the aircraft latitude φ and altitude h . Once known all these parameters the Eötös term can be computed adopting the following formula, derived manipulating the one proposed by (Harlan, 1968):

$$Eo = \frac{v_e^2}{r \frac{v_e^2}{(1-e^2 \sin^2(\varphi))^{\frac{1}{2}}} + h} - 2\omega v_e^2 \cos(\varphi) - \frac{v_n^2}{\frac{r(1-e^2)}{(1-e^2 \sin^2(\varphi))^{\frac{3}{2}}} + h} \quad (20)$$

where r is the Earth's radius at the equator, e^2 is the Earth's first eccentricity and ω is the Earth's angular velocity.

Once the above corrections have been applied to the gravimeter data, another important aspect to deal with is the very different rate of acquisition for the gravimeter and the GNSS receiver. Generally the former acquires data at 128 Hz while the latter usually has an acquisition rate of 10 or 20 Hz . As a consequence the gravimeter observations are characterized by the presence of high frequency signals, due for instance to air turbulence, which are not present in the GNSS counterpart and should be therefore considered as noise. Within this work, a first operation to reduce this noise and the acquisition rate consists in applying a moving average to the gravimeter observations. The size of the moving average window has to be properly chosen in such a way to have mean values at a frequency close to the acquisition rate of GNSS receiver. The importance of this step regards the necessity to leave unchanged the average accelerations which will be subsequently used to determine the gravitational field. Once applied the moving average, the data are downsampled by a factor equal to the size of the moving average itself.

Once both dataset have been adjusted for the errors affecting the measurement units, the final operation, before combining them, consists in the application of cubic splines interpolation, thus allowing the synchronization of the two different measurement systems. After the synchronization of the GNSS and gravimeter acceleration observations, the "raw" gravity acceleration is finally derived simply as the difference of the two dataset:

$$g = f_{grav} - f_{levarm} - f_{E\ddot{o}} - \ddot{x}_{GNSS}. \quad (21)$$

4. METHODOLOGY TO PROCESS THE DATA

4.1 Remove-compute-restore procedure

The gravity accelerations derived from airborne gravimetric observations are still dominated by noise gathered during the acquisition process, e.g. because of the vehicle vibrations and

the atmospheric turbulence. For this reason, the application of a proper procedure is necessary to analyze and elaborate the data in terms of grids or sparse points of gravity anomalies or disturbances. The main problem related to airborne gravity data processing is the extremely high noise-to-signal ratio, e.g. higher than 1000, that has to be properly reduced applying a procedure which can disentangle the noise from the actual gravity signal.

To predict grids of gravity anomalies or disturbances starting from the raw gravity accelerations, derived from airborne measurements, two main problems have to be solved. The first problem is related to the correct separation of the low frequencies signal from the observation colored noise; the second one regards the application of a proper filter to disentangle the high frequencies noise from the actual gravity signal. It is worth to be mentioned that the observation colored noise is characterized by low frequencies due to drifts of the instrumental measurement system and by high frequencies associated to the aircraft vibrations, atmospheric turbulence, etc. The former problem, namely the removal of the low frequencies signal, can be solved nowadays by exploiting Global Gravity Models (GGMs). To retrieve the low frequencies of the local gravity field in fact global models derived from satellite gravimetry/gradiometry (e.g. GRACE and GOCE data) can be used, as well as models obtained from the integration of satellite data with radar altimetry and surface measurements. The latter problem, namely the separation of high frequencies noise from the actual signal, is solved choosing the proper filter to be applied. By merging GGM and local airborne data the combined gravity field signal is characterized, for the low frequencies, basically by the information of GGM and for the medium and high frequencies, by information coming from the filtered airborne signal itself. The most commonly adopted and applied approach to airborne gravity observations is the remove-compute-restore technique (Schwartz et al., 1990) which can be summarized as follows. In the remove step, a low frequency signal, predicted from GGMs, and an high frequency one, obtained from the computation of the gravitational effect of topography, are removed from the observations; the observations are then filtered to separate the signal from the noise. In the compute step, the filtered gravity accelerations are converted in grids or sparse points of gravity anomalies/disturbances using for example the Least Squares Collocation. Finally, after having carried out the compute step, the long-wavelength and short-wavelength signals removed at the beginning are restored back.

The implemented procedure, here presented, is basically a remove-compute-restore -like procedure and the proposed processing scheme is shown in Fig.4 and outlined in the following. The first step consists in creating a reference signal, δg_{ref} , along the aircraft trajectory; it is generated from existing GGMs, adding to it a Residual Terrain Correction (RTC):

$$\delta g_{ref} = \delta g_{GGM} + \delta g_{RTC}. \quad (22)$$

The first term on the right, namely δg_{GGM} , results from a spherical harmonic synthesis of the GGM up to its maximum degree/order L_{max} . This operation consists in using the coefficients $C_{\ell m}$ and $S_{\ell m}$, given by the GGM, to compute the desired functional of the gravitational potential. The second term of Eq.22, namely δg_{RTC} , is the result of the difference between two terrain corrections (Sampietro et al., 2016): the first one computed using a high resolution Digital Terrain Model (DTM) and the second one computed with a smoother DTM obtained applying a moving average window

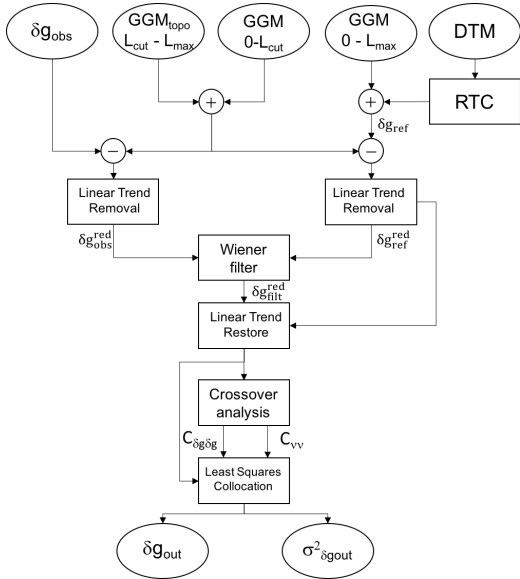


Figure 4. Flow chart of the procedure implemented to filter and grid raw aero-gravimetric data

to the original refined terrain model. The reason why we use a “residual” topography for the terrain effects, is that the low frequency of the terrain gravimetric signal is already incorporated into the global model GGM (see the discussion in (Hirt, 2010)).

Once the reference signal has been created, the following step is the remove one. It consists in subtracting from both the observed and the reference signals, δg_{obs} and δg_{ref} respectively, the contribution of a global model for the low frequencies and of a global model of terrain correction for the medium-high frequencies. The contribution for the low frequencies is estimated from the same global model used to create the reference signal with a spherical harmonic synthesis up to a certain intermediate degree L_{cut} (e.g. 210 or 360). The contribution of the topography instead is derived from a spherical harmonic synthesis of a global gravity model related to the topography (e.g. *dV_ell_ret2012*) from the same L_{cut} to the maximum degree of the model L_{max} . The choice of L_{cut} should be carefully performed since this degree is basically used to define the limit between low frequencies, where for the final estimates only the GGM data are adopted, and medium-high frequencies, in which the airborne observations count more than GGM. Moreover within the remove step, if required, a linear trend for each single flight line, estimated from the reference signal, is also removed. This last operation is required considering that in general the inertial observations are contaminated by drifts and biases. The above procedure leaves the reduced observations δg_{obs}^{red} and the reduced reference signal δg_{ref}^{red} with zero mean and with a smaller amplitude and spatial correlation with respect to the original signals.

The third step is the filtering of δg_{obs}^{red} by means of the application of a Wiener filter along each single flight track. As will be detailed in the next section the Wiener filter filters the reduced raw gravity observations according to the power spectrum expected from the reduced reference model. After the data have been filtered and the colored noise has been separated from the observations, the linear trend removed in the previous step is added back thus obtaining regularly sampled tracks of the filtered reduced gravity disturbances δg_{fil}^{red} . Now, before the compute step in which the Least Squares Collocation is used to derive from δg_{fil}^{red} the gravity disturbances in correspondence

of the interested grid nodes, the covariance functions of both the noise and the signal require to be estimated. Regarding the noise, an analysis of the residuals at the crossovers, i.e. by definition the intersection points between two different aircraft tracks, is performed. The analysis of the residuals of δg_{fil}^{red} at these points can provide an empirical estimate of the noise stochastic properties along the aircraft trajectory. The signal covariance function is instead empirically estimated from the observations, so, differently from the error covariance which is an along-track one, it is a spatial one that is modeled as a linear combination of a set of Bessel functions of the first order and zero degree (22).

A grid or a set of sparse points of δg_{fil}^{red} and their corresponding error are generated by a Least Squares Collocation solution, namely in the compute step and in conclusion, within the restore step, the signal removed at the beginning of the procedure are restored back.

4.2 The Wiener filter

As stated in the previous section the first operation of the whole processing procedure is building a reference signal δg_{ref} , without using airborne data, that has to be as close as possible to the actual gravity field. This signal can be generated by using a high-degree GGM (e.g. EIGEN-6C4 or GECO (Gilardoni, 2016)) and adding to it a residual terrain correction, to fill the missing high frequencies that lack in these global models. The importance of creating this δg_{ref} is due to the fact that the recently developed GGMs in principle exploit the gravity data coming from the ultimate gravimetric satellite missions (i.e. GRACE and GOCE) and this means that their low frequencies are expected to be more reliable or at least better sampled than the ones derived from airborne measurements. For this reason, the δg_{ref} is practically used to retrieve the low frequencies of the filtered signal but, as described further on, it can be used also to estimate the filtered signal stochastic properties.

To filter the reduced observations δg_{obs}^{red} a track-by-track Wiener filter in the frequency domain can be applied. This is a filter generally adopted in signal processing that produces an estimate of the desired random process by the linear time-invariant filtering of an observed process affected by noise, under the assumption of knowing the spectra of both stationary signal and noise. This filter is based on a statistical approach, since it used the Minimum Mean Square Error (MMSE) estimator. The principal assumption for the application of the Wiener filter is that the signal and the additive noise are stationary linear stochastic processes with known spectral characteristics or known autocorrelation and cross-correlation. Given a general system:

$$y(t) = x(t) + \nu(t) \quad (23)$$

where $x(t)$ is the original signal (unknown) at a certain epoch t , $\nu(t)$ is the additive noise (unknown), independent of $x(t)$, and $y(t)$ is the observed signal. The objective is to find a function $g(t)$ that allows to estimate $x(t)$ by the following constitutive formula:

$$\hat{x}(t) = (g * y)(t). \quad (24)$$

In Eq.24, \hat{x} represents the estimate of $x(t)$ that minimizes the mean square error. Moving to the frequency domain, the filter $G(f)$ which is the Fourier Transform of g at frequency f , can be easily described as:

$$G(f) = \frac{S(f)}{S(f) + N(f)} \quad (25)$$

where $S(f)$ and $N(f)$ represent the mean power spectral densities of the original signal $x(t)$ and of the additional noise $n(t)$ respectively. In the frequency domain the filtering operation results in:

$$\hat{X}(f) = G(f)Y(f) \quad (26)$$

with $\hat{X}(f)$ and $Y(f)$ the Fourier Transform of $\hat{x}(t)$ and $y(t)$ respectively. The final filtered signal $\hat{x}(t)$ is obtained by simply performing the inverse Fourier Transform on $\hat{X}(f)$. Rewriting Eq. 25 in the following way, the performance of the Wiener filter becomes apparent:

$$G(f) = \frac{1}{1 + \frac{N(f)}{S(f)}} = \frac{1}{1 + \frac{1}{SNR(f)}}. \quad (27)$$

Here, $SNR(f) = \frac{S(f)}{N(f)}$ is the signal-to-noise ratio. At the frequencies in which the noise increases, the signal-to-noise ratio decreases, so the filter $G(f)$ decreases too. This means that the Wiener filter attenuates frequencies depending on their signal-to-noise ratio.

By considering our observed signal δg , the filter G can be rewritten as:

$$G = \frac{S_{\delta g}}{S_{\delta g} + S_{\nu}} \quad (28)$$

with $S_{\delta g}$ and S_{ν} the power spectral densities of the reduced signal and the observation noise, respectively. The former is computed from the reference signal δg_{ref}^{red} applying the Fourier transform in the following way:

$$S_{\delta g} = | \text{FFT}(\delta g_{ref}^{red}) |^2. \quad (29)$$

The latter is derived from the difference between the spectral density of the observed signal δg_{obs}^{red} and the spectral density of the reference δg_{ref}^{red} .

$$S_{\nu} = | \text{FFT}(\delta g_{obs}^{red}) |^2 - S_{\delta g}. \quad (30)$$

In practice, considering that the reduced reference signal has zero low frequencies, after the application of the Wiener filter we obtain a filtered observed signal that has these low frequencies replaced by the GGM ones. Note that within this step which largely depends on the δg_{ref} model, it is better to underestimate S_{ν} in such a way to be sure that no signal is erroneously filtered and letting the Least Squares Collocation step to refine the Wiener filter.

4.3 The crossover analysis

The characterization of the noise affecting airborne gravity observations, in terms of its stochastic properties, is an important issue to be solved. Within the processing procedure here proposed this problem has been solved by using the crossover analysis. In classical airborne gravity data processing, this method is usually adopted but for different scopes: in particular it is simply used to evaluate the quality of the filtered data (Arabelos et al., 1992) or it is used to retrieve the low frequencies of the gravitational field on the basis of the crossovers (CarbonNet project report, 2012). In this work the crossover analysis is adopted to empirically retrieve the along-track observations error covariance function.

In an airborne gravimetric survey generally there are two main flight directions, perpendicular with each other, that allows to divide the flight lines in two different categories: namely called

traverse and control lines. By definition the crossover is the point at the intersection between a traverse and a control line (see Fig. 5).

To apply the crossover analysis the first thing to do is to model each aircraft track as a straight line, estimating its parameters by means of a Least Squares adjustment. This modeling step is necessary to identify the intersection point between the two considered tracks. Then the gravity field is evaluated in correspondence of the intersections of traverse and control lines, computing separately the gravity field from each single line. After the interpolation, the gravity field values on the modeled lines are predicted at the intersection points. Considering the dynamic environment in which measurements are done, it is possible that the two flight lines at their intersection are characterized by different heights. To overcome this problem and to properly evaluate the residual at the crossovers, the gravity values derived from the two lines at their intersections are moved along the vertical direction. Note

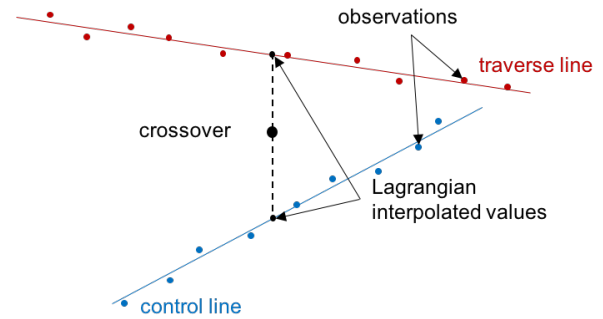


Figure 5. Geometry of the crossover analysis

that to derive the residuals at the crossover, the gravity field data are shifted in both the horizontal and vertical directions. However these “movements” produce in general a limited effect. In fact, analyzing the data of a real acquisition (i.e. the dataset used in the Numerical Tests section) the maximum along-track shift can be in the worst case of 250 meters, while in the vertical direction it is of about 1 m, in both cases these differences are negligible especially when dealing with the reduced signal.

Once evaluated the residuals at the crossovers, they can be associated to the error of the filtered gravity disturbances at the same observed point from different tracks. So, taking each control line the whole set of its estimated errors can be used to compute the empirical along-track error covariances. If the along-track error is stationary (i.e. if we can suppose that its stochastic properties does not change in time and therefore are the same for all the survey tracks), which is a realistic hypothesis to be applied to an airborne gravimetric survey, it is possible to average the error covariances of all the control lines to obtain the final estimate of the empirical along-track error covariance function. This operation guarantees the estimate of a robust error covariance, property that can not be valid for a single flight line, due to the limited number of covariance samples retrievable, in particular for long wavelengths. This empirical error covariance is then interpolated by means of a proper theoretical covariance function and the covariance matrix $C_{\nu\nu}(\psi)$ (with ψ representing the spherical distance along the aircraft track) is generated for the subsequent Least Squares Collocation.

4.4 Signal Covariance Modelling and Least Squares Collocation

In order to compute the final gravity disturbances δg on a grid or on a set of sparse points, besides the empirical covariance of the observation error, also the observed signal empirical covariance requires to be evaluated.

To retrieve this empirical covariance two possible strategies can be followed. The first possibility consists in retrieve it from the original reference global model. In details, a grid of reference gravity disturbances δg_{ref} can be generated from the global model, and, once reduced, it can be used to create the empirical covariance function. The second strategy consists in estimating it from the airborne filtered reduced data only. The principal difference between these two approaches is that the second approach, differently from the first one, is completely independent from the reference gravity model and depends only from the observed airborne data. Within the proposed methodology, the second strategy has been adopted with the aim to define a procedure not strongly dependent from external data. It consists in empirically computing the signal covariance function from the along-track filtered reduced signal, and subsequently modeling it with a linear combination (with positive coefficients) of Bessel functions (Sansó, 1997). The coefficients of this linear combination are estimated by means of a non-negative Least Squares Adjustment.

After that the covariance functions have been modeled, they can be used to build the covariance matrices required for the Least Squares Collocation solution. At this point of the computation so the available data are: a set of along-track filtered and reduced observations δg_{fil}^{red} , the covariance model of this signal and the covariance model of the observation noise. It is important to underline that the data (δg_{fil}^{red}) are independent line by line and characterized by a stationary noise with stochastic properties retrieved from the crossovers analysis. Note that the spatial correlation of the gravity signal is due only to the gravity field.

To predict the gravity signal on a regular planar grid from the “observed” quantities the collocation, which is a stochastic method for the interpolation, is adopted. The corresponding squared error can be derived, by applying the variance propagation law. In conclusion, once estimated the final grid of gravity disturbances, in order to obtain the complete signal, all the frequencies removed before the Least Square Collocation adjustment can be restored back.

5. NUMERICAL TESTS

The implementation of a complete software for airborne gravity data processing, within this research project, was the principal topic to deal with. In fact, besides the definition of an innovative processing methodology for aerogravimetry, the software development, with the integration of the presented algorithms, occupied a major part of the whole project.

To do so, basically each phase of the proposed procedure has been implemented within a module, which can be run independently from all the other ones. This organization is justified by the fact that our purpose was the development of a flexible solution, in which the user has the possibility to analyze the actual results obtained within each step, for a deepen comprehension of the whole processing. Each single module has been firstly realized in a prototype version in Matlab language and then it has been converted in parallel C language. In order to evaluate its performances a numerical test has been

conducted by processing data coming from a real airborne gravity survey. The dataset used, has been acquired in 2014-2015 by one of the major operator providing airborne geophysical surveys for petroleum and mineral exploration. For this reason, to preserve confidentiality, all the plots shown within this chapter do not present any information about the actual coordinates of surveyed area. The test performed is aimed to evaluate the whole preprocessing procedure in terms of accuracy and computational times. As typical for airborne acquisitions for oil and gas exploration, the survey covered an area of about $1 \text{ deg} \times 1 \text{ deg}$, a multi-frequency GNSS receiver that recorded GNSS positional data at 20 Hz was used. The inertial measurement system used is characterized by an inertial platform, which remain fixed in inertial space, independently from the manoeuvres of the aircraft, allowing precise correction of the effects of the vehicle movements. Inertial accelerations are recorded at 128 Hz . The whole aerogravimetric survey required a total of 9 flights to complete around 5000 km (of a complete duration of about 30 hours). During this survey 93 flight lines were flown, divided in 84 traverse lines and 11 control lines. The former type have a line spacing of about 1.500 m . The latter are spaced about 7000 m . The flight trajectory, planned taking into account the expected terrain and the performance of the aircraft at the altitudes to be encountered, was flown at averaged flying speed of about 50 ms^{-1} at averaged altitude of 150 m above sea level. The along track raw gravity disturbances observations are computed by means of the variometric and the gravimeter processing modules. By the subtraction of GNSS derived aircraft accelerations from the inertial ones, applying the Eötvös and the lever arm correction terms and removing the normal gravity effect, the raw gravity disturbances are estimated. The complete dataset of raw gravity disturbances can be seen in Fig.6. From this figure it can be noticed that the anomalous gravitational potential, in particular its functional the gravity disturbance, is largely dominated by noise (as expected). Moreover it can also be observed that the noise is characterized by both low and high frequencies components. This characteristic makes the filtering process a complex process. The first step of the developed processing

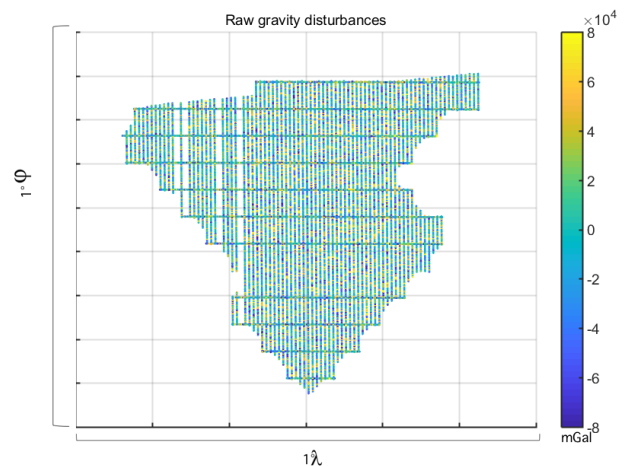


Figure 6. Along track raw gravity disturbances observations

procedure consists in computing the reference signal on the whole set of observation points. This is done by applying the spherical harmonics synthesis to estimate the gravity disturbances from the chosen GGM and by adding to it a

residual terrain correction. In this work the GGM used was the GECO model (Gillardoni et al., 2016), up to its maximum degree/order (i.e. $L_{max} = 2190$). The synthesis has been performed by the spherical harmonics toolbox developed in parallel C language.

For the residual terrain correction (RTC), the terrain correction module was used (Capponi, 2018). In details, RTC has been computed as the difference between the full resolution DTM (we used etop1 (Amante et al., 2009) with 1 arc – minute resolution) and the smoothed DTM obtained by applying a moving average window of about 10 km. The etop1 model has a resolution of about 1.5 km which is acceptable for the present case study since the offshore investigated area has an averaged depth of about 2 km. The second step of the processing procedure is the reduction of both observations and reference signals, for the low and mid-high frequencies. The first component (i.e. the low frequencies) is derived by using again the GECO model, which is known to have very well estimated low frequencies signal, due to the fact that it is derived from GOCE observations and EGM2008 (which contains GRACE data). It has to be underlined that for these frequencies, satellite gravity data are more reliable with respect to airborne local ones since they have a global coverage. The mid-high frequencies component instead has been synthesized using dV_ELL_RET2012 model from L_{cut} and L_{max} (i.e. 100 to 2190).

After the remove step the Wiener filter was applied along track. From the computational time point of view, the Wiener filtering, exploiting the properties of the FFT, requires about 1 s for each flight lines for a total amount of few minutes for the whole dataset. Fig.7 reports, for a sample flight line, the observed gravitational field, the synthesis from the GECO model up to degree 2190 and the reference signal (i.e. derived from GECO plus the residual terrain correction). Again it can be noticed how the observed gravity disturbances are completely dominated by the observation error, which contains not only very high frequencies but also trends and biases. In Fig.8 the filtered reduced signal is compared to

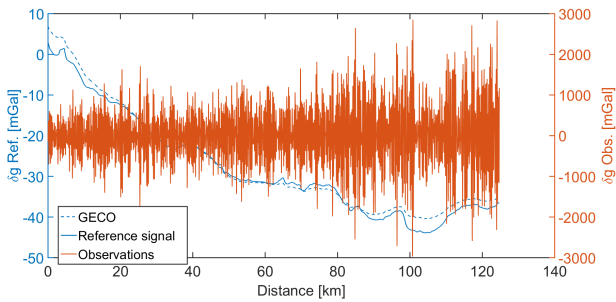


Figure 7. Along track reference and observed gravity disturbances signals

the reference one thus showing the improvements due to the airborne observations, with respect to the initial GGM-based reference signal. The order of magnitude of this improvement is of 2.65 mGal (standard deviation), for the considered flight track, which is coherent with the expected accuracy of the GECO model. Once filtered the reduced gravity disturbances, the crossover analysis was then applied. A total number of 557 crossovers has been identified and analyzed to derive the empirical covariance function of the observation noise. In addition, the empirical covariances obtained from a classical processing and with this new method implemented have been compared. The Fig.9 shows the error covariances (interpolated

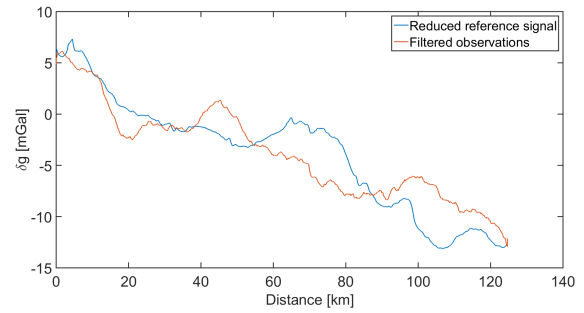


Figure 8. Along track reference and filtered gravity disturbances signals

with a theoretical model) in case of a standard processing (black line), the new processing method by using only GPS constellation for aircraft acceleration estimate (blue line) and by using all available GNSS constellations (red line). As it can be seen the improvements of the innovative processing method are noticeable moving from an error variance of 3 mGal to a new one, in the better scenario, of 1 mGal. This improvement can be practically interpreted as a better final spatial resolution of the signal that, as shown in Fig.10, can be defined as the minimum wavelength for which the signal spectrum is larger than the noise one. From the Fig.10 it emerges that the spatial resolution increase from 3 to 1 km.

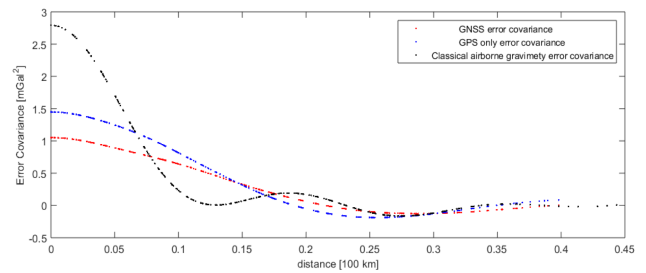


Figure 9. Error covariances comparison

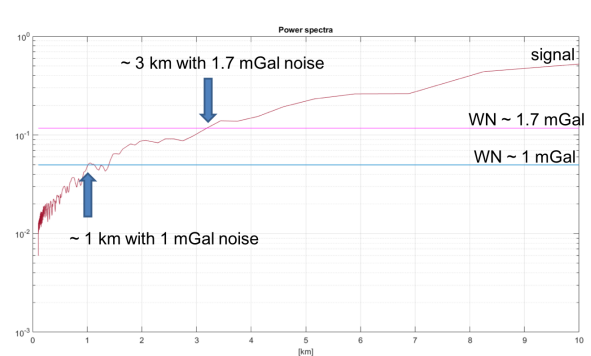


Figure 10. Spatial resolution from power spectra analysis

As for the covariance function of the reduced signal, it has been computed by means of the two methods described in previous section and it is shown in Fig.11. The main differences between the two covariances are due to the fact that the two methods use different inputs (filtered airborne along-track observations and grid of the reference model respectively) and use also different regions to estimate the signal covariance. For the Least Squares Collocation solution, the chosen signal covariance function was the one obtained with the first method, with the objective to

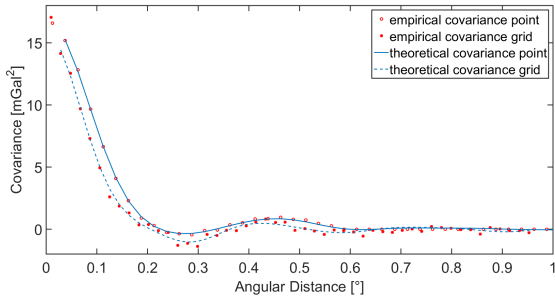


Figure 11. Covariances of the reduced filtered gravity disturbances signal

reduce the influence on the final solution of the GGM adopted. In order to compute the final results by means of the Least Squares Collocation, the dataset has been downsampled by a factor 10. In this way the observations dataset has been reduced to about 80000 points. This is justified also by the fact that the initial dataset is sampled at 2.5 m and it is corrupted by a noise with approximate correlation length of about 2 km. As a consequence the contribution to the final estimate of points closer than 25 m can be assumed to be quite limited. The final results in terms of along-track reduced gravity disturbances and their predicted errors are shown in Figs. 12 and 13. From these figures it can be seen that the predicted error is of the order of 1.3 mGal at a spatial resolution of about 1 km, increasing in proximity of the borders of the surveyed area, accordingly to the signal covariance length, due to the lack of observations in these regions. This final spatial resolution has been identified from a comparison between power spectra of noise and signal, as the minimum resolution at which the signal spectrum results to be larger than the noise one.

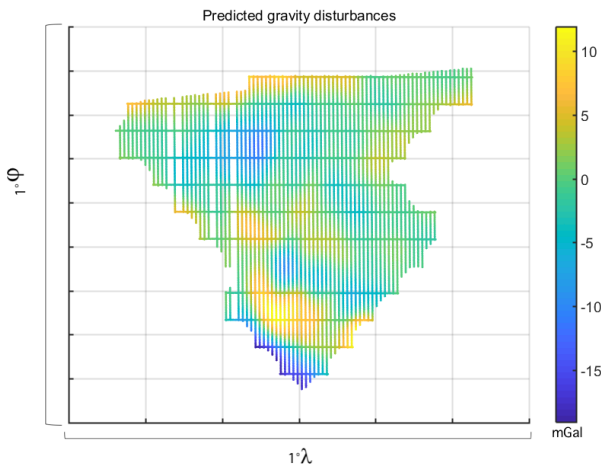


Figure 12. Predicted gravity disturbances signal for along-track points

6. CONCLUSIONS

The present work proposes a new methodology for processing airborne gravity measurements. It is known that the airborne gravimetry is nowadays one of the most efficient techniques ideal to collect gravity observations close to the Earth's surface, in a fast and cost-effective way, that achieved a wide spread with the advent of GNSS technology. The proposed

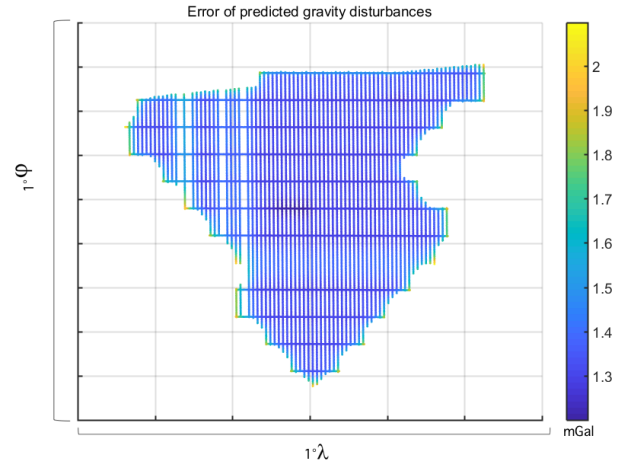


Figure 13. Accuracies of the predicted gravity disturbances signal for along-track points

method is based on an innovative approach for estimating the accelerations of a single GNSS receiver by means of the so called variometric solution that only requires the observations of a single GNSS receiver and the standard GNSS products (orbits and clocks provided with the satellites navigation message). By applying this concept to aerogravimetry, the double differences in time can be considered a valid estimator of the receiver acceleration, allowing to use the GNSS receiver as a velocimeter as well as an accelerometer. The methodology does not only consists in the application of the variometric approach for GNSS processing, but it includes also a complete procedure to process the aerogravimetric data, from the initial pre-processing phase (to derive the raw gravity accelerations) to the filtering and gridding phase (finalized to estimate grid or along track gravity disturbances). The implemented processing procedure is based on a combination of an along track Wiener filter with a classical Least Squares Collocation adjustment. Moreover, since the stochastic properties of the observation error are in general unknown, the developed algorithms include a method that on the basis of the crossovers analysis serves to empirically evaluate them. During the implementation of the whole processing procedure, it was decided to define a methodology not strictly dependent on the GGM used and based as more as possible on the acquired airborne observations. With this purpose, for instance the estimation of the empirical covariances of both the observation noise and the observed signal have been performed by fully exploiting the airborne data, without involving the GGM-derived reference signal. An important part of the whole research project regarded the implementation of a suitable software for airborne gravity data processing. The first preliminary version of this software has been developed and tested in Matlab programming environment, and then the final code has been converted in parallel C programming language. The software is organized in a set of toolboxes, which can be run independently from all the other ones, or in sequence to perform the whole processing. In conclusion, once set the various parameters on the basis of the performed tests, the entire methodology has been tested to derive the final prediction of gravity disturbances and their corresponding errors. The obtained results show a predicted signal with accuracies of about 1.3 mGal at a spatial resolution of about 1 km that degrade, as expected, with the increase of the distance from the airborne observations.

REFERENCES

- Amante, C., & Eakins, B. W., 2009. *ETOPO1 1 Arc-minute global relief model: Procedures, data sources. and analysis*. Tech. Rept. NESDIS NGDC-24, National Geophysical Data Center, National Oceanic and Atmospheric Administration (NOAA), Boulder, Colorado.
- Arabelos, D., & Tziavos, I. N., 1992. *Gravity field approximation using airborne gravity gradiometer data*. Journal of Geophysical Research: Solid Earth, 97(B5), 7097-7108.
- Blakely, R. J., 1996. *Potential theory in gravity and magnetic applications*. Cambridge University Press.
- Capponi, M., Very Improved Kinematic Gravimetry: a new to aerogravimetry, 2018. *Ph.D. Thesis*.
- CarbonNet Project Airborne Gravity Survey, 2012. *Gippsland Basin Nearshore Airborne Gravity Survey, Victoria, Australia*. Victoria: Department of primary industries, Victoria State Government.
- Colon, C. R., 1999. *An efficient GPS Position determination algorithm*. Ph.D. dissertation (No. AFIT/GE/ENG/99M-33), Air Force Institute of Technology, Wright-Pattersonafb, OH.
- Colosimo G., 2012. *VADASE-Variometric Approach for Displacement Analysis Stand-Alone Engine*. Ph.D. dissertation, University of Rome "La Sapienza", Italy.
- Gilardoni, M., Reguzzoni, M., & Sampietro, D., 2016. *GECO: a global gravity model by locally combining GOCE data and EGM2008*. Studia Geophysica et Geodaetica, 60(2), 228.
- Grubbs, F. E., 1950. *Sample criteria for testing outlying observations*. The Annals of Mathematical Statistics, 27-58.
- Harlan, R. B., 1968. *Eotvos corrections for airborne gravimetry*. Journal of Geophysical Research, 73(14), 4675-4679.
- Hirt, C., Featherstone, W. E., & Marti, U., 2010. *Combining EGM2008 and SRTM/DTM2006. 0 residual terrain model data to improve quasigeoid computations in mountainous areas devoid of gravity data*. Journal of Geodesy, 84(9), 557-567.
- Huang, Yangming, et al., 2007. *SGA-WZ: A new strapdown airborne gravimeter*. Sensors 12.7 (2012): 9336-9348.
- Jekeli, C., 1998. *Algorithms and preliminary experiences with the LN93 and LN100 for airborne vector gravimetry*. OHIO STATE UNIV COLUMBUS DEPT OF CIVIL ENGINEERING.
- Karaim, M., Karamat, T. B., Noureldin, A., & El-Shafie, A., 2014. *GPS Cycle Slip Detection and Correction at Measurement Level*. British Journal of Applied Science & Technology, 29(4), 4239-4251.
- Sampietro, D., Capponi, M., Triglione, D., Mansi, A. H., Marchetti, P., & Sansó, F., 2016. *GTE: a new software for gravitational terrain effect computation: theory and performances*. Pure and Applied Geophysics, 173(7), 2435-2453.
- Sampietro, D., Capponi, M., Mansi, A. H., Gatti, A., Marchetti, P., & Sansó, F., 2017. *Space-Wise approach for airborne gravity data modelling*. Journal of geodesy, 91(5), 535-545.
- Sansò, F., 1997. *Il trattamento statistico dei dati*. CittàStudi.
- Sansó, F., & Sideris, M. G., 2013. *Geoid determination: theory and methods*. Springer Science & Business Media.
- de Saint-Jean B., Verdun J., Duquenne H., Barriot J., Melachroinos S., Cali J., 2007. *Fine analysis of lever arm effects in moving gravimetry*. Dynamic Planet, 809-816.
- Schwarz, K. P., Sideris, M. G., & Forsberg, R., 1990. *The use of FFT techniques in physical geodesy*. Geophysical Journal International, 100(3), 485-514.
- Schwarz, K., & Li, Z. , 1997. *An introduction to airborne gravimetry and its boundary value problems*. Geodetic boundary value problems in view of the one centimeter geoid, 312-358.
- Watson G.N., 1995. *A treatise on the theory of Bessel functions*. Cambridge University Press, Montpelier.

NEW APPLICATIONS AND CHALLENGES OF GNSS VARIOMETRIC APPROACH

Giorgio Savastano^{1,2}

¹ Department of Civil, Building and Environmental Engineering, University of Rome, La Sapienza, Rome, Italy

² Ionospheric and Atmospheric Remote Sensing Group, Jet Propulsion Laboratory, California Institute of Technology, USA

KEY WORDS: GNSS, VARION, Real-Time Ionosphere Remote Sensing, TEC, Natural Hazards

ABSTRACT:

Global Navigation Satellite Systems (GNSS) are nowadays widely used in several technical and scientific activities, and they have eventually become a key instrument also for ionospheric and tropospheric remote sensing studies, and for soil features (GNSS reflectometry). In particular, GNSS signals can be used to monitor the ionosphere at different time and space scales. On a global scale, Global Ionosphere Maps (GIM) are generated by measuring the Total Electron Content (TEC) from stations located around the world. On a regional scale, the same signals can be used to detect traveling ionospheric disturbances (TIDs), including those generated by natural hazards, such as tsunami and earthquakes. The Variometric Approach (VA) is a GNSS processing algorithm which is based on single time differences of suitable linear combinations of GNSS carrier-phase measurements, using stand-alone GNSS receivers and standard GNSS broadcast orbits parameters, that are available in real-time. Under the VA's umbrella, this thesis presents a new GNSS processing algorithm, named VARION (Variometric Approach for Real-Time Ionosphere Observation), which is capable of estimating in real time changes in the ionosphere's TEC using stand-alone GNSS receivers. The 2015 IUGG Resolution number 4 was announced at the IUGG General Assembly in Prague with the title "Real-Time GNSS Augmentation of the Tsunami Early Warning System". The scope of this resolution was to push the use of real-time GNSS observations for tsunami detection. For this reason, this thesis also investigates the possibility to apply VARION to real-time ionosphere monitoring and tsunami-TIDs detection, and the effectiveness of this algorithm was proven on the following study cases: 2012 Haida Gwaii earthquake and tsunami event, 2015 Chile earthquake and tsunami event. VARION may represent a significant contribution to science because the ionosphere is strongly coupled to the dynamics of the Earth's surface, neutral atmosphere, and geomagnetic field. In particular, these ionospheric perturbations can be used to detect in real time atmospheric gravity waves due to tsunamis. During the NASA funded GNSS Tsunami Early Warning System 2017 workshop held in Sendai, Japan, July 25-27 2017, the VARION algorithm was appointed as the first real-time GNSS tsunami tracking and warning system based upon JPL's Global Differential GPS system.

1. GOALS AND MOTIVATIONS

The first goal of this thesis is to present a new GNSS processing approach, named VARION (Variometric Approach for Real-Time Ionosphere Observation), which is capable of estimating in real time changes in the ionosphere's TEC using stand-alone GNSS receivers, which can be used for real-time ionosphere remote sensing.

The second main goal is to investigate the possibility of applying VARION to real-time tsunami detection in order to augment existing tsunami early warning systems. In fact, the motivations of this work are inspired by the 2015 IUGG Resolution number 4 (International Union of Geodesy and Geophysics, 2015), which was announced at the IUGG General Assembly in Prague with the title "Real-Time GNSS Augmentation of the Tsunami Early Warning System". The scope of this Resolution was to push the use of real-time GNSS observations for tsunami detection. This Resolution also motivated the launch of the Geohazards Monitoring Focus Area of the Global Geodetic Observing System (GGOS), which promoted the Global Navigation Satellite System to Enhance Tsunami Early Warning System (GTEWS) group. The work developed in this thesis illustrated hereafter contributed to the first GATEW Report (LaBrecque et al., 2018).

2. BACKGROUND

2.1 GNSS Observables

This section reviews some of the most important aspects of the carrier phase GNSS observation equation. Generally speaking, and keeping in mind the differences between various GNSS, it is possible to say that all satellites transmissions are derived from a fundamental frequency which is made available by on-board atomic clocks. Any further detail about signal generation and modulation would be system dependent and is out of the scope of this work.

GNSS observables are nowadays used for several scientific applications. This section focus on real-time ionospheric remote sensing applications. The GNSS based ionospheric remote sensing process is radically different from the GNSS positioning one. For GNSS positioning, all the satellites take part into the least square estimation process in order to obtain receiver positions or velocities. For GNSS ionospheric remote sensing, each satellite-receiver link is processed autonomously and provide independent time series of TEC. Also, each link senses a different region of the sky and each receiver observes a variety of different physical processes at the same time.

Phase observable results from the difference between the phase of the incoming carrier wave (upon which the code is modulated) and the phase of a signal internally generated by the receiver which is synchronized with the receiver clock (Blewitt, 2015). If the recording starts at epoch t_0 , the receiver is capable to measure only the fractional part of the carrier phase

that arrives from the satellite. Hence, the integer number of cycles between the satellite and the receiver at the initial epoch t_0 (the so called “integer ambiguity” N) is unknown, but it remains constant during the period of observations if the tracking of the satellite is continuous (i.e. without loss of lock). In unit of length, the carrier phase observable equation for a signal propagating from a GNSS satellite (S) to a ground-based receiver (R), and passing through the Earth’s atmosphere reads as follows:

$$L_{iR}^S(t) = \rho_R^S(t) + \lambda_i N_{iR}^S + c(\delta t_R - \delta t^S) + T_R^S(t) - I_R^S(t) \quad (1)$$

where i = frequency index
 ρ_R^S = geometric distance
 λ_i = wavelength of carrier signal
 N_{iR}^S = integer ambiguity
 c = speed of light
 δt_R = receiver clock error
 δt^S = satellite clock error
 T_R^S = tropospheric delay
 I_R^S = ionospheric delay

The negative sign of the ionospheric delay indicates that the ionized gases in the ionosphere cause the phases of the electromagnetic waves to advance. This phase advance leads to a phase velocity greater than the speed of light. This does not contradict Einstein’s postulate of the universal characteristic of the speed of light, since no information is transmitted by a single electromagnetic wave (Hoffman-Wellenhof et al., 2008). A more complete version of Eqn 1 includes the sum of relativistic effects, phase center variations, and phase windup, which can all be grouped in the term p_R^S ; and the multipath and noise terms, which can be written as m_R^S and ϵ_R^S , respectively. In the next sections we will quantify the ionospheric advance for GNSS phase observations.

2.2 Atmospheric Delays

GNSS signals propagate through atmospheric regions (troposphere and ionosphere) of different nature and variable state, and thus experience different kind of delays. Perturbations may occur to the direction of propagation, to the velocity of propagation and to the signal strength. For positioning applications in geodesy and geophysics the atmosphere introduces unwanted errors. The main impact on the observational results are, in many cases, due to the ionosphere. Consequently, ionospheric effects have to be eliminated directly by measurements (ionosphere-free combination) or through corrections (Klobuchar, 1987). On the other hand, information on the state of the ionosphere can be obtained by retrieving the ionospheric advance in the GNSS signals (geometry-free combination).

Electromagnetic waves having frequency greater than 20 MHz propagate through the ionosphere, although the ray path is still influenced by it. The ionospheric refraction is modeled as a function of the electron density which is influenced by the solar activity, diurnal and seasonal variations, and the Earth’s magnetic field. Following (Seeber, 2003): p. 54, and cutting off, after the quadratic term, the series expansion that represents the phase refractive index, it is possible to provide an approximation of the ionospheric delay as

$$I_R^S = \frac{40.3}{f^2} \int_R^S N_e ds = \frac{40.3}{f^2} sTEC \quad (2)$$

where $sTEC$ (slant total electron content) is defined as the integral contains the total number of electrons that are included in a column with a cross-sectional area of $1 m^2$, counted along the signal path between the satellite S and the receiver R :

$$sTEC = \int_R^S N_e(s) ds \quad (3)$$

The unit of measurement of $sTEC$ is the TECU (Total Electron Content Unit) which is equal to $1 * 10^{16} el/m^2$. For a numerical example, an advance of $I_R^S = 0.18 m$ is obtained if a frequency of 1.5 GHz and one TECU is substituted. Values of TEC vary between 10^{16} and 10^{19} electrons per m^2 along the radio wave path (Seeber, 2003). The electron density is highly variable and depends mainly on: geographic location, time of the day, season of the year and solar activity. Regions of highest TEC are located approximately ± 15 to ± 20 degrees each side of Earth’s magnetic equator. The day to day variability has a standard deviation of $\pm 20\%$ to 25% of monthly average conditions (Klobuchar, 1987). Short term variations are traveling ionospheric disturbances (TIDs) with periods of minutes to about 1 hour, and ionospheric scintillation with a period of seconds. Eqn. 2 indicates that the phase advance of the radio signal propagation is proportional to the inverse of the squared frequency and that higher frequencies are less affected by the ionosphere.

2.3 Geometry-free Combination

Linear combinations of the original phase observations are often used in order either to eliminate systematic biases (e.g. ionosphere-free combination) or to estimation atmospheric parameter (e.g. geometry free combination to estimate the ionospheric delays). The main drawback of the linear combinations is that the noise of the observable is higher than the original ones. The formulation of the generic linear combination reads as follows

$$L_{LC} = \alpha L_i + \beta L_j \quad (4)$$

where α and β are the real coefficients of the combination and L_i and L_j represent the original observations (either the code or phase observations) in length units and with frequencies i and j , respectively.

For the interest of this work, we focus on the geometry-free combination, which is used in the VARION algorithm. The geometry-free combination is used to remove terms that are non-dispersive with respect to the GNSS frequency, like the geometry, clocks and the tropospheric delay. For this reason this combination is insensitive to receiver motion. The geometry-free combination is formed from Eqn. 4 using the following coefficients

$$\alpha = 1 \quad \beta = -1 \quad (5)$$

The geometry-free combination for two carrier phase observations with frequencies i and j is formed as follows

$$L_{GF} = (\lambda_i N_{iR}^S - \lambda_j N_{jR}^S) - (\frac{A}{f_i^2} TEC_R^S - \frac{A}{f_j^2} TEC_R^S) + IFB \quad (6)$$

where epoch tag has been eliminated for the sake of simplicity, whereas the term of Inter-frequency Bias (IFB) has been added. Inter-frequency bias (IFB) is present in all dual frequency combinations of GNSS carrier phase observables. It is caused by the path dependent signal delays in both the satellite and receiver (Holaschutz et al., 2008). However, the receiver and the satellite IFBs in the carrier-phase ionospheric observable can be assumed as constant for a given period of 1-3 days (Bishop et al., 1994, Sardon et al., 1994, Brunini et al., 2005, Ciraolo et al., 2007).

3. VARION ALGORITHM FOR NATURAL HAZARDS

3.1 Coupling between Natural Hazards and Ionosphere

It is well known that TEC variations in GNSS signals can be exploited to detect perturbations in the ionosphere caused by a wide variety of sources. Natural hazards such as earthquakes, tsunamis, volcanic eruptions, or deep convective events (large hurricanes or tornadoes), generate atmospheric perturbations. Man-made sources such as explosions and rocket ascents, and external sources such as geomagnetic storms, aurora, and plasma instabilities, are also detectable. This analysis can be performed from ground-based GNSS receivers by estimating the relative change of the ionospheric TEC over time directly from the GNSS phase observations. The GPS approach was first used to detect small electron density and TEC variations generated by surface displacements resulting from the 1994 M6.7 Northridge, California earthquake (Calais, Minster, 1995, Calais, Minster, 1998). These TEC anomalies occur following the deformation of the solid Earth indicates that there exists a coupling between the Earth's surface and the atmosphere. Two of the main mechanisms by which motions of the Earth's surface induce variations in electron density in the ionosphere are acoustic and gravity waves. Over some periods these acoustic and gravity wave modes are coupled and both may need to be considered (Watada, 1995, Artru et al., 2001). The compressions and rarefactions of the ionospheric electron density produce deviations in TEC from the dominant diurnal variation. For many applications, such as TID detection, is the deviations (also known as fluctuations or perturbations) from the background level that are of interest. The precision of the measurements of deviations from the background ranges from around 0.01 to 0.1 TECU (Galvan et al., 2011).

3.1.1 Acoustic waves Pressure-induced TEC anomalies from earthquakes have been widely observed in the last decade, for example, coseismic ionospheric disturbances (CIDs) were documented with the 2003 M_W 8.3 Tokachi-oki, Japan and the 2008 M_W 8.1 Wenchuan, China earthquakes (Rolland et al., 2011b) observed at Japanese GEONET sites (Sagiya et al 2000). CIDs produced by the 2011 M_W 9.0 Tohoku-oki, Japan earthquake were widely reported by several independent research groups (Galvan, D. A. et al., 2012, Komjathy et al., 2013, Rolland et al., 2011a). Volcanic eruptions can also excite acoustic waves and induce anomalies in the TEC measurements (Dautermann et al., 2009, Shults et al., 2016).

When an earthquake occur, direct (or shock) acoustic waves (SAWs) are produced in the proximity of the epicenter (within 500 km), and secondary acoustic waves caused by surface Rayleigh waves propagating far from the epicenter. These pressure waves, upon reaching the ionosphere, will locally affect electron density through particle collisions between the neutral atmosphere and the electron plasma (Kherani et al., 2009). Motions of the Earth's surface produce SAWs, which are pressure waves that propagate upwards through the atmosphere at the local speed of sound. The onset of the anomalies following the geophysical event is typically about 10min (Dautermann et al., 2009, Galvan et al., 2011) and reflects the time needed for the first acoustic waves to propagate at the speed of sound to the F layer density peak. Many studies have found the horizontal propagation speed of the anomaly to be around 600-1000 m/s , in agreement with the speed of sound at typical F layer heights (Astafyeva et al., 2009, Galvan, D. A. et al., 2012, Liu et al., 2017). High amplitude surface waves, particularly Rayleigh waves, are also capable of generating acoustic waves (Astafyeva, Heki, 2009). As the surface wave travels away from the epicenter, they becomes a moving source of coupled atmospheric acoustic and gravity waves, which propagate upwards to the ionosphere.

It is important to highlight that only acoustic waves which have a frequency greater than the cut-off frequency can propagate up to the ionosphere (Ducic et al., 2003). Such frequency is defined as $\omega_a = \frac{\gamma g}{2c_s}$ where c_s is the speed of sound, γ and g are respectively the ratio of specific heats and gravitational acceleration (Artru et al., 2004, Tahira, 1995). Thus, the waves with a frequency greater than the cut-off one reach the ionosphere and their amplitude grows of a factor 10^4 - 10^5 as the atmosphere density decreases with altitude; such amplification is due to the conservation of kinetic energy. Otherwise amplitude decreases exponentially with altitude (Artru et al., 2004) and in this case, the waves are named evanescent. The typical values of cut-off frequency fall within the range 2.1-3.3 mHz (Artru et al., 2004, Dautermann et al., 2009).

3.1.2 Gravity waves Gravity waves form when air parcels are lifted due to particular fluid dynamic and then pulled down by buoyancy in an oscillating manner. This can occur when air passes over mountain chains (Queney, 1948) or when a "mountain", which is read as tsunamis wave, is moving with a certain velocity. Let us imagine the displacement of a volume of atmospheric air from its equilibrium position, it will then find itself surrounded by air with different density. Buoyant forces will try to bring the volume of air back to the undisturbed position but these restoring forces will overshoot the target and lead it to oscillate about its neutral buoyancy altitude. It will continue this oscillation about an equilibrium point, generating a gravity wave that can propagate up through the ionosphere.

Perturbations at the surface that have periods longer than the time needed for the atmosphere to respond under the restoring force of buoyancy will successfully propagate upwards. This is known as the Brunt-Vaisala frequency N and represents the maximum frequency for vertically propagating gravity waves. In an isothermal atmosphere where $\partial T/\partial z = 0$, $N \approx 0.02 s^{-1}$ and the buoyancy period is about 5 min at the Earth's surface (Galvan et al., 2011). Holton (Holton, 1992) gives $N \approx 0.012 s^{-1}$ for average tropospheric conditions, so that the buoyancy period is about 8 min. Tsunamis have periods longer than this frequency and thus excite gravity waves in the atmosphere. The notion that gravity waves generated by

tsunami waves (even with wave heights of few centimeters in deep ocean) can propagate upward in the atmosphere and ultimately cause perturbations in the TEC of the ionosphere was first established by Daniels (Daniels, 1952), and was theoretically further developed by Hines (Hines, 1960, Hines, 1972). Peltier and Hines (Peltier, Hines, 1976) subsequently showed that these TEC variations can be detected through ionosonde measurements.

Using this solid foundation and the abundance of GPS observations, researchers have set out goals to develop models and establish observational systems to provide reliable tsunami forecasts before the actual tsunami waves reach coastlines. It has been demonstrated that effects of an ocean tsunami can potentially be remotely observed as traveling ionospheric disturbances (TIDs) produced by the gravity waves. These TIDs were detected using different methods of observations, including ground-GPS (Artru et al., 2005, Rolland et al., 2010, Galvan, D. A. et al., 2012), Jason-1 radar altimeter (Occhipinti et al., 2006, Mai, C.-L., and J.-F. Kiang, 2009), incoherent scatter radar (ISR) (Lee, M. C. et al., 2008) and space-based measurements (Coisson et al., 2015, Yang, Y.-M. et al., 2014b).

Additional investigations highlighted that the detection of tsunami-driven TIDs is not always straightforward since there exists several other causes for TIDs, such as intense or large-scale tropospheric weather (Hung et al., 1978, Kelley, M. C., 1997, Xiao et al., 2007), geomagnetic and auroral activity (Richmond, Matsushita, 1975, Nicolls et al., 2004), earthquakes (Calais, Minster, 1995, Artru et al., 2001, Kelley et al., 1985), and even unknown mechanisms (Tsugawa et al., 2007). Therefore, the relationship between detected TIDs and those that are induced by a tsunami has to be proven, for example by verifying that the horizontal speed, direction and spectral bandwidth of the TIDs match that of the ocean tsunami (Galvan, D. A. et al., 2012).

The vertical propagation speed of an atmospheric gravity wave at these periods is 40-50 *m/s* (Artru et al., 2005), so these perturbations should first be observed about 2 *h* after the onset of the tsunami. The TEC anomalies can be identified by their horizontal propagation speed, which is much slower (200-300 *m/s*) than that of the acoustic TID or Rayleigh-wave-induced anomalies and follows the propagation speed of the tsunami itself, which is, much like the Rayleigh waves in the acoustic case, a moving source of gravity waves. However, following the 2011 M_W 9.0 Tohoku-oki, Japan event, which provided dense near-field TEC observations, it was noted that the onset of the gravity-wave-induced TEC anomalies was shorter, at about 30 *min* after the start of the earthquake, and not the 1.5-2 *h* predicted by previous theoretical computations (Galvan, D. A. et al., 2012). This is explained as evidence that it might not be necessary for the gravity wave to reach the F layer peak (around 300 km altitude) for the TEC disturbance to be measurable. Rather, disturbances at lower altitudes within the E layer and the lower portion of the F layer might be substantial enough to be seen in the TEC observations. This is supported by previous modeling results that showed significant TEC perturbations over a broad area around the F layer peak (Rolland et al., 2011a). Through comparisons with tsunami simulations of the event it was convincingly demonstrated that the tsunami itself must be the source of the observed gravity waves (Galvan, D. A. et al., 2012). In light of these observations, ionospheric soundings may be used to monitor tsunamis and issue warnings in advance of their arrival at the coast (Komjathy et al., 2013, Occhipinti et al., 2013, Savastano et al., 2017).

While there has been progress in experimental work, along with theoretical modeling of the interactions between the ocean surface, atmosphere, and ionosphere (Occhipinti et al., 2006, Occhipinti et al., 2008, Occhipinti, et al., 2011), (Hickey et al., 2009, Meng, X. et al., 2015), recent reviews (Jin et al., 2015, Komjathy A. et al., 2016) concluded that the core scientific problems regarding the nature of the coupling between the ocean and ionosphere are still not sufficiently understood. To provide useful geophysical data on the inferred amplitude, period, and velocity of a tsunami, based on the estimated gravity waves induced TIDs, a number of real-time TEC monitoring systems are being developed utilizing the present capabilities of GNSS technology and infrastructures. As a matter of fact, up to now TEC variations are routinely estimated and geolocated in a post-processing mode.

3.2 Tsunami

A tsunami is a series of ocean waves that are typically generated by an underwater geological event such as an earthquake, volcanic eruption, or a submarine landslide. The resulting abrupt change in sea-surface height sends a set of long waves propagating outward from the point of origin. As the waves approach the coastline and the water shoals, they are amplified and can be extremely destructive, depending on the shape of the coastline and the bathymetry. Earthquakes are the most common source of tsunamis. The types of earthquakes that generate tsunamis are typically dip-slip events of magnitude (M) 6.5 or greater. Because earthquakes generate tsunamis primarily through vertical coseismic displacement of the seafloor and overlying water column, dip-slip earthquakes are more efficient at generating tsunamis than strike-slip earthquakes (Ward, 1980, Okal, 1988). They frequently occur in the Pacific, where dense oceanic plates slide under the lighter continental plates. When these plates slide, they may cause a vertical movement of the seafloor that allows a quick and efficient transfer of energy from the solid earth to the ocean. Because earth movements associated with large earthquakes are thousand of square kilometers in area, any vertical movement of the seafloor immediately changes the sea-surface. The resulting tsunami propagates as a set of waves whose energy is concentrated at wavelengths corresponding to the earth movements (~ 100 km), at wave heights determined by vertical displacement (~ 1 m), and at wave directions determined by the adjacent coastline geometry. Because each earthquake is unique, every tsunami has unique wavelengths, wave heights, and directionality. From a tsunami warning perspective, this makes the problem of forecasting tsunamis in real time challenging.

The existing tsunami warning systems currently rely on numerical modeling (as MOST) and buoy observations (Galvan, D. A. et al., 2012). Since the 2003 Rat Island tsunami, the NOAA Center for Tsunami Research (NCTR) has developed a real-time model-forecast methodology ingesting deep-ocean tsunami measurements into the MOST model to produce timely and accurate tsunami forecast for potentially vulnerable U.S. coastal communities (Titov, V.V. et al., 2005, Sardon E, 2009, Wei, Y. et al., 2008, Wei et al., 2013, Tang, L., V.V. et al., 2012). As a major model component of this forecast system, MOST has been used to develop a database of tsunami propagation model results for nearly 2,000 unit tsunami sources covering all subducting zones on earth. Based on an inversion algorithm (Percival, D.B. et al., 2011), the forecast method rapidly estimates the tsunami source to obtain a best fit between the pre-computed tsunami propagation database and the real-time tsunami measurements supported by a global tsunameter

system composed of 65 deep-ocean bottom pressure sensors. Ground-GNSS observations processed in real-time may have the potential to enhance the current system by providing the tsunami speed and amplitude.

3.3 VARION Approach

The VARION approach is based on single time differences of geometry-free combinations of GNSS carrier-phase measurements, using a standalone GNSS receiver and standard GNSS broadcast products (orbits and clocks corrections) that are available in real-time. If no cycle slips occurred, the unknown carrier-phase ambiguity can be considered constant between two consecutive epochs (Sec. 2.1). The receiver and the satellite IFBs in the carrier-phase ionospheric observable can also be assumed as constant for a substantially long period, as already mentioned. For these reasons, by differentiating Eqn. 1 in time between two consecutive epochs (t and $t+1$), and applying the geometry-free combination (Eqn. 6), we obtain the geometry-free time single-difference observation equation, with no need of estimate in real-time the phase ambiguity and the IFB:

$$L_{GF}(t+1) - L_{GF}(t) = \frac{f_1^2 - f_2^2}{f_2^2} \left[I_{1R}^S(t+1) - I_{1R}^S(t) \right] \quad (7)$$

where f_1 and f_2 are the two GNSS frequencies, which for GPS are 1575.42 MHz and 1227.60 MHz respectively. Taking into account the ionospheric refraction along the geometric range, we compute the $sTEC$ variations between two consecutive epochs:

$$\delta sTEC(t+1, t) = \frac{f_1^2 f_2^2}{A(f_1^2 - f_2^2)} \left[L_{GF}(t+1) - L_{GF}(t) \right] \quad (8)$$

The discrete derivative of $sTEC$ over time can be simply computed dividing $\delta sTEC$ by the interval between epochs t and $(t+1)$. A complete description of VARION algorithm is provided in (Savastano et al., 2017). The $sTEC$ observations are modeled by collapsing them to the ionospheric pierce point (IPP) between the satellite-receiver line-of-sight and the single-shell layer located above the height of F2 peak, where the electron density is assumed to be maximum. The IPP position can be computed in real time using standard GNSS broadcast orbits parameters (Savastano et al., 2017), after having chosen the height of the F2 peak. This is the so called single-shell ionospheric approximation, meaning that the ionospheric $sTEC$ is assigned to an IPP point which renders a 2D picture without vertical dependence of any parameter. In this 2D representation of the ionosphere, $\delta sTEC$ is equivalent to a total derivative over time where the observational point (IPP) moves independently of the motion of the medium (ionospheric plasma). In this particular case, the total derivative encompasses both the variation in time in a certain fixed position ($sTEC$ partial time derivative) and the variation in time due to the $sTEC$ horizontal spatial variation and to the horizontal motion of the IPP relative to the horizontal plasma flow ($sTEC$ horizontal space gradient times the relative IPP velocity):

$$\frac{d sTEC(t, s)}{dt} = \frac{\partial sTEC(t, s)}{\partial t} + (\vec{V}_{pla} - \vec{V}_{ipp}) \cdot \nabla sTEC(t, s) \quad (9)$$

where \vec{V}_{ipp} = horizontal plasma vector velocity field
 \vec{V}_{ipp} = horizontal IPP's vector velocity field
 $\nabla sTEC(t, s)$ = $sTEC$ spatial gradient

Note that the IPP does not follow the ions velocity field, since the IPP velocity vector is driven by the satellite orbit and the receiver location/motion on the ground. It is clear that the ionospheric remote sensing based on GNSS ground-based observations depends on the time-dependent position of the IPPs. To get the total $\Delta sTEC$ variation over a certain interval while the IPP is moving along its path, Eqn. 9 is integrated over time (from t_0 to t_f):

$$\Delta sTEC(t_f, t_0) = \int_{sTEC_0}^{sTEC_f} d sTEC(t, s) \quad (10)$$

Eqn. 10 is used to detect tsunami-TIDs in real-time. It is worth to underline each VARION equation 8 can be written for a specific satellite-receiver link, for two generic consecutive epochs (t and $t+1$). The only unknown parameter ($\delta sTEC$) is different for each satellite-receiver link. This means that if we assume that n satellites are viewed by the receiver both at epochs t and $t+1$, the system has n equations and n unknown parameters and the redundancy of the system is zero. For this reason, each satellite-receiver link can be processed in parallel as an independent thread.

VARION is an open source, entirely Python-based software (VARION Development Team, 2016). It was derived from the VADASE (Variometric Approach for Displacements Analysis Standalone Engine) algorithm that was successfully applied to estimate in a real-time scenario the ground velocities and displacements induced by several earthquakes (e.g. the Tohoku-Oki earthquake, USGS Mw 9.0, 11 March 2011, 05:46:24 UTC; the Emilia earthquake, USGS Mw 6.0, 20 May 2012, 02:03:52), using a stand-alone GNSS receiver (Colosimo et al., 2011, Branzanti et al., 2012, Benedetti et al., 2014). The VADASE algorithm was later modified and applied to geometry-free combinations of GNSS carrier-phase measurements for estimating TEC variations. Using the VARION algorithm each dual-frequency GNSS receiver is expected to provide time series of real-time TEC variations in a stand-alone operational mode.

3.4 IPP Position Estimation

This section explains the numerical method implemented in VARION in order to compute in real time the IPP coordinates (and then SIP). Starting from the ECEF (earth-centered, earth-fixed) coordinates of the GNSS receiver (X_R, Y_R, Z_R) and the satellite (X^S, Y^S, Z^S) at a certain epoch t , we can compute the midpoint M_i between the receiver and the satellite (X_M, Y_M, Z_M). Subsequently, we convert this point into geographical coordinates (ϕ_M, λ_M, h_M), and for each iteration, the h_M value is checked against the height of ionospheric layer h_I (e.g. 350 km):

1. if $h_M > h_I$ (condition always true at the first iteration), then a new midpoint M_{i+1} between the receiver and the previous midpoint M_i is computed
2. when $h_M < h_I$, then the midpoint M_k is computed between the two previous midpoints M_{k-1}, M_{k-2}

This algorithm stops when the condition $h_M - h_I < \epsilon$ is met, where ϵ was set to 10 km. This new algorithm, compare with e.g. Klobuchar algorithm (Klobuchar, 1987), has the advantage that the IPP is surely located on the line of sight satellite-receiver.

3.5 Geometric Effects

3.5.1 Doppler Effect The fact that the IPP moves with a certain velocity \vec{V}_{ipp} implies the fact that any ionospheric perturbations detected from GNSS remote sensing observations experience a Doppler shift. Recalling the concept seen in 3.1.1, when an earthquake occur, direct (or shock) acoustic waves are produced in the proximity of the epicenter. These pressure waves, upon reaching the ionosphere, will locally affect electron density through particle collisions between the neutral atmosphere and the electron plasma (Kherani et al., 2009). An observer moving with a velocity \vec{V}_{ipp} will “hear” a frequency

$$f_{observed} = \frac{\nu + V_{ipp}^s}{\nu} f_{source} \quad (11)$$

where ν is the value of the sound speed at a certain temperature T , and V_{ipp}^s is the velocity component along the source direction. Since the V_{ipp} has not a constant value with time, also $f_{observed}$ will change with time.

3.5.2 Trend and Noise The fact that the module of the vector \vec{V}_{ipp} changes with elevation, means that the term $\vec{V}_{ipp} \cdot \nabla sTEC$ of Eqn. 9 becomes significant below 30 degrees elevation angle. This term represents the spatial trend’s component in the $sTEC$ observations. This section presents a statistical analysis over 186 receivers located in New Zealand. For this analysis we considered the day September 9, 2017, which had a quite geomagnetic activity. Fig. 1 shows the impact of the IPP motion on the GNSS $sTEC$ observations, which is highly correlated with the time evolution of the IPP velocity (see Eqn. 9). The four panels show 4 different satellites in view from different stations (different colors). The blue line represents the \vec{V}_{ipp} magnitude computed in real-time with the algorithm described in Sec. 3.4. It is clear the strong correlation between the \vec{V}_{ipp} magnitude and the noise in the $sTEC$ variations.

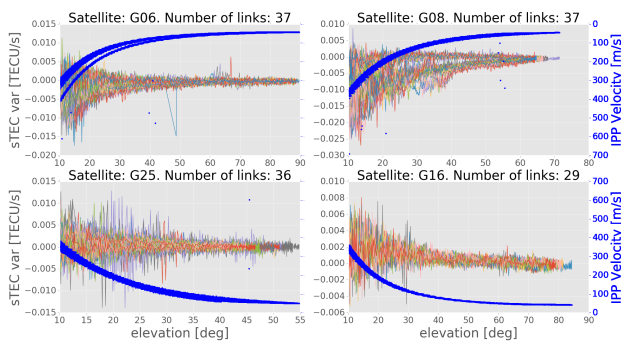


Figure 1. $sTEC$ variations and \vec{V}_{ipp} magnitude (blue) plotted as a function of elevation angle. The four panels show 4 different satellites in view from different stations (different colors)

4. CASE STUDY IN REAL-TIME SCENARIO

4.1 2012 Haida Gwaii Event

4.1.1 Dataset Using the VARION algorithm we compute TEC variations at 56 GPS receivers in Hawaii as induced by the

2012 Haida Gwaii tsunami event. We used GPS observations collected at 56 Plate Boundary Observatory (PBO) sites located on the Hawaiian Islands. All the GPS permanent stations are located in Big Island, (see Fig. 2) and acquired observations at 15 and 30 seconds rate. We observe TEC perturbations with amplitudes of up to 0.25 TEC units and traveling ionospheric perturbations (TIDs) moving away from the earthquake epicenter at an approximate speed of 277 m/s. We perform a wavelet analysis to analyze localized variations of power in the TEC time series and we find perturbation periods consistent with a tsunami typical deep ocean period. Finally, we present comparisons with the real-time tsunami MOST (Method of Splitting Tsunami) model produced by the NOAA Center for Tsunami Research and we observe variations in TEC that correlate in time and space with the tsunami waves.

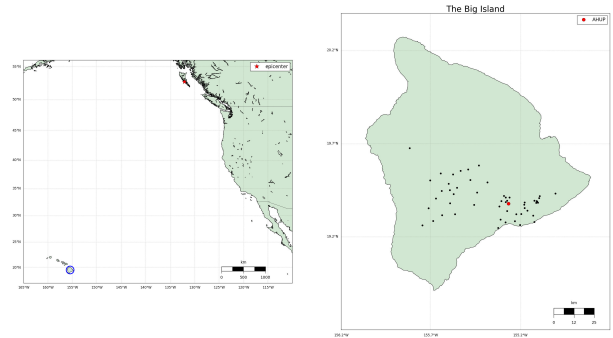


Figure 2. Map indicating the epicenter of the 10/27/2012 Canadian earthquake (left panel) and zoomed-in image of the Hawaii Big Island, where the 56 used GPS stations are located.

4.1.2 Results and Discussion We processed the GPS observations from the 56 PBO GPS stations to estimate TEC variations at 15 s and 30 s rate with both VARION and JPL algorithms (Komjathy et al., 2005). These two algorithms are designed to directly estimate two different parameters. The JPL algorithm is able to directly obtain the absolute TEC values, after estimating highly precise satellite and receiver Inter-Frequency Biases (IFBs) using about 200 GPS receivers distributed worldwide [e.g., refs (Mannucci, A. J. et al., 1998, Mannucci, A. J. et al., 2004)]. On the other hand, the direct outputs of the VARION algorithm are the $sTEC$ total derivative (Eqn. 9), subsequently integrated over a certain time period; the variometric approach overcomes the problem of estimating the phase initial ambiguity and the IFBs, thus being ideal for real-time applications. In order to highlight the TIDs, the TEC time series for each satellite were filtered to remove the TEC low-frequency variations (such as diurnal variations and multiple hour trends due to changing satellites elevation angles); VARION results were filtered using an 8th order polynomial, while the JPL algorithm uses a band-pass filter (0.5 to 5 mHz) (Yang, Y.-M. et al., 2014a).

Fig. 3 shows the $sTEC$ time series for two hours (08:00 to 10:00 UT - 28 October 2012) for 7 satellites in view from the AHUP station obtained with the two approaches. The vertical black line represents the time when the tsunami arrived at the Hawaiian Islands according to the MOST model. Very good agreement (RMS differences at the level of few hundredths TEC units) is evident, the differences are mostly due to the different data filtering methods applied. Moreover, we see significant TIDs for 5 satellites (PRNs 4, 7, 8, 10, 20) at different

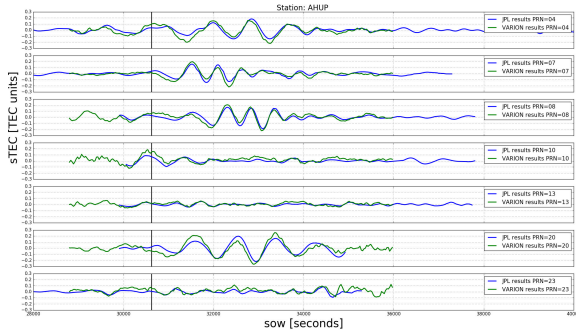


Figure 3. Comparison between TEC time series obtained from the VARION and JPL techniques. The TEC variations are computed for 7 satellites (PRNs 4, 7, 8, 10, 13, 20, 23) in view from the AHUP station on the Hawaiian Islands (latitude: 19.379 deg, longitude: 155.266 deg, height: 1104.881 m). The black vertical line represents the time when the tsunami reached the Hawaiian Islands. TIDs were clearly detected, with good agreement between the two approaches.

times due to the different locations of the ionospheric piercing points (IPPs) and the sub-ionospheric points (SIPs : IPPs projections onto the ellipsoid). In particular, for the satellite PRN 10 the TEC perturbation occurred before the tsunami reached the Hawaiian Islands; this is in fact due to the geometry corresponding to the particular elevation and azimuth angles of satellite PRN 10 as the tsunami-generated TIDs were detected when tsunami the wave front was still about 150 km away from the coast. For satellites PRN 13 and 23 no significant TIDs were detected, likely due to elevations and azimuthal positions with respect to the tsunami as a possible cause of the TIDs.

We performed a wavelet analysis using the Paul wavelet (that gives better time localization than the Morlet one) and we determine both the dominant modes of variability and how those modes vary in time (Torrence, Compo, 1998). This technique allows us to highlight and evaluate the TIDs wave periods. Here, the wavelet analysis has been performed in python using scripts running the wavelet software based on C. Torrence and G. Compo (Predybaylo, E., 2014). We processed 260 sTEC time series, for all the satellites in view at the 56 GPS permanent stations. We found periods in the range of 10 to 30 minutes, similar to the periods of the tsunami ocean waves, which can range from 5 min up to an hour with the typical deep ocean period of only 10-30 wavelengths around 400 km, and the velocity approximately 200 m/s.

Fig. 4 show the sTEC time series wavelet analysis for the 7 satellites in view at the station AHUP. The upper panels show the sTEC time series obtained with the VARION software in a real-time scenario, as plotted in Fig. 3. The bottom panels indicate the wavelet spectra. The colors represent the intensity of the power spectrum and the black contour encloses regions of greater than 95 % of confidence for a red noise process. We can identify 5 satellites (PRNs 4,7,8,10,20) with peaks consistent in time and period with the tsunami ocean waves. These results clearly show TIDs appearing after the tsunami reached the islands, with an increase of the power spectrum for periods between 10 and 30 minutes during the TIDs.

Fig. 5 displays a map of the region around the Hawaiian Islands, the area of our focus in order to highlight the most significant sTEC variations. The colored tracks show the positions of the

SIPs (equal to corresponding IPPs, when seen on the map) for each of the 7 satellites considered in Fig. 3 as seen from the 56 GPS permanent stations during an observation span of two hours (8:00 to 10:00 UT, 28 October 2012). The colors represent the variation in sTEC, obtained by VARION processing; the TIDs are clearly visible in the interval of significant sTEC variations (from positive to negative values and vice-versa).

Fig. 6 shows time sTEC variations for two hours (08:00 to 10:00 UT – 28 October 2012) at the IPPs vs. distance from the Haida Gwaii earthquake epicenter, for the same 7 satellites under consideration. The TIDs are clearly visible in the interval of significant sTEC variations (from positive to negative values and vice-versa). The vertical and horizontal black lines represent the time (when the tsunami arrived at the Hawaii Islands) and the distance (between the epicenter and the Big Island), respectively. In this way, we identify the green rectangle as the alert area and it is evident that satellite PRN 10, the closest to the earthquake epicenter detected TIDs before the tsunami arrived at Hawaiian Islands (08:30:08 UT). In the distance vs time plots (also called hodochrons) the slope of the straight line, fitted considering corresponding sTEC minima for different satellites, represents the horizontal speed estimate of TIDs. This plot indicates that the linear least-squares estimated speed of the TIDs is about 316 m/s and it is found to be in good agreement with a typical speed of the tsunami gravity waves estimated with ground-based GNSS receivers (see Appendix B). We note that such speed determinations via hodochron are not available in real-time, but neither are these estimates needed for real-time tsunami detection.

Fig. 7 displays a sequence of maps of the region around the Hawaiian Islands showing the variations in sTEC (determinable in real-time) at IPP/SPI locations on top of the MOST model sea-surface heights. Note that, just as the MOST model wavefronts are moving past the IPPs, the sTEC variations in the region become pronounced, correlated with the passage of the ocean tsunami itself. In particular, at 08:22:00 GPS time (08:21:44 UT) we are able to see sTEC perturbations from 56 stations looking at satellite PRN 10. The propagation of the MOST modeled tsunami passes the ionospheric pierce points located NW of the Big Island and offers insight with regard to the ionospheric response to the tsunami-driven atmospheric gravity wave. These perturbations are detected before the tsunami reached the islands as seen from the locations of the SIP points. The following frames indicate the tsunami-driven TIDs detected from the other 4 satellite (PRNs 4,7,8,20) tracking the propagating tsunami (see supplementary video SV1 online).

5. CONCLUSIONS

We have found observational evidence of variations in GPS sTEC measurements in the range of 0.1–0.2 TEC units (on the order of 1% of the background TEC value) that are associated with the Haida Gwaii tsunami of 28 October 2012. We compared two independent signal processing techniques, one available in real-time and one available in post-processing, and a good agreement was found between the JPL (post-processed) and VARION (real-time capable) results. We performed a wavelet analysis and we observed sTEC variations with a typical period between 10 and 30 minutes, consistent with the ocean tsunami waves. We estimated the speed of the TIDs generated by the tsunami-driven IGWs and we found a typical speed of about 316 km/s. From the comparison between the

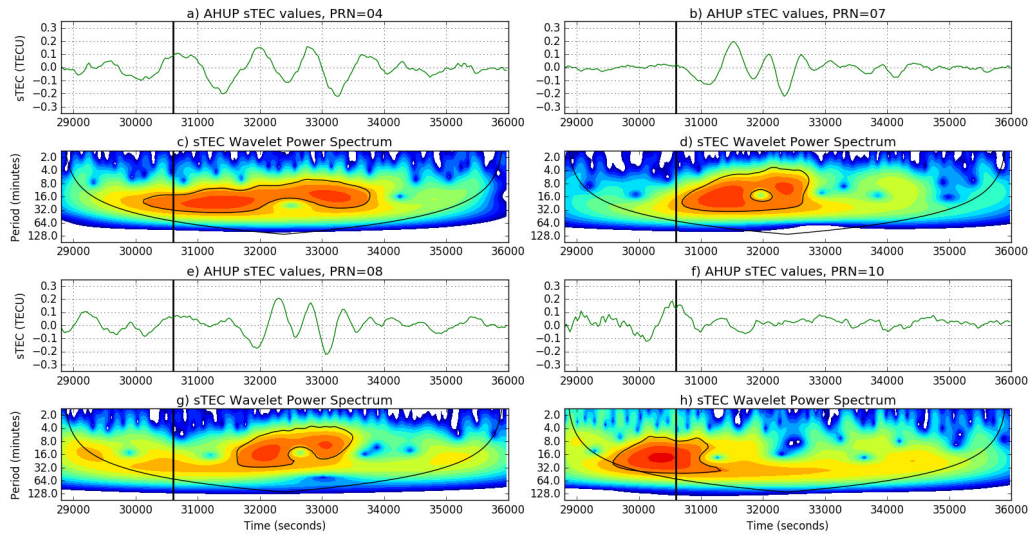


Figure 4. (a), (b), (e), (f) Four of 260 time series used for the wavelet analysis, station AHUP, satellite PRN 4,7,8,10. (c), (d), (g), (h) The wavelet power spectrum used the Paul wavelet. The vertical axis displays the Fourier period (min), the horizontal axis is time (s). The black vertical line represents the time when the tsunami reached the Hawaiian islands. The color panels represent the intensity of the power spectrum; the black contour encloses regions of greater than 95 % confidence for a red-noise process with a lag-1 coefficient of 0.72; the external black line indicates the cone of influence, the limit outside of which edge effects may become significant.

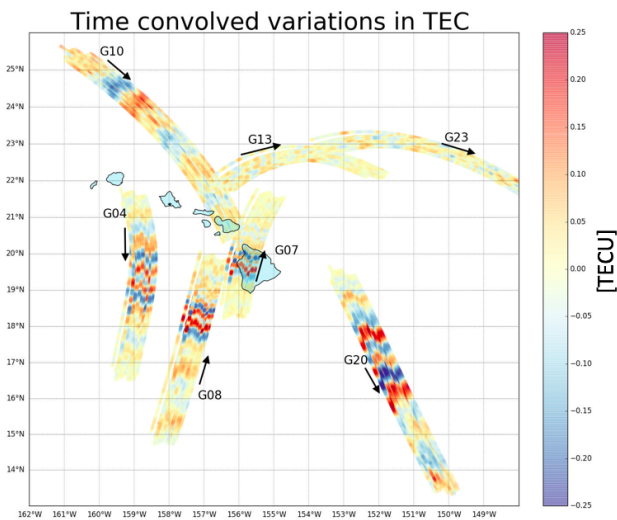


Figure 5. Space–time sTEC variations over two hours (08:00 to 10:00 UT – 28 October 2012) at the SIPs (same positions of the corresponding IPPs on the map) for the 7 satellites seen from the 56 Hawaii Big Islands GPS permanent stations, after the Haida Gwaii earthquake. The TIDs are clearly visible in the interval of significant sTEC variations (from positive to negative values and vice-versa). It is also shown that PRN 10 detected TIDs prior to the tsunami arrival at Hawaii Islands (08:30:08 UT).

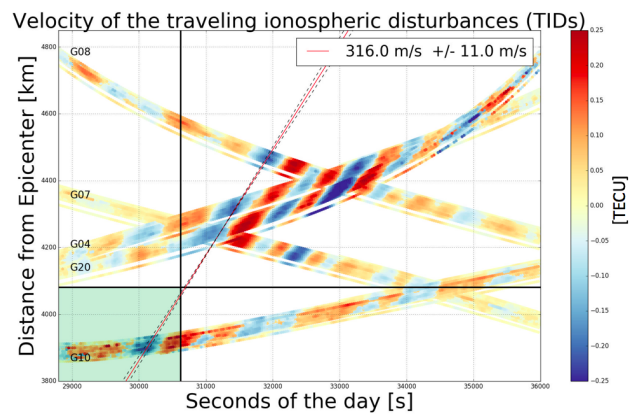


Figure 6. sTEC variations for two hours (08:00 to 10:00 UT – 28 October 2012) at the IPPs vs. distance from the Haida Gwaii earthquake epicenter, for the 7 satellites observed from the 56 Hawaii Big Islands GPS permanent stations. The TIDs are clearly visible in the interval of significant sTEC variations (from positive to negative values and vice-versa). The vertical and horizontal black lines represent the time (when the tsunami arrived at the Hawaii Islands) and the distance (between the epicenter and the Big Island), respectively; it is evident that PRN 10 detected TIDs before the tsunami arrived at Hawaii Islands (08:30:08 UT). The slope of the straight line fitted, considering a linear least-squares regression for corresponding sTEC minima for different satellites, represent the TIDs mean propagation velocity.

MOST model results and TECs measurements we have validated our results in time and space. Using signals from 56 GPS stations located on the Hawaiian Islands, we have detected TEC perturbations before the actual tsunami arrival; this is due to the geometry of the satellite PRN 10 (elevation and azimuth angles) and so the position of the SIPs at that time.

We have demonstrated that the real-time capable VARION algorithm is able to detect the TIDs generated by tsunami-driven gravity waves and may be considered as a novel contribution to future integrated operational tsunami early warning systems.

Fig. 8 shows the implementation of the VARION algorithm in the JPL's Global Differential GPS (GDGPS) system, which provides real-time access to 1-Hz data streams from about 50 global real-time stations collecting data from multiple constellations including GPS, Galileo, GLONASS and BeiDou. With real-time streams of data the polynomial fit has been implemented as a finite duration impulse response (FIR) high-pass filter.

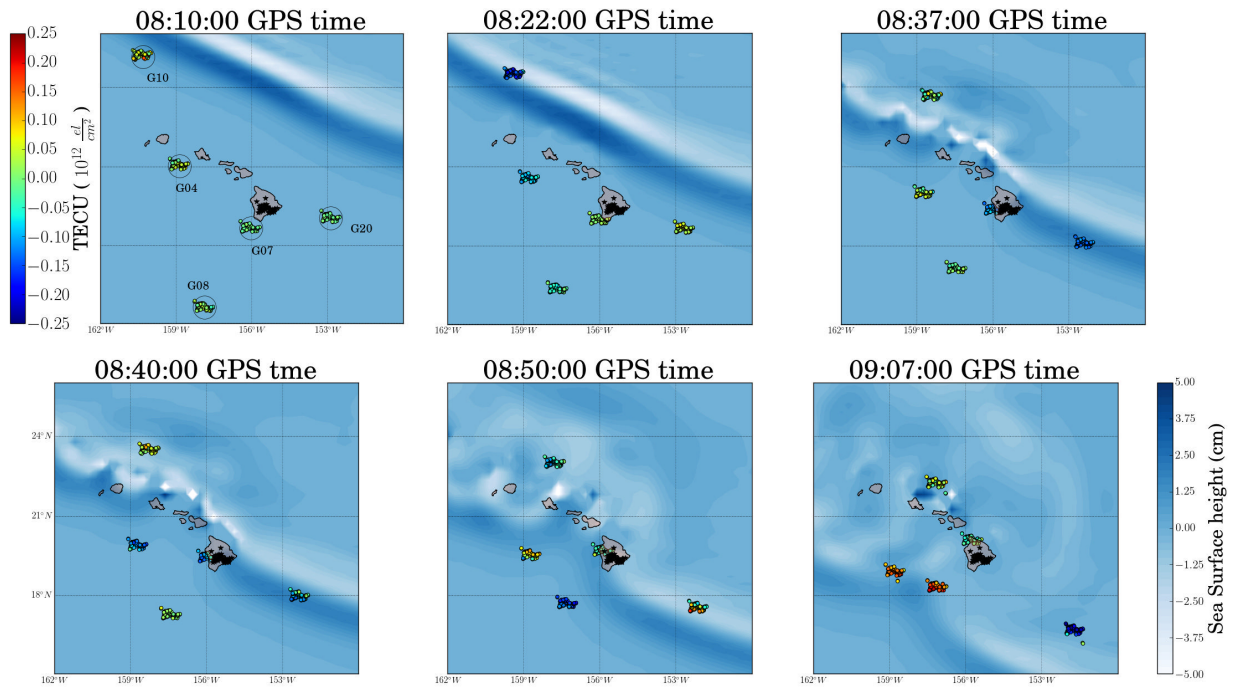


Figure 7. Space-time sTEC variations at 6 epochs within the two hours interval (08:00 to 10:00 UT – 28 October 2012) at the SIPs for the 5 satellites showing TIDs, over-plotted the tsunami MOST model. TIDs are consistent in time and space with the tsunami waves.

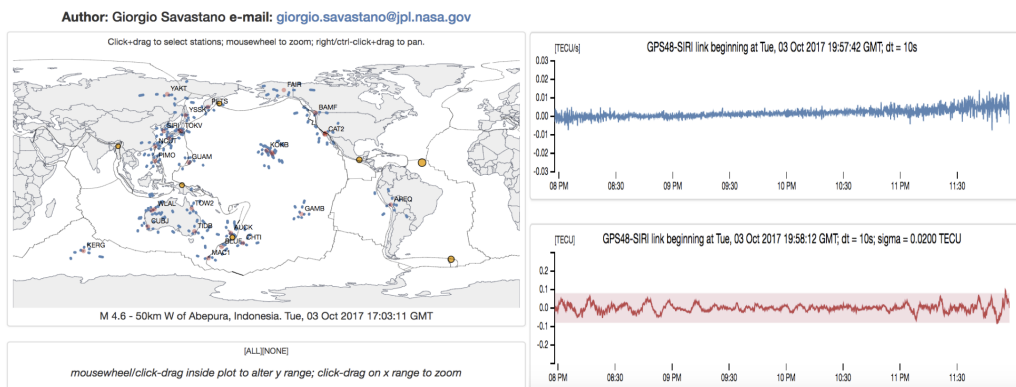


Figure 8. Implementation of the VARION website. The real-time stream of data from the JPL’s GDGPS system is continuously processed using the VARION algorithm.

A real-time tsunami detection system could be designed using VARION combined with real-time data from different sources (e.g. seismometers, buoys, GNSS receivers). Once an earthquake is detected in a specific location, such a system will begin processing the real-time TEC outputs using multiple stations located near the epicenter searching for ionospheric signals that may be correlated with the tsunami propagation. The measurements would be collected and processed by a central processing facility also providing risk assessments and maps related with a particular earthquake event. The use of multiple independent data types will be expected to contribute significantly to the robustness of the system.

6. FUTURE PERSPECTIVES

A first future perspective of this thesis is to investigate and combine the use of observations from geostationary (GEO) satellites (e.g. SBAS, BeiDou) with standard GNSS medium Earth orbit

(MEO) satellites, in order to separate the spatial and the temporal contributions in Eqn. 9, and to detect in real time, as far in advance as possible, natural hazards that are directly observable in Earth’s ionosphere. In fact, in order to reduce the detection latency of the natural hazards with observable perturbations of the ionosphere, it is critical to address the issue of noisier observations at low elevation angles in Sec. 3.5 and to properly separate the standard sTEC background variability from the natural hazards’ perturbations as fast and reliable as possible.

A second perspective is to use ship-based GNSS receivers to increase the ionosphere monitoring coverage over the oceans and to improve the reliability of real-time tsunami detection. In fact, since VARION is based on the geometry-free combination (Eqn. 6), the receiver motion does not affect the sTEC estimation process.

ACKNOWLEDGEMENTS

I would like to acknowledge and thank my thesis advisor: Prof. Mattia Crespi from Sapienza University of Rome; and my two thesis coadvisors: Dr. Attila Komjathy, from the Jet Propulsion Laboratory, California Institute of Technology, and Prof. Augusto Mazzoni from Sapienza University of Rome.

REFERENCES

- Artru, J., Ducic, V., Kanamori, H., Lognonné, P., Murakami, M., 2005. Ionospheric detection of gravity waves induced by tsunamis. *Geophys. J. Int.*, 20, 840-848. <http://dx.doi.org/10.1111/j.1365-246X.2005.02552.x>.
- Artru, J., Farges, T., Lognonné, P., 2004. Acoustic waves generated from seismic surface waves: propagation properties determined from Doppler sounding observations and normal-mode modelling. *Geophys. J. Int.*, 158. <http://dx.doi.org/10.1111/j.1365-246X.2004.02377.x>.
- Artru, J., Lognonné, P., Blanc, E., 2001. Normal modes modelling of postseismic ionospheric oscillations. *Geophys. Res. Lett.*, 28. <http://dx.doi.org/10.1029/2000GL000085>.
- Astafyeva, E., Heki, K., 2009. Dependence of waveform of near-field coseismic ionospheric disturbances on focal mechanisms. *Earth, Planets and Space*, 61(7), 939-943. <http://dx.doi.org/10.1186/BF03353206>.
- Astafyeva, E., Heki, K., Kiryushkin, V., Afraimovich, E., Shalimov, S., 2009. Two-mode long-distance propagation of coseismic ionosphere disturbances. *Journal of Geophysical Research: Space Physics*, 114(A10), n/a-n/a. <http://dx.doi.org/10.1029/2008JA013853>. A10307.
- Benedetti, E., Branzanti, M., Biagi, L., Colosimo, G., Mazzoni, A., Crespi, M., 2014. Global Navigation Satellite Systems Seismology for the 2012Mw6.1 Emilia Earthquake: Exploiting the VADASE Algorithm. *Seism. Res. Lett.*, 85 no. 3, 649-656. <http://dx.doi.org/10.1785/0220130094>.
- Bishop, G., Walsh, D., Daly, P., Mazzella, A., Holland, E., 1994. Analysis of the temporal stability of GPS and GLONASS group delay correction terms seen in various sets of ionospheric delay data. *Proceedings of the 7th International Technical Meeting of the Satellite Division of The Institute of Navigation (ION GPS 1994)*, 1653-1661.
- Blewitt, G., 2015. 3.11 - GPS and Space-Based Geodetic Methods. G. Schubert (ed.), *Treatise on Geophysics (Second Edition)*, second edition edn, Elsevier, Oxford, 307 - 338.
- Branzanti, M., Colosimo, G., Crespi, M., Mazzoni, A., 2012. GPS near real-time coseismic displacements for the great Tohoku-Oki earthquake. *IEEE Geoscience and Remote Sensing Letters*. <http://dx.doi.org/10.1109/LGRS.2012.2207704>.
- Brunini, C., Meza, A., Bosch, W., 2005. Temporal and spatial variability of the bias between TOPEX- and GPS-derived total electron content. *J Geod.*, 79. <http://dx.doi.org/10.1007/s00190-005-0448-z>.
- Calais, E., Minster, J. B., 1995. GPS detection of ionospheric perturbations following the January 17, 1994, Northridge earthquake. *Geophys. Res. Lett.*, 22. <http://dx.doi.org/10.1029/95GL00168>.
- Calais, E., Minster, J. B., 1998. GPS, earthquakes, the ionosphere, and the Space Shuttle. *Phys. Earth Planet. Inter.*, 105. [http://dx.doi.org/10.1016/S0031-9201\(97\)00089-7](http://dx.doi.org/10.1016/S0031-9201(97)00089-7).
- Ciraolo, L., Azpilicueta, F., Brunini, C., Meza, A., Radicella, S., 2007. Calibration errors on experimental slant total electron content (TEC) determined with GPS. *J Geodesy*. <http://dx.doi.org/10.1007/s00190-006-0093-1>.
- Coisson, P., Lognonne, P., Walwer, D., Rolland, L. M., 2015. First tsunami gravity wave detection in ionospheric radio occultation data. *Earth and Space Science*, 2, 125-13. <http://dx.doi.org/10.1002/2014EA000054>.
- Colosimo, G., Crespi, M., Mazzoni, A., 2011. Real-time GPS seismology with a stand-alone receiver: A preliminary feasibility demonstration. *Journal of Geophysical Research: Solid Earth*, 116(B11). [10.1029/2010JB007941](http://dx.doi.org/10.1029/2010JB007941).
- Daniels, F. B., 1952. Acoustic energy generated by ocean waves. *d. Acoust. Soc.*, 24, 83.
- Dautermann, T., Calais, E., Lognonné, P., Mattioli, G. S., 2009. Lithosphere-atmosphere-ionosphere coupling after the 2003 explosive eruption of the Soufriere Hills Volcano, Montserrat. *Geophysical Journal International*, 179(3), 1537-1546. <http://dx.doi.org/10.1111/j.1365-246X.2009.04390.x>.
- Ducic, V., Artru, J., Lognonne, P., 2003. Ionospheric remote sensing of the Denali earthquake Rayleigh surface waves. *Geophys. Res. Lett.*, 30. <http://dx.doi.org/10.1029/2003GL017812>.
- Galvan, D. A. et al., 2012. Ionospheric signatures of Tohoku-Oki tsunami of March 11, 2011: Model comparisons near the epicenter. *Radio Sci.*, 47, RS4003. <http://dx.doi.org/10.1029/2012RS005023>.
- Galvan, D. A., Komjathy, A., Hickey, M. P., Mannucci, A. J., 2011. The 2009 Samoa and 2010 Chile tsunamis as observed in the ionosphere using GPS total electron content. *J. Geophys. Res.*, 116, A06318. <http://dx.doi.org/10.1029/2010JA016204>.
- Hickey, M. P., Schubert, G., Walterscheid, R. L., 2009. Propagation of tsunami-driven gravity waves into the thermosphere and ionosphere. *J. Geophys. Res.*, 114, A08304. <http://dx.doi.org/10.1029/2009JA014105>.
- Hines, C. O., 1960. Internal atmospheric gravity waves at ionospheric heights. *Can. J. Phys.*, 38, 1441-1481. <http://dx.doi.org/10.1139/p60-150>.
- Hines, C. O., 1972. Gravity waves in the atmosphere. *Nature*, 239, 7378. <http://dx.doi.org/10.1038/239073a0>.
- Hoffman-Wellenhof, B., Lichtenegger, H., Wasle, E., 2008. *GNSS - Global Navigation Satellite Systems. GPS, GLONASS, Galileo and more*. Springer-Verlag.
- Holaschutz, D., Bishop, R. H., Harris, R. B., Tolman, B., 2008. Inter-frequency Bias Estimation for the GPS Monitor Station Network. *Proceedings of the 21st International Technical Meeting of the Satellite Division of The Institute of Navigation (ION GNSS 2008)*, 2405-2415.
- Holton, J. R., 1992. *An Introduction to Dynamic Meteorology*. New York: Academic Press.

- Hung, R. J., Phan, T., Smith, R. E., 1978. Observation of gravity waves during the extreme tornado outbreak of 3 April 1974. *J. Atmos. Terr. Phys.*, 40, 831–843. [http://dx.doi.org/10.1016/0021-9169\(78\)90033-8](http://dx.doi.org/10.1016/0021-9169(78)90033-8).
- International Union of Geodesy and Geophysics, 2015. IUGG Resolution. <http://www.iugg.org/resolutions/IUGGResolutions2015.pdf>.
- Jin, S., Occhipinti, G., Jin, R., 2015. GNSS ionospheric seismology: recent observation evidences and characteristics. *Earth-Science Reviews*, 147, 54–64. <http://dx.doi.org/10.1016/j.earscirev.2015.05.003>.
- Kelley, M. C., 1997. In situ ionospheric observations of severe weather related gravity waves and associated small scale plasma structure. *J. Geophys. Res.*, 102, 329–335. <http://dx.doi.org/10.1029/96JA03033>.
- Kelley, M. C., Livingston, R., McCreedy, M., 1985. Large amplitude thermospheric oscillations induced by an earthquake. *Geophys. Res. Lett.*, 12, 577–580. <http://dx.doi.org/10.1029/GL012i009p00577>.
- Kherani, E. A., Lognonné, P., Kamath, N., Crespon, F., Garcia, R., 2009. Response of the ionosphere to the seismic triggered acoustic waves: electron density and electromagnetic fluctuations. *Geophys. J. Int.*, 176, 1–13. <http://dx.doi.org/10.1111/j.1365-246X.2008.03818.x>.
- Klobuchar, J. A., 1987. Ionospheric Time-Delay Algorithm for Single-Frequency GPS Users. *IEEE Transactions on Aerospace and Electronic Systems*, AES-23(3), 325–331. <http://dx.doi.org/10.1109/TAES.1987.310829>.
- Komjathy A. et al., 2016. Review and perspectives: Understanding natural-hazards-generated ionospheric perturbations using GPS measurements and coupled modeling. *Radio Sci.*, 51, 951–961. <http://dx.doi.org/10.1002/2015RS005910>.
- Komjathy, A., Galvan, D. A., Stephens, P., Butala, M. D., Akopian, V., Wilson, B., Verkhoglyadova, O., Mannucci, A. J., Hickey, M., 2013. Detecting ionospheric TEC perturbations caused by natural hazards using a global network of GPS receivers: The Tohoku case study. *Earth, Planets and Space*, 64(12), 24. <http://dx.doi.org/10.5047/eps.2012.08.003>.
- Komjathy, A., Sparks, L., Wilson, B. D., Mannucci, A. J., 2005. Automated daily processing of more than 1000 ground-based GPS receivers for studying intense ionospheric storms. *Radio Sci.*, 40, RS6006. <http://dx.doi.org/10.1029/2005RS003279>.
- LaBrecque, J., Rundle, J., Bawden, G., 2018. GATEW Report. http://www.ggos.org/media/filer_public/64/36/6436cc04-00cf-407a-a365-e79ce26378f2/gtews2017.pdf.
- Lee, M. C. et al., 2008. Did tsunami-launched gravity waves trigger ionospheric turbulence over Arecibo? *J. Geophys. Res.*, 113, A01302. <http://dx.doi.org/10.1029/2007JA012615>.
- Liu, H., Ding, F., Zhao, B., Li, J., Hu, L., Wan, W., Ning, B., 2017. Ionospheric response following the Mw 7.8 Gorkha earthquake on 25 April 2015. *Journal of Geophysical Research: Space Physics*. <http://dx.doi.org/10.1002/2016JA023079>.
- Mai, C.-L., and J.-F. Kiang, 2009. Modeling of ionospheric perturbation by 2004 Sumatra tsunami. *Radio Sci.*, 44, RS3011. <http://dx.doi.org/10.1029/2008RS004060>.
- Mannucci, A. J. et al., 1998. A global mapping technique for GPS derived ionospheric total electron content measurements. *Radio Sci.*, 33, 565–582. <http://dx.doi.org/10.1029/97RS02707>.
- Mannucci, A. J. et al., 2004. GPS-based remote sensing of the geospace environment: Horizontal and vertical structure of the ionosphere and plasmasphere. *Proc. SPIE Int. Soc. Opt. Eng.*, 5660, 1–13. <http://dx.doi.org/10.1117/12.580048>.
- Meng, X. et al., 2015. A new physics-based modeling approach for tsunami-ionosphere coupling. *Geophys. Res. Lett.*, 42, 4736–4744. <http://dx.doi.org/10.1002/2015GL064610>.
- Nicolls, M. J., Kelley, M. C., Coster, A. J., González, S. A., Makela, J. J., 2004. Imaging the structure of a large scale TID using ISR and TEC data. *Geophys. Res. Lett.*, 31, L09812. <http://dx.doi.org/10.1029/2004GL019797>.
- Occhipinti, et al., 2011. Three-dimensional numerical modeling of tsunami-related internal gravity waves in the Hawaiian atmosphere. *Earth Planets Space*, 63 (7), 847–851.
- Occhipinti, G., Kherani, E. A., Lognonné, P., 2008. Geomagnetic dependence of ionospheric disturbances induced by tsunamigenic internal gravity waves. *Geophys. J. Int.*, 73, 753765. <http://dx.doi.org/10.1111/j.1365-246X.2008.03760.x>.
- Occhipinti, G., Lognonné, P., Kherani, E. A., Hbert, H., 2006. Threedimensional waveform modeling of ionospheric signature induced by the 2004 Sumatra tsunami. *Geophys. Res. Lett.*, 33, L20104. <http://dx.doi.org/10.1029/2006GL026865>.
- Occhipinti, G., Rolland, L., Lognonné, P., Watada, S., 2013. From Sumatra 2004 to Tohoku-Oki 2011: The systematic GPS detection of the ionospheric signature induced by tsunamigenic earthquakes. *Journal of Geophysical Research: Space Physics*, 118(6), 3626–3636. <http://dx.doi.org/10.1002/jgra.50322>.
- Okal, E. A., 1988. Seismic parameters controlling far-field tsunami amplitudes: A review. *Natural Hazards*, 1(1), 67–96. <https://doi.org/10.1007/BF00168222>.
- Peltier, W. R., Hines, C. O., 1976. On the possible detection of tsunamis by a monitoring of the ionosphere. *J. Geophys. Res.*, 81 12, 1995–2000.
- Percival, D.B. et al., 2011. Extraction of tsunami source coefficients via inversion of DART® buoy data. *Nat. Hazards*, 58 1, 567–590, doi:10.1007/s11069-010-9688-1.
- Predybaylo, E., 2014. Wavelet Python Software. <http://atoc.colorado.edu/research/wavelets/>.
- Queney, P., 1948. The Problem of Airflow over Mountains. A Summary of Theoretical Studies. *Bulletin of the American Meteorological Society*, 16–26.
- Richmond, A. D., Matsushita, S., 1975. Thermospheric response to a magnetic substorm. *J. Geophys. Res.*, 80, 2839–2850. <http://dx.doi.org/10.1029/JA080i019p02839>.
- Rolland, L. M., Lognonné, P., Astafyeva, E., Kherani, E. A., Kobayashi, N., Mann, M., Munekane, H., 2011a. The resonant response of the ionosphere imaged after the 2011 off the Pacific coast of Tohoku Earthquake. *Earth, Planets and Space*, 63(7), 62. <http://dx.doi.org/10.5047/eps.2011.06.020>.

- Rolland, L. M., Lognonné, P., Munekane, H., 2011b. Detection and modeling of Rayleigh wave induced patterns in the ionosphere. *Journal of Geophysical Research: Space Physics*, 116(A5). <http://dx.doi.org/10.1029/2010JA016060>.
- Rolland, L. M., Occhipinti, G., Lognonné, P., Loevenbruck, A., 2010. Ionospheric gravity waves detected offshore Hawaii after tsunamis. *Geophys. Res. Lett.*, 37, L17101. <http://dx.doi.org/10.1029/2010GL044479>.
- Sardon E, Rius A, Z. N., 2009. *Tsunami forecasting*. Tsunamis, 15, Harvard University Press, Cambridge, MA and London, England, chapter 12, 371–400.
- Sardon, E., Rius, A., Zarraoa, N., 1994. Estimation of the transmitter and receiver differential biases and the ionospheric total electron content from Global Positioning System observations. *Radio Sci*, 29, 577–586.
- Savastano, G., Komjathy, A., Verkhoglyadova, O., Mazzoni, A., Crespi, M., Wei, Y., Mannucci, A. J., 2017. Real-Time Detection of Tsunami Ionospheric Disturbances with a Stand-Alone GNSS Receiver: A Preliminary Feasibility Demonstration. *Sci. Rep.*, 7, 46607. <http://dx.doi.org/10.1038/srep46607>.
- Seeber, G., 2003. *Satellite geodesy: foundations, methods, and applications, 2nd edition*. Walter de Gruyter, Berlin New York.
- Shults, K., Astafyeva, E., Adourian, S., 2016. Ionospheric detection and localization of volcano eruptions on the example of the April 2015 Calbuco events. *Journal of Geophysical Research: Space Physics*, 121(10), 10,303–10,315. <http://dx.doi.org/10.1002/2016JA023382>.
- Tahira, M., 1995. Acoustic Resonance of the Atmospheric at 3.7 Hz. *Journal of the Atmospheric Sciences*, 52(15), 2670–2674. [https://doi.org/10.1175/1520-0469\(1995\)052<2670:AROTAA>2.0.CO;2](https://doi.org/10.1175/1520-0469(1995)052<2670:AROTAA>2.0.CO;2).
- Tang, L., V.V. et al., 2012. Direct energy estimation of the 2011 Japan tsunami using deep-ocean pressure measurements. *J. Geophys. Res.*, 117, C08008. <http://dx.doi.org/10.1029/2011JC007635>.
- Titov, V.V. et al., 2005. Real-time tsunami forecasting: Challenges and solutions. *Nat. Hazards*, 35(1), 41–58.
- Torrence, C., Compo, G. P., 1998. A practical guide to wavelet analysis. *Bull. Amer. Meteor. Soc.*, 79, 6178.
- Tsugawa, T., Otsuka, Y., Coster, A. J., Saito, A., 2007. Medium scale traveling ionospheric disturbances detected with dense and wide TEC maps over North America. *Geophys. Res. Lett.*, 34, L22101. <http://dx.doi.org/10.1029/2007GL031663>.
- VARION Development Team, 2016. VARION Software. <https://github.com/giorgiosavastano/VARION>.
- Ward, S. N., 1980. Relationships of tsunami generation and an earthquake source. *J. Phys. Earth*, 28, 441–474.
- Watada, S., 1995. *Near-source acoustic coupling between the atmosphere and the solid earth during volcanic eruptions*. PhD Thesis California Institute of Technology, Pasadena, CA.
- Wei, Y., Chamberlin, C., Titov, V., Tang, L., Bernard, E. N., 2013. Modeling of the 2011 Japan tsunami - Lessons for near-field forecast. *Pure Appl. Geophys.*, 170(6–8), 1309–1331. <http://dx.doi.org/10.1007/s00024-012-0519-z>.
- Wei, Y. et al., 2008. Real-time experimental forecast of the Peruvian tsunami of August 2007 for U.S. coastlines. *Geophys. Res. Lett.*, 35, L04609. <http://dx.doi.org/10.1029/2007GL032250>.
- Xiao, Z., Xiao, S., Hao, Y., Zhang, D., 2007. Morphological features of ionospheric response to typhoon. *J. Geophys. Res.*, 112, A04304. <http://dx.doi.org/10.1029/2006JA011671>.
- Yang, Y.-M. et al., 2014a. The 2013 Chelyabinsk meteor ionospheric impact studied using GPS measurements. *Radio Sci.*, 49, 341350. <http://dx.doi.org/10.1002/2013RS005344>.
- Yang, Y.-M. et al., 2014b. Tohoku-Oki earthquake caused major ionospheric disturbances at 450 km altitude over Alaska. *Radio Sci.*, 49, 1206–1213. <http://dx.doi.org/10.1002/2014RS005580>.



Associazione **U**niversitari di **T**opografia **e** **C**artografia

Sezione Tematica 2 Fotogrammetria e Laser Scanner

*

*Thematic Section 2
Photogrammetry and Laser Scanner*

SUMMARY OF PHD THESIS: HOLISTIC GENERATIVE MODELING PROCESS FOR HBIM

F.Banfi · *

Dept. of Architecture, Build Environment and Construction Engineering, Politecnico di Milano, Milan, Italy –
fabrizio.banfi@polimi.it

KEY WORDS: Modeling requirements, Grade of generation (GOG), Historic Building Information Modeling (HBIM), Scan-to-BIM, BIM application, Application Programming Interface (API), IT developments, Plug-in

ABSTRACT:

In a world of exponential growth, Architecture, Engineering and Construction (AEC) sector is facing a great re-engineering of the processes thanks to the latest technological developments in the field of geomatics and information technology (IT) such as Terrestrial Laser Scanning (TLS) and Building Information Modelling (BIM). BIM is an innovative method capable to support the new paradigm of *'process'* of the new buildings during their lifecycle (BLM). On the other hand, the intricate reality of the built heritage and the growing need to represent the actual geometry using *'informative'* models collide with the paradigms of complexity and accuracy of heritage buildings. Against this backdrop, this research proposes novel Scan-to-BIM modeling requirements and the development of an add-in/plugin (Facility Tool) for one of the most used BIM application, improving the generation of complex elements from point cloud data (Terrestrial laser scanning TLS, Digital Photogrammetry DP), facing the paradigm of complexity (built heritage and its architectural and structural elements) against the regularity of BIM libraries (simple geometric shapes for new buildings).

1. INTRODUCTION

1.1 Background and context

In recent years, digital modeling has been one of the main resources for the generation of *'informative'* models and interactive digital environments (Virtual and augmented reality VR-AR) able to support the life cycle of the building and increase the sharing of information between different disciplinary sectors and fields of application (Ioannides & Quak 2014) (Balletti et al.,2015). Thanks to the development of methods and research in the field of geomatics and the 3D survey, it was possible to place the *'value of the measure'* at the centre of the process and the importance of the correct generation of digital models able to correspond to the reality detected (Brumana et al., 2018) (Tucci & Bonora2011). Thanks to the integration of the most advanced survey techniques such as laser scanning and digital photogrammetry, it was possible to store and analyse large amounts of data from the buildings were captured such as point clouds, photo planes and orthophotos. The value of the measurement and the sharing of these data were also decisive for different disciplines and sectors other than design such as restoration, structural analysis, the construction site, and facility management (Banfi 2016) (Della Torre 2015). The introduction of BIM in the field of built heritage has also allowed innovative studies to go beyond the simple 2D vector representation. In recent years, 2D CAD drawings have been replaced more and more by innovative BIM approaches. Innovative research has also shown that the quality of models, the levels of detail (LOD) and information (LOI) represent primary requirements for appropriate use of models for different types of analysis. The accuracy of the models, in fact, has brought significant advantages in different application fields such as the finite element analysis (FEA), rapid prototyping, virtual and augmented reality, restoration and

rehabilitation processes of buildings of high historical and institutional value (Fai et al.,2011) (Kuo et al.,2018) (Dore& Murphy 2017). On the other hand, the wealth of these data is not always handed down among the various experts involved in the building requalification, monitoring and maintenance process, leading to the loss of a large amount of information gathered during the survey phases and to the analysis of the building.

1.2 Gaps in HBIM generation and orientation for different BIM-based analysis

The vast amount of information and data, which originate from the 3D survey, need a quick implementation of the modeling method, as well as update of the main information-sharing techniques during the life cycle of the building. An advanced modeling generative process based on 3D survey data should develop an architecture of objects for complex elements that can take note of the complexity of the different phases: constructive, stratigraphical information, morphological, technological, and geometrical deformations of various origin. The identification of the cognitive stream of the proposed research was enucleated from the juxtaposition of two paradigms (Modeling and Information) that identify the level of complexity and knowledge in HBIM models:

- **Modeling** : it consists of a main actor's transcendence operation (transformation of different data sources) into an upgradeable digital model (3D objects oriented to built heritage). Modeling for heritage building, composed of unique and complex elements, should be flexible and sustainable for each type of user. Therefore, modeling requirements (GOGs and GOA), new internal functions and guidelines (Developments of plug-in and protocols) for HBIM are required.

* Corresponding author

- Information** : it develops the concept of knowledge as assimilation of complex information within a digital platform (Knowledge = Information associated with the model) and a consequent subdivision of the model in single units proportional to the amount of information collected during the BLC (Levels of complexity = Subdivision of the Model in Architectural and Structural elements = oriented Historic Parametric Objects). Digital Repository (Cloud) and new levels of interoperability (new exchange 3D formats) for different BIM-based analysis are required to improve the utility of the model.

Currently, the creation of a parametric model involves a series of difficulties mainly related to the generative aspect. BIM technology applied to complex buildings and infrastructures should be aimed at the subsequent BIM-based analysis's software, by allowing an adequate read of HBIM. The main problems encountered for the generation of an as-found model (AF-BIM) and HBIM models can be summarized in:

- Problem 1** - Long phases of processing and filtering of surveyed data: the point clouds are not real digital models that follow the constructive logic of the building. They require the identification of points of interest and the subsequent cleaning for a targeted three-dimensional reconstruction. The most important question in connection with this is: *Which are the best post-processing procedure for 3D survey data?*
- Problem 2** - BIM applications are not able to quickly generate 3D parametric objects corresponding to the real shapes of the detected artefact, leading to the generation of models characterized by low levels of detail (LOD) and information (LOI) for built heritage. The most important question in connection with this is: *How is it possible to get the proper integration of complex elements in BIM application?*
- Problem 3** - The generation of HBIM models requires the mapping of specific information not included in the parametric logic of the software. In BIM application, 3D objects represent standard elements such as a simple wall, doors, windows, roof, ceiling but are not present historic elements such as vaults, arches, pillar and decorations. The most important question in connection with this is: *Is the parametrization of unique 3D objects and digital databases achievable in BIM application?*
- Problem 4** - For the most part, the BIMs created do not have the appropriate characteristics for the transmission of geometric and information requirements for subsequent analysis phases. The restoration, finite element analysis, energy analysis, monitoring and GIS require models with specific characteristics. The most important question in connection with this is: *is digital model utility for different BIM-based analysis improvable?*

2. RELATED WORKS AND RESEARCH OBJECTIVES

The tangible and intangible values, the uniqueness, richness and irregularity of the shapes of historic buildings such as vaults, arches, variable section walls, walls with double curvatures, columns and historical decorations represented one of the main challenges in the field of digital reconstruction.

For this reason, in a first phase, the following research has investigated and deepened the main modeling techniques with the aim of identifying the main causes that prevent the spread and adoption of HBIM models and Scan-to-BIM processes for

the built heritage. It was found that one of the main causes is given by the absence of modeling techniques, practices and tools capable of transforming survey data (primary data sources) and historical documentation and technical analysis (secondary data sources) into models corresponding to detected reality. As it well know, the main BIM applications are characterised by a limited number of modeling tools and libraries of objects that geometrically represent simplified architectural elements. Once the main barriers in the Scan-to-BIM process have been identified, this research has established new generative requirements for the creation of models able to represent the buildings surveyed with a high grade of accuracy such as Basilica of Collemaggio in Aquila (ITA), Masegra Castel in Sondrio (ITA), Azzone Visconti bridge in Lecco (ITA), DEMO Aler in Cinisello Balsamo (ITA), Parliament building in Ottawa, Ontario (CA), and Basilica of Saint Ambrose in Milan (ITA). In summary, the research objectives applied to these research case studies were:

- To integrate 3D Data Capture techniques (3D Laser and Photogrammetry) in order to acquire accurate measurements of historic/existing buildings and show how can be generated through internal automation proper basis for the generation of H-BIMs.
- To improve the utility of Scan-to-BIM process through the use the automation of Advanced Modelling Techniques (AMT) able to reach accurate architectural and structural elements such complex vault, arches, columns, decorations and irregular walls by new grade of generation (GOG).
- To manage the complexity of the architectural and structural elements with high-grade accuracy (GOA), favouring high dissemination of information linked to HBIM (GOI).
- To cluster exchange formats and verification system for as-built BIM, facilitating the interoperability between free-form models (NURBS models), BIM database (parametric models) and other BIM-based analysis such as Finite element analysis, Virtual Reality, Augmented Reality, Monitoring, Computing.
- To integrate the proposed Scan-to-BIM method in new user-friendly Revit Add-in.
- To show the research impact and to prove the economic benefits of the proposed method (Fig. 1).

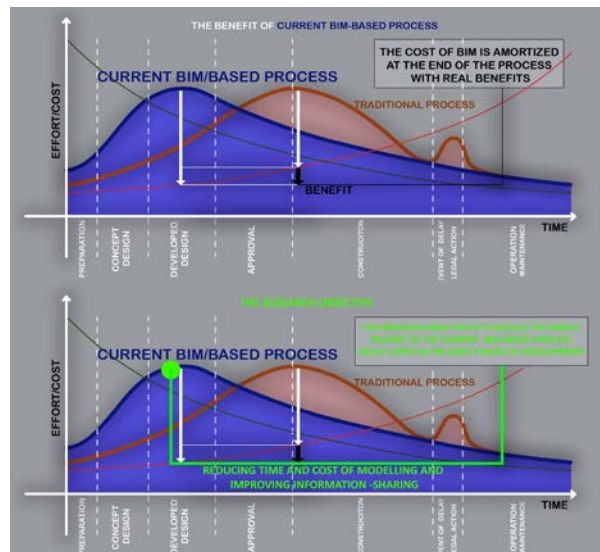


Figure 1 – The main research objective.

3. THE RESEARCH METHODOLOGY: THE ESTABLISHMENT OF SCAN-TO-BIM MODELING REQUIREMENTS FOR HERITAGE BUILDINGS

3.1 The management of 3D survey data: from point clouds to a proper 3D reconstruction

Currently, market applications of 3D data capture technology such as total station (TS), terrestrial laser scanning (TLS), unmanned aerial vehicle (UAV) and high-resolution cameras for digital photogrammetry is validating to be quick and accurate methods for the proper 3D building survey (Masiero et al., 2017). The main instruments used for the 3D survey of the research case studies were Faro Laser Scanner Focus, Canon EOS-1D X, Astec Falcon 8 equipped with RGB camera Sony NEX - 5N and Leica TS30. As shown in figure 1, 3D survey produced 3D scans (called also point clouds) that are not real digital models that follow the constructive logic of the building. In order to answer the question *‘Which are the best post-processing procedure for 3D survey data?’* surveys of the presented case studies are characterised by the innovative integration of various techniques and tools.

Thanks to the integrated use of point clouds from laser scanning, photogrammetry and total station it has been possible to achieve a proper base for the digital reconstruction of the research case studies, reducing return site visits and saving a significant amount of money and time (Guarnieri et al., 2006). The creation of geodetic networks composed of surveyed points and new interest points allowed the proper referencing of all the scans obtained with a laser scanner and photogrammetry, giving a single system with shared coordinates in all modelling applications. Point clouds are composed of a huge amount of data, which require a post-processing phase characterised by the selecting of the best exchange procedure (input/output formats) and setting to proper NURBS / BIM-based modelling environment. For each proposed case study, laser scanning measured the locations of a huge number of 3D points in a range up to 60-80 meters. The average scan resolution of the research case studies was about 100 million points per scan, which is directly related to the point density to ensure accurate primary data sources for 3D reconstruction (Fig. 2).

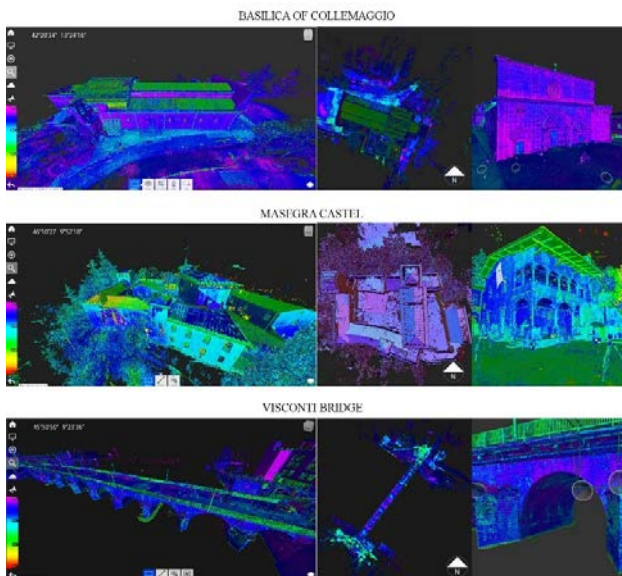


Figure 2 – Laser scanning data – Primary data sources used for the generation of HBIMs of the research case studies.

Experimental investigations were carried out to improve the interoperability level of the exchange format between Autodesk ReCap, MC Neel Rhinoceros, and Autodesk Revit.

The proper use of output and input files were the key to reduce point cloud size (in terms of memory consumption and efficient visualization) for a better transmission from their native format in the used modelling applications. Scene, Autodesk ReCap and Bentley Pointools permitted the first operations of cleaning and editing. The data output of these application allowed to transform 3D scans in PTS, RCS, e57, PCG, ASCII XYZ and POD exchange formats. They are text-based formats that contain point clouds commonly generated by a 3D scanner such as Faro Focus 3D. These files retain all the original scan’s information such as transformation matrices and scanner location. The definition of the best input/output formats and the setting of the NURBS software permits the activation of each point of the scans in the digital space, giving the best base for the generation and extraction of geometric primitives. The definition of exchange formats such as .dwg and sat. also allowed the development of the level of interoperability of data between 3D Survey, NURBS models and BIM application with the same georeferenced environment, enabling semi-automatic update phases of the model without having to translate, adapt BIM objects in different spatial positions. This requirement made it possible to considerably reduce the integrating of model portions carried out in different periods and providing a reliable reference base at the same time. In addition to the laser scanning, the application of advanced photogrammetry techniques also allows the acquisition of the shadow areas of the 3D scans and to generate true orthophotos of every single structural element at the same time. The building’s components have been identified directly on the field thanks to the support of historical documents, structural reports and 2D drawings (secondary data sources) which, can complete the interpretive analysis of the building, description of pathologies and materials used for the digital reconstruction (Fig. 3).



Figure 3 – Geodetic networks and digital photogrammetry data are secondary data sources used for the generation of HBIMs.

3.2 Embodying heritage building complexity: from complex NURBS surface to 3D parametric BIM object

The digitalisation of heritage buildings in BIM application from dense point clouds directly clashes with the difficulty of expanding the information system of the model in a digital environment. As anticipated, the main reason is the limited number of BIM modelling tools that are not able to help users to create as-built models in a user-friendly way. Free-form modelling and NURBS functions can help the implementation of a new grade of generation. In order to show the innovative contribution of the proposed method, it has been decisive to classify the main modelling functions included in the BIM applications. These tests have benefited from an applied experience on different national and international case studies and the study/implantation of advanced BIM protocols oriented to the generations of Scan-to-BIM models.

The acronym NURBS (Non-Uniform Rational Basis Splines) take account of B-spline. One of the most important benefits of NURBS modeling and the B-spline is the high level of flexibility to complex model shapes. On the other hand, the lack of NURBS modeling tool in BIM application such as Autodesk Revit and Graphisoft Archicad required not only to study the main function splines but to generate complex shapes from a set of geometric primitives.

Thanks to a large number of tests that offered the case studies of national and international relevance of this research, it was possible to define and develop a generative method that bases itself on the study of the most complex elements of historic buildings: the vaulted systems. As shown in figure 4, thanks to a series of unique tests on different vaulted systems, it was possible to generate intelligent models of historical architectural elements not present in the BIM libraries and to connect and share a large amount of information thanks to the parametric logic of Autodesk Revit.

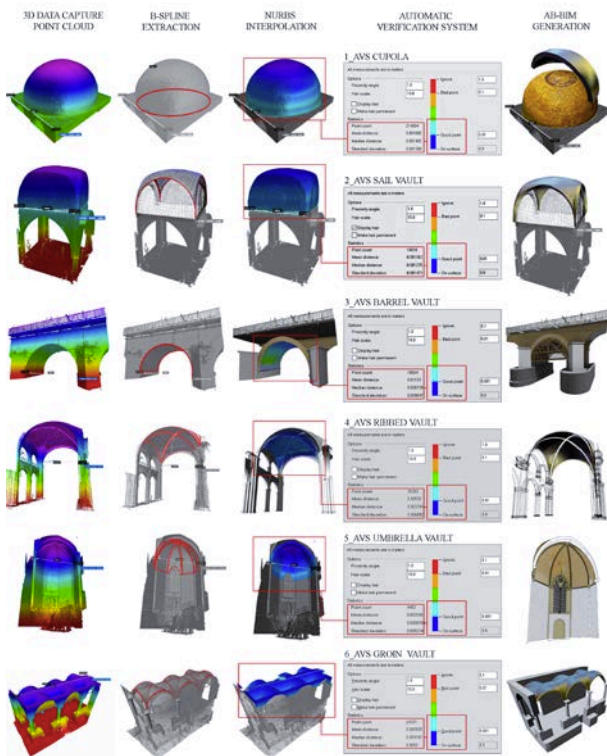


Figure 4. HBIM objects of different type of vaulted system.

In particular, the use of generative modeling based on NURBS geometry was fundamental for interpreting complex three-dimensional vaults (cupola, barrel, going vaults etc) without manual segmentation and long slicing phases. Free-form modeling application today require closed edge and internal B-spline curves in order to create a NURBS surface. In dense and accurate point clouds, composed of 70/100 millions of points, has proved to be difficult to close the perimeter and to connect each B-splines (internal curves) with the 3D borders. The research study has found a proper way in the application of NURBS interpolation function in order to bridge this practical modeling gap. The key idea was to use the points of the 3D scans directly, avoiding the slicing and improving the level of automation for Scan-to-BIM model at the same time. To understand the benefits and techniques of the proposed method have been investigated the principles and bases of NURBS interpolation in order to optimize, finalize and simplify the method for the generation of accurate digital models. According to Piegl's results, the data points to a limited number of values of the independent variable. NURBS surface generation has considered the internal curves and a closed surface border. The key idea of this study was to replace the internal isocurves with the point cloud for the automatic generation of a NURBS surface, thus giving the necessary input to the patch.

Thanks to a series of tests, the specific requirements for the correct modelling of the patch surface have been identified: a point cloud portion previously cleaned that corresponds to the element to generate, and a closed edge able to intercept the main shape's borders. Figure 5 shows how a closed edge (curve extracted from points) and the correctly imported points in the NURBS modeling software allows generating a surface corresponding to the laser scanning thus avoiding long manual procedures and improving the level of automation of the generative process.

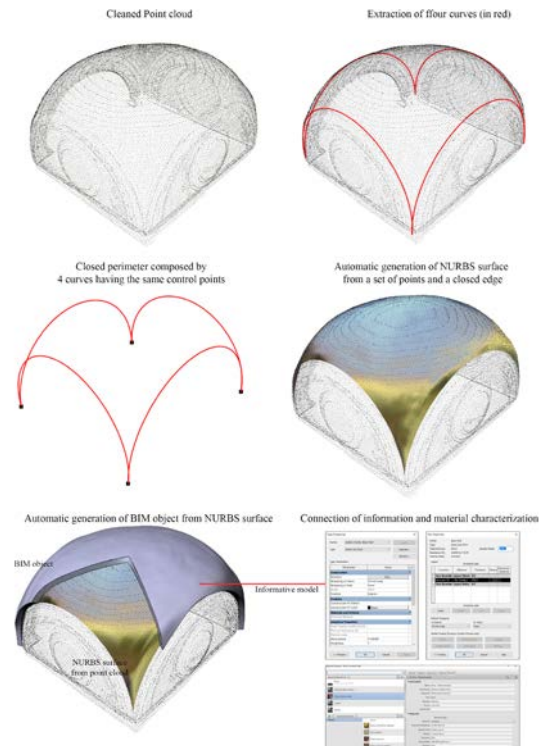


Figure 5. The main Scan-to-BIM modeling steps for a sail vault.

In summary, the study of the free-form curves' generative properties based on NURBS geometry has led to identifying a method able to automate the generation of wire-frame models thanks to the appropriate use of the points that make up the 3D scans.

This first result has consequently made it possible to lay the foundations for the generation of three-dimensional curve models automatically extracted from point clouds with a high level of accuracy and high tolerance, reducing to a minimum the user's manual error. In the following chapters, the grade of accuracy (GOA) of the proposed method and how NURBS interpolation can prove useful for the generation of Scan-to-BIM models are demonstrated.

3.3 Definition of novel Grades of Generation (GOG) for Scan-to-BIM models

This proposed method made possible to lay the scientific and operational bases for the definition of a technique capable of collecting different data sources such as point clouds and 2D CAD drawings and convert them into a Scan-to-BIM model (Banfi 2017). In order to classify the grade of modelling generation, generative modelling tests on the interpolation of 3D survey data have highlighted the lack of advanced modelling tools within BIM applications and have been used to define the development of Revit's add-in structure.

The flexibility of the method is based on a free interpretation of the data and a free identification of the points for the automatic or semi-automatic extraction of geometrical primitives useful for the generation of digital models.

The application of NURBS-interpolation algorithms between outer edges and known points has allowed an automatic generation of complex surfaces with a high number lot of internal U, V subdivisions.

The next paragraph analyses the scalability and flexibility of the proposed method and demonstrate how more GOGs can be oriented for different interoperability levels.

This paragraph, instead, shows as the hierarchization of GOGs has identified the main modelling tools available in the BIM applications and has allowed outlining a growing hierarchy at the same time: from the simplest to the most complex to use. Figure 6 summarises the 10 GOGs.

They divided into two categories:

- the first eight grades of generation correspond to the modelling functions integrated into the BIM application.
- the last two grades (9-10) of generation correspond to two new advanced modelling techniques (slicing and automatic interpolation) capable of transforming dense point clouds into the digital parametric model.

The grade of generation 9-10, unlike the first 8 GOGs, does not represent a greater grade of difficulty from a modeling point of view but rather the extreme synthesis of what was outlined in the previous parameter and directly experimented on the main case studies of this research over the years. The proposed classification emphasises the importance of introducing new requirements for modeling both from an operational point of view and from an interoperability perspective. For this reason, it was necessary to define hierarchy requirements. From a semantic point of view, the word 'grade' has been chosen to explain this necessity in the best possible way. It stands for a 'particular level of rank, quality, proficiency, or value'.

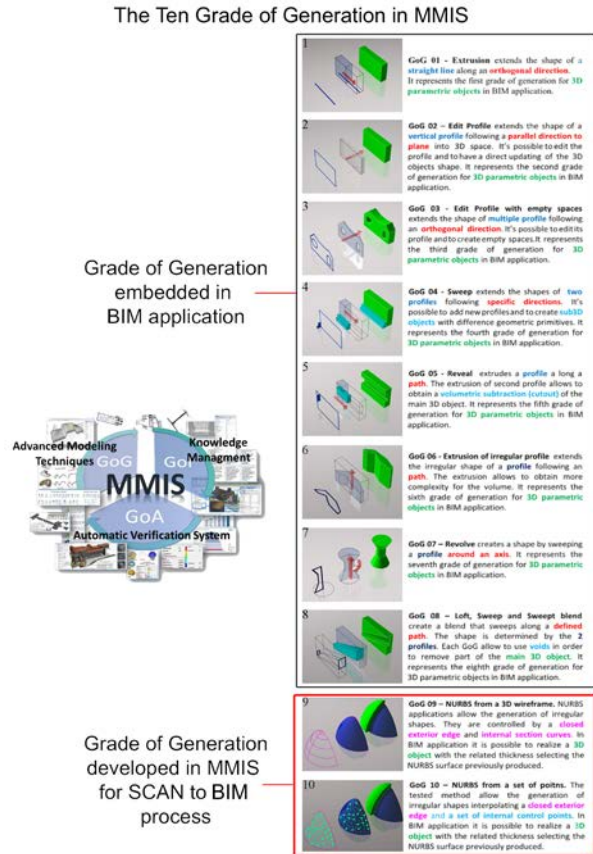


Figure 6. Novel Scan-to-BIM modeling requirements: the ten Grade of Generation SOURCE: Banfi, F. (2017). BIM ORIENTATION: GRADES OF GENERATION AND INFORMATION FOR DIFFERENT TYPE OF ANALYSIS AND MANAGEMENT PROCESS. International Archives of the Photogrammetry, Remote Sensing and Spatial Information Sciences, 42(2/W5).

Autodesk Revit, as is well known, proposes precise rules for the correct implementation of a BIM model. On the other hand, as repeatedly stressed in this paper, a holistic process must be able to relate to different types of analyzes, disciplines and needs. To achieve this goal, the proposed method also considers two new Scan-to-BIM modeling requirements (GOG 9 & 10) able to reach higher levels of interoperability with other BIM platforms and modeling software, thus ensuring a dual solution for both open-source software and BIM applications of leading developers such as Autodesk, Bentley and Graphisoft (Banfi 2017). This hierarchical scale allows the generation of 3D models of different LODs (100, 200, 300, 400, 500). The integration and simulated use of the various modelling functions for a single wall object also allows the generation of AB-BIMs with LOD 500. The first eight GOGs consequently clearly explain how a wall can be realised in Autodesk Revit GOGs defines the techniques and requirements used to improve the quality of the BIM. The complexity of the built heritage and the generation of irregular walls currently involve the direct insertion of the wall object into the three-dimensional space through the GOG 1 and subsequently through the GOGs 2,3,4 it is possible to model and increase the LOD. On the other hand, when the point clouds express volumetric irregularities and complex geometry, to achieve a level of detail higher than 300, the use of voids is crucial.

Volumetric subtraction removes irregular portions and consequently from a simple wall object and thanks to subtraction operations is possible to achieve the real geometric conditions. This procedure, for the most part, is not applied on the large scale of the model due to low flexibility in the voids tool. GOG 8 must, therefore, be considered a solution that can also be applied to the generation of HBIM models, but which was born principally to increase the LODs and complexity of new buildings. The generative logic of NURBS-based software is different from the parametric modelling logic in BIM application. In the first case, the problem is the generation of geometric entities such as splines, polylines, surfaces, and solids. In the second phase, the modelling logic is based on a limited set of (parametric) modelling tools not able to automatic extract geometric primitives from point clouds, or to create complex surfaces with automatic interpolation algorithms, which are instead available in software such as Autodesk AutoCAD and Mc Neel Rhinoceros. The proposed research method integrates NURBS modeling and BIM generation by GOG 9 and 10.

GOG 9 is a modeling procedure that summarises the known slicing technique. The traditional process of generating 2D CAD models and drawings is essentially based on the manual extraction of cross-sections from point clouds. The sections, usually used for technical drawings, are used as a generative basis for three-dimensional modelling in the digital space. GOG 9, instead, bypass 2D drawings and permits the generation of complex geometric models through the automatic extraction of geometric primitives. GOG 9 is based on the generation of NURBS from 3D wireframe. They are controlled by a closed exterior edge and internal section curves (in pink). In BIM application, it is possible to realise a 3D object (in green) with the related thickness selecting the NURBS surface previously produced (in blue). Figure 7 shows the GOG 9 application for some complex vaulted system of Masegra Castel. The modelling procedure is composed of four steps:

1. Generation of a closed exterior edge
2. Extraction of internal section curve
3. Automatic generation of NURBS surface (50x50 UV)
4. The parametrisation of NURBS surface in BIM object

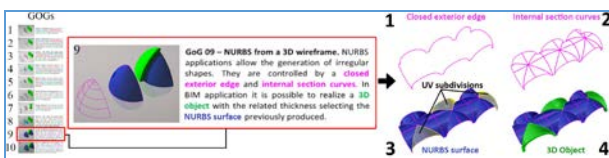


Figure 7. GOG 9: Automatic extraction of proper geometric primitives (1-2) for the NURBS model (3) and the subsequent automatic generation of complex SCAN-to-BIM object (4).

The *mass command* in Autodesk Revit was able to recognise the imported surface automatically. Once correctly introduced through the .sat/.dwg exchange format, it has been possible to create irregular vaults and irregular walls. Numerous tests have

been carried out to identify a novel method capable of automating the generation of complex shapes directly from point clouds, avoiding the slicing technique. Thanks to the identification and targeted application of NURBS interpolation algorithms (Piegl, 2012), GOG10 has been developed. This method provides the automatic generation of complex surfaces directly from point clouds, avoiding step 2 (Internal section curve extraction).

GOG 10 is a three-step modelling procedure that has allowed the reduction of time necessary for the generation of AB-BIM. The generation of internal curves able to interchange the irregular internal shapes of the irregular elements was substituted with 2 requirements. Geometrics can maintain a grade of accuracy and realize AB-BIM with a level of detail 500. For this reason, GOG 10 should be the first requirement for the generation of historical and unique elements and accordingly also for the Italian levels F and G.

The digitalisation of built heritage requires a user-friendly modelling method able to intercept the geometrical and structural anomalies inherited from a millenary historical heritage.

GOG 10 is a modelling procedure able to generate a NURBS from a set of point (Fig.116). The tested method allows the generation of irregular shapes interpolating a closed exterior edge and a set of internal control points. In BIM application, it is possible to realise a 3D object with the related thickness selecting the NURBS surface previously produced.

NURBS interpolation algorithms were able to generate complex surfaces that interpolate a large number of points of the 3D scan.

Once the point cloud is converted into the NURBS surface by defining specific exchange formats, it is possible to parameterise the NURBS surface within Autodesk Revit. Figure 8 shows the GOG 10 application on a complex vaulted system.

Three steps compose the modelling procedure:

1. Generation of a closed exterior edge
2. Automatic generation of NURBS surface (50x50 UV)
3. The parametrisation of NURBS surface in BIM object

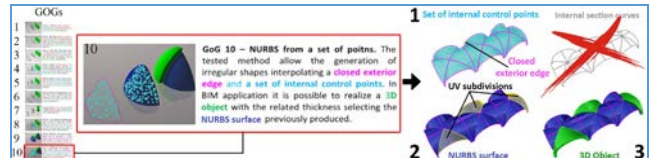
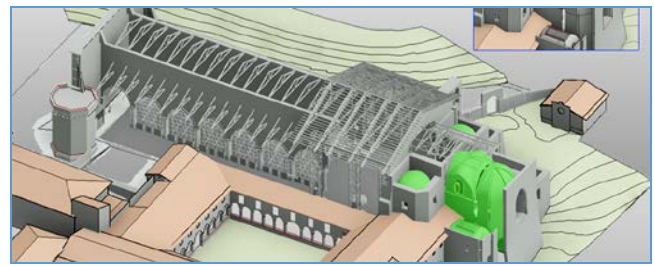


Figure 8. GOG 10: allowed the generation of any vault with a GOA of 1 mm from the 3D scan (1), the automatic generation of the 3D objects (3) from a NURBS model (2) in Revit.

The first benefit of this integration between NURBS modelling, 3D scans, and BIM applications is the automation of the generative procedure for complex elements. This method based on GOG 9 and GOG 10 has ensured to preserve all the

geometric anomalies of each architectural and structural element in HBIM and to link a great quantity of information to every single 3D object for the restoration process.

3.4 Automatic verification system (AVS) of the grade of accuracy (GOA) for Scan-to-BIM model

The previous paragraph showed how NURBS-based modeling appears to be a valid tool to improve the generation of very detailed complex architectural elements from point cloud data. The absence of advanced tools in the BIM software and the presence of modeling tools such as the extrusion, the sweep and swept blend, as illustrated in the previous paragraph, do not allow the generation of complex elements characterized by a high number of irregular architectural components.

The test results laid the foundations for the establishment of parameters and modeling procedures able to fill this generative gap. The tests highlighted the possibility to create BIM objects without to directly model it Autodesk Revit and Graphisoft Archicad, maintaining a high level of interoperability with every type of modeling software. As a consequence, before carrying out this transformation from NURBS to BIM object, the analysis of the surfaces has been analysed in order to improve a system able to certify the quality of the model. For this reason, thanks to the analysis of the surface's curvature, an automatic verification system (AVS) has been identified to calculate the grade of accuracy (GOA) and accurately provide the value of the standard deviation between NURBS surface and 3D scan.

Point set deviation has been identified as the most suitable type of analysis of the proposed AVS in order to evaluate the grade of accuracy of the model between the point cloud and NURBS surfaces. A quantitative value is provided to quantify the quality of the models produced directly from the acquired point cloud. This provides numerical values that represent the standard deviation between point clouds and the whole model without to define parameters 'analysis. This solution is not only an overall indication, but it can be reused to improve model quality over time and, thanks to its direct computation, it results in vast time savings.

The used values are:

Point count: the total number of points n used in the comparison;

Mean distance: average distance between the model and the point cloud

$$\mu = \frac{1}{n} \sum_{i=1}^n r_i$$

This value should be similar to zero so that systematic errors (bases) do not affect the 3D model;

Median distance: a robust index used to evaluate the presence of gross errors, when compared to the other indexes. The median separates the higher half of the r_i values from the lower half;

Standard deviation: index obtained from the squares distances between model and point cloud s is given by

$$\sigma = \sqrt{\frac{\sum(x_i - \mu)^2}{n - 1}}$$

where:

- μ= average of all distances of points from the surface,
- n = number of points analysed and
- x = distance of each point from the surface

The value should be similar to the precision of the laser scanner used. The term r_i in the previous relationships represents the distance between a single point and the surface. Thanks to different case studies it was possible to apply the proposed method over the years and see how the optimization of modeling procedures allowed one to reach a very high GOA through new generative requirements such as GOG 9 and above all the GOG 10. Figure 9 summarizes the AVS on some historic vaulted system of the research case studies examined to demonstrate how the analysis can be applied on any type of wall structure without having considerable competences on modeling. Mostly, after application of the above formula, the objectives were:

- to Automatically compute NURBS surface from point cloud
- to analyse very detailed SCAN-to-BIM model
- to allow the analysis also to users who do not possess advanced knowledge of generative modeling
- to transmit the quality of the model through a numerical value and 3D graphic representations
- to save time for model quality certification procedures
- to provide a valid tool for model certification.

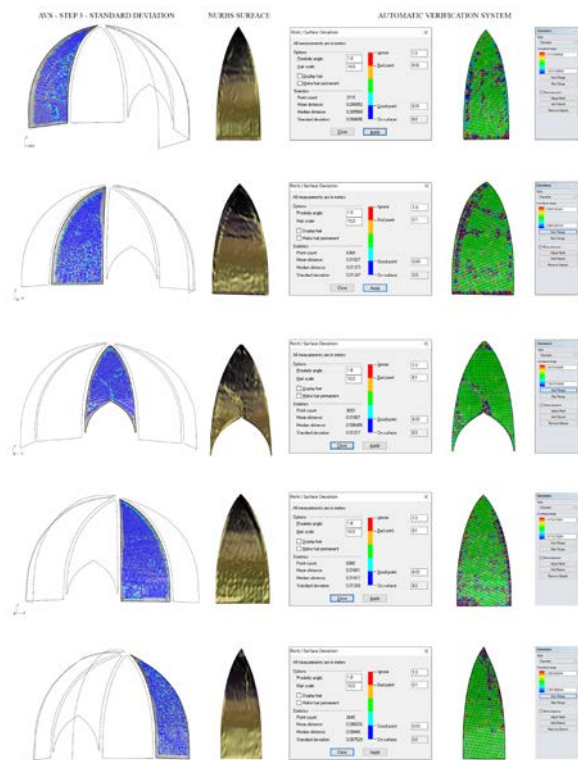


Figure 9. The proposed method has defined a control system able to shows the related deviation value to the users involved in the process.

This study, following different computational tests and comparisons between different software like Meshlab, etc., is based on the direct use of the PointDeviation command in Mc Neel Rhinoceros.

In particular, this command not only provides the point count, the mean and median distance and the standard deviation but also allows one to have a graphic representation through different colours, thus making it particularly immediate to understand and check the grade of approximation achieved. The three-dimensional chromatic graphic representation can highlight valid and invalid points directly.

The points excessively deviate from the surface are highlighted in red and orange and are not considered valid.

3.5 The proposed Scan-to-BIM process applied to the Italian and international case studies

The growing need to represent the detected reality of heritage buildings has allowed the definition of the GOG 9 and GOG 10, simplifying the modeling practice, but also, maintaining high levels of geometry (LOG) and complexity for each digitally reconstructed HBIM object. The geometric representation, through the drawing and the understanding of the building's constructive logic with its architectural and structural relationships, turns out to be a fundamental concept for DCH. The three-dimensional geometric representation must face with the most advanced modeling techniques in the field of HBIM and the need to correctly interpret the paradigm of complexity appropriately by integrating different data sources. Previous paragraphs showed how GOGs could transform each type of historical and complex element from a different type of geometric primitives. The BIM expert should manage the automatic or semiautomatic generation of wireframe model composed of a different type of geometric primitives to a proper generation of holistic HBIM models. From a geometric point of view, each line that builds the wireframe model should be represented and oriented to the generation of an infinite number of historical architectural and structural elements. This great variety, consequently, involves the knowledge by the BIM expert of the construction logic of the building, the three-dimensional representation techniques based on unique geometries of their kind and the intangible value of each detected element. In order to find a modelling solution to this issue, the GOGs were also implemented to be used simultaneously for a single detected object.

For this reason, this paragraph demonstrates how the multiple uses of the GOGs can be integrated both to reconstruct an HBIM model in its entirety and to create a single architectural or structural element, attaching increasing importance to the concept of 'geometry' a not the 'detail'. To better explain the management of complexity through multiple GOGs for the same element, three types of constructive elements of the basilica of Collemaggi were considered

- one of the main exterior wall (the north wall),
- the damaged pillars of the nave and
- the rib vault of the apse.

The North wall after the earthquake of 2009 was characterized by a long series of problems related to both its structural stability and the deterioration of the individual elements (stones and bricks) that made it up. Figure 10 shows the main

geometric irregularities of the wall found both during the survey campaign and the production of the as-found and the generative process of HBIM drawings.

One of the most interesting and complex elements found after the laser scanning survey was very accentuated out of plumb of about 7-8 cm. It is clear how the concept of geometry is decisive for the correct representation of this specific structural element characterised by decorative elements, historic windows, the first holy door in the history (13th century), different damaged wall portions with different wall stratigraphy and cracks. The challenge for this specific artefact was given by the integrated use of different GOGs, from the simplest to the most complex from a morphological point of view. In fact, from the figure 120, it is possible to notice how different GOGs have been applied to the representation of every single element in order to support the structural consolidation and the identification of decay areas for the restoration process.

In particular for

- the historic windows, GOG 3 (Edit profile with empty spaces) and the GOG 8 (The voids) have been sufficient to intercept the shape of the opening given by different vertical and horizontal sections,
- for the decoration, GOG 2 (Edit profile), GOG 4 (The sweep) and GOG 5 (The reveal) have allowed to extrude and edit the elements in addition to the main wall, and finally
- the integrated use of GOG 9 (BIM object from 3D wireframe) and GOG 10 (BIM object from a set of the point) for the main wall and its related decay areas allowed the generation of HBIM object with GOA of 2 mm.

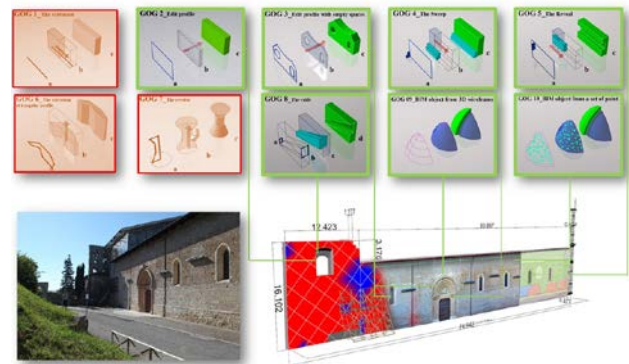


Figure 10. Every GOGs allowed the creation of BIM objects corresponding to the detected area and a high information-sharing from the large-size element (doors and windows) to detailed and micro element (decay areas and cracked wall portions).

The damaged pillars of the nave required a level of geometry (LOG) based on the generation of every single stone to generate a conceptual model able to transmit the detected shapes by laser scanning and direct survey (manual measurements for stone and joints) and also which stone needed to be preserved. In particular, generative modeling tests were conducted to support restorers for preserving as much as possible the stone not damaged by the heart quake's action. Figure 11 shows the structural damages caused by the earthquake and the level of complexity of each element from the stone that makes up the pillar to the capital. In this case, the generation of the HBIM model provided for the application of multiple GOGs in order to highlight a GOI oriented towards preservation.

In particular for

- the pillar's stone, the GOG 6 (The extrusion of the irregular profile) and the GOG 8 (The voids) have been sufficient to intercept the different shapes of each element
- for the ornaments, decoration and the capital, GOG 4 (The sweep) has allowed the generation of an element based on complex geometric primitives and to properly represent pillar's subelements.

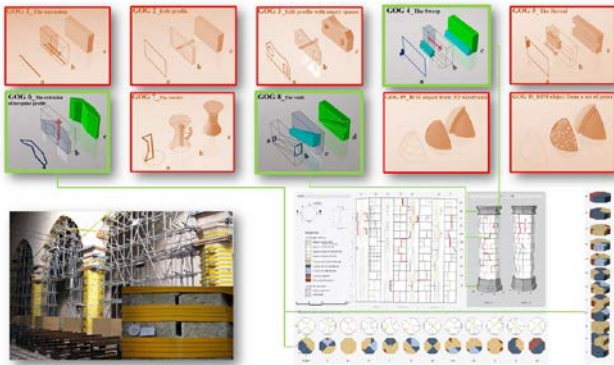


Figure 11. For the generation of every single stone that constitutes the pillars the use of the GOG 9 and GOG 10 based on NURBS interpolation was not necessary.

The rib vault of the apse has suffered different structural damage by earthquake's action, causing cracks, surface detachments of the finishing layers collapse of some elements that made up the ribs and the pointed arch of the umbrella vault. From the morphological point of view, this type of vault presented a formidable challenge for the correct three-dimensional geometric representation. As stressed several times in the previous chapters, the uniqueness of the shapes of the vaults required a three-dimensional representation able to generate HBIM objects with a high GOA in order to support the structural analysis, the analysis of the decay areas and finally the automatic extraction of 2D CAD drawings. The generative process, consequently, was characterised by the use of the

- GOG 9 (BIM object from 3D wireframe model) and GOG 10 (BIM object from a set of points) for the complex curved shapes of the vault,
- GOG 4 (The sweep) for the vault's ribs and damaged walls,
- GOG 2 (Edit profile) and GOG 8 (The voids) for arches and windows

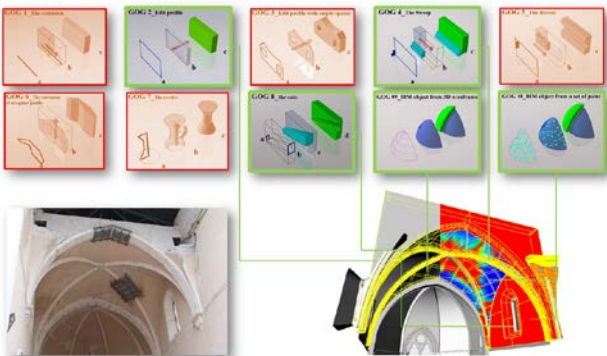


Figure 12. The integrated use of GOG 9 and GOG 10 allowed the generation of the vault with a GOA 2 mm.

4. FROM RESEARCH TO IT DEVELOPMENTS: THE DEVELOPMENT OF AN ADD-IN BASED ON THE PROPOSED SCAN-TO-BIM METHOD TO GUIDE USERS IN AUTODESK REVIT

4.1 The add-in structures and its functionalities

GOGs 9 and GOG 10 have provided for the integration and orientation of digital models for different types of BIM-based analysis and uses. The direct application in the field of HBIM has allowed to identify the modeling gap in the main BIM applications and to implement a method capable of interoperating with more data sources and software. The concept of the utility of HBIM is positively reflected in the identification of physical characteristics of digitised buildings from point clouds.

Thanks to the creation of models with a GOA of about 1 mm, it has been possible to state the creation of HBIM from 3D scans, avoiding to reduce the details and geometry of complex elements. The relationship between 3D objects and information is supported by a set of inter-physical links based on innovative IT developments able to migrate and orient GOI to different types of BIM-based analysis thanks to the identification of specific exchange formats.

As a result, BIM represents a digital repository oriented to any field of research. The flexibility of GOGs also underlined the shortcomings of BIM applications from a generative point of view. The presence of a great number of tools in different modeling applications of the same manufacturer demonstrates the producers' willingness to diversify the market offer for different disciplinary sectors. Autodesk is the international leader for digital applications oriented to the construction sector, has made available new exchange formats and generative logics that are less binding than in past decades.

On the other hand, the absence of NURBS functions able to interpolate the points of the scans (GOG 10), and the absence of instruments able to automatically extract geometric primitives from slices (GOG 9) in BIM application has been interpreted as a commercial decision by the main software manufacturers. However, in light of this, the availability of shared languages known as Application Programming Interface (API) published online in cloud developer platforms (Autodesk Forge and Revit API), has allowed this research to undertake the design of a Revit add-in with the main objective of transferring the proposed method and its GOGs, AVS and GOA within the application.

The main goal was to reduce the generative time and cost of HBIM (modeling phase), simplifying as much as possible the process within Revit which requires multiple command sequences and modeling requirements (GOG and GOA). In order to integrate the MMIS in Autodesk Revit, it has been decided to gradually supplement the HBIM modeling requirements by a more robust system linked to 4 main steps. Thanks to Scan management, Modeling, database creation and Interoperability sections, Add-in integration has been performed as facility management of the whole process.

The four objectives for each oriented sections were (Fig 13):

- **Scan management**_to facilitate the import of the 3D scan and to support the setting of Revit project for Scan-to-BIM process
- **Modeling (GOGs)**_to integrate GOGs (9 & 10) in Revit architecture and to guide users in the creation of complex walls and historical elements with generative modeling
- **Database generation (GOIs)**_ to automate database generation and to enable the addition of new custom parameters
- **Interoperability levels**_to define novel exchange formats and to transfer HBIM model to different BIM-based analysis

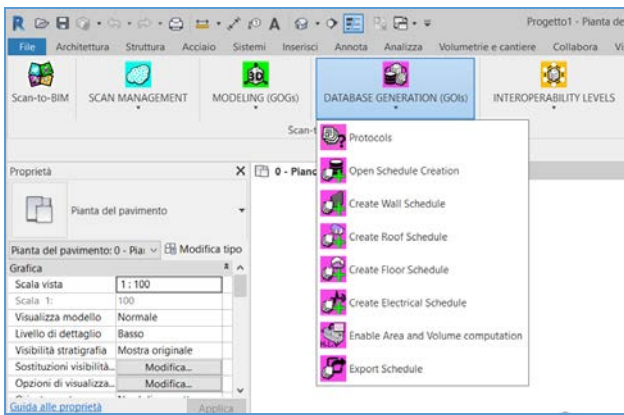


Figure 13. The add-in interface in Autodesk Revit

From an operative point of view, IT development involved the use of Revit API docs. Application Programming Interface databases made it possible to identify the procedures available to the programmer, grouped to form a set of specific tools for the accomplishment of a specific task within Autodesk Revit. Thanks to My First Plug-in has been possible to have a self-paced tutorial guide for a smooth introduction to the programming world. This first step is a one-stop shop learning path for users who know Revit but are new to programming and are thinking about taking the plunge.

The guide has introduced how to work the Revit .NET API programming language. Autodesk Revit provides a rich and powerful .NET API which can be used to automate repetitive tasks, extend the core functionality of Revit in simulation, conceptual design, construction and building management. Revit .NET API allows the programming with any .NET compliant language including VB.NET, C#, and C++/CLI. The Software Development Toolkit (SDK) provides extensive .NET code samples and documentation to support the developing with the Revit API. Autodesk has made available Revit API enhancements added since the initial release of Revit 2018.

An on-course funded Fesr project has supported add-in development. Within this framework, it has been implemented an add-in aimed to lower cost and based on an innovative development workflow. An accurate study of the APIs was necessary in order to have an efficient development approach based on a great number of tests.

The flexibility of the development language has allowed to try a long series of codes and reduce the number of clicks for every single command created. The dimming of clicks allowed the

consequent reduction of the times for every single function, benefiting the whole HBIM process.

In particular, thanks to the IT support, it has been possible to write the code in order to transfer the know-how of this research in the Revit add-in, bridging the gap of BIM's rigid logic with a real product for each type of user.

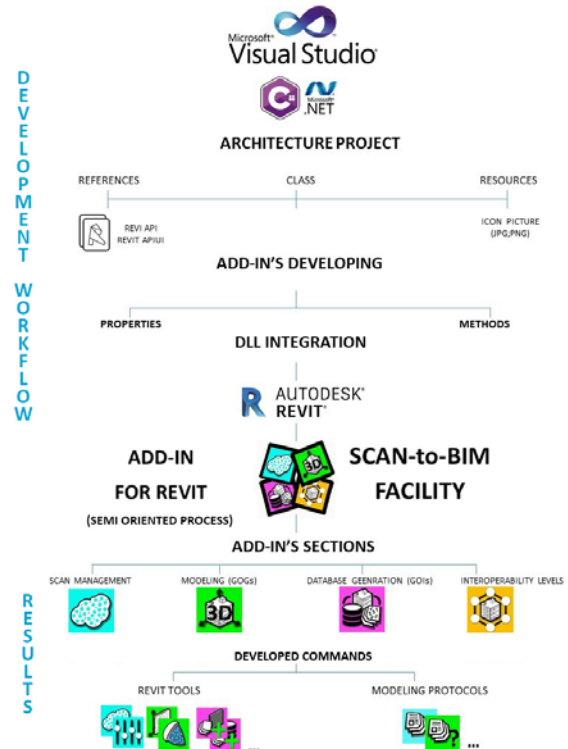


Figure 14. The development process of Scan-to-BIM Facility tool. This add-in allows the integration of the proposed method in BIM application, supporting the user with a semi-guided process.

The add-in structure is mainly composed of four oriented families able to interact with each other. Each family has been developed with Visual Studio (Fig.15)

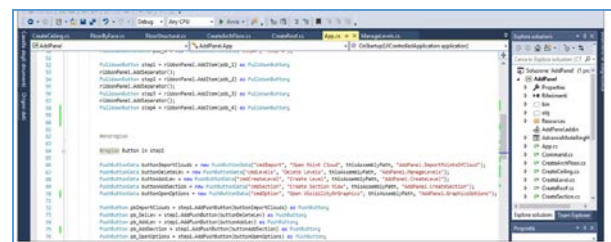


Figure 15. The add-in's development phases in Visual Studio.

Families are based on

- internal reorganised internal Revit's functions,
- functions implemented by Revit APIs and
- on the combined development of multiple Revit tools.

Internal Revit functions. Autodesk Revit is known for the difficulty of activating modelling tools and functions quickly. The first reason is the lack of a user-friendly interface for advanced functions. Thanks to the complete knowledge of the functions integrated into the software, it was possible to define

a hierarchy oriented to Scan-to-BIM. Internal functions were recalled and hierarchized to improve the BIM generation.

Functions implemented by the Revit APIs: after the download of the various APIs library (in technical jargon the Revit API provided by Autodesk), it is possible to create a project in Visual Studio. This project needs the use of objects, properties and related methods which allowed to implement some commands.

Combined development of multiple Revit tools: the modeling in Revit is characterised by a series of procedures indispensable for the setting and management of the generative process. These procedures, for most of the time, require the activation of useful support toolsets such as the section box, the setting of the reference plane, the setting of the successive levels, the display modes and so on. Thanks to the IT development, it was possible to combine the activation of several instruments through a single function. The main benefit was the reduction of project setup times and a more simplified mode of activation of advanced tools such as automatic database generation, schedules and material sheets.

4.2 Scan-to-BIM facility tool: the impact of a semi-guided process based on novel modeling requirements

The ability to develop some commands has been fully exploited, while where the APIs and source data were not shared by Autodesk Revit the development had to stop. This gap has been filled by the inclusion of BIM protocols able to accompany the user step by step in all four families of the add-in with the final objective of reducing the time and costs of the generative process. The add-in represents a product able to guide the user step by step through advanced protocols able to integrate the NURBS modeling in the HBIM projects.

Figure 139 shows the results obtained, applying the add-in to the generation of each element that makes up the Basilica of Collemaggio. GOGs 9 and ten are applied after a previous BIM generation of the same case study to show the difference in terms of Scan-to-BIM generation.

The add-in 'Scan-to-BIM Facility Tool', from an operational point of view, provides the requirements for an advanced modelling able to integrate NURBS geometry into BIM applications and guidelines where it was not possible to develop new Revit commands. Consequently, this add-in represents the maximum possible result in terms of development oriented to integrate the research process in Autodesk Revit.

Add-in facility tool has allowed:

- 3D scans integration into BIM application through a guided path,
- the reduction of the modeling costs and the production time of the Basilica by 70%, maintaining a GOA of 1 mm,
- Scaling the process by creating databases for complex historical objects to customize and create new parameters for each object BIMt,
- better BIM orientation thanks to new levels of interoperability for different BIM-based analysis such as computing, cloud and virtual reality.

5. RESULT

Information Technology is the bedrock of our modern world. The modernisation of our instruments, software and process is an essential factor for different disciplines in the AEC sector.

Modern buildings, design, historical monuments entirely depend on our capacity to improve our IT knowledge daily. Thanks to the Italian scholarship of ABC Department, the support of GICarus Lab in Politecnico di Milano and CIMS lab in Carleton University, Ottawa, and a research period in Autodesk research Toronto under the international programme New Tools/ New Paradigm funded by the Social Sciences and Humanities Research Council (SSHRC), this study could improve novel Scan-to-BIM modeling requirement for heritage buildings. In particular, the results obtained by the integration of Non-Uniform Rational Basis-Splines (NURBS) modeling based on mathematical algorithms proved a reduction of both cost and time for the creation of the complex architectural and structural elements characterised by variable morphology, alterations, damages and inhomogeneous materials.

This structure has been quantified in typical and morphological terms by establishing new modeling rules such as the grades of generation (GOG) and accuracy (GOA) to support and guide users to the generation of different type HBIM models, from basilica, castells to medieval infrastructures.

The grade of accuracy of the digital model has been verified and evaluated with a novel Automatic Verification System (AVS) able to statistically compare the original data (3D scan) with the final output (digital model), becoming a requirement to attest the quality of the proposed approach. Such validation can be extended to the whole model of some specific parts, resulting in a mathematical definition of the geometric accuracy achieved through easy-to-understand indexes behind a complex comparison, but also useful and mandatory to control the paradigm of simplification where needed.

Finally, once the specific modeling requirements have been determined, an plug-in (software component) has been developed for Autodesk Revit in order to support users in the generation of proper Scan-to-BIM models in a single digital workflow, improving the cooperation and interoperability among different actors and scientific disciplines such as geomatics and restoration.

6. CONCLUSION

The research method introduces novel modeling requirements with the aim of increasing automation in the generative process through logics able to interoperate open source modeling applications. International standardization experiences such as - PAS 1192 parts 1-2-3-4-5 (Great Britain); - COBIM- Common Bim Requirements- 2012 (Finland); - Statsbygg BIM Manual 1.2.1 (Norway); - AIA Document E201-2013 Project Digital Data Protocol Form and AIA Document E203-2013 BuildingInformationModelling and Digital Data Exhibit (USA) have identified pros and cons for the management of heritage buildings. Compared to international systems, the UNI 11337 standard introduced new guidelines and LOD for restoration. This innovative aspect is a step forward compared to the criteria for qualifying the built heritage in other countries. On the other hand, this study tries to support, through new grades of generation, accuracy and information (GOG, GOA), the construction of 'smart' models able to represent the reality detected, opening a reflection on different experiences made in the geomatics and restoration fields.

The aim of highlighting some requirements in the modeling allows us to focus on the usefulness of the models produced.

Each case study has brought important results in different fields of application and analysis, transforming the model from a three-dimensional representation to a management process of the built heritage. The holistic approach to generating accurate and informative models should become a requirement of every modeller and BIM expert, not simply thinking of BIM as an instrument able to produce a single centralized model. This research, in addition to increasing the level of automation of the generative process of information models, has shown that built heritage requires the knowledge of theories and techniques applicable to different phases of the life cycle of the building.

Built heritage is characterized by complex long-term processes. A building is not the serial reproduction of a single prototype, but rather a holistic representation where different subjects contribute and the activities flow into the life cycle. The management of these processes, if left to chance, produces enormous diseconomies. Therefore, the management and multiplicity of these processes, over an undefined period of time, raise the problem of knowledge management, i.e. the sharing, archiving and restitution of a great deal of data.

The enhancement of information and intrinsic culture of a specific artefact can be improved through the potential of the proposed Scan-to-BIM process. The potential of geomatics and the 3D survey techniques opens the door to various forms of digital modeling and information sharing, extending to the field of built heritage. In this specific context, the importance and the centrality of the user and his knowledge of modeling are the primary sources for the correct management of the process. It is, therefore, necessary to unify efforts, define general rules that allow users to understand the wealth of tangible and non tangible built heritage values but without creating a *'straitjacket'* to modeling techniques, the latter is considered one of the most important *'driving forces'* behind information sharing in this digital era.

ACKNOWLEDGEMENTS

The research leading to the results of this paper is partially funded by Regione Lombardia - Bando "Smart Living: integrazione fra produzione servizi e tecnologia nella filiera costruzioni-legno-arredo-casa" approvato con d.d.u.o. n.11672 dell'15 novembre 2016 per la presentazione di progetti di sviluppo sperimentale e innovazione (S&I) a favore della filiera dello "Smart Living" e nell'ambito del progetto "HOMEbim liveAPP: Sviluppo di una Live APP multi-utente della realtà virtuale abitativa 4D per il miglioramento di comfort-efficienzacosti, da una piattaforma cloud che controlla nel tempo il flusso BIM-sensori – ID 379270".

The author wants to thank Prof. Raffaella Brumana, Prof. Steven Fay, Prof. Maurice Murphy and Prof. Ying-Mei Cheng for their support in these years of applied research to unique cases studies in built heritage domain. The author wants to thank Social Sciences and Humanities Research Council of Canada as part of the New Paradigms New Tools internship program of the Carleton Immersive Media Studio, and the Complex Systems Research Group at Autodesk Research Toronto. The authors would like to thank also all the specialists of Mainlab srl. In particular, Stefano Mantovani and Nicola Lazzara for their advanced computer skills that helped the author to get the results of better quality.

REFERENCES

- Balletti, C., & Guerra, F., (2015). The survey of cultural heritage: a long story. *Rendiconti Lincei*, 1(26), 115-125.
- Banfi, F., (2016, October). Building information modelling—a novel parametric modeling approach based on 3d surveys of historic architecture. In *Euro-Mediterranean Conference* (pp. 116-127). Springer, Cham.
- Banfi, F. (2017). BIM ORIENTATION: GRADES OF GENERATION AND INFORMATION FOR DIFFERENT TYPE OF ANALYSIS AND MANAGEMENT PROCESS. *International Archives of the Photogrammetry, Remote Sensing & Spatial Information Sciences*, 42.
- Brumana, R., Condoleo, P., Grimoldi, A., Banfi, F., Landi, A. G., & Previtali, M. (2018). HR LOD based HBIM to detect influences on geometry and shape by stereotomic construction techniques of brick vaults. *Applied Geomatics*, 10(4), 529-543
- Della Torre, S. (2015). Shaping tools for built heritage conservation: from architectural design to program and management. *Community involvement in heritage*, 1, 93.
- Dore, C., & Murphy, M. (2017). CURRENT STATE OF THE ART HISTORIC BUILDING INFORMATION MODELLING. *International Archives of the Photogrammetry, Remote Sensing & Spatial Information Sciences*, 42.
- Fai, S., Graham, K., Duckworth, T., Wood, N., & Attar, R. (2011, September). Building information modelling and heritage documentation. In *Proceedings of the 23rd International Symposium, International Scientific Committee for Documentation of Cultural Heritage (CIPA)*, Prague, Czech Republic (pp. 12-16).
- Guarnieri, A., Remondino, F., & Vettore, A. (2006). Digital photogrammetry and TLS data fusion applied to Cultural Heritage 3D modeling. *International Archives of Photogrammetry, Remote sensing and spatial information sciences*, 36(5), 1-6.
- Ioannides, M., & Quak, E. (2014). 3D research challenges in cultural heritage. *Lecture notes in computer science*, 8355, 151.
- Kuo, C. L., Cheng, Y. M., Lu, Y. C., Lin, Y. C., Yang, W. B., & Yen, Y. N. (2018, October). A Framework for Semantic Interoperability in 3D Tangible Cultural Heritage in Taiwan. In *Euro-Mediterranean Conference* (pp. 21-29). Springer, Cham.
- Masiero, A., Fissore, F., Guarnieri, A., Piragnolo, M., & Vettore, A. (2017). Comparison of low cost photogrammetric survey with TLS and Leica pegasus backpack 3d models. *The International Archives of Photogrammetry, Remote Sensing and Spatial Information Sciences*, 42, 147.
- Piegl, L., & Tiller, W. (2012). *The NURBS book*. Springer Science & Business Media.
- Tucci, G., & Bonora, V. (2011, September). Geomatic techniques and 3D modeling for the survey of the Church of the Holy Sepulchre in Jerusalem. In *Proceedings XXIII CIPA Symposium, Prague, Czech Republic* (Vol. 12, p. 16).

ADVANCED METHODS FOR LIDAR AND PHOTOGRAMMETRIC DATA PROCESSING: FROM PROCRUSTES ANALYSIS TO DEEP LEARNING

E. Maset

DPIA – University of Udine, Via delle Scienze, 206 – 33100 Udine, Italy
maset.eleonora@spes.uniud.it

KEY WORDS: Procrustes Analysis, Orientation Problems, Photogrammetry, Deep Learning, Classification, LiDAR

ABSTRACT:

The soul of the thesis is dual, reflecting the different research activities that characterized this PhD project, which was carried out part at the University and part at Helica s.r.l., an Italian company specialized in airborne remote sensing. In the first part, orientation problems in photogrammetry and laser scanning are studied from a methodological point of view and solved via *Procrustes Analysis*, a set of least squares mathematical tools used to perform transformations among corresponding points belonging to a generic k -dimensional space, in order to satisfy their maximum agreement. In this thesis, novel Procrustes models are developed and exploited in several applications, ranging from the exterior orientation of an image, to the matching between two sets of keypoints and to the registration of point clouds. The second part, instead, focuses on the implementation of novel algorithms for the processing of airborne LiDAR data. In particular, an innovative method based on deep learning and Convolutional Neural Networks is proposed to perform the classification of full-waveform LiDAR data.

Part I – Solving Orientation Problems via Procrustes Analysis

Photogrammetry and laser scanning are two scientific fields whose analytical models are fundamentally based on geometrical transformations of point coordinates defined in different reference frames. The main issue of these transformations is that they are expressed, almost always, by nonlinear models, that are usually solved resorting to the linearization of the equations and requiring therefore the approximate value of the unknowns. In this thesis we propose an alternative approach, well known in the multifactorial analysis field as *Procrustes Analysis*, that allows to directly solve via least squares nonlinear systems. Procrustes algorithms do not require approximate numerical solutions of the unknown parameters and offer the capability to take into consideration weights of the systems involved, requiring only matrix products and the singular value decomposition of a matrix.

1. ORTHOGONAL PROCRUSTES ANALYSIS MODELS

The term *Procrustes Analysis* is referred to a set of least squares mathematical models used to perform transformations among corresponding point sets belonging to a generic k -dimensional space, in order to satisfy their maximum agreement. Due to the nature of the problems encountered in photogrammetry and laser scanning, we will focus only on *Orthogonal Procrustes* models, that impose an orthogonal constraint to the transformation matrix, and, in particular, we are interested in rotation matrices, i.e., orthogonal matrices with positive determinant. Among them, we mention the *Extended Orthogonal Procrustes Analysis* (EOPA) model, that allows to compute a similarity transformation between two point sets, and the *Anisotropic Extended Orthogonal Procrustes Analysis* (AEOPA) model, that computes translations, rotations and an anisotropic scale factor for each point.

1.1 Ordinary Least Squares Solutions

Let us consider a matrix \mathbf{A} (origin or source) and a matrix \mathbf{B} (destination or objective), containing a set of numerical data, e.g., the coordinates of p -points in \mathbb{R}^k expressed in two different reference frames. In the ordinary least squares (LS) form, EOPA solves a similarity transformation problem, allowing to directly define the rotation matrix \mathbf{R} , the translation vector \mathbf{t} and the global scale factor c for the model (Schönemann, Carroll, 1970):

$$\mathbf{B} + \mathbf{E}_B = c\mathbf{A}\mathbf{R} + \mathbf{j}\mathbf{t}' \quad (1)$$

under the orthogonality condition $\mathbf{R}'\mathbf{R} = \mathbf{I}$, minimizing the square of the Frobenius norm of the transformation residual matrix, i.e., $\|\mathbf{E}_B\|_F^2 = \|\mathbf{B} - c\mathbf{A}\mathbf{R} + \mathbf{j}\mathbf{t}'\|_F^2$. It is easy to retrieve the following solving equations:

$$\mathbf{R} = \mathbf{V} \text{diag}(1, 1, \det(\mathbf{V}\mathbf{W}')) \mathbf{W}' \quad (2)$$

with $\mathbf{S} = \mathbf{V}\mathbf{D}_s\mathbf{W}'$ Singular Value Decomposition (SVD) of $\mathbf{S} = \mathbf{A}' \left(\mathbf{I} - \frac{\mathbf{j}\mathbf{j}'}{j'j} \right) \mathbf{B}$ and $\mathbf{j} = [1_1, \dots, 1_p]$,

$$c = \frac{\text{tr} \left[\mathbf{R}'\mathbf{A}' \left(\mathbf{I} - \frac{\mathbf{j}\mathbf{j}'}{j'j} \right) \mathbf{B} \right]}{\text{tr} \left[\mathbf{A}' \left(\mathbf{I} - \frac{\mathbf{j}\mathbf{j}'}{j'j} \right) \mathbf{A} \right]}, \quad (3)$$

$$\mathbf{t} = (\mathbf{B} - c\mathbf{A}\mathbf{R})' \mathbf{j} / p. \quad (4)$$

The EOPA model (1) can be generalized by substituting the isotropic scale factor c with an anisotropic scaling characterized by a diagonal matrix $\mathbf{\Gamma}$ of different scale factors:

$$\mathbf{B} + \mathbf{E}_B = \mathbf{\Gamma}\mathbf{A}\mathbf{R} + \mathbf{j}\mathbf{t}', \quad (5)$$

obtaining the AEOPA model. In this case the solution is more complex and cannot be expressed in closed form (Garro et al., 2012). One must resort to the following *block relaxation scheme*, where each variable is alternatively estimated while

keeping the others fixed, until convergence:

1. Assuming known Γ , find

$$\mathbf{R} = \mathbf{V} \text{diag}(1, 1, \det(\mathbf{V}\mathbf{W}')) \mathbf{W}' \quad (6)$$

with $\mathbf{A}'\Gamma'(\mathbf{I} - \mathbf{j}\mathbf{j}'/p)\mathbf{B} = \mathbf{V}\mathbf{D}_S\mathbf{W}'$, and

$$\mathbf{t} = (\mathbf{B} - \Gamma\mathbf{A}\mathbf{R})'\mathbf{j}/p \quad (7)$$

2. Given \mathbf{R} and \mathbf{t} , solve for Γ

$$\Gamma = (\mathbf{A}\mathbf{A}' \odot \mathbf{I})^{-1} (\mathbf{A}\mathbf{R}(\mathbf{B}' - \mathbf{t}\mathbf{j}') \odot \mathbf{I}) \quad (8)$$

where \odot denotes the Hadamard product;

3. Iterate over steps 1. and 2. until convergence.

1.2 Errors-In-Variables Models

Classical LS Procrustes solutions find the transformation parameters between the two point sets assuming that all random errors are confined to the destination matrix \mathbf{B} , whereas \mathbf{A} is noise-free. However, this assumption is often unrealistic, since both \mathbf{B} and \mathbf{A} are corrupted by errors if they derive from measurements. Therefore, it seems appropriate to introduce the *Errors-In-Variables* (EIV) model, which is a more general model wherein both matrices \mathbf{B} and \mathbf{A} are assumed to be contaminated by errors. The problem of parameters estimation in the EIV model is often called the total least squares (TLS) problem. (Arun, 1992) showed that, for rigid transformations ($c = 1$), the classical LS Orthogonal Procrustes solution coincides with the TLS one. (Felus, Burtch, 2009) started from a Errors-In-Variables Extended Orthogonal Procrustes model to compute the unknown parameters of a similarity transformation, showing that, in this case, LS and TLS solution are not coincident.

In this section we derive instead a novel TLS solution of the AEOPA, called EIV-AEOPA, that allows an anisotropic scaling and considers the errors affecting both origin matrix \mathbf{A} and destination matrix \mathbf{B} , namely:

$$\mathbf{B} + \mathbf{E}_B = \Gamma(\mathbf{A} + \mathbf{E}_A)\mathbf{R} + \mathbf{j}\mathbf{t}'. \quad (9)$$

Following a Lagrangian approach, the target function to be minimized can be written as

$$F(\mathbf{E}_B, \mathbf{E}_A, \mathbf{G}, \mathbf{L}, \mathbf{t}, \mathbf{R}, \Gamma) = \frac{1}{\beta} \text{tr}(\mathbf{E}_B \mathbf{E}_B') + \frac{1}{\alpha} \text{tr}(\mathbf{E}_A \mathbf{E}_A') + 2 \text{tr}[\mathbf{G}'(\mathbf{B} + \mathbf{E}_B - \Gamma\mathbf{A}\mathbf{R} - \Gamma\mathbf{E}_A\mathbf{R} - \mathbf{j}\mathbf{t}')] + 2 \text{tr}[\mathbf{L}(\mathbf{R}'\mathbf{R} - \mathbf{I})] \quad (10)$$

where \mathbf{G} and \mathbf{L} are the matrix of Lagrangian multipliers, whereas $1/\alpha$ and $1/\beta$ are different weights assigned to \mathbf{A} and \mathbf{B} , respectively. This can be solved by setting to zero the partial derivatives with respect to the unknowns. Eventually, the translation vector can be obtained as:

$$\mathbf{t} = (\mathbf{B} - \Gamma\mathbf{A}\mathbf{R})'(\beta\mathbf{I} + \alpha\Gamma^2)^{-1} \frac{\mathbf{j}}{\varepsilon} \quad (11)$$

where $\varepsilon = \mathbf{j}'(\beta\mathbf{I} + \alpha\Gamma^2)^{-1}\mathbf{j} = \text{tr}[(\beta\mathbf{I} + \alpha\Gamma^2)^{-1}]$. The rotation matrix is computed as

$$\mathbf{R} = \mathbf{V} \text{diag}(1, 1, \det(\mathbf{V}\mathbf{W}')) \mathbf{W}' \quad (12)$$

where $\mathbf{S} = \mathbf{V}\mathbf{D}_S\mathbf{W}'$ is the SVD of

$$\mathbf{S} = \mathbf{A}'\Gamma'(\beta\mathbf{I} + \alpha\Gamma^2)^{-1} \left[\mathbf{I} - \frac{\mathbf{j}\mathbf{j}'}{\varepsilon}(\beta\mathbf{I} + \alpha\Gamma^2)^{-1} \right] \mathbf{B} \quad (13)$$

and the scale factors derive from

$$(\alpha\Gamma\mathbf{X}\mathbf{Y}'\Gamma + \beta\Gamma\mathbf{X}\mathbf{X}' - \alpha\mathbf{Y}\mathbf{Y}'\Gamma - \beta\mathbf{Y}\mathbf{X}') \odot \mathbf{I} = 0 \quad (14)$$

with $\mathbf{X} = \mathbf{A}\mathbf{R}$ and $\mathbf{Y} = \mathbf{B} - \mathbf{j}\mathbf{t}'$. Equation (14) can be solved independently for each element c_i of matrix Γ . Similarly to the LS solution of the AEOPA problem, the TLS solution of the EIV-AEOPA model requires a block relaxation scheme to estimate the unknowns \mathbf{R} , \mathbf{t} and Γ .

1.3 Exterior Orientation with EIV-AEOPA

The AEOPA and the EIV-AEOPA models can be applied and compared for solving the problem of estimating the position and orientation of a perspective camera given its intrinsic parameters and a set of world-to-image correspondences (Garro et al., 2012), known as *exterior orientation* problem in photogrammetry or *Perspective-n-Point* camera pose in computer vision.

First of all, we briefly review here how this problem can be formulated in terms of model (5) or (9). Given at least three control points and their projections, the exterior orientation problem requires to find a rotation matrix \mathbf{R} and a vector \mathbf{t} (specifying attitude and position of the camera) such that the vector form of collinearity equations:

$$\mathbf{a}_i = c_i^{-1} \mathbf{R}(\mathbf{b}_i - \mathbf{t}) \quad (15)$$

is satisfied for some positive scalar c_i , where \mathbf{b}_i is the coordinate vector of the i -th control point in the external system, \mathbf{t} is the coordinate vector of the projection center in the external system, c_i is a positive scalar proportional to the “depth” of the point (the distance from the i -th control point to the plane containing the projection center and parallel to the image plane), \mathbf{R} is the rotation matrix transforming from the external system to the camera system and \mathbf{a}_i is the coordinate vector of the i -th control point in the camera system, where the third component is equal to the principal distance or focal length.

Expressing (15) with respect to \mathbf{b}_i and extending to p control points $\mathbf{b}_1 \dots \mathbf{b}_p$, it results:

$$\mathbf{B} = \Gamma\mathbf{A}\mathbf{R} + \mathbf{j}\mathbf{t}' \quad (16)$$

where \mathbf{A} is the matrix by rows of image point coordinates defined in the camera frame, \mathbf{B} is the matrix by rows of point coordinates defined in the external system, Γ is the diagonal (positive) depth matrix. Formula (16) can then be rewritten in the form of the AEOPA model (5) or the EIV-AEOPA model (9), according to whether the error is assumed to affect only \mathbf{B} or both \mathbf{A} and \mathbf{B} . It is particularly significant in this photogrammetric application the capability of our solution (Section 1.2) to take into account the different variances of \mathbf{E}_A and \mathbf{E}_B , since image coordinate \mathbf{a}_i and 3D points coordinate \mathbf{b}_i are measured with different accuracy.

(Garro et al., 2012) compared the LS solution of (5) with state-of-the-art algorithms that perform the exterior orientation, showing that AEOPA reaches the best trade-off between speed and accuracy. In this work, we therefore tested EIV-AEOPA for solving the exterior orientation of an image against

the LS formulation (Garro et al., 2012). To carry out the simulation, $p = \{6, \dots, 30\}$ 3D points were randomly distributed in a sphere of unit radius centered on the origin and perturbed with random noise with standard deviation $\sigma_B = \{0.10, 0.27, 0.71, 1.88, 5.00\}$ [mm] (corresponding to five logarithmically spaced values from 0.10 to 5.00). The camera was positioned at distances of 5 and 10 meters from the origin and the focal length was chosen so as to yield a view angle of 60° with an image size of 1000 x 1000 pixels. Different values of noise $\sigma_A = \{1, \dots, 5\}$ [pixel] were added to the image coordinates obtained from the projection of the noise-free 3D points. For each setting the test was run 500 times and the mean and median error norms were computed. In all the experiments the initial depths were set to one.

Results are reported in Figs. 1 and 2. As a figure of merit only the rotation errors are shown, since the behavior of the translation errors is similar. The rotation error is the angle of the residual rotation, computed as $\|\log(\mathbf{R}'\hat{\mathbf{R}})\|_F$, where \mathbf{R} is the ground truth, $\hat{\mathbf{R}}$ is the actual rotation and $\|\cdot\|_F$ is the Frobenius norm.

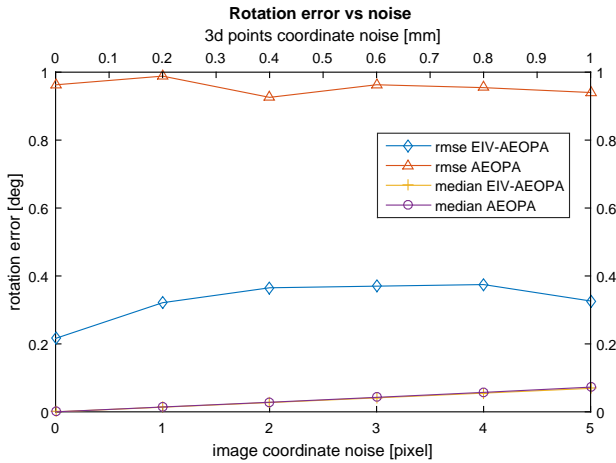


Figure 1. Rotation error vs noise using 10 correspondences and a distance of the camera from the origin equals to 10 m.

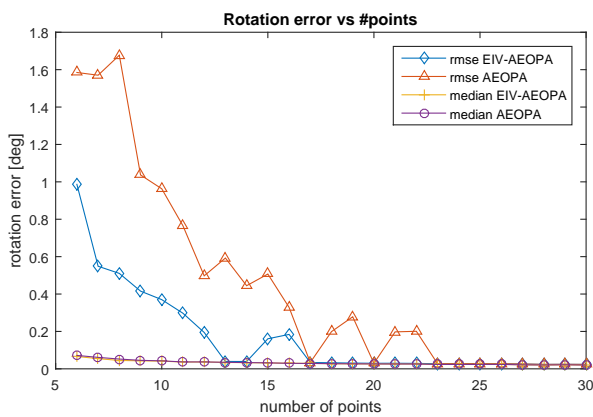


Figure 2. Rotation error vs number of points using a distance of the camera from the origin of 10 m. The standard deviation of the noise added is 3 pixel for the image coordinate and 0.71 mm for the 3D points coordinate.

Comparing the median error, one can notice that EIV-AEOPA and AEOPA lead almost to the same accuracy. On the other hand, the root mean square error (RMSE) is different when the number of correspondences in the image is small ($n \leq 15$)

(this is clear in Fig. 1 where 10 points are considered). This is due to the fact that AEOPA in a few cases converges to wrong results, that are not sufficient to skew the median, but affects the mean error. The rundown of this simulation is that the new TLS solution works better than the ordinary LS algorithm when the number of reference points (whose coordinate are known in both the camera and the external reference frame) is small, which is a common situation in photogrammetry.

2. PERMUTATION PROCRUSTES PROBLEM AND VARIATIONS

The various Orthogonal Procrustes Analysis models presented in the previous section require that the correspondences among points belonging to the two sets are known in advanced, but in some applications establishing correspondences between key-point sets is not a straightforward task.

The majority of works on this topic focus on finding correspondences between only two sets, a problem that can be formulated as a Permutation Procrustes Analysis (PPA) (Gower, Dijkstra, 2004). In fact, given two matrices $\mathbf{A}, \mathbf{B} \in \mathbb{R}^{m \times m'}$, the matching problem corresponds to identifying the permutation \mathbf{Q} that best align \mathbf{B} onto \mathbf{A} , i.e., solving

$$\|\mathbf{A} - \mathbf{B}\mathbf{Q}\|_F = \min \quad (17)$$

under the condition that \mathbf{Q} is a total permutation matrix, i.e., exactly one entry in each row and column is equal to 1 and all other entries are 0. Setting $\mathbf{B} = \mathbf{I}$ in (17), the solution \mathbf{Q} is the closest permutation matrix to \mathbf{A} and this can be used also to project a matrix onto the set of permutations.

When not all the points are present in both sets, one must solve a Partial Permutation Procrustes Analysis (PPPA) problem, where the involved permutation matrix is partial, i.e., it has at most one nonzero entry in each row and column, and these nonzero entries are all 1.

The minimization of (17) is equivalent to

$$\text{tr}(\mathbf{P}\mathbf{C}) = \max \quad (18)$$

with $\mathbf{P} = \mathbf{Q}'$ and $\mathbf{C} = \mathbf{B}'\mathbf{A}$. Considering the case of partial permutations, the relaxed problem can be written as:

$$\begin{aligned} & \text{maximize} && \sum_{i=1}^n \sum_{j=1}^n p_{ij} S_{\lambda}(c_{ij}) \\ & \text{subject to} && p_{ij} \geq 0 \\ & && \sum_{i=1}^n p_{ij} \leq 1 \\ & && \sum_{j=1}^n p_{ij} \leq 1. \end{aligned} \quad (19)$$

where a soft thresholding is applied to c_{ij} with a small threshold, otherwise even a negligible c_{ij} would justify a $p_{ij} = 1$, which would compel the solution to be always a total permutation. This is a linear programming problem, hence its solution must occur at a vertex of the feasible region, which corresponds to a permutation matrix. This is in fact an assignment problem, which can be solved by the Hungarian method (Kuhn, 1955) ($-c_{ij}$ is the cost of assigning agent i to task j , and p_{ij} represents the assignment).

2.1 Multi-view Matching

In many tasks (e.g., structure-from-motion and point cloud registration) it is often required to find matches across multiple views. Recent studies have suggested that jointly optimizing the correspondences across the whole set can lead to significant improvements when compared to computing matches between pairs of views in isolation (Pachauri et al., 2013), since pairwise matching algorithms can generate noisy and unreliable results. Hence, one can apply higher level constraints that arise from the closed-loop consistency of matching across multiple views. This is called *joint matching* or *multi-view matching* by some authors and it is a problem that cannot be solved via the Permutation Procrustes model, so one must resort to different formulations.

Let us assume that all the keypoints extracted from all the views belong to a *universe* set. Let $\mathbf{P}_i \in \{0, 1\}^{m_i \times d}$ denote the partial permutation matrix representing the correspondences between the keypoints in view i and those in the universe, where d denotes the size of the universe. In the absence of noise, the correspondences between view j and view i can be equivalently represented by first computing the matches between view j and the universe, and then from the universe to view i , namely

$$\mathbf{P}_{ij} = \mathbf{P}_i \mathbf{P}_j'. \quad (20)$$

Equation (20) is called the *consistency constraint*. The matrix \mathbf{P}_i (resp. \mathbf{P}_j) is referred to as the *absolute* permutation of view i (resp. j) and the matrix \mathbf{P}_{ij} is referred to as the *relative* permutation of the pair (i, j) . Matrix \mathbf{P}_{ij} is constructed as follows: $[\mathbf{P}_{ij}]_{h,k} = 1$ if keypoint k in view j is matched with keypoint h in view i ; $[\mathbf{P}_{ij}]_{h,k} = 0$ otherwise. If row $[\mathbf{P}_{ij}]_{h,\cdot}$ is a row of zeros, then keypoint h in view i does not have a matching keypoint in view j . If column $[\mathbf{P}_{ij}]_{\cdot,k}$ is a column of zeros, then keypoint k in view j does not have a matching keypoint in view i . Figure 3 graphically shows how a partial permutation matrix is related to keypoints correspondences.

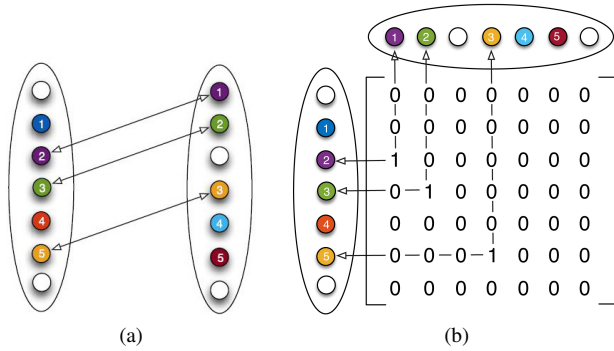


Figure 3. (a) Keypoint matches between two sets of views and (b) corresponding partial permutation matrix.

The consistency constraint can be expressed in a compact matrix form if all the absolute and relative permutations are collected in two block-matrices $\mathbf{X} \in \{0, 1\}^{m \times d}$ and $\mathbf{Z} \in \{0, 1\}^{m \times m}$ respectively, where $m = \sum_{i=1}^n m_i$, namely

$$\mathbf{X} = \begin{bmatrix} \mathbf{P}_1 \\ \mathbf{P}_2 \\ \dots \\ \mathbf{P}_n \end{bmatrix}, \quad \mathbf{Z} = \begin{bmatrix} \mathbf{P}_{11} & \mathbf{P}_{12} & \dots & \mathbf{P}_{1n} \\ \mathbf{P}_{21} & \mathbf{P}_{22} & \dots & \mathbf{P}_{2n} \\ \dots & \dots & \dots & \dots \\ \mathbf{P}_{n1} & \mathbf{P}_{n2} & \dots & \mathbf{P}_{nn} \end{bmatrix}. \quad (21)$$

Note that \mathbf{Z} may contain zero blocks: if all the keypoints in view i do not match with any keypoint in view j , then $\mathbf{P}_{ij} = 0$. Using this notation, Equation (20) becomes

$$\mathbf{Z} = \mathbf{X}\mathbf{X}' \quad (22)$$

which implies that \mathbf{Z} is symmetric positive semidefinite and has rank d .

2.2 Our Method

In practice, pairwise correspondences contain errors, hence what we measure is an estimate $\widehat{\mathbf{P}}_{ij}$ of the relative permutation between view i and view j (in the following we use the hat accent to denote approximate quantities). The goal is to compute a set of partial permutation matrices $\{\mathbf{P}_{ij}\}_{i,j=1}^n$ such that the consistency constraint is satisfied and \mathbf{P}_{ij} is as close as possible to its measure $\widehat{\mathbf{P}}_{ij}$, namely $\mathbf{P}_{ij} \approx \widehat{\mathbf{P}}_{ij}$ for all $i, j \in \{1, \dots, n\}$. A possible approach consists in considering the following optimization problem

$$\max_{\mathbf{Z}} \langle \widehat{\mathbf{Z}}, \mathbf{Z} \rangle = \max_{\mathbf{Z}} \text{tr}(\widehat{\mathbf{Z}}\mathbf{Z}') \quad \text{s.t. } \mathbf{Z} = \mathbf{X}\mathbf{X}' \quad (23)$$

$$\iff \max_{\mathbf{X}} \langle \widehat{\mathbf{Z}}, \mathbf{X}\mathbf{X}' \rangle = \max_{\mathbf{X}} \text{tr}(\mathbf{X}'\widehat{\mathbf{Z}}\mathbf{X}) \quad (24)$$

where $\widehat{\mathbf{Z}}$ denotes the block-matrix containing the measured relative permutations $\widehat{\mathbf{P}}_{ij}$ and \mathbf{X} is constrained to be composed of partial permutation matrices. The cost function counts the number of keypoints equally matched by permutations contained in $\widehat{\mathbf{Z}}$ and \mathbf{Z} .

Searching the solution for \mathbf{X} has the drawback of being dependent from the knowledge of the size of the universe, which is difficult to estimate. For this reason, we develop a novel solution independent from this parameter, that aims at finding relative permutations instead of absolute ones. Our algorithm, called MATCHEIG, proceeds as follows:

1. Given the pairwise correspondences, compute the eigenvalue decomposition of matrix $\widehat{\mathbf{Z}}$, keeping only the \widehat{d} largest eigenvectors and eigenvalues:

$$\widehat{\mathbf{Z}}_{\widehat{d}} = \mathbf{U}\mathbf{D}\mathbf{U}'.$$

2. Set to zero all the entries smaller than a given threshold t ($t = 0.5$ in our experiments).
3. Project each block of $\widehat{\mathbf{Z}}_{\widehat{d}}$ onto the space of permutation matrices using PPPA (obtaining the closest permutation) or the following greedy strategy (obtaining a permutation, although not necessarily the closest one):

- a) Compute maximums over rows/columns, which represent putative matches;
- b) Sort such maximums by decreasing magnitude;
- c) Initialize the output matrix \mathbf{P} to zero;
- d) Starting from the largest element, analyze sequentially each maximum, indexed by (i, j) , and place a 1 in correspondence of $[\mathbf{P}]_{i,j}$ provided that \mathbf{P} remains a partial permutation.

The algorithm is very simple and can be coded in a few lines of Matlab. Note also that the projection step (either via the

Dataset	n	\hat{d}	Input	MATCHEIG			MATCHALS (Zhou et al., 2015)			SPECTRAL (Pachauri et al., 2013)		
			PR [%]	PR [%]	CM	T [m]	PR [%]	CM	T [m]	PR [%]	CM	T [m]
<i>Herz-Jesu-P8</i>	8	386	94.40	95.08	4545	< 1	94.87	4047	2	94.41	3987	< 1
<i>Entry-P10</i>	10	432	75.11	79.24	5978	5	74.17	5726	4	76.10	6236	4
<i>Fountain-P11</i>	11	374	94.35	94.70	6988	3	94.15	6717	3	91.92	7849	3
<i>Castle-P19</i>	19	314	70.29	75.21	5109	3	66.22	7014	9	34.41	7605	3
<i>Herz-Jesu-P25</i>	25	517	90.20	93.45	25120	7	89.23	32528	41	47.86	32876	8
<i>Castle-P30</i>	30	445	72.32	81.01	16754	8	68.92	24844	57	34.67	25884	10
<i>Temple Ring</i>	47	396	73.72	88.25	18426	6	55.91	40096	260	28.99	46432	7
<i>Dino Ring</i>	48	340	75.37	92.11	23406	2	66.66	44215	94	34.49	48979	3
<i>Temple</i>	312	689	55.50	89.06	$3.8 \cdot 10^5$	153	–	–	–	14.56	$1.6 \cdot 10^6$	228
<i>Dino</i>	363	493	63.48	95.66	$8.6 \cdot 10^5$	88	–	–	–	18.97	$2.2 \cdot 10^6$	111

Table 1. Results on the EPFL and Middlebury datasets. n is the number of images, PR is the precision, CM is the number of correct matches returned, T is the time expressed in minutes.

PPPA or via the approximate strategy) can be performed in parallel, since each view pair is independent from the others, thus speeding up the process. Synthetic experiments showed that the algorithm is not sensitive to the estimate \hat{d} of the size of the universe d , provided that $\hat{d} \geq d$. Moreover, we compared the two proposed projection procedures and demonstrated that there is no significant loss of accuracy when using the approximated projection onto permutations (greedy strategy) with respect to the exact closest permutation, as done by PPPA. So, since the PPPA is computationally much more expensive than the approximate procedure, only the fastest version was used in the following experiments.

2.3 Experiments and Results

For evaluating the applicability of the proposed method in real scenarios, we tested our method on popular benchmark datasets (EPFL (Strecha et al., 2008) and Middlebury (Seitz et al., 2006) datasets) and compared to other techniques from the state of the art, namely MATCHALS (Zhou et al., 2015) and SPECTRAL (Pachauri et al., 2013). To generate the input to the algorithms, a set of keypoints was first extracted in each image with SIFT (Lowe, 2004). Subsequently, correspondences between pairs of images were established using nearest neighbor and ratio test as in (Lowe, 2004).

We evaluated the performance in terms of precision (number of correct matches returned divided by the number of matches returned). In these experiments the universe set is not known, so we estimated its dimension as twice the average number of keypoints present in each image, and provided all the methods with this estimate.

Results shown in Tab. 1 demonstrate that MATCHEIG outperforms the competing methods both in speed and precision. Moreover, our algorithm also handles large-scale datasets (with more than 300 images), whereas the other methods either fail to produce a solution or return useless results. Figure 4, that refers to a pair of images belonging to the *Dino* dataset (Seitz et al., 2006), gives a visual demonstration of the improvements that can be achieved through MATCHEIG with respect to pairwise matching: joint matching reduces the number of false matches and complete the matches with new ones retrieved indirectly via loop closure.

3. CLOSEST POINT VARIATION OF THE GENERALIZED PROCRUSTES ANALYSIS

Orthogonal Procrustes models previously described (Sec. 1) allow to compute transformations only between two sets. In order

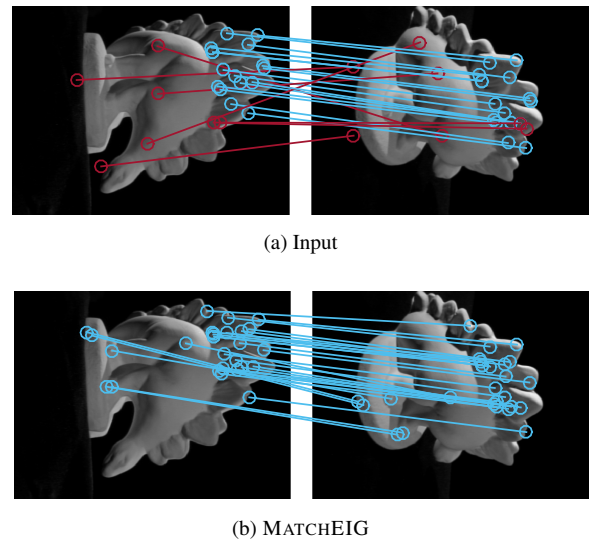


Figure 4. Representation of the matches between two images of the *Dino* dataset. Wrong matches are drawn in red.

to simultaneously consider $m > 2$ matrix configurations, one must resort to the so called *Generalized Procrustes Analysis* (GPA), proposed in (Gower, 1975). In this case, all the matrices are independently and simultaneously rotated, scaled and translated so to satisfy a prefixed objective function. Figure 5 gives a geometric interpretation of the problem. Given m matrices $\mathbf{A}_1, \dots, \mathbf{A}_m$, each one containing the coordinates of the same p points in \mathbb{R}^k defined in m different reference systems, GPA retrieves for each matrix \mathbf{A}_i the similarity transformation that allows to obtain the best alignment with respect to all the other ones or, equivalently, the transformation that minimizes the residual with respect to the unknown matrix \mathbf{Z} , containing the true coordinates of the p points defined into a common mean coordinate frame.

3.1 Original GPA Solution

Exploiting the concept of the *centroid*, i.e., the arithmetic mean of all the sets \mathbf{A}_i , the GPA problem can be solved through the following iterative scheme (Commandeur, 1991):

1. For each matrix \mathbf{A}_i , compute via EOPA (Sec. 1.1) the similarity transformation that best aligns matrix \mathbf{A}_i to the centroid \mathbf{C} , obtaining $\mathbf{A}_i^p = c_i \mathbf{A}_i \mathbf{R}_i + \mathbf{j} \mathbf{t}_i$;

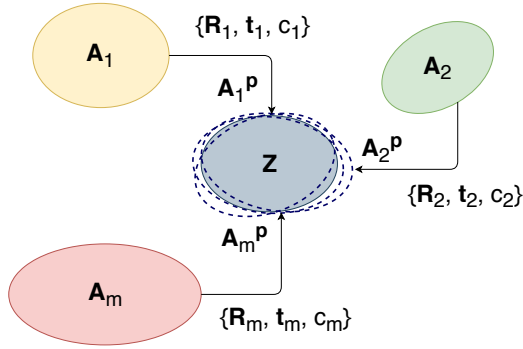


Figure 5. The Generalized Procrustes Analysis concept.

2. Update the centroid C with

$$C = \frac{1}{m} \sum_{i=1}^m A_i^p. \quad (25)$$

3. Iterate from step 1. until convergence, i.e., until the stabilization of the centroid C .

GPA can be easily applied also to the case in which the m matrices do not contain all p points, i.e., one or more rows are missing from each matrix. In this case, EOPA is substituted by its weighted variant, the *Weighted Extended Orthogonal Procrustes Analysis* (WEOPA). This model is nothing but the EOPA (Sec. 1.1), where matrix A is substituted with $P_R A$, matrix B with $P_R B$ and j with $P_R j$ in the solving formulas. Matrix P_R is a $p \times p$ diagonal matrix that assigns a different weight to each point. To cope with missing points in the m sets, an appropriate weight matrix is assigned to each set, that is a matrix P_R having 0 in correspondence of the missing values and 1 otherwise.

In the last years, GPA has been applied to several fields, including photogrammetry and laser scanning, e.g., to register several point clouds acquired by a laser scanner (Beinat, Crosilla, 2001), relying on manually selected corresponding tie points. A main limitation emerges from these works: to apply the GPA solution, correspondences among points must be known in advance. This restriction has been partially overcome in (Toldo et al., 2010), that takes advantage of the GPA to define an iterative closest point algorithm that can register multiple views in a simultaneous way. To broaden the GPA application fields, avoiding the manual search of the point matches, it is therefore necessary to introduce inside the GPA framework the automatic estimation of the correspondences.

3.2 Closest Point GPA

In this section we propose to extend the GPA solution to the case in which correspondences are missing, embedding the matching step within the GPA iterative process. The general scheme of this, called *Closest Point Generalized Procrustes Analysis* (CP-GPA), is the following:

1. Heuristically establish *tentative* correspondences among points in different views;
2. Compute the centroid;
3. Align each view to the centroid using WEOPA;

4. Iterate from step 1. until convergence.

Step 1. can be instantiated with any heuristic, but usually it is one informed by the “closest point” relation, defined as follows: given two sets A and B , two points $a \in A$ and $b \in B$ are in the relation $cp(a, b)$ iff b has the shortest distance (a notion of distance must be defined, usually the Euclidean one) to a among all the points in B . Please note that cp is not symmetric ($cp(a, b) \neq cp(b, a)$) and not transitive ($cp(a, b) \wedge cp(b, c) \not\Rightarrow cp(a, c)$). Better results are usually obtained by considering the “mutual closest-point” symmetric relation, that can be formally defined as $cp^* = cp \cap cp^{-1}$ (this is also the greatest symmetric subset of cp). When working with multiple point clouds, the problem is how to extend pairwise matches to multiple-view correspondences. A straightforward approach is taking the transitive closure of cp , cp^* . The points in the relation constitute a *track*, in the same way as (a, b) with $cp^*(a, b)$ is a match. Another way to define the tracks is the following: consider the undirected graph where points are the nodes and edges represent matches; a track is a connected component of that graph.

The heuristic we propose for step 1. include our multi-view matching algorithm (Sec. 2.2) and the subsequent detection of closed-loop consistency violation: if vertices of the aforementioned graph are labeled with the view the points belong to, an inconsistency arises when in a track a label occurs more than once. In summary, our heuristic for step 1. of CP-GPA is the following:

- a) Compute mutual closest-points between pairs of views;
- b) Apply the multi-view matching algorithm MATCHEIG;
- c) Connect point matching into tracks and discard the inconsistent ones.

Our CP-GPA can be directly applied to the registration of multiple point clouds.

As a final remark, it is interesting to note that CP-GPA does not only extend the GPA, but it is also a generalization of the Iterative Closest Point (ICP) algorithm (Besl, McKay, 1992), the most common solution in literature to align two point clouds. ICP can be summarized as follows:

1. Compute mutual closest-points between the two views and pretend these are corresponding points;
2. Align the two views using EOPA;
3. Iterate from step 1. until convergence.

This is CP-GPA restricted to two views and with a simple mutual closest-point heuristic in step 1.

4. AFFINE PROCRUSTES ANALYSIS

To conclude this first part devoted to Procrustes Analysis, in this section we propose a variation of the classical EOPA model (Sec. 1.1), that allows to compute the transformation between two matrices composed by both points and vectors. The method is called *Affine Extended Orthogonal Procrustes Analysis* (Affine-EOPA), because it actually extends the space where EOPA can be applied from Euclidean (points) to affine (points and vectors).

This model finds application in civil engineering, and in particular in the Virtual Trial Assembly (VTA) of a steel structure (Case et al., 2014). In the field of steel constructions, in fact, it is often necessary to verify in the factory the geometric congruence of the manufactured elements with respect to the nominal values and whether all the connecting points of the various elements guarantee the final assembly of the building, in compliance with the required tolerances. Since a physical trial assembly is often unfeasible due to time and cost, it can be replaced by a trial assembly made in a virtual environment. If this process detects some problems, within the VTA it is possible to define shape and dimensions of the corrective elements, by means of which the assembly of the structure can be achieved. The case study that will be presented is the VTA of the elements of a complex steel structure, the so called *dogbones* of *Vessel* in New York.

4.1 Affine EOPA with Undetermined Motion Components

As previously described, classical EOPA model (Sec. 1.1) allows to directly estimate the unknown parameters of a similarity transformation between origin matrix \mathbf{A} and destination matrix \mathbf{B} operating in the Euclidean space, whose elements are *points*. We can straightforward extend this to an *affine* space, where points and *vectors* are represented, each one by \mathbb{R}^k .

If matrix \mathbf{A} is partitioned into points \mathbf{A}_{pt} and vectors \mathbf{A}_n , and \mathbf{B} accordingly into \mathbf{B}_{pt} and \mathbf{B}_n , it is easy to see that the rotation is computed as usual by

$$\mathbf{R} = \mathbf{V} \text{diag}(1, 1, \det(\mathbf{V}\mathbf{W}')) \mathbf{W}' \quad (26)$$

where $\mathbf{S} = \mathbf{V}\mathbf{D}_s\mathbf{W}'$ is the Singular Value Decomposition of $\mathbf{S} = [\mathbf{A}_{pt}\mathbf{J}, \mathbf{A}_n]'[\mathbf{B}_{pt}\mathbf{J}, \mathbf{B}_n]$ and $\mathbf{J} = (\mathbf{I} - \mathbf{jj}'/p)$ is the centering matrix, whose role is to translate the matrix values to which it is applied to the corresponding barycenter. Please note that points are “centered”, whereas normals are not. The translation vector instead depends only on points (not on vectors):

$$\mathbf{t} = (\mathbf{B}_{pt} - c\mathbf{A}_{pt}\mathbf{R})' \mathbf{j}/p. \quad (27)$$

This model will be henceforth dubbed *Affine Extended Orthogonal Procrustes Analysis* (Affine-EOPA).

Let us now assume that we can partition the point set into planes (at least two) and that each plane can slide along its normal without this influencing the transformation result. In other words, the position of each plane is undetermined along its normal. Point coordinates shall be used in the Affine-EOPA in such a way they do not pose any constraint on \mathbf{t} along the normal of the plane they belong to. The Affine-EOPA solution can be then constructed as follows:

1. Rotation is computed only from plane normals;
2. For each plane, the formula for \mathbf{t} (27) is projected onto the plane itself, therefore cancelling any component along the normal.

Hence, rotation is computed from the SVD of

$$\mathbf{S} = \mathbf{A}'_n \mathbf{B}_n. \quad (28)$$

As for the translation, let us consider plane i and let \mathbf{n}_i be its normal. Moreover, let $\mathbf{N}_i = \mathbf{I} - \mathbf{n}_i \mathbf{n}_i'$ be the projector onto the

plane orthogonal to \mathbf{n}_i . By applying the projection to Equation (27) we get:

$$\mathbf{N}_i \mathbf{t} = \mathbf{N}_i (\mathbf{B}_{pt}^i - \mathbf{A}_{pt}^i \mathbf{R})' \mathbf{j}/p. \quad (29)$$

This is a system of three equations in the unknown \mathbf{t} . Since $\text{rank}(\mathbf{N}_i) = 2$ by construction, only two are independent. With at least two planes we can stack enough independent equations and solve for \mathbf{t} the resulting least squares system. In the remaining part of this work, we will refer to Affine-EOPA with undetermined motion components as Affine-EOPA*.

For a better comprehension of the proposed model, we now give a simple geometric interpretation of the searched solution. In the analyzed problem points belong to planes and we want to minimize the distance between destination point \mathbf{p}^B and the projection \mathbf{p}^n on the destination plane of the origin point \mathbf{p}^A , previously rotated through matrix \mathbf{R} . The situation is illustrated in Fig. 6.

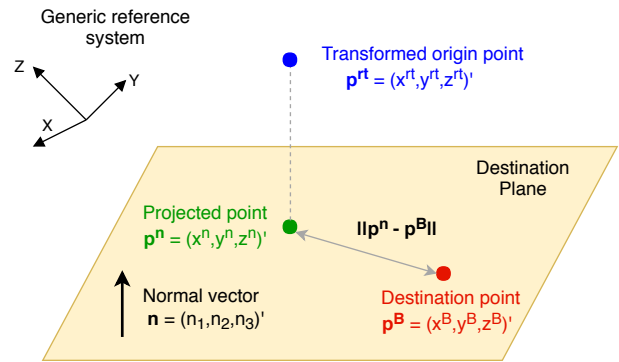


Figure 6. Minimization of the distance on the destination plane between destination and origin points.

The objective function to be minimized takes into account all the k_{pt} points belonging to each i -th plane. Assuming a total number of k_n planes, the cost can be written as

$$\begin{aligned} F(\mathbf{t}) &= \sum_{i=1}^{k_n} \sum_{j=1}^{k_{pt}} \|(\mathbf{p}^n)_{i,j} - (\mathbf{p}^B)_{i,j}\|_2^2 = \\ &= \sum_{i=1}^{k_n} \sum_{j=1}^{k_{pt}} \|\mathbf{N}_i \mathbf{t} + \mathbf{N}_i \mathbf{R}' (\mathbf{p}^A)_{i,j} - s_i \mathbf{n}_i - (\mathbf{p}^B)_{i,j}\|_2^2 \quad (30) \end{aligned}$$

where subscript j refers to the j -th point of plane i . Plane i is defined by the custom equation $n_1 x + n_2 y + n_3 z + s = 0$, with $\mathbf{n} = (n_1, n_2, n_3)'$ normal vector and s constant term. The components of matrix \mathbf{N} depend only from the destination planes, therefore a matrix \mathbf{N}_i is defined for each plane. Setting to zero the derivatives of $F(\mathbf{t})$ with respect to the unknowns $\mathbf{t} = (t_x, t_y, t_z)$, it is easy to verify that one obtains the normal equations of system (29).

4.2 Application of Affine-EOPA* for the VTA of *Vessel*

Vessel is a steel structure under construction at the center of the Hudson Yards district of New York (Fig. 7). Among the different structure elements characterizing *Vessel*, the most important for the aims of this work are the so called *dogbones*. These represent the steel units of the building, that are connected to the neighbor ones by a series of four connection flanges per dogbone.



Figure 7. Rendering of *Vessel* and a construction phase.

The body of the dogbone (Fig. 8) is constituted by a central gabion, to which four horns are successively welded. A shim plate is located between the flanges of two adjacent dogbones, whose thickness can be modified in order to correct errors in the elements geometry, if necessary. Two different kinds of mechanical machining follow the welding step: first, the milling process of each flange and the lateral planes of the structure, then the boring of the flange plane.

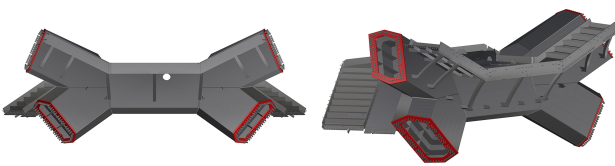


Figure 8. The characteristic *Vessel* element: the *dogbone* (courtesy of Cimolai S.p.A.).

The geometric survey of a completed element is carried out by a laser tracker that measures the plane of the flanges and the holes on each flange. Eventually, the result of the topographic survey is constituted by a series of points and vectors belonging to the interpolated flange plane. Thanks to the laser tracker survey, the as-built geometry of each dogbone is known with high precision and can be compared to the project values. Moreover, the Virtual Trial Assembly of the whole structure can be performed to understand how possible defects of the dogbones belonging to the lower levels and discrepancies with respect to the theoretical shape can influence the assembly of the upper level elements. In the next section, we show that Affine-EOPA* is the best Procrustes model to perform these tasks.

4.3 EOPA vs Affine-EOPA* in the VTA Process

Let us first demonstrate how the classical EOPA can produce misleading results, if applied for the VTA of *Vessel* elements. When comparing the as-built geometry of an element to the project one with EOPA, the origin and destination matrices contain the coordinates of the measured and nominal holes, respectively. In particular, exploiting the EOPA solution with fixed unitary scale factor ($c = 1$), the survey of the dogbone can be aligned to the theoretical configuration via a roto-translation and the residuals represent the differences between real and project values. Similarly, for the VTA process the origin matrix contains the surveyed points of the dogbone to be assembled, whereas the destination matrix is composed by the coordinates of the dogbones belonging to the lower level, virtually assembled in a previous step. Please note that, since dogbones of the same level do not touch each other and the assembly of an element depends only on the position assumed by the lower level ones, each element can be analyzed independently.

Moreover, it is important to consider that, during the machining of the dogbone flanges, the most common flaw that can be

generated is that some of them can be milled with an *offset* of some millimeters in the orthogonal direction to the plane. This difference does not represent a problem for the assembly of the whole structure, because it can be easily filled by a shim plate of adequate thickness. Nevertheless, ordinary EOPA does not take into account the possible offset and does not allow to reach the correct alignment between the survey and the project model, since it minimizes the 3D Euclidean distance between corresponding points. Figure 9 illustrates the problem and the result obtained by the direct application of the EOPA solution, assuming a unitary scale factor. It is therefore easy to see that the

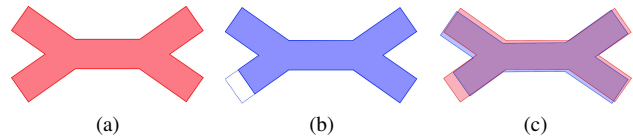


Figure 9. Problem connected to the EOPA application. The red dogbone represents the theoretical configuration, the blue element is instead the measured one. The alignment obtained by ordinary EOPA solution is shown in (c).

solution is represented by Affine-EOPA with undetermined motion components (Affine-EOPA*). In fact, the method proposed in Sec. 4.1 allows to first find the rotation that best aligns the plane normals. The alignment between the bolt holes is determined in a subsequent step, through an estimate of the translation between the rotated configuration and the theoretical one, that takes also into account that the position of the bolt holes does not pose any constraint along the normal of the plane they belong to. Thanks to this approach, if a flange present an offset, it is successfully aligned to the nominal configuration, as shown in Fig. 10. After the application of the roto-translation parameters estimated by the Affine-EOPA* solution to the measured points, the residuals with respect to the nominal configuration can be studied. In particular, the projection on the plane of the residual vector is compared to the tolerance imposed for the realization of the bolted connection.

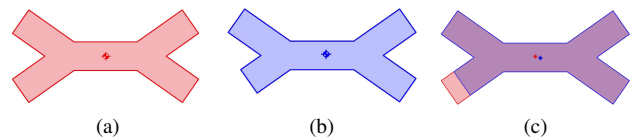


Figure 10. Project configuration (a), as-built geometry (b) and alignment obtained via Affine-EOPA* (c).

When performing the VTA of the structure, machining flaws can be easily identified by Affine-EOPA* and corrected by the shim plates, avoiding to compute incorrect rigid transformations that, propagating through the various levels, lead to a configuration far from the project values (see Fig. 11).

The proposed method has been successfully applied to verify the as-built geometry of the elements of *Vessel* and to perform the VTA of some levels. The validity of the algorithm was confirmed during the construction of the structure. In fact, the results of the VTA were compared with the surveys carried out on site, showing a tight correspondence between what was predicted by the VTA and what was realized on site. Moreover, the absence of problems for the dogbones installation demonstrated the correctness of the values chosen for the shim thickness, calculated through the previously described procedure.

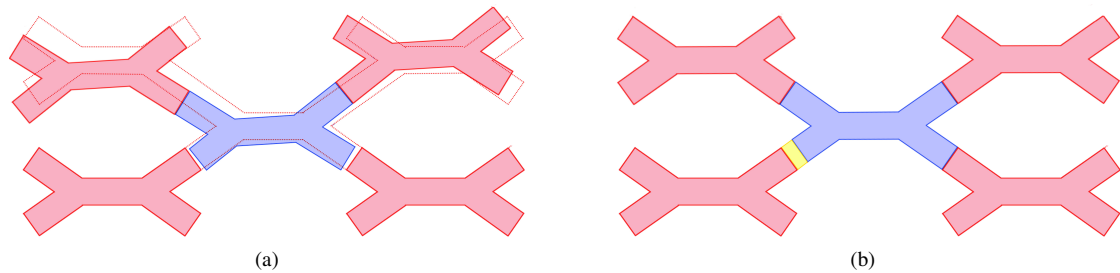


Figure 11. VTA performed by the ordinary EOPA solution (with $c = 1$) (a) and using Affine-EOPA* (b). The yellow rectangle in (b) represents the shim plate placed to correct the machining flaw.

Part II – Advanced Methods for Remote Sensing Data Processing

Applications of remotely sensed data are countless: environmental monitoring, planning, management and maintenance of electric power lines, quantification of mining activities, monitoring of anthropic activities like deforestation and urban development, evaluation of land use or surveillance, just to name a few. However, in order to be used for these purposes, remotely sensed data such as LiDAR point clouds and aerial images require some processing steps that are often expensive and time consuming. For this reason, the research activity carried out at Helica s.r.l. was application oriented and focused on implementing novel algorithms for the processing of photogrammetric and LiDAR data acquired by helicopters or drones. In particular, we present in the following section an innovative method based on deep learning to perform the classification of full-waveform LiDAR data.

5. FULL-WAVEFORM AIRBORNE LIDAR DATA CLASSIFICATION USING CONVOLUTIONAL NEURAL NETWORKS

Among remote sensing techniques, one of the most widespread nowadays is laser scanning. Also known as LiDAR (Light Detection and Ranging), laser scanning is an active technique that measures the time of flight of a short laser pulse traveling to the target and back, so to compute the distance between the sensor and the target. Range is then converted to discrete 3D point using GNSS (Global Navigation Satellite System) and IMU (Inertial Measurement Unit) data. In the last years, the so called full-waveform laser scanners have appeared on the market. These instruments are able to record the entire return pulse energy distribution as a function of time, allowing to derive from the waveform shape scattering properties and geometrical information of the target. This can then be used for the subsequent stage of LiDAR point cloud classification.

In almost all the applications, this is a necessary processing step required, e.g., to create Digital Terrain Models (DTMs), to perform analyses on data belonging to particular classes (e.g., to evaluate the vegetation density) and to automatically determine the relationships between different classes (e.g., to calculate the distance between power line conductors and vegetation or buildings).

Several classification methods have been proposed in the literature using full-waveform data and the features derived from them (Fieber et al., 2013). These algorithms usually rely on hand-crafted features, that are subsequently fed to statistical classifiers or simple machine learning algorithms.

In the last years disciplines such as computer vision have pushed forward and exploited the potential of deep learning (Goodfellow et al., 2016). Approaches based on hand-engineered features can nowadays be effectively replaced by methods that learn both features and classifier from the data end-to-end. In particular, Convolutional Neural Networks (CNNs) represent the most powerful and reliable tool for classification and segmentation (Ronneberger et al., 2015).

While many researchers are focused on the development of new architectures for image and video processing, the application of deep learning to LiDAR data – and, notably, to full-waveform data – is still almost unexplored. We propose a novel system that treats the LiDAR data classification task as a problem of image segmentation solved with a Fully Convolutional Network (FCN) and that takes advantages also on the full-waveform data processed by a CNN classifier.

5.1 Proposed Framework

The entire architecture we developed is summarized in Fig. 12 and described in detail in the following.

5.1.1 Waveform Classifier In the first step of the algorithm, raw waveform data are given as input to a classifier that outputs a vector of length n (with n total number of classes) containing the probability that the analyzed input belongs to a certain class. The idea is to train a CNN classifier that provides a compact way to describe each waveform. In fact, CNNs are particularly suited for processing data that have a known grid-like topology, so they can also be applied to time series data such as audio tracks or, as in this case, the recorded waveforms.

The architecture of the CNN used in the proposed method is shown in the upper part of Fig. 13. More in detail, the waveform, consisting of a vector of 160 elements, is fed into two consecutive 1D convolutional layers with kernel size 3, that have 32 and 64 filters, respectively. Both layers are followed by a rectified linear unit (ReLU) activation function and a max-pooling layer with kernel size 2. After the convolutional layers, the network exploits two fully connected layers to perform the classification. The number of neurons is 2048 and 1024, respectively. Both fully connected layers are followed by a ReLU activation function and a dropout layer with a dropout rate of 0.5. The output layer is a n neurons layer followed by *softmax* activation function which produces a probability distribution over n classes.

5.1.2 Point Cloud to Image The accuracy that can be achieved by the first CNN, that exploits only raw waveform data, is not sufficient, thus additional spatial information must be considered for a precise classification. The idea is then to

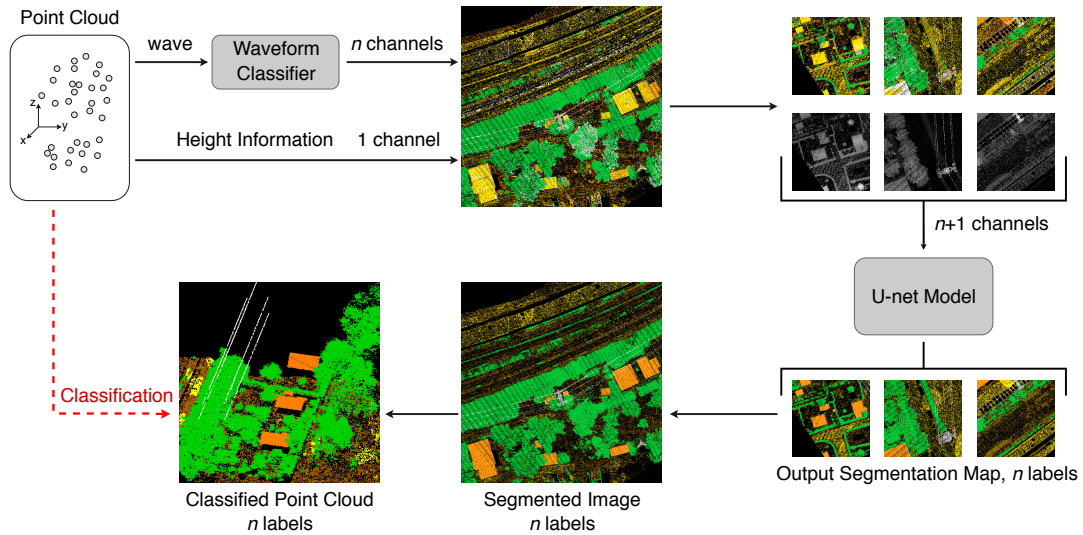


Figure 12. Workflow of the proposed method. First, the waveform classifier (a CNN) predicts the point class only exploiting full-waveform data. Predictions are then mapped into an image, together with the height information derived from the 3D coordinates of the points. The resulting multi-channel image is then processed by a FCN (U-net) that refines predictions using spatial information.

map the point cloud into a two-dimensional image, exploiting (x, y) coordinates of the points that correspond to first return (echo) registered in each waveform. In this way, spatial positions and geometrical relationships between neighbouring data are taken into account. The resulting image has multiple channels: every pixel stores the n -dimensional probability distribution vector, provided by the classifier employed in the first stage of the procedure, and the height of the data falling in the pixel. The point cloud classification problem can therefore be cast to the segmentation of an image, that assigns a class label *per-pixel*. This task can be solved by a Fully Convolutional Network (FCN), as described in detail in Sec. 5.1.3.

During the mapping procedure a loss of information inevitably occurs because of *collisions*, i.e., more than one point is mapped to the same pixel. This phenomenon has a negative impact on the accuracy of the algorithm. It is possible to limit collisions by reducing the pixel size, which entails enlarging the image, and at the same time increasing the computing time. Please note however that collisions are problematic only when involving points of different classes, otherwise a single class label is adequate for all the points. With the parameters chosen in our experiments, approximately 5% of the points of the dataset collides, but fortunately less than 0.5% involve points with different labels. In that cases, the point with the highest altitude value is chosen, in order to improve classification of small and thin objects such as transmission towers and power lines, which are the most critical classes.

5.1.3 Image Segmentation via U-net CNNs were firstly designed to solve image classification tasks, where the desired output is a single class label assigned to the input image. However, in recent years several architectures have been proposed to perform image segmentation, allowing to assign a class label to each pixel. In particular, we started from the so called U-net model (Ronneberger et al., 2015) and implemented a FCN to segment the multi-channel image created as described in the previous section. A FCN is composed only of convolutional layers without any fully-connected ones. This allows to operate on an input of any size, producing an output of corresponding spatial dimensions.

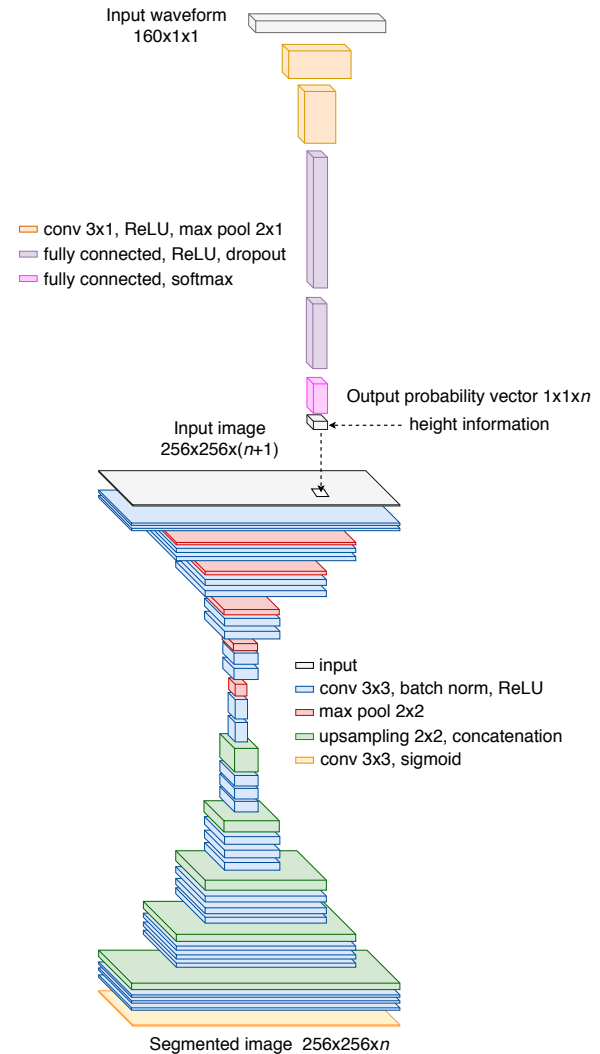


Figure 13. Architecture of the proposed networks. At the top, the waveform classifier. At the bottom, the U-net model used for the image segmentation.

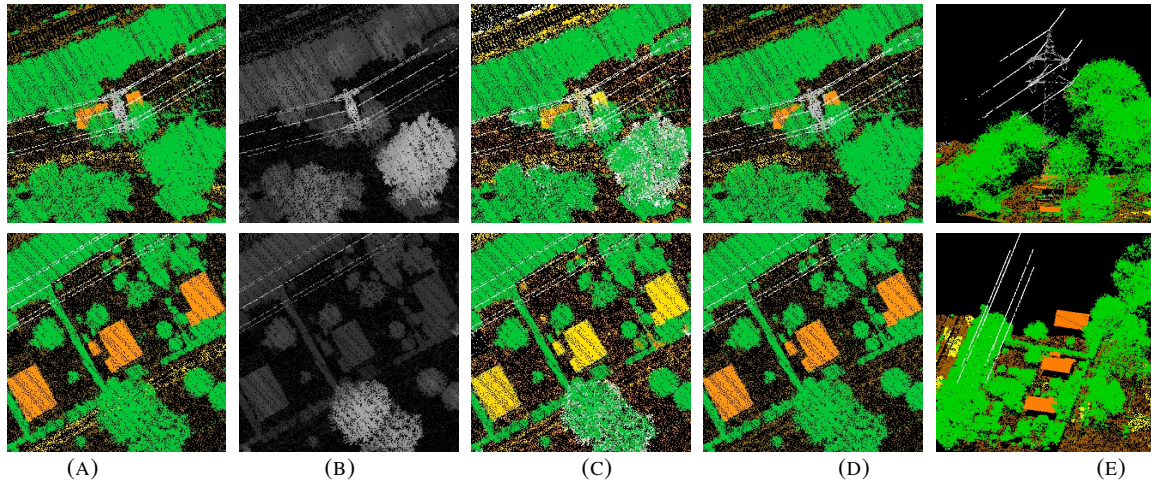


Figure 14. Sample images (256×256) and results. (a) Ground truth images used for training and validation; (b) Height channel; (c) Labels predicted by the waveform classifier (maximum probability) that are fed to the U-net; (d) Labels produced by the U-net (maximum probability); (e) 3D views of the classified point cloud, coloured with the predicted labels. Classes: *ground* (brown), *vegetation* (green), *building* (orange), *power line* (white), *transmission tower* (grey), *street path* (yellow).

The network we employed, illustrated in Fig. 13, consists of a contracting path (upper part) and an almost symmetrical expansive path (bottom part). In the contracting path, the network looks like a typical CNN able to recognize both low and high level features. Each layer is composed by two 3×3 convolutions, each followed by batch normalization and ReLU activation function. A 2×2 max-pooling operation is then applied to reduce the representation size by a factor of two, starting from an input of dimensions 256×256 and reaching a size of 8×8 at the final layer of the contracting path. The number of feature channels is doubled at each layer with respect to the previous one. The first layer outputs 64 feature maps, whereas the last one 2048. Every layer in the expansive path consists instead of an upsampling of the feature maps that increases the resolution of the output of the previous layer, a concatenation with the corresponding feature maps from the contracting path and three 3×3 convolutions, each followed by batch normalization and a ReLU activation function. At the final layer a 1×1 convolution is used to map each 64 components feature vector to the desired number of classes. While the contracting path captures context information, the expansive path enables precise localization (Ronneberger et al., 2015), thus allowing a *per-pixel* labelling.

The U-net consumes the multi-channel image created as described in Section 5.1.2. The first layer of the U-net model is designed so as to take in input images of fixed size (256×256 in our case) but a point cloud can be mapped in a much larger image. An image of arbitrary size can be processed by an overlap-tile strategy. Since convolutions in our U-net are padded, the *valid* portion of the 256×256 output layer is reduced by 14 pixels at each side. Therefore input tiles must overlap (by 28 pixels) in order to provide a valid output for each pixel.

5.2 Experiments and Results

The networks have been implemented in Keras (Chollet, 2015) and run on a Tesla K40c GPU. Validation has been performed on a dataset that we manually labelled, acquired by Helica s.r.l. with a Riegl LMS-Q780 full-waveform airborne laser scanner. Three different information are associated to every measured point contained in the dataset, namely the waveform registered by the LiDAR full-waveform sensor, described by a

vector of 160 values, the 3D coordinates of the point and the label that shows the class to which the point belongs. Six classes were identified: *ground*, *vegetation*, *building*, *power line*, *transmission tower* and *street path*.

To train the waveform classifier, we employ 200 thousand waveforms per class, for a total of 1.2 million samples. Regarding the U-net, the training is done using 15 thousand 256×256 windows with 7 channels for each pixel (see Fig. 14). Six channels correspond to the probability vector over the six classes provided as output by the classifier, while one channel contains the height information. Please note that the training images are randomly cut out and extracted from the much larger image in which the training point cloud is mapped.

	<i>ground</i>	<i>vegetation</i>	<i>building</i>	<i>power line</i>	<i>tower</i>	<i>street</i>
<i>ground</i>	0.84	0.07	0.00	0.00	0.00	0.09
<i>vegetation</i>	0.03	0.97	0.00	0.00	0.00	0.00
<i>building</i>	0.01	0.06	0.93	0.00	0.00	0.00
<i>power line</i>	0.00	0.05	0.00	0.91	0.04	0.00
<i>tower</i>	0.01	0.07	0.00	0.04	0.88	0.00
<i>street</i>	0.30	0.01	0.00	0.00	0.00	0.69

Figure 15. Confusion matrix: each row of the matrix represents the instances in an actual class while each column represents the instances in a predicted class. Values are normalized so that the sum of every row is equal to 1.

In order to report results that are independent from the training stage, to some extent, five trainings were performed independently, each time initializing the weights from scratch and randomly extracting the training dataset from the entire point cloud. The resulting overall accuracy, computed on the test set, is equal to $92.6(\pm 0.7)\%$, while the average per class accuracy is $87.0(\pm 0.3)\%$.

As can be noticed from the confusion matrix represented in Fig. 15, that reports the results for one out of the five trainings, the network performs very well for the classes *vegetation*, *building*, *power line* and *transmission tower*. Instead, points

belonging to the class *street path* are often confused with the class *ground*. This is probably due to the fact that the shape of the waveforms belonging to these two classes are often indistinguishable and also the geometric characteristics of *ground* and *street path* points can be very similar. In practical applications (e.g., for the creation of DTMs) these two classes are usually merged together. If we consider *ground* and *street path* as a unique class, the overall accuracy increases to 96.1(± 0.2)% and the average per class accuracy to 92.5(± 0.5)%, suggesting that our method compares favourably with the state of the art.

To summarize, we presented an innovative algorithm based on CNNs to perform full-waveform LiDAR point cloud classification. The proposed network employs directly the raw full-waveform data, learning both features and classifier end-to-end, unlike other methods that require preliminary extraction of features. It can be applied to the classification of points belonging to any kind of area and no prior knowledge on the data characteristics is required.

6. CONCLUSIONS

In the first part of this thesis, orientation problems in photogrammetry and laser scanning were studied from a methodological point of view and solved via *Procrustes Analysis*, a set of least squares mathematical tools used to perform transformations among corresponding points belonging to a generic k -dimensional space, in order to satisfy their maximum agreement. Starting from a comprehensive survey on Procrustes Analysis, we proposed novel Procrustes models that can be useful in several applications. The second part of this work was instead devoted to LiDAR applications. In particular, we described a novel method to perform LiDAR point cloud classification, that is based on Convolutional Neural Networks and takes advantage of full-waveform data registered by modern laser scanners. Thanks to the employed architecture, even challenging classes such as power line and transmission tower can be automatically identified.

We hope that the algorithms developed in this thesis could represent valuable tools to reduce time and costs of photogrammetric and LiDAR data processing, facilitating the use and interpretation of the acquired data.

ACKNOWLEDGMENTS

I would like to thank my supervisor, Prof. Andrea Fusiello, and my co-supervisor, Prof. Fabio Crosilla, for guiding me during these three years. This work would not have been possible without their support and help.

REFERENCES

Arun, K. S., 1992. A Unitarily Constrained Total Least Squares Problem in Signal Processing. *SIAM Journal on Matrix Analysis and Applications*, 13(3), 729-745.

Beinat, A., Crosilla, F., 2001. Generalized procrustes analysis for size and shape 3D object reconstruction. *Optical 3-D Measurement Techniques*, Wichmann Verlag, 345-353.

Besl, P., McKay, N., 1992. A Method for Registration of 3-D Shapes. *IEEE Transactions on Pattern Analysis and Machine Intelligence*, 14(2), 239-256.

Case, F., Beinat, A., Crosilla, F., Alba, I., 2014. Virtual trial assembly of a complex steel structure by Generalized Procrustes Analysis techniques. *Automation in Construction*, 37, 155-165.

Chollet, F., 2015. Keras. <https://github.com/fchollet/keras>.

Commandeur, J. J. F., 1991. *Matching configurations*. DSWO Press.

Felus, Y., Burtch, R. C., 2009. On symmetrical three-dimensional datum conversion. *GPS Solutions*, 13(1), 65-74.

Fieber, K. D., Davenport, I. J., Ferryman, J. M., Gurney, R. J., Walker, J. P., Hacker, J. M., 2013. Analysis of full-waveform LiDAR data for classification of an orange orchard scene. *ISPRS journal of photogrammetry and remote sensing*, 82, 63-82.

Garro, V., Crosilla, F., Fusiello, A., 2012. Solving the pnp problem with anisotropic orthogonal procrustes analysis. *Second Joint 3DIM/3DPVT Conference: 3D Imaging, Modeling, Processing, Visualization and Transmission*, 262-269.

Goodfellow, I., Bengio, Y., Courville, A., 2016. *Deep learning*. 1, MIT press Cambridge.

Gower, J. C., 1975. Generalized procrustes analysis. *Psychometrika*, 40(1), 33-51.

Gower, J. C., Dijksterhuis, G. B., 2004. *Procrustes problems*. Oxford Statistical Science Series, Oxford University Press.

Kuhn, H. W., 1955. The Hungarian method for the assignment problem. *Naval Research Logistics Quarterly* 2, 2, 83 - 97.

Lowe, D. G., 2004. Distinctive Image Features from Scale-Invariant Keypoints. *International Journal of Computer Vision*, 60(2), 91-110.

Pachauri, D., Kondor, R., Singh, V., 2013. Solving the multi-way matching problem by permutation synchronization. *Advances in Neural Information Processing Systems* 26, 1860-1868.

Ronneberger, O., Fischer, P., Brox, T., 2015. U-net: Convolutional networks for biomedical image segmentation. *International Conference on Medical image computing and computer-assisted intervention*, Springer, 234-241.

Schönemann, P., Carroll, R., 1970. Fitting one matrix to another under choice of a central dilation and a rigid motion. *Psychometrika*, 35(2), 245-255.

Seitz, S., Curless, B., Diebel, J., Scharstein, D., Szeliski, R., 2006. A comparison and evaluation of multi-view stereo reconstruction algorithms. *IEEE Conference on Computer Vision and Pattern Recognition*, 1, 519-528.

Strecha, C., von Hansen, W., Gool, L., Fua, P., Thoennessen, U., 2008. On benchmarking camera calibration and multi-view stereo for high resolution imagery. *Proceedings of the IEEE Conference on Computer Vision and Pattern Recognition*.

Toldo, R., Beinat, A., Crosilla, F., 2010. Global registration of multiple point clouds embedding the generalized procrustes analysis into an ICP framework. *International Symposium on 3D Data Processing, Visualization and Transmission*, 109-122.

Zhou, X., Zhu, M., Daniilidis, K., 2015. Multi-image matching via fast alternating minimization. *Proceedings of the International Conference on Computer Vision*, 4032 - 4040.

RAPID MAPPING STRATEGIES TOWARD BUILT HERITAGE 3D DENSE MODELING. SUITABILITY AND VALIDATION OF INFORMATION EXTRACTION FROM INTEGRATED SOLUTIONS

G. Sammartano¹,

¹ Politecnico di Torino, DAD – Department of Architecture and Design, Torino, Italy - giulia.sammartano@polito.it

KEY WORDS: 3D models, rapid mapping, built heritage, optimization, validation, damage assessment, UAV photogrammetry, SLAM, mobile mapping, LiDAR

ABSTRACT:

The documentation of Cultural Heritage is continuously involved into experimentation both for technological advances in integrated digitization and for optimization workflows directed to sharing and communication strategies in order to enhance the use of tailored dense 3D models in user-oriented purposes and diversified application fields concerning the conservation and management of our built legacy. The increasing availability of rapid mapping and need of low-cost approaches and their adaptability in some kind of critical operational context, offers interesting research issues and shall also requires necessary tests of metric content validity status. The ongoing efforts of geomatics applied research should be thus arranged also in the validation procedures exploring the suitability perspectives of imaging and ranging sensor-based modelling in such a context full of requirements that is the one of the vulnerable built structures belonging to the heritage assets. The proposed methodology here presented, summarizing the PhD thesis research work, is based on a multi-parameter validation approach (about data effectiveness, timeliness, accuracy, richness) that make use of a set of test-dataset in order to complement the more established approaches with encouraging innovative 3D survey workflow that could benefits from more recent solution as SLAM-based mobile mapping and UAV photogrammetry. The validation of the metric and non-metric content on these multi-sensor and multi-purpose 3D models at architectural and urban-scale, in those varying risk contexts, offers sundry geospatial products supporting high-scale documentation and morphological phenomena interpretation and proving once again the positive participation of Geomatics integrated techniques in time-cost ration inside on-site activities, especially whenever it implies the safety of operators.

1. INTRODUCTION

The active role of Geomatics techniques applied to the documentation of built heritage face up with ever-continuous open issues in research: they are related to the measurements, optimization, enrichment and sharing of 3D dense models and mostly geospatial data, also for those regarding actions on diffuse urban heritage and their operative workflows efficiency and strategies validation. They are regarding both the improvement of new integrated methodological approaches in data acquisition and modelling and the tuning consolidated ones in order to provide the high level of richness in 3D information and oriented to the users and for dissemination purposes. The possibility of implementation for integration purposes in the reading and in interpretation methods based on the 3D geospatial data is crucial, especially in the regards of the vulnerable built structures requirements. Hence, as an applied science, the role of geomatics in geospatial applications is thus closely related to the multidisciplinary attitude firmly required by the historical buildings, especially in order to ensure common languages for navigation and queries in interoperable databases. The proposed methodological principles, the technological solution and the operative workflows must be tailored according to the specific requirements for the 3D models analysis and enrichment in the role of a multi-dimensional database (Bitelli et al., 2017; Tucci, Bonora, Conti, & Fiorini, 2017). This research path fits into the geomatics integrated survey techniques with methodological validation purposes approach. Furthermore, it deals with the validation of data generation and information mining, starting from 3D dense models with multi-sensor workflow implemented on historical structures facing their risk context and the need of documentation for their morphological conditions. The favoured use of rapid mapping techniques is also recommended as an

alternative to established pipelines and consolidated techniques. In accordance with the needs of this discussion flow, after a brief overview on 3D digitization principles applied to Cultural Heritage, the methodological approach is proposed with the multi-parameter frame. Then, the reality-based modelling is presented through the methods and techniques tackled as an integration-driven approach. Formerly, the proposed method is focused as support to the documentation of built heritage in critical contexts. Lastly, the testing dataset are briefly summarized in the main requirements and goals, with a conclusive discussion on the proposed methodological approach.

1.1 3D digitization workflow: variables and requirements

The long-time shared principles and protocols in the wide domain of Cultural Heritage conservation that drive the data recording workflows, finalized on metric survey operations on build heritage, are faced in countless research occasions and according to different perspectives: *GCI Conservation perspectives, 2017; Historic England specifications, 2015; RecordIM 2003-2007; Core Data Index to Historic Buildings and Monuments of the Architectural Heritage, 1993; Athens Charter, 1933* (Letellier, Schmid, LeBlanc, Eppich, & Cabbi, 2011; Stylianidis & Remondino, 2016). In fact, many recognized organizations and institutes contribute with many efforts to spread among scientific communities the heritage management and protection principles e.g. UNESCO, ICOM, ICOMOS, ICCROM; WMF, CIPA, The Getty Conservation Institute (GCI). Likewise, the standardization of disciplines and documentation approaches as well as the normalization of data exchange in the era of digital information technology is mostly pursued in order to encourage disambiguation, interoperability, and open data sharing (e.g. *London Charter, Digital Agenda, INSPIRE, European Heritage*

Network) (Kioussi, Karoglou, Bakolas, & Moropoulou, 2012). In this framework, the use of advanced ICT technologies for 3D digitization doesn't not expire in the data collection and documentation phases, but moves alto toward multi-disciplinary investigation and visualization/communication/dissemination technologies. Basically, a summary of needs and requirements that can be listed about digital workflows in 3D metric documentation, as investigated in widespread literature (Bitelli et al., 2017; Tucci et al., 2017), is: *interdisciplinary propensity; tailored detail richness and accuracy; flexibility; density of information; multi-dimension data (multi-scalar, multi-temporal)*.

The weighted combination of these features leads to different workflows in the 3D modelling, that should follow both principles of *reality-based* modelling and *user-oriented* content richness, directing to consider the whole sustainability of the integrated documentation approach. Variables that can be synthetically defined in the proper methodological approach fulfilment are here proposed as: *Quality, Time, Costs*, whose applicability was partially investigated in Di Giulio et al., (2017). *Quality*, is intended as the reliability of the survey. Reliability is based on the maintenance of metric quality of data, on the possibility of updating a database and integrating parts or upgrading the details, and on ensuring non obsolescence of the technologies and tools rapidly evolving. *Time*, provides information of the usability of the survey. Usability evaluated in terms of the possibility of the exploitation of data validity for a period as long as possible and the assurance of saving time in collaborative and endorsed procedures. *Costs*, describe the effectiveness of the survey. Effectiveness depending on the resources which comprehensively endow on the variables cost ratio: time spending, technology, skills and data density cost ratio. These are the baseline issues for the multi-parameter validation proposed in the research and synthesized in next paragraph.

1.2 Methodological approach: multi-parameters validation

The methodological approach follows the concept of *Validation*, in the meaning of “verification, where the specified requirements are adequate for an intended use.” (CISIS guidelines in Brovelli et al., 2009; ISO/IEC Guide 99:2007 & JCGM 200, 2007). In the context of building scale documentation and in the rapid mapping scenario for critical context, the research questions can be summarized in: *how to extract simplified but suitable and focused data? Where to manage embedded information? Which methodologies can define a 3D documentation of the CH as reliable and effective in achieving the aim for which it was conceived?* In other words, when and where can it be validated? The proposed parameters are listed below:

- *Reliability*, or the confidence level of the metric aspects.
- *Contents*, or the richness of the embedded data.
- *Completeness*, or comprehensiveness of gatherable information.
- *Operational efficiency*, or the practicality and sustainability of data achievement.

1.2.1 Reliability. The reliability is basically related to the metric quality and control of the collected data and the 3D information modelling, and depend form the initial assumption of the required scale (intended here from 1:50 to 1:200 scale). The research takes into consideration the overall metric confidence level that it can be possible to obtain from the metric products with related uncertainties, mainly expressed by statistical indexes analysis: accuracy, mean error, precision, standard deviation, bias, noise (ASPRS, 2015; JCGM, 2008). Among others, *accuracy* is generally evaluated with *RMSE* control belonged to reference measurements or ground-truth surface (Point cloud comparison (Lague, Brodu, & Leroux, 2013) and deviation analysis), together with the *St.dev* control in the 3D model *precision* control.

Unpredictable noise errors are adjusted by means of outliers' removal procedures and segmentation and filtering procedures.

1.2.2 Content. The estimation of the metric and non-metric content is related to the richness verification i.e. the level of detail embedded in the acquired data and is related both in geometric aspects and appearance attributes (radiometric data). Whereas the basic geometric aspects can be discussed analysing the different high-scale data capability to measure not only the main shapes (distinctive plane, generation of volumes) but also the morphological anomalies by section examination and surface deviation analysis (*Out of plumb, misalignment, bulging, loss of connection, cracking, collapses, etc.*), by means of large-scale data is possible to study the relationship with the terrain topography/micro-topography by DSM analysis and information extraction too. On the other hand, the radiometric content allows to support the study of masonry texture, material state of conservation and decay, structural damages and cracking patterns, constructive components/relationship between parts, other attributes for endogenous problems.

1.2.3 Completeness. The concept of model completeness is strictly related to the content parameter, and refers to the effectiveness and continuity of the 3D metric content and requires the evaluation of the satisfaction about the gatherable information in the whole geometry reconstruction. Strategies in the direction of survey improvement help in the direction of maximizing this parameter. Actually, the environmental conditions are affecting the data collection and results quality (for both image based and range based approaches). The survey planning in terms of spatial overlapping coverage can ensure geometric continuity, avoiding the lack of data on undercuts and shadows areas. The management and optimization of baseline data, i.e. points cloud and the integration of sensor contribution, especially in the 3-dimension, guarantee the best spatial resolution. The geolocalization and compatibility of subsequent collected data, wherever necessary/possible in the time dimension, works in the direction of a temporal resolutions.

1.2.4 Operational efficiency. The efficiency parameter is proposed from an operational point of view and is centred on technological deployment, pre- and post- acquisition, technical feasibility in the datasets collection and processing: it is therefore the overall practicality and sustainability of data achievement of each proposed integrated or stand-alone approach (Table 1).

Table 1. Variables of operational efficiency parameter

ACQUISITION	PROCESSING	RESULTS
 <i>Instrument autonomy</i>	 <i>Hardware work</i>	 <i>Scale detail</i>
 <i>Operator work</i>	 <i>User work</i>	 <i>Errors occurrence</i>
 <i>Acquisition time</i>	 <i>Processing time</i>	 <i>Data size</i>

2. REALITY-BASED MODELING FOR CH DOCUMENTATION AT BUILDING SCALE: RAPID-MAPPING AND LOW-COST APPROACHES

The variety of available geomatics techniques applicable in CH contexts documentation and mainly their combination, is proved by the countless researches in the testing many purpose-driven effective data recording strategies. The conducted research gathered a state of the art review according to the investigation purposes and the constrained application context, here only outlined. It can be stated that the combined use of optical sensors (image- and range-based data) effectiveness is now well-proven in terms of data integration/fusion not just in the sense of data merging and information enrichment but also for mutual benefits and an effective contribution of the sensor (or data coming from

a sensor) or on the improving the performance of the other sensor (or data coming from another sensor) (Bastonero, Donadio, Chiabrandò, & Spanò, 2014; Ramos & Remondino, 2015). One of the most practiced and worthy data integration is surely the joint terrestrial and aerial point of view, for noticeable completeness reasons, and this is proposed in the tested dataset. This could be an advantage for the satisfaction of different topics:

- To obtain a more robust operational performance.
- To extend the data coverage and enhance resolution in the spatial/temporal dimension and where lower or higher details are needed.
- To reduced ambiguity, increased confidence, control uncertainty.
- To improved detection performance (point-based, object-based, feature-based, etc...)
- To complete the 3D geometric information in the vertical and horizontal extents and where gaps caused by occlusions have to be closed.
- To improve the radiometric information quality in point clouds (RGB data or other wavelengths range) and to overcome the lack of continue texture due to obstructions or non-collaborative material/surfaces for visualizing and interpreting the final models.

From a methodological point of view, the flanked deployments of consolidated and innovative techniques lead not only to the contribution in continuous development of technological innovation testing, but also to the implementation of the more recent so-called *rapid-mapping* techniques and related workflows (Boccardo, 2013; Huang et al., 2019). This is particularly needed to be weighted for those contexts where the gathering of information extraction is strictly related to the possibility of operating according to well established workflows. The increasingly frequent combined use of techniques based on *low-cost* sensing systems (Calantropio, Patrucco, Sammartano, & Teppati Losè, 2017), becomes more and more necessary if in certain contexts the survey approach requires a limited economic investment, as the CH ones are prone to both the needs of action continuity and scarcity of resources. Consequently, here UAV photogrammetry combined with SLAM based Mobile Mapping System is proposed and validated as methodological approach for the documentation of the historical structures in critical context in their morphology and state of conservation. This is conducted in order to evaluate and quantify the achievement of accurate as well as rapid 3D reconstruction, of radiometric interpretation of façades, of metric information extraction, of support in damage assessment and cracks mapping assessment with the detection of deformation phenomena.

2.1 Close-range acquisitions. Among the close-range and terrestrial approach for 3D documentation, well-established since almost two decades and largely applied for cultural heritage domain (architecture, archaeology, urban areas), the consolidated TLS measurement is combined with digital photogrammetry that become increasingly competitive, despite supported by topographic measurements pipelines, in terms of algorithms, sensors quality and commercial answers (Remondino, Spera, Nocerino, Menna, & Nex, 2014). In many occasions the geometric resolution and richness of TLS survey should be weighted with the acquisition operations, the scan size management and storage, that could be time-consuming process, with high levels of operator interaction. Otherwise, some weakness can be listed in the applicability framework of heritage requirements: the price and execution and data management; the lack in radiometric continuity and points continuity according to geometric shadings depending on scans positions and coverage; the different materials radiometric response and the influence of environmental light, the overall redundancy of acquired points that many times are now more than halved for an effortless management and processing (Remondino, 2011). The algorithms developed by computer vision based on SfM approached and

photogrammetric image-matching (Westoby, Brasington, Glasser, Hambrey, & Reynolds, 2012) leads to multi-scale and multi-resolution 3D models with high level of point-based radiometric information and continuous textures.



Figure 1. A planar view of the RGB scan data (Castelmagno village), left; a zoomed excerpt of the dovecot tower (Dataset I).

In the research tests (Figure 1) a Faro Focus^{3D} 120 ToF scanner low/medium price range was employed (Dataset II). The high resolution camera is able to assign radiometric values to points, that are delivered in point clouds formats (X, Y, Z, i, R, G, B). The use of topographic measurements helped del scans registration based both on manual tie points and ICP-like algorithms (Bellekens, Spruyt, & Weyn, 2014), and supported the accuracy control on control points residuals. In the photogrammetric approach different COTS digital reflex cameras are employed (Dataset I, II, IV) for the image acquisition according to established workflows (Waldhäusl, Ogleby, Lerma, & Georgopoulos, 2013). A Canon D800E with 36MP sensor and 4.89 µm pixel size was equipped with 14-24 lens. A Canon Eos 1Ds Mark II with 16.7 MP sensor and 7.19 µm pixel size was equipped with 20 mm and 24-105 mm lens. Commercial platforms performing image-matching procedural workflows are used with the use on GCP and CP measured by topographic approach: Photoscan by Agisoft and Pix4D by EPFL (Aicardi et al., 2016).

2.1.1 SLAM-based mobile mapping system. Mobile Mapping Systems (MMSs) offer nowadays many solutions for balancing time and operator involvement in the acquisition phase for both indoor and outdoor mapping. MMSs are hybrid systems based on fusion of ranging, imaging and positioning technologies (Puente, González-Jorge, Martínez-Sánchez, & Arias, 2013). It allows the acquisition in movement of complete range PCs of the environments crossed along a trajectory. Most of them are based on moving vehicles or systems equipped with a central unit: a mapping sensor (active and/or passive 3D imaging systems), a positioning and navigation unit (GNSS, IMU) for spatial referencing, and a time referencing unit (Nocerino, Menna, Remondino, Toschi, & Rodríguez-González, 2017).

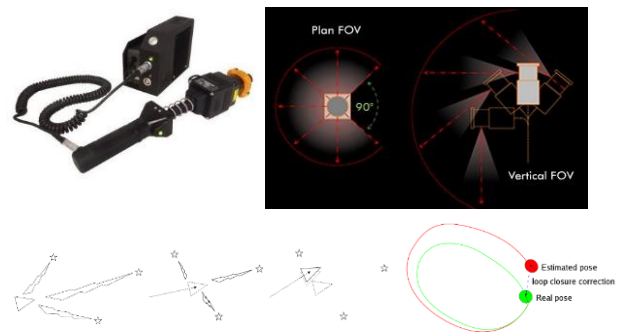


Figure 2. The ZEB technology by GeoSLAM: the data logger with the FOV of the moving head. The acquisition system is based on SLAM algorithm where position estimation is based on feature recognition; it may suffer from drift error.

Among all the solutions the portable ones seem to be very promising, trolley, wearable backpack and others. Here a handheld scanner is investigated: the ZEB-1 by GeoSLAM (Figure 2), one of the first release of this SLAM-based technologies, that currently are have been developed on the Zeb REVO-RT still under investigation (Sammartano & Spanò, 2018). The Zebedee prototype (Bosse, Zlot, & Flick, 2012), born as handheld 3D range-based sensor conceived as a mechanically simple and low-weighted/low-cost 2D time-of-flight laser range scanner (Hokuyo UTM-30LX scanner, (Nikoohebat, Peter, Oude Elberink, & Vosselman, 2017), rigidly coupled with an inertial measurement unit and mounted on a spring that freely and passively swings during the operator/vehicle movement.

In the ZEB1 the moving head is equipped with a laser profilometer 905 nm wave length acquiring almost 43200pps and an inertial measurement unit (with gyros accelerometers and magnetometers). The solution of the positioning problem is solved with a SLAM-based algorithm (Søren Riisgaard & Morten Rufus Blas, 2005) implemented in the scanning system and in the processing phase. The extracted profiles are continuously aligned during the progressive geometric surface reconstruction with an ICP like algorithm along the time marked trajectory $[T(\tau)]$, with 6 DOF, in a sequence of translations $t(\tau)$ and rotations $r(\tau)$ aimed at minimizing correspondences errors. The $[T(\tau)]$ is time-marked as well as the point cloud and quality values of SLAM are associated both to the trajectory and the point cloud (Figure 3). The system, along with the recent Zeb REVO-RT updating, leads to a scan speed 2.5 times faster, 100 rotations/second, used through a real-time data viewer on portable device interface. The declared range distance capability is 15m outdoor and 30m indoor, and the several times verified accuracy in literature is less than 5 cm (indoor) and 10 cm (outdoor) comparable to 1:100-1:200 scale. The crucial issues of the technological solution use to maximize the precision of the measurement approach are: (1) the environments rich in geometric features; (2) the trajectory intended as the closed loop path in outward and return, with the same starting/ending point; (3) probability of drift errors of the SLAM based reconstruction if trajectory is too long or in too regular settings or in care of non-closed mapping.

The ZEB1 acquisitions were tested (Dataset III) in the urban context of earthquake scenario and damage mapping with different length, speed, time, types trajectories (Dataset III) and processed with dedicated GeoSLAM software able to perform re-computation of algorithm according to parameters and balancing IMU data and SLAM-based trajectory according to the followed path.

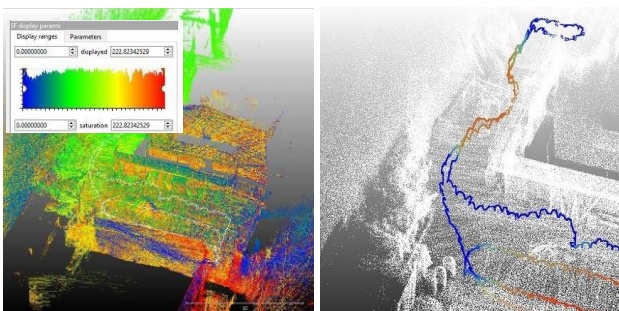


Figure 3. ZEB 1 point cloud time-marked and the trajectory points featured by SLAM condition

2.2 UAV photogrammetry approach. The aerial point of view in the metric documentation approach has been favoured by the introduction of Unmanned Aerial Vehicles (UAVs) sensor equipped for metric purposes by photogrammetric approach in agriculture and forestry, traffic monitoring, urban environments, landscape heritage, emergency management, archaeological areas, built heritage documentation and modelling (Colomina & Molina, 2014; Eisenbeiß, 2009).

Nowadays they flank traditional remote sensing approaches as aerial photogrammetry by aircraft platform and satellites data and they increasingly take place in the built heritage documentation approach both in urban, archaeological and landscape scenarios, giving the possibility for almost some years now to combine nadir and oblique point of view (Aicardi et al., 2016; Chiabrando, Lingua, Maschio, & Teppati Losè, 2017). Avoiding here to listing the entire investigation and comparative analysis performed in the research, it is possible to say that the mapping purposes for large and isolate objects in critical context largely benefit of UAV, as a data acquisition platform, from their ability in time cost competitiveness and efficiency in surveying operations deployment, and for the possibility to survey at various scales and closer distances. The on-board sensors, the flight plan and camera configuration are the main topics to take into configuration in to the UAV photogrammetric survey performance. The crucial issues and open tasks for the optimization of data acquisition and processing for geometry reconstruction:

- The aircraft equipment fix wings and multi rotor affecting the flight height and the final scale detail
- The sensor payload camera resolution sensor lens expected pixel size (ensuring high results in image matching densification process and radiometric reliability for the geospatial products
- The flight plan with flight height and strips overlap ensuring the required detail and the 3D completeness
- The camera configuration for accurate DSM and orthoimage processing, ensuring the required detail and the 3D completeness
- Automation in large images dataset
- Combination of image convergence in nadir/oblique flight plan for complex objects to ensure a coverage as uniform as possible in terms of GSD and accuracy.
- Methodological solutions for multi-temporal dataset in relation to image blocks configuration and ground points references
- In a general framework the operative practicability of UAV photogrammetry, with some aspect around normative regulation, patents and authorization for pilots' qualification.



Figure 4. UAV acquisition in Amatrice by Phantom DJI (top, left) and in Pescara del Tronto (top, right); Mikrokopter take off and flight plan and DSM in Castelmagno (down).

In the research tests (Dataset II, III, IV) different kind of photogrammetric approaches are deployed according to the proposed workflow, with two type of platform configuration (Figure 4). A fix wing drone (eBee by Sensfly equipped by Canon PowerShot S110RGB customized for eBee). Multi-rotor approach has been performed both with Hexakopter® by Mikrokopter customised equipment by PoliTo research group (equipped with Sony α ILCE 5100) and a couple of DJI platforms: the quadcopter Phantom 4Pro by DJI (Equipped with 12.4MP sensor camera) and the Inspire1 by DJI (Equipped with Zenmuse X7 24MP) customised by Italian Firefighters RPAS group. As introduced in the previous paragraph, image-matching algorithms implemented in commercial GUI with consolidated processing workflows. The use of derived DSM and 3D triangulated mesh will be exposed in next datasets parts.

3. 3D DOCUMENTATION SUPPORTING CRITICAL CONTEXTS

A variety of *user-oriented* implementation cases typically features the employment of multi-sensor and multi-content 3D models in the wide spectrum of CH documentation and conservation needs (Figure 5). It demands some considerations mainly about the collection of geospatial data, the use of standardized integrated workflows, the information extraction and models enrichment, in order to provide a starting point 3D database among specialists involved in the analysis, restoration, preservation and management policies in the long-expected tangible interdisciplinary approach. They could be: architecture and historic studies; archaeology and digging activities; landscape studies and planning projects; material decay and diagnosis; restoration practices; constructive technology expertise; geology, geomorphology, hydrogeology; structural engineering and restoration; technicians for emergency services and rescue operations, etc. This heterogeneity of purposes, targeting several features as much as individual methodological approaches and derived data, should also ensure multi-source data integration, information sharing and languages interoperability. Among this variety of tasks in which the Geomatics approaches should fit in, the integration of methods is increasingly called upon supporting metric documentation of the built heritage

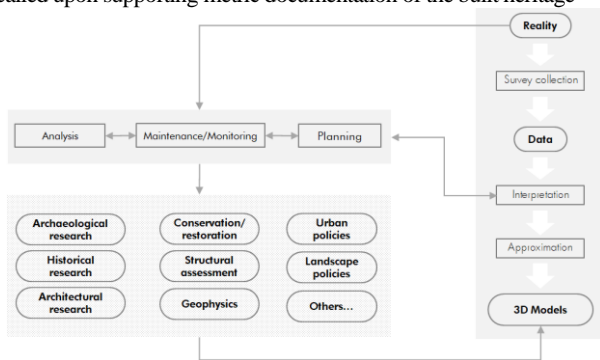


Figure 5. Application areas for 3D models supporting built heritage interpretation, maintenance and monitoring and planning.

specifically in critical contexts or risk scenarios according to different forms: from the restoration and conservation-driven survey to preventive risk documentation and damage measurement and assessment. In fact, different kind of risks could affect historical structures, depending both on the vulnerability aspects of the object own predisposition and on the potential hazard state in which they may run into, due to emergency events or local damage condition that can arise. The ISCR listed and analysed in the “*Carta del rischio*” in a spatial database the local and global condition of risks in the Italian context, that “has a medium-high seismic hazard (due to the frequency and intensity of phenomena), very high

vulnerability (due to the fragility of building, infrastructural, industrial, production and service assets) and an extremely high exposure (due to population density and its historical, artistic and monumental heritage that is one of its kind in the world)” (<http://www.protezionecivile.gov.it>).

3.1 Geomatics methods in critical context damage mapping

When validation approach is proposed for survey methods in such environments, it is interesting to tailor the evaluation on the maximization of data collection and information extraction from multi-scale models as well as on the issues related to the technologies applicability, i.e. the deployments of on-site techniques according to accessibility and danger circumstances. For these reasons, different context datasets are proposed, as listed in Par.3.2.

3.1.1 Emergency mapping and Damage Assessment. In order to perform emergency mapping, geomatics techniques are required to conduct research for sustainable technologies and algorithms supporting the rapid and extensive documentation delivery in emergency events and damages contexts with strict deadlines: i.e. earthquakes, fires, flooding, wars and humanitarian crisis, etc. (*Emergency Mapping Guidelines*, 2015). In this research the particular condition of built urban heritage post-earthquake event is also encountered.

Commonly the operations in post-disaster mapping are performed by a well-established image-based data centred on remote sensing techniques. The Copernicus Emergency Management Service (EMS, <http://www.copernicus.eu>) for example offers a prompt emergency response in express delivery of cartographic products. The procedures of Building Damage Assessment (BDA) are usually based on visual interpretation from satellite and aerial nadir views, with manual and time-consuming operators’ work (Boccardo & Giulio Tonolo, 2015; Kerle, 2010): the high resolution images allows detection and measurements of damaged buildings, debris, structural deformations, roofing conditions, etc.. However, due to their scale, their geometric configuration and ultimately their intrinsic features of restricted vertical view, nadir imaging does not fully satisfy the particular requirements of details and information (Lemoine, Corbane, Louvrier, & Kauffmann, 2013). Typical damages phenomena featuring the vertical dimension such as reductions in the volume and height, changes in the inclination of building and damage effects largely expressed along the façades, as well as the size of the debris data cannot be easily visible and localized and thus accurately measured (Figure 6).

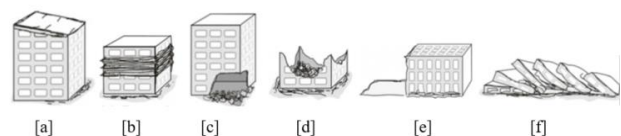


Figure 6. Example of damages building types and collapse catalogue in (Schweier & Markus, 2004).

In the case of 2015 post-earthquake event in Port-au-Prince (Haiti) the use of Pictometry® oblique imaging is firstly tested in BDA based on damage pattern detection with the help of supervised classification models and computer vision algorithms (Gerke & Kerle, 2011). Currently, the use of UAV oblique images and video frames are recently under interest in the rapid mapping strategies for damage assessment (Boccardo, Chiabrando, Dutto, Tonolo, & Lingua, 2015; Duarte, Nex, Kerle, & Vosselman, 2017; Fernandez Galarreta, Kerle, & Gerke, 2015). In fact, the recently experienced approaches to extract damages features are related to the availability of UAV high-scale images processed with photogrammetric methods for semi-automatic or automatic data extraction based by *pixel* and *object-based* methods, i.e. Object

Based Image Analysis (OBIA) or damages pattern recognition in 3D point clouds based on deep-learning approaches (Vetrivel, Gerke, Kerle, Nex, & Vosselman, 2017). The remote sensing data are actively under investigation in the balancing of timeliness and accuracy, and time-costs ratio and human involvement. Notwithstanding, the closer ground-based traditional survey approaches still needs the in-situ involvement of expert operators and first-aid staffs during the post-events intervention, despite in dangerous condition. The purpose that could open more and more interesting perspectives is to maximize the in situ data collection for massive amounts of information embedded in 3D models, preferring ex-post data processing and manual and assisted analysis according to the in force regulations. The current directives in terms of Damage Assessment have guided the analysis of strict data requirements in terms of information extraction, that will be differently possible to extract from rapid mapping dense models thanks to the metric and non-metric content optimization, as proposed in this research.

3.1.2 National and international regulation framework for damage assessment. In the European and Mediterranean area, the EMS-98 (European Macroseismic Scale) (Grünthal, 1998) is an interpretative classification of seismic events related to effects classes of structural damages visible on the structures according to the building types: masonry buildings, reinforced building, steel and wooden structures, etc. It is thus a classification driven by a visual interpretation of the whole building and aggregates and is based on typological codes (descending from a to E). In fact, the EMS is an intensity-based classification that involves both engineering and seismologic point of view: the so-called “*macroseismic intensity*” defines the gravity of ground-shaking on the bases of the observed effects. The damage assessment is not tailored for the building-architectural scale. It is the starting principle for the damage classification of the Copernicus EMS mapping.

Being a visual-based regulation for Damage Assessment, it can considerably benefit from the contribution of geo-spatial data, especially if enriched by a multi-temporal dimension. In order to effectively support the structural assessment, the contents of the EMS codes can be defined as reachable by means of radiometric (R) or geometric (G) contents extracted from the metric surfaces deriving from the rapid mapping strategies. The scale is distinguished in 5 grades: from 1 (Negligible to slight damage, where no structural damages are present); 2 (moderate damage that slightly affect the structural behaviour); 3 (A substantial damage); 4 (Very heavy damage); up to 5 (Destruction, totally or nearly collapsed).

- Hair-line and diffuse cracks, extensive cracks pattern (R) leading to serious failure of walls (G)
- Fall of few or many pieces, plaster or stones (R/G), up to individual elements or partitions, floors (G)
- Collapses of chimneys (G), fractures in roofs and tiles detachments (R), up to roof failure (G)

In the Italian regulation the Ministry propose within the last ten years the use of standardized documents for the post-disaster in-situ survey and for the indexing and assessment of built heritage, (*AeDES datasheets*) particularly for churches and masonry buildings (*A-DC and B-DP datasheets*).

The AeDES datasheets for practicability and damages in seismic emergency (“*Schede per l’Agibilità e Danno nell’Emergenza Sismica*”, C.N.R.- G.N.D.T. and S.S.N. in the Department of Civil Protection) concerns an interpretative process of assessment in the direction of the European EMS principles. The n°9 sections are referring to different descriptive steps related to both physic/typological condition, soils and instability background information, accessibility judgement and hazard evaluation. Particularly for the first 3 sections the metric and descriptive non-metric content of the datasheet is strictly related

to the survey phase and could largely take advantages from the digital reconstruction.

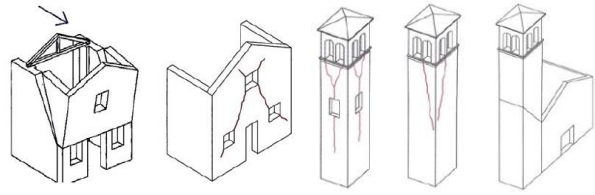


Figure 7. Excerpts from “Abacus of collapse mechanisms” in case of cultural heritage damages, datasheet A-DC “Churches”

The ministry datasheets for damage mapping of built heritage (“*Scheda per il rilievo del danno ai Beni Culturali*”) A – DC for churches and B – DP for buildings subjected to seismic events, specifically deal with filling scheduled demands regarding damage positioning detection, annotation, estimation (DPCM 23.02.2006/GU 7.03.2006, n°55 and subsequently amended).

The “collapses abacus” (Figure 7) consider structural and architectural elements codifying them with visual representation of the structural behaviours and collapse mechanisms: it can be defined as more suitable to the building scale assessment.

The research proposes the use of the following dataset-based validation procedure to evaluate the data collection and information extraction from the multi-scale and multi-content 3D models delivered from the experienced integrated approaches, in order to demonstrate them as a useful base supporting damage assessment operation: (1) geometrically accurate portray of objects at foreseen scale, plans, profiles, details; (2) radiometric characterisation of façades for the visual interpretation of masonries and architectural elements correlated to the metric evaluation thereon; (3) detection of thin or accentuated deformation phenomena, like misalignment, bulging, tilting, out-of-plumb, etc.; (4) damages documented through the recognition of debris, rubble piles, spalling, roofing, uncovering; (5) damage assessment of the system of cracks and the so-called post-crack behaviour; (6) prevent structural instability behaviour anticipating the collapse phenomena, for things or people in danger, through safety measures and emergency consolidations; (7) mappings of the passage and escape routes and the obstructions caused by debris; (8) changes in the detection and volume variation assessment due to the availability of multi-temporal acquisitions by change-detection OB or PB algorithms.

3.2 Proposed approach for test datasets

The goal of different test dataset compendium is to look for a link or cause relationship between the approach and the operational context, such as, on the one hand, the use of a consolidated or more alternative workflow proposal operating in a given condition framework and object extension and, on the other hand, the choice of methodological approach in digital documentation that it is possible or it could be much appropriate to deploy in it. Starting to comparable approach in survey purposes and different required metric data results, it is well-known from practical experiences that geomatics is forced to come to terms with the real context of applicability and therefore with the on-field workflow arrangement (Table 2). Three types of increasing hazard for the context scenery have been considered, that cross with two defined object extensions. The building scale documentation in an ordinary-type of context is faced up in *Dataset I*, Par.4, with a XV century trunk-conic masonry rural dovecote tower in the Monferrato landscape (TO). At the urban scale dimension, the ancient stone masonry structures in an alpine hamlet (CN) is use in *Dataset II*, Par.5 to provide a validation scenario of critical context of operation.

In the framework of an emergency context, after 2016 earthquake two different objects have been considered in order to study and

validate integrated methodological approaches. The International and national guidelines have been taken into account for an interpretative assessment of the aggregates (EMS-98) in the ruins of Pescara del Tronto (AP) village [Dataset III, Par.6] and with the help of the Italian datasheets guidelines at the architectural scale, for the ruins of S. Agostino church in Amatrice (RI) [Dataset IV, Par.7].

Table 2. Images related to heritage datasets grouping according to the extension and critical issues of the survey performance

		OBJECT EXTENSION	
		A	B
CONTEXT HAZARD	Ordinary	 [I]	-
	Critical	-	 [III]
	Emergency	 [IV]	 [IIII]

4. MULTI-SCALE PHOTOGRAMMETRIC MODELS ASSISTING MORPHOLOGICAL ANALYSIS: A RURAL TRUNK-CONIC DOVECOTE TOWER

For the *Dataset I*, a stand-alone dovecote tower dated back to the XV century, is examined, as what remains of the simple defensive system of a fortified mansion in the Monferrato Piedmont countryside (Sammartano & Spanò, 2017). Due to its context it is exposed to an ordinary of risk for its own nature; on the masonry structure is visible a physiological degradation in its particular trunk-conic shape. The noticed morphological anomaly of the structure is attributed to an arrangement in the building phase. The research proposes to face up the suitability validation by multi-parameters approach on the easy-to-use single approach of close-range photogrammetry, for multi-scale and multi-content 3D modelling oriented to HQ orthoimage computation and, furthermore, for the historical structures analysis, based on shape detection and morphological analysis and deformation assessments for decay and conducted for restoration actions. Specifically, the proposed documentation approach uses a double sets of images acquired with two different focal lens equipping a COTS digital reflex camera in order to validate the accuracy of the derived 3D models and their content and completeness. This lead to the morphological analysis on the tower volume, showing the descriptive capabilities in: surface analysis and shape detection; volume assessment and anomalies; surface analysis and orthoimage generation

4.1 The photogrammetric acquisition and data processing for multi-scale model

The two sets of images (1) 20mm and (2) 70mm focal length (n°32 images for dataset) as Figure 8, are used in the photogrammetric process of internal and external orientation with the use of topographic GCP, and evaluated in *stand-alone* use and *combined* in multi-scale 3D model.

The final GSD for the (1) block is almost 7mm along the tower volume, and 2.5mm for (2) block related to the upper dovecote volume. The final RMSE of the combined bundle block adjustment is 0.022m for GCPs and 0.035 for CPs, despite the only (2) reported better residual errors result: GCP =0.013m and CP=0.024m.

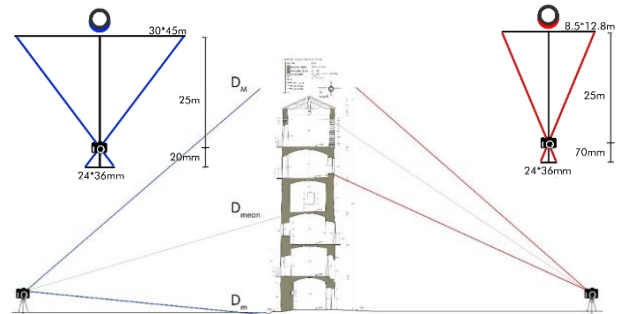


Figure 8. The multi-scale shooting acquisition planning

4.2 The surface analysis and shape detection for masonry structure and volume assessment

The multi-scale 3D point cloud was used for the volume analysis and extraction, and in parallel, a reference continuous surface i.e. 3D mesh was calculated by triangulated interpolation. The point cloud data undergone to a morphological analysis based on shape detection and volume estimation in order to further evaluate anomalies and deformation (Figure 10 and Table 4): the analysis of the directrices centers of the cone pointed out an out of plumb in the NS direction of tilt. The cylindrical approximation of the dovecote allowed a surface unrolling and orthoimage high-scale extraction (Figure 11).

Table 3. Metric evaluation of the PC comparison with the computed reference surfaces

	APPROXIMATION SURFACE	Deviation error by surface comparison [m]	
		Mean	St. Dev
I	Cylinder	0.0176	0.1115
II	Cone	0.0061	0.0960
III	3D mesh from profiles	0.0003	0.0993

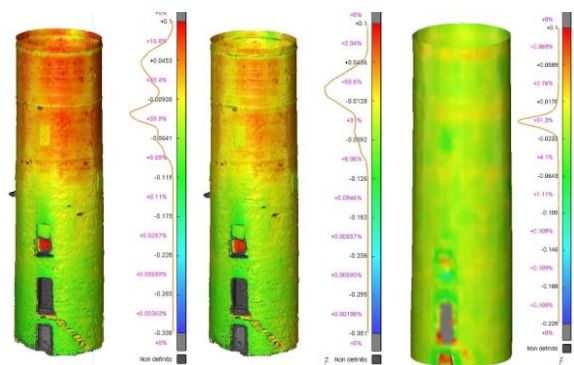


Figure 9. Deviation analysis of point cloud from 3D model shape detection based on cylinder, cone, section profile-based triangulated mesh

Three different approximation levels have been tested aimed at defining the real volume of the dovecote tower: a cylinder, a cone, and a computed surface reality-based generated on extracted profiles. Deviation results from comparison validation is reported in (Figure 9 and Table 3).

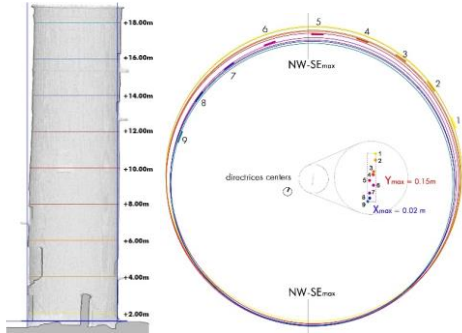


Figure 10. Analysis of the trunk-cone directrices centers trend obtained by progressive planar cut sections profile

Table 4. Evaluation of the main direction of the volume tilt
EVALUATION OF THE OUT-OF-PLUMB

	$0.00 < x < 0.10m$	$0.10 < x < 0.20m$	$0.20 < x < 0.40m$
NW	4.2%	16.4%	79.4%
SE	28.1%	65.7%	6.2%



Figure 11. The high-scale 3D model and orthoimage excerpt (1:50)

5. BOOSTING DOCUMENTATION IN CRITICAL CONTEXT BY FUSION-BASED DSM: A ANCIENT STONE MASONRY STRUCTURES HAMLET IN THE ALPINE LANDSCAPE

The *Dataset II* tested an integrated 3D metric survey in a perched semi-abandoned village consisting of drystone masonry buildings, Campofei. The Castelmagno valley in Southern Alps at Piedmont is involved in a process of the protection and promotion of Alpine culture and local economy, and supports the decision-making processes regarding the enhancement scenarios with the aim to recover them and create conditions so that people can live there again, in line with the Regional Landscape Plan guidelines and the European as well as local funding projects. (Chiabrando et al., 2016). Here, the restricted accessibility to spaces and the narrow collapsed structures in impervious conditions limited the deployment of methodological approaches and influence the performance of technological solutions; morphological context of the valley amid the high mountains, caused non-operation of GNSS receivers together with by prosaic problems of the rich canopy cover. The terrestrial CRP and TLS is evaluated together with the contribution of UAV photogrammetry, proposed by two different platforms that provide an accurate and complete aerial mapping of the structures in its relationship with the acclivity in the Alpine terrain: for the initial purposes the expected accuracy and related scale was around 1:50-1:100.

The issues pursued in this experimental approach were twofold: the enhancement of geospatial products derived by UAV photogrammetry multi-scale mapping and combine them wherever possible with higher level of detail by terrestrial approach. Thus, the landscape heritage documentation and

valorisation in this dataset was challenged by a multi-scale and multi-sensor survey on the historical structures despite the critical accessibility issues. The topographic context was extremely crucial for the building-scale analysis as well as the aggregate analysis in their relationship with terrain morphology.

- LiDAR & UAV photogrammetry were proposed in a fusion-based approach
- UAV-based multi-scale mapping and DSM analysis and validation tested in such complex and inclined slope for DTM from DSM extraction

The tested approach proposed thus some reflections about alternative acquisition strategies in this critical context of extensive urban heritage.

5.1 UAV-based multi-scale mapping

Twofold UAV acquisitions were performed in the Castelmagno valley over the village. The collected images in the two flight plan are featured by high overlapping and have been planned in order to achieve two different expected scale results, due to the great flight height difference, as Table 5, for the fix-wing eBee and the multirotor Mikrokoper Figure 12. The performances in descriptive capabilities of the two high scale DSM in proposed and evaluated in the research and employed for two different analysis approaches, here only presented.

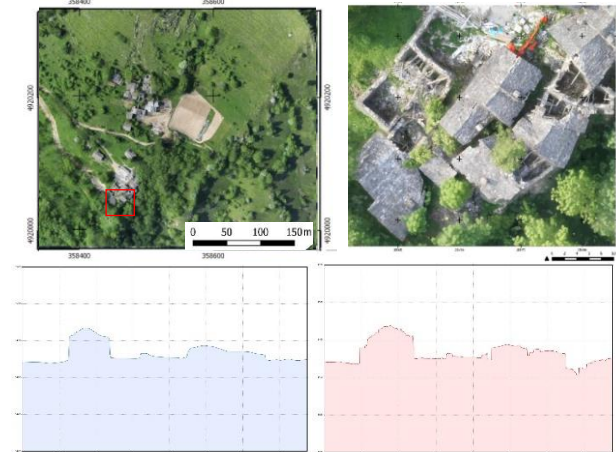


Figure 12. Zoomed excerpts of the eBee (left) and multicopter (right) flight orthoimages). Geometric details description from section profiles of the dry-stone ruins extracted on respective DSM.

Table 5. UAV acquisition datasets and results

	N° images	Area [km ²]	Pixel size [µm]	Focal length [mm]	Flight height [m]	GSD [mm/px]
eBee	545	2.43	1.86	5.2	150	50
MkK	626	0.18	5	16	70	30

5.1.1 DSM to DEM validation for surface analysis and feature extraction

The fix-wing was tested because of difficulties in the use of this UAV DSM for the DEM extraction: for the high-scale detail, the richness in continuous canopy and the high sloped morphology, that make overall difficult the usual application of endorsed procedures of filtering and segmentation. The approach (Sammartano & Spanò, 2016) makes use of morphological approaches in GIS SAGA analysis of terrain micro-topography to extract the featuring discontinuities and detect incoherent objects and use them to segment bare earth surface Figure 13. The method was validated with deviation analysis between the extracted DEM from the UAV DSM, and the reference GPS/GNSS values for a set of GCP as (Brovelli et al., 2009).

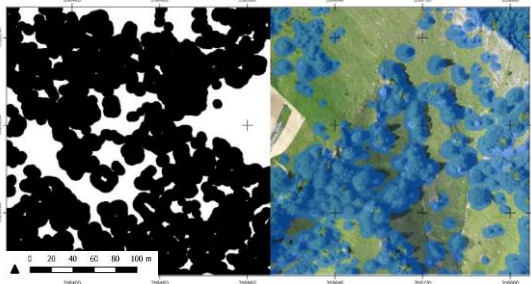


Figure 13. Features recognition by terrain ruggedness index applied on the DSM and creation of the vector layer mask.

5.2 LiDAR optimization strategy

The use of the high-scale DSM from multi-rotor platform was employed for a fusion-based strategy in order to improve the TLS scans registration in such kind of environment where the use of topographic methods are difficult to deploy. Different test steps are performed in the enrichment of measured manual tie points in the ICP-like fine registration of the complex scanning project (30 scans position, 20*10⁶ points/scans) with GPS measured target and DSM extracted 3D points. RMSE for the registration are reported in Table 6. Accuracy results delivered RMSE on reference CPs of Δ = X=0.018, Y=0.017, Z=0.1495m.

Table 6. Validation results for the three steps via accuracy control after clouds alignment strategies

	TS control points	GPS GCPs	UAV GCPs	RMSE
1 st stp	●	-	-	20 mm (st.dev=16)
2 nd stp	●	●	-	28 mm (st.dev=10)
3 rd stp	●	●	●	2 mm (st.dev=3)

6. COMBINING SLAM-BASED AND UAV EMERGENCY MAPPING IN URBAN-SCALE DOCUMENTATION: THE 2016 EARTHQUAKE OVER PESCARA DEL TRONTO VILLAGE

The *Dataset III* concerns the framework of the seismic events that affected diffuse urban heritage in Central Italy in the second half of 2016 and propose an integrated strategy of limited human involvement in relatively time-consuming operations for the operative survey is a post-disaster scenario.

Pescara del Tronto was a perched village in the Arquata del Tronto (AP) municipality and the Politecnico di Torino Task Force and the Italian Firefighters RPAS core have been involved in a huge reconnaissance mission in October 2016 in which multiple rapid mapping approaches were deployed and combined for 3D extensive documentation of damages and accessibility issues (Chiabrando, Sammartano, & Spanò, 2017).

The tested and validated integrated approach pointed out the role of rapid mapping strategy both aerial and whereas possible terrestrial point of view in large-scale aggregates documentation and diffuse collapses measurements.

The employment of a consolidated, high-definition, range-based approach like the TLS was excluded a priori, in favour of a more rapid data capturing solution: the ZEB1 SLAM-based handheld scanner acquisitions was performed walking along the available trajectories, across rubbles and collapses. The proposed approach is intended to be compared and integration with UAV photogrammetry mapping. Integration purposes in the emergency mapping: UAV and SLAM-based solution. The integration of the multi-sensor data is proposed during the processing phase and aimed at combining the accurate 3D reconstruction of MMSs from a close-range perspective

according to different acquisition plans, with a photogrammetric images block acquired both in oblique and nadir configuration as well recognized in workflows, tailoring both fix wing and multirotor equipped platforms.

Three areas are the focus of the research test and validation, and here for synthesis reasons the only central aggregate of building blocks is reported. A photogrammetric flight was performed with Inspire drone by DJI capturing 256 images (4608x3456px) with a GSD of 0.017m. The bundle block adjustment has been verified and the accuracy reported a mean GCPs RMSE= 0.034m: a dense cloud was generated with a density of about 1700 [pt/m²]. These photogrammetric models, achieved with discrete and unstable ground control, works in the direction of a high detailed radiometric documentation of the building and the geometric reconstruction of aggregates in a 1:100-1:200 scale. Metric products of first aid are orthophoto and surface models.

Table 7. Metric evaluation synthesis of the acquired SLAM-based PC in the centre block

	Area covered [m ²]	time traj. [min]	Aver. length traj. [m]	Aver. v [m/s]	n° points	SLAM closure error [m]	Av. density [pt/m ²]
Centre block	3000	10	210	0.35	16 mln	1.5	30.000

Then the SLAM-based 3D mapping was performed according to Table 7, collecting a point cloud of about 200MB and 16mln points. The (geo)positioning can be performed attributing coordinates on identifiable homologous points, but is less accurate due to the lack of radiometric information allowing identification of matching points (Figure 14). Then, the fine registration with the reference surface (UAV DSM, Figure 15) can be conducted with ICP-like algorithms and then verified by surface comparison. Currently the implemented version of Zeb REVO-RT provides the automatic measurement of reference points to be associated to known coordinates.

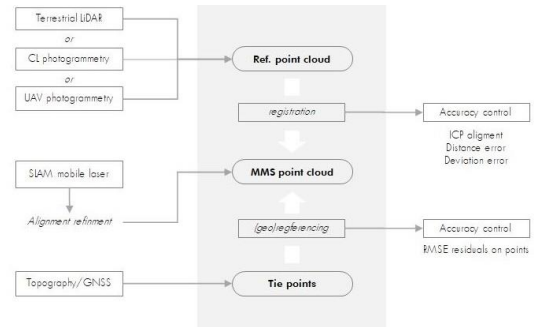


Figure 14. MMS SLAM-based processing pipeline for (geo)referencing and integration

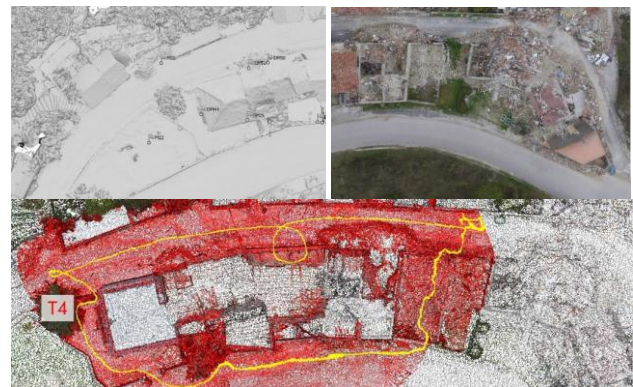


Figure 15. The UAV flight derived DSM and the SLAM-based mapping with red trajectory

6.1 Content and completeness validation from integration

Lastly, both the 3D reconstruction in the test areas have been evaluated in terms of the multi-parameters, especially favouring content data richness and completeness, i.e. continuity of information (Figure 16).

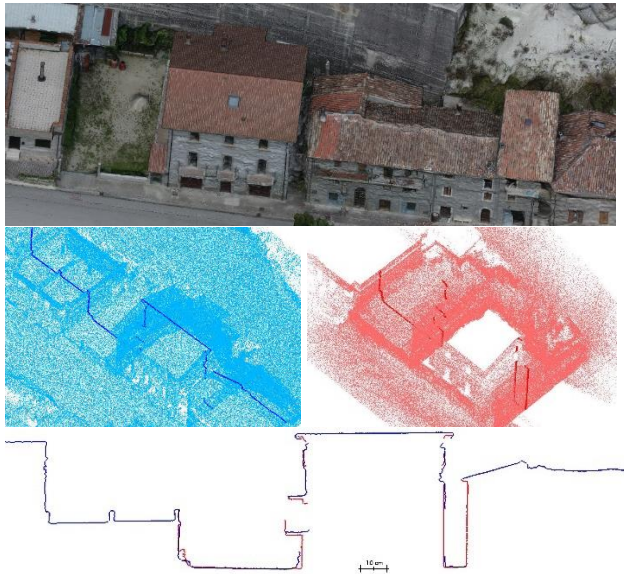


Figure 16. Analysis of surface coverage, completeness and content of respectively (blue) UAV DSM and (red) ZEB1 DSM

7. UAV PHOTOGRAMMETRIC APPROACH IN MULTI-TEMPORAL MODELING FOR THE S. AGOSTINO CHURCH IN AMATRICE UNDERGOING THE 2016-2017 SEISMIC EVENTS

The *Dataset IV* deal with the strategy validation for damage documentation of a single building scale object belonging to the cultural heritage in a crucial post-disaster scenario. The 3D modelling was planned to support structural analysis, in a multi-temporal perspective too (Grazzini, Chiabrando, Foti, Sammartano, & Spanò, 2019). The S. Agostino church in Amatrice, with its sandstone façade and decorated marble portal, was a Late Gothic complex of almost lost elevated cultural value not only within the local community, located in the south-east corner of the village and it suffered from reiterate seismic events from August 2016 up to first months of 2017 (Chiabrando, Di Lolli, et al., 2017). Both aerial and terrestrial image-based dataset were acquired in multi-temporal reconnaissance missions operate by Politecnico di Torino Task Force and Italian Firefighters RPAS group, in September 2016 (T1), in December 2016 (T2) and in January 2017 (T3). The lack of uniform topographic measurements (available only for (T1), is an existing problem that was take into consideration in order to elaborate operative considerations for such kind of context documentation, in order to obtain as much as possible accurate and suitable data for damage assessment and related mechanical phenomena extractable from the structural behaviour of the masonry. The use of stand-alone UAV oblique and nadir photogrammetry is analysed with and without close-range photogrammetry (CRP) influence, and proposed if adequate for the stated requirements. So, in the research the multi-sensor datasets contribution evaluation was employed for the validation strategy for the (T1) only (Table 8). Furthermore, the multi-temporal evaluation about the morphological analysis and the support for damage assessment were performed using UAV photogrammetric models solo for (T1), (T2), (T3).

The suitability evaluation in this highly-vulnerable object documentation and monitoring want to demonstrate the crucial role of time-cost optimisation issues in the emergency post-disaster scenario and specifically: the role of integrated 3D survey: UAV and close-range photogrammetry; the morphological and multi-temporal analysis.

7.1 T1: the sensors integration validation for content and completeness from integrated solution

Here the accuracy validation is conducted in the (T1) only. The accuracy of separate use of image-based dataset in the photogrammetric block has been validated and then with their integrated use: (CRP), GCPs RMSE=15mm, (UAV) RMSE=20mm, (Int) RMSE=10mm, demonstrating a suitability of the UAV 3D model for the required quality and purposes.

Table 8. UAV and close-range acquisition datasets in T1

	Images	GSD [mm/px]	GCPs RMSE [mm]	Av. Density [pt/m ²]
UAV	449	90	15	3.700
CRP	212	20	12	38.000
Int	661	70	10	10.200

Content and completeness validation, as well as operational efficiency have been favoured by the use or remotely piloted devices as acquisition platform, giving up the operator access to the area by means of close-range photogrammetry. The geometric comparison among UAV, CRP and integrated model is conducted in the research and reported by the extracted profiles and the density analysis operated of the point cloud (Figure 17).

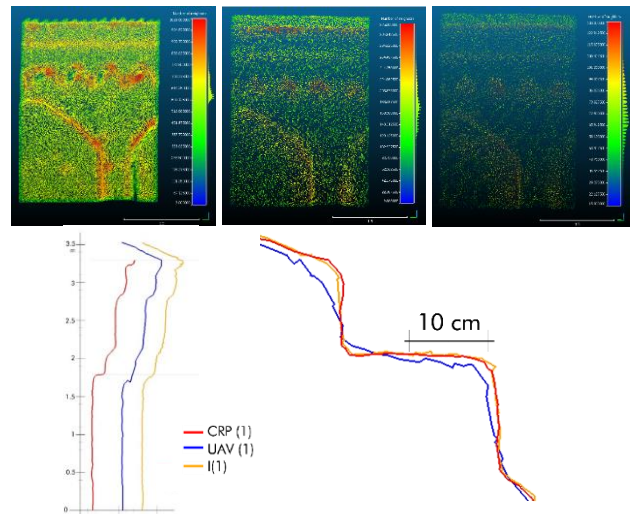


Figure 17. Surface densification for (from left) UAV, CRP, integration, and respective extracted profiles

7.2 T1-T2-T3: the multi-temporal acquisition validation supporting damage assessment



Figure 18. the three-times 3D survey modelling

Table 9. UAV and close-range acquisition datasets in T1, T2, T3

	Close - range photo.	UAV	Topogr.	Tot. images	GSD [mm/px]
(T1)	•	•	•	661	70
(T2)	•	•	-	97	55
(T3)	-	•	-	116	80

The metric and radiometric *validation* of the multi-temporal models (Figure 18) for their ability to support in diachronic mode the morphological and damages analysis and assessment is conducted by means of orthoimage interpretation DSM analysis and difference. Specifically, morphological aspects investigated are regarding the structure deformation (Figure 19): *out-of-plumb of the belfry volume, misalignment of walls surface, bulging of curtain walls, loss of connection in masonry pattern, cracking distributed as shear stress traces, reiterated collapses.*

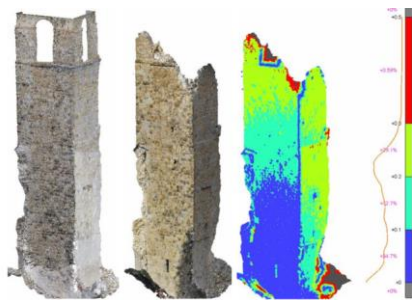


Figure 19. Deviation analysis from T2-T1 belfry tower point cloud

8. DISCUSSION

The presented research proposes a suitability evaluation of advanced survey techniques based on the concepts of rapid mapping and low-cost solutions, in their behaviour in case of single-use or multi-sensor solution, for the specific purposes related to the critical areas of built heritage documentation. The selected test-datasets belong to the architecture and landscape heritage domain, and each one purposely deals with specific scale and context requirements and then with targeted user-oriented requirements and consequently, variable 3D dense models. The validation test was synthetically based on the fulfilment of those individual requirements of the built structures, differently complex and affected by morphological anomalies or structural damages. So, the suitability evaluation of integrated survey solution investigated the descriptive capability in metric and non-metric content provision of the proposed methodological approach, that are the UAV photogrammetry and SLAM-based mapping, to deliver effective 3D models and support the documentation of historical structures in critical contexts especially in supporting the damage assessment. In this framework, the role of geomatics in improving the operators' role in the fieldwork and the reduction of his permanence in case of risk is the goal that is proposed to be investigated too.

The validation strategy has followed a multi-parameter approach which considers not only the metric products and confidence level, but rather the overall efficiency on the deployment of such approach in such contexts: they are *reliability, content, completeness, effectiveness.*

The model-based analysis and interpretation phase is crucial for the prefixed purposes and despite the metric accuracy of manipulated datasets shall responds to specific requirements reasonably validated in each test, in some cases they actually suffer from operative constraints related to the operative contexts. For these reasons more exploitable and effective solutions have been proposed as rapid mapping strategies in parallel to more consolidated TLS approach. The opportunity to

geometrically quantify directly the spatial distribution of a phenomenon thanks to the density content and thus recognizable details by means of radiometric content too is a central issue, together with the possibility to link morphological evaluation straight to a visible material or structure behaviour via surface analysis that reports deviation signs from an expected trend, i.e. the verticality or coplanarity.

In this scenario, the aerial point of view is surely an increasing challenging approach by use of UAV photogrammetry, as cost effective and context adaptable solution according to the last released commercial devices equipped by high resolution sensors and the possibility to perform very close distances flights or, in parallel, large scale mapping of wide areas in landscape-scale contexts. The reliability provided by the only use of UAV DSM for damage assessments scopes in the operative fieldwork, considering emergency condition, can be defined as successfully adequate for the interpretation of damage phenomena.

For higher accuracy and for very high-scale morphological analysis and orthophoto generation, the "human" point of view of close-range photogrammetry proves a valuable easy-to-use supporting approach to be integrated, wherever feasible, despite the unavoidable topographic measurement cooperation.

On the other hand, the use of a portable handheld scanner as the ZEB1 tested in this research (and nowadays available in advanced releases as well as the many other portable solutions), can integrate from a terrestrial point of view, with a careful trajectory execution, the mapping of wide built heritage spaces with spatial complexity and rich geometric characterization. Portable MMS locally delivers for the tested dataset higher density than UAV 3D models at architectural scale detail (between 1:100-1:200). It demonstrates flexible and suitable usage to critical contexts and seems to be a promising approach for the rapid and accurate achievements of 3D data, with continuity of surface density thank to the absence of undercuts due to the single scans positions and the flexibility of trajectory performance. The answer to the initial question if proposed approaches implementation could be validated in specific operational contexts and if there is the possibility of sustainability of the data achievement and information extraction, it has been shown to be yes. The rapid mapping strategies, particularly for the in emergency areas, demonstrate to be efficient in their proposed pipelines and in the overall time-costs consuming balancing.

CONCLUSIONS AND FUTURE PERSPECTIVES

The technological innovation of geomatics applied methodologies shall increasingly investigate the open issues related to the heritage documentation and conservation toward the typical requirements derived by interdisciplinary approach. A great opportunity to encourage to the boosting dissemination into endorsed practices of conservation, management and intervention on built heritage is left open by the ongoing research. The overall efforts are thus devoted towards the built heritage and its own vulnerability scenarios by providing with the spatial data, the essential metric value of whatever representation of reality with tailored pipelines.

These new approaches can operatively support 3D reality-based reconstruction in order to weighing up the safety for the operator in the fieldwork and reduce the time exposure to danger, with new performing devices and high-resolution sensors.

New rapid mapping solutions can move into the direction of sustainability, i.e. data density selection, optimization and 3D models enrichment, to a tangible user-oriented practice, encouraging the ability to meet, for each context, the individual needs of the object and its surroundings. For each methodological approach, a crucial role is always played by the frameworks of suitability and validation practices to define terms usability and confidence level of geomatics-based geospatial products.

ACKNOWLEDGEMENTS

I would like to recognize my gratitude especially to my tutors Prof.ssa Nannina Spanò and Prof. Filiberto Chiabrando, my colleagues and my family too: with them I gathered experiences and I shared this precious path.

REFERENCES

- Aicardi, I., Chiabrando, F., Grasso, N., Lingua, A., Noardo, F., & Spanò, A. T. (2016). UAV photogrammetry with oblique images: first analysis on data acquisition and processing. *ISPRS - International Archives of the Photogrammetry, Remote Sensing and Spatial Information Sciences, XLII-B1*, 835–842. <https://doi.org/10.5194/isprsarchives-XLII-B1-835-2016>
- ASPRS. (2015). ASPRS Positional Accuracy Standards for Digital Geospatial Data. *Photogrammetric Engineering & Remote Sensing*, 81(3), 1–26. <https://doi.org/10.14358/PERS.81.3.A1-A26>
- Bastoner, P., Donadio, E., Chiabrando, F., & Spanò, A. T. (2014). Fusion of 3D models derived from TLS and image-based techniques for CH enhanced documentation. *ISPRS Annals of Photogrammetry, Remote Sensing and Spatial Information Sciences*, II-5, 73–80. <https://doi.org/10.5194/isprsannals-II-5-73-2014>
- Bellekens, B., Spruyt, V., & Weyn, M. (2014). A Survey of Rigid 3D Pointcloud Registration Algorithms. *AMBIENT 2014, The Fourth International Conference on Ambient Computing, Applications, Services and Technologies. 2014.*, (c), 8–13.
- Bitelli, G., Balletti, C., Brumana, R., Barazzetti, L., D'Urso, M. G., Rinaudo, F., & Tucci, G. (2017). Metric documentation of Cultural Heritage: research directions from the italian GAMHER project. *ISPRS - International Archives of the Photogrammetry, Remote Sensing and Spatial Information Sciences, XLII-2/W5*, 83–90. <https://doi.org/10.5194/isprs-archives-XLII-2-W5-83-2017>
- Boccardo, P. (2013). New perspectives in emergency mapping. *European Journal of Remote Sensing*, 46(1), 571–582. <https://doi.org/10.5721/EuJRS20134633>
- Boccardo, P., Chiabrando, F., Dutto, F., Tonolo, F., & Lingua, A. (2015). UAV Deployment Exercise for Mapping Purposes: Evaluation of Emergency Response Applications. *Sensors*, 15(7), 15717–15737. <https://doi.org/10.3390/s150715717>
- Boccardo, P., & Giulio Tonolo, F. (2015). Remote Sensing Role in Emergency Mapping for Disaster Response. In *Engineering Geology for Society and Territory - Volume 5* (pp. 17–24). Cham: Springer International Publishing. https://doi.org/10.1007/978-3-319-09048-1_3
- Bosse, M., Zlot, R., & Flick, P. (2012). Zebedee: Design of a Spring-Mounted 3-D Range Sensor with Application to Mobile Mapping. *IEEE Transactions on Robotics*, 28(5), 1104–1119. <https://doi.org/10.1109/TRO.2012.2200990>
- Brovelli, M. A., Cina, A., Crespi, M., Lingua, A., Manzano, A., & Garretti, L. (2009). *Ortoimmagini E Modelli Altimetrici a Grande Scala-Linee Guida*. (CISIS, Ed.).
- Calantropio, A., Patrucco, G., Sammartano, G., & Teppati Losè, L. (2017). Low-cost sensors for rapid mapping of cultural heritage: first tests using a COTS Steadycamera. *Applied Geomatics*, 1–10. <https://doi.org/10.1007/s12518-017-0199-6>
- Chiabrando, F., Di Lolli, A., Sammartano, G., Patrucco, G., Spanò, A. T., & Teppati Losè, L. (2017). Multitemporal 3D modelling for cultural heritage emergency during seismic events: Damage assessment of S. Agostino church in Amatrice (RI). *ISPRS Archives*, 42(5W1), 69–76. <https://doi.org/10.5194/isprs-Archives-XLII-5-W1-69-2017>
- Chiabrando, F., Di Pietra, V., Lingua, A., Maschio, P., Noardo, F., Sammartano, G., & Spanò, A. T. (2016). TLS models generation assisted By UAV survey. *ISPRS Archives*, 41(July), 413–420.
- Chiabrando, F., Lingua, A., Maschio, P., & Teppati Losè, L. (2017). The influence of flight planning and camera orientation in UAVs photogrammetry. a test in the area of Rocca San Silvestro (LI), Tuscany. *ISPRS - International Archives of the Photogrammetry, Remote Sensing and Spatial Information Sciences, XLII-2/W3*, 163–170. <https://doi.org/10.5194/isprs-archives-XLII-2-W3-163-2017>
- Chiabrando, F., Sammartano, G., & Spanò, A. T. (2017). A comparison among different optimization levels in 3D multi-sensor models. A test case in emergency context: 2016 Italian Earthquake. *ISPRS - International Archives of the Photogrammetry, Remote Sensing and Spatial Information Sciences, XLII-2/W3*(March), 155–162. <https://doi.org/10.5194/isprs-archives-XLII-2-W3-155-2017>
- Colomina, I., & Molina, P. (2014). Unmanned aerial systems for photogrammetry and remote sensing: A review. *ISPRS Journal of Photogrammetry and Remote Sensing*, 92, 79–97. <https://doi.org/10.1016/j.isprsjprs.2014.02.013>
- Di Giulio, R., Maietti, F., Piaia, E., Medici, M., Ferrari, F., & Turillazzi, B. (2017). Integrated data capturing requirements for 3D semantic modelling of cultural heritage: the INCEPTION protocol. *ISPRS - International Archives of the Photogrammetry, Remote Sensing and Spatial Information Sciences, XLII-2/W3*, 251–257. <https://doi.org/10.5194/isprs-archives-XLII-2-W3-251-2017>
- Duarte, D., Nex, F., Kerle, N., & Vosselman, G. (2017). Towards a more efficient detection of earthquake induced façade damages using oblique UAV imagery. *ISPRS - International Archives of the Photogrammetry, Remote Sensing and Spatial Information Sciences, XLII-2/W6*, 93–100. <https://doi.org/10.5194/isprs-archives-XLII-2-W6-93-2017>
- Eisenbeiß, H. (2009). *UAV Photogrammetry*. ETH Zurich - Institute of Geodesy and Photogrammetry. PhD thesis
- Emergency Mapping Guidelines*. (2015). # Working Paper Version 1 .0 – as of Decemb er 201 5 International Working Group on Satellite - based Emergency Mapping (IWG - SEM).
- Fernandez Galarreta, J., Kerle, N., & Gerke, M. (2015). UAV-based urban structural damage assessment using object-based image analysis and semantic reasoning. *Natural Hazards and Earth System Science*, 15(6), 1087–1101. <https://doi.org/10.5194/nhess-15-1087-2015>
- Gerke, M., & Kerle, N. (2011). Automatic structural seismic damage assessment with airborne oblique pictometry imagery. *Photogrammetric Engineering and Remote Sensing*, 77(9), 885–898. Retrieved from <https://research.utwente.nl/en/publications/automatic-structural-seismic-damage-assessment-with-airborne-obli>
- Grazzini, A., Chiabrando, F., Foti, S., Sammartano, G., & Spanò, A. (2019). A Multidisciplinary Study on the Seismic Vulnerability of St. Agostino Church in Amatrice following the 2016 Seismic Sequence. *International Journal of Architectural Heritage*, 0(0), 1–18. <https://doi.org/10.1080/15583058.2019.1575929>
- Grünthal, G. (1998). *European Macroseismic Scale 1998*. *European Center of Geodynamics and ...* (Vol. 15). Retrieved from <http://scholar.google.com/scholar?hl=en&btnG=Search&q=intitle:Europe an+Macroseismic+Scale+1998#0>
- Huang, H., Sun, G., Zhang, X., Hao, Y., Zhang, A., Ren, J., & Ma, H. (2019). Combined multiscale segmentation convolutional neural network for rapid damage mapping from postearthquake very high-resolution images. *Journal of Applied Remote Sensing*, 13(02), 1. <https://doi.org/10.1117/1.JRS.13.022007>
- ISO/IEC Guide 99:2007, & JCGM 200. (2007). International vocabulary of metrology — Basic and general concepts and associated terms (VIM).
- JCGM. (2008). JCGM 200:2008 International vocabulary of metrology — Basic and general concepts and associated terms (VIM) Vocabulaire international de métrologie — Concepts fondamentaux et généraux et termes associés (VIM). *International Organization for Standardization Geneva ISBN*, 3(Vim), 104. [https://doi.org/10.1016/0263-2241\(85\)90006-5](https://doi.org/10.1016/0263-2241(85)90006-5)
- Kerle, N. (2010). Satellite-based damage mapping following the 2006 Indonesia earthquake—How accurate was it? *International Journal of Applied Earth Observation and Geoinformation*, 12(6), 466–476. <https://doi.org/10.1016/j.jag.2010.07.004>
- Kioussi, A., Karoglou, M., Bakolas, A., & Moropoulou, A. (2012). Integrated Documentation Protocols Enabling Decision Making in Cultural Heritage Protection (pp. 211–220). Springer, Berlin, Heidelberg. https://doi.org/10.1007/978-3-642-34234-9_21
- Lague, D., Brodu, N., & Leroux, J. (2013). Accurate 3D comparison of complex topography with terrestrial laser scanner: Application to the Rangitikei canyon (N-Z). *ISPRS Journal of Photogrammetry and Remote Sensing*, 82 (2013), 10–26. <https://doi.org/10.1016/j.isprsjprs.2013.04.009>
- Lemoine, G., Corbane, C., Louvrier, C., & Kauffmann, M. (2013). Intercomparison and validation of building damage assessments based on post-Haiti 2010 earthquake imagery using multi-source reference data.

- Natural Hazards and Earth System Sciences Discussions*, 1(2), 1445–1486. <https://doi.org/10.5194/nhessd-1-1445-2013>
- Letellier, R., Schmid, W., LeBlanc, F., Eppich, R., & Cabbi, A. (2011). *Recording, documentation, and information management for the conservation of heritage places Guiding principles*. (Getty Conservation Institute, Ed.). Donhead Pub.
- Nikoohemat, S., Peter, M., Oude Elberink, S., & Vosselman, G. (2017). Exploiting Indoor Mobile Laser Scanner Trajectories for Semantic Interpretation of Point Clouds. *ISPRS Annals of Photogrammetry, Remote Sensing and Spatial Information Sciences*, IV-2/W4(September), 355–362. <https://doi.org/10.5194/isprs-annals-IV-2-W4-355-2017>
- Nocerino, E., Menna, F., Remondino, F., Toschi, I., & Rodríguez-González, P. (2017). Investigation of indoor and outdoor performance of two portable mobile mapping systems. In F. Remondino & M. R. Shortis (Eds.), *Videometrics, Range Imaging, and Applications XIV, edited, SPIE 2017* (p. 103320I). <https://doi.org/10.1117/12.2270761>
- Puente, I., González-Jorge, H., Martínez-Sánchez, J., & Arias, P. (2013). Review of mobile mapping and surveying technologies. *Measurement*, 46(7), 2127–2145. <https://doi.org/10.1016/j.measurement.2013.03.006>
- Ramos, M. M., & Remondino, F. (2015). Data fusion in Cultural Heritage: A Review. *ISPRS - International Archives of the Photogrammetry, Remote Sensing and Spatial Information Sciences*, XL-5/W7(5W7), 359–363. <https://doi.org/10.5194/isprsarchives-XL-5-W7-359-2015>
- Remondino, F. (2011). Heritage Recording and 3D Modeling with Photogrammetry and 3D Scanning. *Remote Sensing*, 3(12), 1104–1138. <https://doi.org/10.3390/rs3061104>
- Remondino, F., Spera, M. G., Nocerino, E., Menna, F., & Nex, F. (2014). State of the art in high density image matching. *The Photogrammetric Record*, 29(146), 144–166. <https://doi.org/10.1111/phor.12063>
- Sammartano, G., & Spanò, A. (2018). Point clouds by SLAM-based mobile mapping systems: accuracy and geometric content validation in multisensor survey and stand-alone acquisition. *Applied Geomatics*, 10(4), 317–339. <https://doi.org/10.1007/s12518-018-0221-7>
- Sammartano, G., & Spanò, A. T. (2016). DEM generation based on UAV photogrammetry data in critical areas. *GISTAM 2016 - Proceedings of the 2nd International Conference on Geographical Information Systems Theory, Applications and Management*, (Gistam), 92–98. <https://doi.org/10.5220/0005918400920098>
- Sammartano, G., & Spanò, A. T. (2017). High scale 3d modelling and orthophoto of curved masonries for a multipurpose representation, analysis and assessment. *International Archives of the Photogrammetry, Remote Sensing and Spatial Information Sciences - ISPRS Archives*, 42(5W1), 245–252. <https://doi.org/10.5194/isprs-Archives-XLII-5-W1-245-2017>
- Schweier, C., & Markus, M. (2004). Assessment of the search and rescue demand for individual buildings. In *13th WCEE - World Conference on Earthquake Engineering*. Vancouver, B.C., Canada.
- Søren Riisgaard, & Morten Rufus Blas. (2005). *SLAM for Dummies. A Tutorial Approach to Simultaneous Localization and Mapping*. MIT OCW. <https://doi.org/10.1017/S0025315400002526>
- Stylianidis, E., & Remondino, F. (2016). *3D Recording, Documentation and Management of Cultural Heritage*. (E. Stylianidis & F. Remondino, Eds.). Whittles Publishing.
- Tucci, G., Bonora, V., Conti, A., & Fiorini, L. (2017). Digital Workflow for the Acquisition and Elaboration of 3D Data in a Monumental Complex: the Fortress of Saint John the Baptist in Florence. *ISPRS - International Archives of the Photogrammetry, Remote Sensing and Spatial Information Sciences*, XLII-2/W5(September), 679–686. <https://doi.org/10.5194/isprs-archives-XLII-2-W5-679-2017>
- Vetrivel, A., Gerke, M., Kerle, N., Nex, F., & Vosselman, G. (2017). Disaster damage detection through synergistic use of deep learning and 3D point cloud features derived from very high resolution oblique aerial images, and multiple-kernel-learning. *ISPRS Journal of Photogrammetry and Remote Sensing*. <https://doi.org/10.1016/j.isprsjprs.2017.03.001>
- Waldhäusl, P., Ogleby, C. L., Lerma, J. L., & Georgopoulos, A. 3 x 3 rules for simple photogrammetric documentation of architecture (2013). Retrieved from <http://cipa.icomos.org>
- Westoby, M. J., Brasington, J., Glasser, N. F., Hambrey, M. J., & Reynolds, J. M. (2012). ‘Structure-from-Motion’ photogrammetry: A low-cost, effective tool for geoscience applications. *Geomorphology*, 179, 300–314. <https://doi.org/10.1016/J.GEOMORPH.2012.08.021>



Associazione **U**niversitari di **T**opografia **e** **C**artografia

Sezione Tematica 3 GIS e Remote Sensing

*

*Thematic Section 3
GIS and Remote Sensing*

VISIBILITY ANALYSES USING 3D URBAN MODELS GENERATED BY LOW-COST MULTI-SENSOR APPROACHES

N. Grasso ^{1,*}

¹ Politecnico di Torino, DIATI – Department of Environmental, Land and Infrastructure Engineering, Torino, Italy – nives.grasso@polito.it

KEY WORDS: Visibility analyses, Safety assessment, Mobile Mapping Systems, Low-cost sensors, Mass market, Close-range photogrammetry, Computer Vision, 3D models

ABSTRACT:

The conditions of visibility of a user moving through an outdoor or indoor environment affect his safety. In both environments it is fundamental to guarantee a sufficient visibility in order to avoid possible collisions. The available sight distance (ASD) is that part of the roadway ahead which is visible to the driver and should be of sufficient length to allow a vehicle to stop before colliding with a stationary object. For indoor environment, in particular for public buildings it is necessary to identify the easiest paths to follow in order to ensure a fast and efficient escape route in emergency cases. The ways in which a person is able to move within the environment are strongly influenced by the space he is able to see in front of himself and by the position of some objects. Today, the estimation of the ASD and the visible space are still carried out on digital terrain models (DTM) or 2D maps, without considering the effects of sight obstructions. The aim of this research work is to propose automatic methods for the visibility analysis, that take into account the dynamism of the individual and the environment. Since it is essential to have a 3D model on which to base the analyses, the first part of the research, will be focused on the investigation of rapid, flexible and low-cost survey methods for collecting 3D information of environment at different scales. A goal of this work is related to evaluate the possibility to realize and to use low-cost mobile mapping systems (MMSs) as an alternative for obtaining 3D information of urban infrastructure. The second part of the activities aimed at the development of automatic procedures to perform visibility analysis exploiting the obtained 3D model. Different tools for the visibility analysis and the estimation of the ASD from a driver's point of view were compiled and tested, taking into account the dynamicity of the movement. Finally, a procedure for quantitatively assessing the complexity of a known path to follow in emergency cases inside of public buildings was proposed.

1. INTRODUCTION

Attention to the urban environment has recently been further strengthened with the introduction of research programs called "Smart Cities". These programs aim at improving the quality of life of citizens through the use of innovative technologies in different fields. Among these, several studies are aimed at improving the safety of individuals moving within the urban infrastructure. Specifically, safety in environments, both outdoors and indoors, in which people and objects are in motion, must also be guaranteed through the satisfaction of the conditions of mutual visibility at the points where any conflict event could occur. Obviously, the problem of visibility verifications must be treated differently for outdoor and indoor environment, because the conditions of motion and the aspects that influence it are different.

In the urban road networks, the available sight distance (ASD) in front of the driver to detect possible conflicts with unexpected obstacles is fundamental for traffic safety. To reduce crashes and their worst consequences in terms of injuries and fatalities, road engineers are committed in protecting road users limiting vehicles' operating speeds and increasing the sight distances from the conflict points and/or potential obstacles along the driving path. According to standards and policies, the driver must have a visible space along his trajectory (ASD) (Figure 1) that she/he uses to control her/his vehicle, to avoid striking an unexpected object or other road users in the carriageway (Ministero delle Infrastrutture e Trasporti, 2001; AASHTO, 2011). The use of road design

software (RDS) is today limited to the road at the design stage and their analysis are typically conducted on two-dimensional maps or digital terrain models (DTM) at small scales.

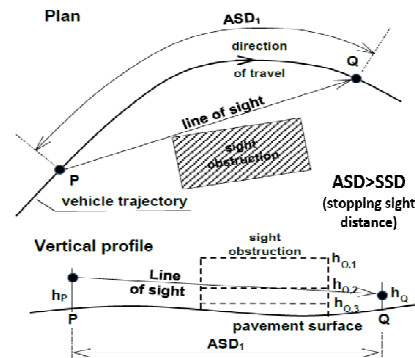


Figure 1. Estimation of the ASD along a road section with sight obstructions of different heights.

Unfortunately, the evaluation of ASD still represents an issue in the case of existing road, and the object of discussion in the research community. To avoid problems related to the limitation associated with the use of DTMs typically employed in RDS, the Geographic Information Systems (GIS) software can use digital surface models (DSM) which are more flexible in the modelling of sight obstruction due to vegetation, street furniture, and vertical surfaces largely diffused in urbanized areas. Above all because these verifications should take into

* Corresponding author

account a 3D model of the road infrastructure that also contains all the objects placed on the roadside.

In indoor environment, the situations that can affect the user's safety are those in which he finds himself walking in an environment of which he has little knowledge, such as a public building, at a sufficiently high speed, as can happen in emergency situations. On these occasions, it is important that the main escape routes are correctly signalized. In these situations, a large number of people must easily flow even in highly articulated environments. It is necessary to identify the easiest paths to follow in order to ensure a fast and efficient escape. The ways in which a person is able to move within the environment are strongly influenced by the space he is able to see in front of himself. The indoor geometry of buildings and the position of some objects can limit the visibility, affecting the perception of the paths through which it is possible to navigate. Different methods have been analyzed to identify the visible space from a certain point of view, by linking the user's perception with the surrounding environment, but only some have proposed methods to quantify how much is complex walking through it (Benedikt, 1979; Turner et al., 2001; Van Bilsen, 2008). However, many of these studies are aimed at a two-dimensional environment analysis, or do not take into account a possible dynamic configuration of the motion.

The literary review has shown not only a lack in visibility analysis procedures, specific to the cases described above, but has highlighted the need for large-scale 3D representations of the urban environment, on which apply these techniques and which take into account all the objects, static and dynamic, that characterize the environment and that have a role in these verifications. The main aim of this research is to develop automatic procedures to perform visibility analyses, both in outdoor and indoor environment.

To achieve this goal it is therefore necessary to realize 3D georeferenced representation of the environment with controlled accuracy for the application to the analyses of visibility. Methods and techniques of acquisition used to create a model of the environment depend on the type of detail required, the spatial extension of the area of interest and related applications. Nowadays, geomatics offers different solutions, methodologies and technologies for collecting 3D information and one of the main research topics in photogrammetry and computer vision is the 3D reconstruction of objects at different scales.

Indeed, three-dimensional representation is now carried out using techniques based on active or passive sensors. Active sensors such as laser scanners or structured light systems are commonly used to capture dense clouds and are set for their ease of use, speed of acquisition, and the ability to capture millions of points in a very limited time. On the other hand, the image-based approach has been recently developed thanks to the contribution of Computer Vision (Hartley, Zisserman, 2003; Remondino and El-Hakim, 2006; Goesele et al., 2006), which offers automatic procedures for image orientation (Remondino et al., 2014), and for the three-dimensional reconstruction of objects (Haala, 2013). Complex objects and scenes can be detected and reconstructed using sequences of images with very satisfactory results in terms of accuracy. In particular, dense image matching methods are increasingly used making the point cloud become fundamental in the process of survey and representation: given both by the laser scanning and the photogrammetric survey, it is the first result of a series of operations, but also intermediate data that leads to further processing and choices depending on the needs and purposes of the research. The raw data – the point cloud - is a real-world digital representation (defined by points) that can be archived and subsequently interpreted. The final products to represent the

environment could be orthophoto, three-dimensional meshes for surfaces or the most traditional 2D maps

In recent decades, many progress has been made in the study of sensors integration in mobile mapping systems (MMS). Since this research is focused on surveying and modeling the dense urban environment, there is a great interest in terrestrial MMS devices. These systems are equipped with a variety of sensors, such as laser scanners, multiple digital cameras, panoramic cameras, positioning sensors, such as GNSS receivers, odometers and inertial platforms, which are integrated and they require to be synchronized in time between them (Schwarz & El-Sheimy, 2004). The data collection is realized by onboard computers, which are connected to units for data storage. Given their large size and weight, MMSs are generally mounted on vehicles as van or car (Haala et al., 2008; Anguelov et al., 2010) and only some solutions were specifically designed to be mounted on bicycles or other mobile platforms (Kukko et al., 2012). However, the high price of these solutions, still represents a huge limit for public administration and the private sector.

Moreover, a faithful representation of the real urban environment must consider the continuous evolution to which it is subjected and therefore be repeatedly updated. In relation to these considerations emerges the need to guarantee the updating of the model through geospatial information measurement operations that can easily be repeated over time. In this regard, it could be advantageous to exploit acquisition tools and methods that limit the costs of updating activities, considering that generally the public administrations do not have large financial resources.

Taking into account the aspects related to the generation of urban 3D models, the second purpose of this work is to propose low-cost technologies for the acquisition of 3D data, flexible enough to be used in different contexts but which allow to obtain 3D models of the environment, with such accuracy that they can be used to perform visibility analysis.

For this reasons, the thesis covered the following:

- The proposal of low-cost technologies and methodologies to acquire 3D data and to generate 3D models of the urban environment, since the use of the existing MMSs is often limited due to their high costs and sizes, in order to use them as basis for the visibility analyses.
- The development of a tool for the ASD estimation that is able to analyze a 3DCM represented by surfaces, digital surface models or by point cloud.
- The proposal of a methodology for the assessment of the complexity of a path in a 3D indoor environment.

2. 3D DATA SURVEY TECHNIQUES

In the framework of this thesis, the acquisition of the three-dimension information related to the urban environment was one of the main topics, since it is essential to have an updated 3D model on which to base the visibility analyses. The first part of the research, was focused on the investigation of rapid and flexible survey methods, capable of adapting to different urban context.

The increasing development and improvement of new sensors, data capture approaches and multi-resolution 3D representation contributed significantly to the growth of research in 3D modelling. Today, it is possible to get three-dimensional information about the environment in the form of point clouds in a quick and easy way and at high levels of details thanks to the various types of existing sensors like Laser Imaging Detection and Ranging (LiDAR) or Red Green and Blue (RGB), Red-Green-Blue-Depth (RGB-D) sensors etc..

To correctly perform analysis on 3DCM, an updated 3D model of the environment is needed. The main advantage of using these technologies is that they can quickly get an accurate model of the environment. In fact, often the 2D maps available are not sufficient to describe all the features, over their relationship, in the space and, moreover, represent the area of interest to a design state, which, most of the time, do not match the "as built" conditions.

Besides, it is important to define which could be the best technique to acquire the 3D geometry of an object, by taking into account the model, as well as the function of the object itself in the analysis and the most suitable level of the detail. This implies that the achievable accuracy, reliability, and data density could be decisive to effectively survey the needed information, in particular for large representation scales.

Depending on the object of interest, it changes the way in which its geometry is acquired. Specifically, in the urban context, some objects have to be measured individually and manually modeled and inserted into 3DCM (e.g. urban furniture with particular shapes), which usually requires high costs of production. This research work was aimed at proposing an automatic procedure that enables to capture this data. In order to achieve more accurate and complete surveying results, it is crucial to be aware of the properties a certain technique needs to respond.

The techniques for 3D shape acquisition, which employ optical, mechanical and computerized instruments, are categorized with respect to the measurement principle they are based on and, most of the sensor used, can be distinguished in passive and active techniques:

- Photogrammetric techniques: aerial, satellite and close range (passive sensors);
- Laser scanner: aerial and terrestrial (active sensors);
- Classic survey (e.g. total station or GPS)
- Hybrid: a combination of the previous.

Passive sensors use radiometric information contained as intensity measure in 2D image pixels. Using different strategies, including stereo matching and the structure from motion approaches, it is possible to reconstruct three-dimensional point clouds from these intensity images. This procedure requires at least two images to derive 3D data. The increasing automation of image matching algorithms, the ability to align and orient a huge number of unordered images, also deriving from different camera devices (Goesele et al. 2006; Hartmann et al., 2016) and the great potential, as well as the spread of these sensors in the mass-market, have increased the use of passive sensors in different projects. The advantage of using these techniques lies in the fact that, given the limited size of imaging sensors, these are embedded in commonly used devices such as smartphones and tablets. Potentially, anyone can access the data acquisition and extraction of 3D information. If in the past image-based sensors were used primarily for the survey of single-object with regular geometric shapes (Remondino, 2010), their development and the possibility to mount them on image acquisition platforms (aerial and terrestrial), they are considered a good solution for the acquisition of 3D geometry of the urban realities. Nevertheless, the complete automation of the process is still an open issue, as the user interaction is still necessary not only for the 3D surveying, but also in the georeferencing and, above all, for the quality control part (Remondino, 2010).

Scanning devices that emit a signal and record information from scene observation are known as active sensors or range sensors (Remondino, 2010). Depending on the type of sensor, it varies the type of the emitted signal; in fact, these instruments are able to actively manipulate the scene through the emission of a

coded structured light pattern in the visible or infrared spectrum or through electromagnetic radiation in the form of a modulated laser light (Weinmann, 2016). The first group of these sensors comprises scanning devices which emit a signal in the form of a coded structured light pattern in the visible or infrared spectrum, manipulating the illumination of the scene. The projected pattern is captured by a camera, which allows the generation of synthetic images of the scene by a codification of the pattern. The principle of this procedure is to extract the 3D surface shape based on the information from the distortion of the projected structured-light pattern, caused by non-planar surfaces. The 3D coordinates of the objects are subsequently recovered by triangulation algorithms. The second group of scanning devices exploits Time-of-Flight (TOF) or phase measurement. Generally, such devices are categorized with respect to modulation technique, measurement principle, detection technique or configuration between emitting and receiving components. These sensors analyze the backscattered signal of the emitted laser light, which is partially reflected by the object surface. Amplitude, frequency, polarization, time and phase are the properties of the signal which are measured and analyzed to extract the 3D information. If in the past the laser scanner cost was quite high and they were also quite bulky, today it is possible to find cheaper and smaller solutions, such as profiler (linear laser scanner), in which the rotation of the device occurs around a single rotation axis, providing measurements on a 1D scan grid (Bassani et al. 2015) and handheld laser scanner devices (Sirmacek et al. 2016). However, to correctly employ active sensors, it is required some expertise based on knowledge of the characteristics of each different technology at the desired range. Moreover, the resulting raw data must be further filtered and edited. Finally, most of these systems focus only on the acquisition of the 3D geometry, providing only a monochrome intensity value for each range value and need to be combined with passive sensors to obtain chromatic information of the surface.

The georeferencing of the model is needed to locate the model in a defined reference system, to give a metric value to the products and to spatially relate it with other objects or sites. The registration of a laser scanner point cloud is performed through a first manual or automatic alignment using markers or natural points; then a global registration is done through procedures based on iterative closest points or least square method. A similar procedure can be applied for the georeferencing of image point clouds. Measured targets can be identified in the images as reference to orient the point cloud. A procedure to directly orient a photogrammetric point cloud (direct photogrammetry) is used to simultaneously measure the coordinates of image acquisition center or the range sensor position and, in some cases, the device asset, while the data is acquired, by combining these sensors with GNSS/INS sensors. In the geomatics field discussions are still opened on which is the more suitable technique to use for 3D modeling purposes, but one of the answers to this issue could be the combination of different strategies and the integration of data deriving from different sensors (Remondino 2010), especially when surveying a complex site as an urban area.

The methodology that integrates into a common platform digital imaging, active electronic sensors, often with multi-spectral capabilities, with direct geo-referencing tools, GNSS and IMU, is defined as digital mobile mapping (Schwarz & El-Sheimy, 2004). Specifically, about images, this procedure can provide the exterior orientation parameters (position and orientation of the frame) directly by independent measurements, without the use of further GCPs or block adjustment procedures. The positioning information, in general, can be obtained by GNSS

technique in real time through differential positioning methodology. These considerations are not always valid when the area of interest is an urban canyon or, in e.g., a tunnel, where the GNSS does not work. In these situations, the easiest solution is to integrate GNSS sensors with odometer, to measure distances, associated with an orientation sensor, such as magnetic compass, or by using in combination an IMU platform. The simultaneous acquisition of GNSS/IMU information carry out further advantage to the definition of the position and in the determination of the exterior camera parameters in real-time, allowing a real-time georeferencing.

The MMS approach guarantees to acquire a great amount of data and 3D information in a fast way, with accuracy which depend on the chosen sensors but which can reach millimeter order. The use of specific sensors and technique, the a-priori calibration of the sensors would allow a real-time processing of the data, but, to this purpose, the relative position of the devices, the definition of a reference system and a correct time synchronization between them are not negligible. The system cost is a great limit of this approach: costs depend above all on the choice of the sensors and hardware for the management, but also the choice of vehicle to be equipped has a significant impact. Mobile systems are generally implemented on machines and aerial vehicles; however, technological development in recent years has also led to a decrease in the size of these devices, enabling them to be installed even on smaller platforms such as small UAVs or bicycles. Different mobile platforms equipped with sophisticated and expensive sensors were already proposed in many research studies (Haala et al., 2008) and many solutions which include all the sensors connected between them are sold on the market (Optech Lynx, Riegl VMX-1HA, Leica Pegasus 2, etc.). Today, the images sensors have reached such a smaller dimension to be implemented even in smaller and mass-market devices, such as smartphones, without losing quality and performance in terms of resolutions.

With respect to one of the aims of this research work, there is no interest in an aerial data acquisition, as only the features visible from the ground, at eye level, are subjects of interest.

Another great disadvantage of many of many MMSs, is the needs of specific and technologically advanced instruments, which are still very expensive (e.g. terrestrial laser scanner or complete mobile mapping systems); this issue can be translated in a huge limit for the public administration or anyone is in charge to acquire the data. In fact, although it is essential to have up-to-date maps and models, to use them as decision support for urban planning and management, it is not always possible to address the costs involved in these operations.

Starting from these considerations, the aim of the work was to propose an alternative approach to the acquisition of the geometrical information using, instead of the classical technologies, low-cost and mass-market solutions of the same sensors. The instruments taken into account in this research needs to respond to the following requirements: low-cost, able to acquire high-quality data, small dimensions to be mounted both on car or bicycle, easy-to-use, flexible, in order to guarantee the system operation in different conditions (indoor/outdoor environments, lights variations, speed variations etc.).

Among the various sensors that can be integrated into an MMS, the positioning sensors are of great importance. The great development of these sensors has allowed today to greatly reduce sizes and costs, bringing them into the mass-market application. Taking into account the need of acquiring data both in indoor and outdoor to estimate the position with high accuracy a combination of u-blox EVK M8T GNSS receiver

and an IMU platform Microstrain 3DM-GX3[®]-35 was chosen. In this research work, further analysis to evaluate the real performances of these sensors were not performed, but we referred to previous studies existing in the literature (Daboue & Manzino, 2014).

Nowadays, the market of digital cameras offers different solutions and, due to the small size of the image sensors, are now widely available compact solutions. For this study different non-conventional devices were selected: a camera “card” Raspberry Camera Module v2, a medium range webcam Logitech HD Pro Webcam C920, an action cam a Garmin Virb Elite, equipped with wireless connection, GPS, compass, altimeter, and accelerometer, which can be itself considered a MMS, and a spherical camera NCTech iSTAR (Table 1).

	Raspberry Pi Camera Module v2	Logitech HD Pro Webcam C920	Garmin VIRB Elite		NCTech iSTAR
Type	Digital camera	Webcam	Action-cam	Number of cameras	4
Sensor	CMOS Sony IMX219	5.14x3.5mm CMOS	1/2.3" CMOS	Sensor	CMOS
Lenses	Plane	Plane	Wideangle	Lenses	Fish-eye
Focal length [mm]	3.04	3.67	-	Single images resolution (pixel)	2748x2664 (single shot)
Max image resolution (pixel)	3280 x 2464	1920 x 1080	4664x3496	Spherical image resolution (max) (pixel)	1374x1832 (video mode) (2fps)
Max video resolution (pixel)	1920 x 1080 (30 fps)	1920 x 1080 (30 fps)	1920 x 1080 (30 fps)	Spherical FOV	5656x2828 pixel (15 Mp) (2fps)
Frame rate [fps]	on	-	120	Focal length	300° x 137° +/- 5°
GPS	No	No	Yes	Weight	2,67 mm
Storage	External	External	Internal	Dimension	120 x 120 x 120 mm
Dimension [mm]	23.85 x 25 x 9	94 x 71 x 43	32 x 53 x 111	Price	1.4Kg
Weight	3.4g	796 g	236 g		6.400 €
Price	25 €	80 €	259 €		

Table 1. Selected imaging sensors.

2.1 Imaging sensors calibration

Since the adopted imaging sensors were not realized for photogrammetric purposes, it was necessary to estimate their interior orientation parameters. Specifically, these cameras are subjected to strong distortions, above all the action cam and the spherical camera, which mount wide-angle optics. To this purpose, it has been considered necessary to conduct several calibration tests with various software and methodologies, since good camera calibration is a prerequisite for obtaining accurate products. The results obtained using the Matlab tool *Camera Calibrator*, the *Calib 3V* software, designed in the Laboratory of Photogrammetry of the University IUAV of Venice, and Agisoft Photoscan Professional were than compared for each sensor. The calibration procedures have been conducted according to the sensors configurations (image or video), which would then be set during campaign acquisitions. The conducted tests have demonstrated in particular that it is not possible to obtain stable parameters that describe the internal orientation of the employed devices. Each software has, in fact, calculated different values and, sometimes, are not even coherent between them. Anyhow, the radial distortion coefficient values, estimate for the cameras taken into account, are in general very high and not negligible in a traditional application of photogrammetric measurement, due to they can cause significant distortion to the images. The parameters calculated by the Matlab Camera Calibration Tool have been used as initial approximate parameters for processing data acquired in the test and campaign phases, as they have been shown to be the most stable after having repeated the tests on the calibration also with different datasets of images.

2.2 Sensors synchronization for integrated acquisition

The management of information from sensors involves the acquisition and archiving of data. Generally, digital cameras and action cams are “independent” systems and have their own memory card for the data storage, but this is not the case of

webcams or Raspberry Pi Camera Module, which need to be powered and managed by a computer, also used for archiving data. In the next paragraphs two solutions designed in order to synchronize in time these devices with the GNSS receiver for georeferenced data acquisition will be described.

BEAtool. With the aim of acquiring multiple data from an MMS, a dedicated application called BEAtool for images acquisition through the webcams and their synchronization with the GNSS/INS platform was realized in collaboration with the Bea s.r.l.¹ company. The application was specifically developed to manage different sensors mounted on a car. The acquisition software is composed of two modules: one that manages a GPS receiver and another that uses the high-resolution webcam to acquire synchronized and georeferenced images. The target chosen for the development of the prototype was a mobile PC, but the tool can be eventually implemented on cheap mini-computer. The software was written in Java and uses the open source libraries. The software module called *ubloxLogger*, which manages the GPS, stores the position information, the reference UTC time and the reference to the RAW format useful for post-processing position information provided by the receiver. The second module called *webcam* can be used to acquire images in sequence at a defined frame rate. The software is able to manage at the same time one or more webcams and it is realized to optimize the simultaneity of frames taken by the webcams in the established shooting instants. On the chosen folder are saved only the pictures and a log file, which correlates the pictures with the PC clock timestamps. As both the *ubloxlogger* and *webcam* applications are executed on the same PC, the PC clock timestamp, can be used to georeference the acquired images positions interpolating the values written in U-blox log file. The webcam tool uses the Open Source OpenCV library for the management of the webcams and of the images.

The real performances of the BEAtool in presence of one or more webcams were evaluated by some dedicated tests, in order to verify the number of frames acquired every second with respect to the value established during the setting phase and if this property can be maintained by varying the number of webcams and the images resolution. Subsequently, it was necessary to verify the performance of the software with a long-term test to simulate a real acquisition with the sensors and to evaluate, in addition to the prolonged operation in time of the program, also the volume of data generated and the stability of the set frame rate.

RPiBike. The need to mount the sensors on a bicycle required the realization of a more compact system for sensors management than a PC. An acquisition system consisting of two RaspiCAM v2, connected respectively to two Raspberry Pi, was realized; the system also included a u-blox EVK M8T GNSS receiver and a Microstrain 3DM-GX3[®]-35 IMU platform for direct image georeferencing. Lastly, the Hokuyo UTM-30LX Laser Scanner profilometer can also be connected to the system to acquire georeferenced 3D point clouds of the environment. It was designed as an automatic system which implies that all the sensors connected to it start automatically without any further command. A power bank is employed to power both Raspberry Pi systems and guarantees 15 hours of work.

Two RaspiCAM have 8 MP (3280 × 2464 pixel) of resolution and they can be set up to 60 frames per second for low-resolution images (640 × 480 pixel). The system allows

employing both the RGB or NIR version. An app in python was developed to control and capture images with both cameras and save them with a GPS timestamp automatically, to enable the integration between images and other sensors data. As no applications were available for Linux system for the management of data acquisition from the IMU sensor, a new application has been developed in the Python programming language. Then, the IMU was set in order to collect both GPS timestamp and its internal timestamp. RTKRCV and STR2STR are the two AP's from RTKLIB used in this system to get real time GNSS position and store raw data for post-processing. The correction from an external server can also be collected with this software by using TCP/IP, NTRIP, local log file and FTP/HTTP protocols. STR2STR takes raw data from the receiver and divides it into two streams. One stream is saved to a file in .ubx format to be processed later after applying corrections downloaded from nearest permanent base station. The other data stream is given to RTKRCV, which performs real-time positioning after applying corrections taken from SPIN GNSS network through NTRIP protocol.

The system was tested with static mode for two baselines: zero baseline and 100 meters baseline with known coordinates. The accuracy of real-time position was up to millimetre level on North and East coordinates whereas up to centimetre level for height coordinate. An open source software, ExifTool, was installed on the RPi system to geotag all collected images from the RGB and NIR cameras. The software supports many formats and in this work, positioning data in the NMEA format were compared to the time stamp of the images to geotag them.

3. GENERATION OF 3D MODELS USING A LOW-COST MULTI-SENSOR APPROACH

After having analyzed and studied the characteristics and behavior of many components of the mobile mapping systems employed, the performances and drawbacks of different configurations of this multi-sensor approach were evaluated. The systems for the acquisition of three-dimensional data have been tested.

A series of tests will be examined, in which the whole acquisition system proposed in this research was analysed. The survey campaigns were carried out with multiple configurations of low-cost MMS. Different areas diffused in the city of Turin, have been chosen as case studies. Such places have been generally, selected according to the poor visibility conditions that characterize the road infrastructure, as the idea was to exploit these 3D models to carry out road safety analysis. All the acquired imaging data were processed with the software Agisoft Photoscan Professional as it meets one of the requirements of this thesis, that is, being simple to use and intuitive with respect to other photogrammetric software. The software, indeed, ensures to get the good results even through an "automatic" photogrammetry, but at the same time allows the operator greater control of operations and therefore greater accuracy of the results.

For the orientation of the datasets through bundle block adjustment and to improve the positioning solution obtained through the GNSS receivers, GCPs, spread over the areas were measured with topographic instruments.

Many of the results obtained from each case study will be compared with those produced by laser scanning systems to test the accuracy achieved through the low-cost system proposed in this research. In cases where the study area was too large to acquire a LiDAR model, topographically measured check points were used to evaluate the accuracy of the results.

¹ <http://www.beanet.it/index.html>

Data elaborations and analyses were conducted using a computer *hp EliteBook*, mounting a processor Intel® Core™ i7-4600U CPU 2.1 GHz-2.7 GHz, with Ram of 16GB and an architecture of 64 bit; to which all the processing time are referred.

Since it is not possible to describe in deeper all the tests conducted, in Table 2 are summarized the various cases of study, the followed approaches, the used platforms, the involved sensors and synchronization tools.

Pedestrian surveys	Bicycle survey
<ul style="list-style-type: none"> Roundabout in Lungo Dora Siena (TO) - 1 Garmin Virb Elite action cam 	<ul style="list-style-type: none"> Campidoglio District (TO) (Cargo bike) – 500m - BEAtool: 2 Webcam Logitech 920C HD + 1 U-blox LVK M8T
<ul style="list-style-type: none"> Laboratory of Geomatics (POLITO) (static) 1 NCTech iStar panoramic camera 	<ul style="list-style-type: none"> 1 Microstrain 3DM-GX3 1 NCTech iStar spherical camera
<ul style="list-style-type: none"> Aisles of POLITO – (dynamic) 1 NCTech iStar panoramic camera 	<ul style="list-style-type: none"> 1 Raspberry Pi Camera module 1 PC
<ul style="list-style-type: none"> Van survey C.so Castelfidardo (TO) – 500m - 1 Garmin Virb Elite action cam (GNSS integrated) - BEAtool: 2 Webcam Logitech 920C HD + 1 U-blox EVK M8T - 1 Microstrain 3DM-GX3 - 1 PC 	<ul style="list-style-type: none"> Crocetta District (TO) - 1000m RpiBike tool: 2 Raspberry Pi Camera Module v2 (RaspiCAM) RGB/NIR, 1 Microstrain 3DM GX3* 35, 1 u-blox EVK M8T, 1 Hokuyo UTM-30LX

Table 2. Tests conducted with the proposed integrated systems.

Table 3 shows the results obtained from the data processing. Since, for each acquisition tests datasets deriving from different devices have been processed separately from each other, all the resulting accuracies were reported.

Case study	Area characteristics	N. Control points	N. Check points	Total accuracy on check points [m]	Image pre-processing time	Image processing time	Filtering operation
Pedestrian survey – Garmin Virb	Area of 1600m ²	7	5	0,017	30 min	8 h	5 min
Pedestrian survey – 360° - static	Area of 50m ²	14	6	0,0045 – 0,0073	30 min	3h – 2,5h	30 min for each dataset
Pedestrian survey – 360° - dynamic	Aisle of 150x4m	10	5	0,06 – 0,085	30 min for each dataset	6h for each dataset	30 min for each dataset
Van survey	Four carriageways of 500m (2000m in total)	30	12	0,295	2 h for each dataset	7 days for each dataset	30 min for each dataset
Cargo bike surveys	500m roadway	18	8	0,41 – 0,258 – 0,139 – 0,109	30 min for each dataset	4 – 2 – 5 – 5 days	c.a 1 h for each dataset
Bicycle survey	1000m roadway	13	7	0,187	-	5 days	30 min

Table 3. Summary of the results obtained from each case study.

Discussion: The various surveys, tests and case studies analyzed during this part of the research have shown how the combined use of MMS, realized with Low-cost devices, and SfM software now offers more than acceptable results for medium scale (1: 500-1000). Indeed, generally, it is possible to obtain results with accuracies which varies between 10 and 25 cm. Of course, these performances are still quite far from those obtained with high-end instruments, but, if the purpose is to exploit these models to analyze the visibility along the road infrastructure in the urban environment, this is a big step forward. Today the analyses related to the ASD are conducted on existing two-dimensional maps in scale 1:10000-5000 or by employing DEMs with a grid of 20-50 meters, therefore, the proposed methodology could give a great improvement to these operations.

One of the issues that most affect the accuracy of the generated model is the estimation of calibration parameters by SfM software. In the various case studies, the internal orientation parameters were imported as approximate initial parameters to facilitate alignment of the images. However, these are

subsequently recalculated from the software and, for the same camera, the result varies slightly from one case study to another. This problem is certainly attributable to the mobile mapping system acquisition procedures described in this research, which do not guarantee an optimum acquisition geometry for calibration and, therefore, the accuracy is not guaranteed. From the tests performed on the panoramic camera NCTech iSTAR Fusion it also emerged that a correct estimation of the calibration parameters is crucial for the generation of spherical images from the plane ones and to, subsequently, use these products for the realization of metrically correct 3D models.

The problem of the acquisition geometry also affects the noise of the final point cloud (Figure 2). In fact, it should be remembered that major distortions are always at the margins of the frames, which for this type of acquisition represent the areas from which to extract more information about the urban environment. In order to overcome this limit, in addition to assessing the correct frame rate to ensure sufficient overlap between the frames, it is advisable to exploit a system that integrates two or more image sensors, maybe converging to each other.



Figure 2. The dense point cloud representation of Corso Castelfidardo obtained by merging the **Garmin Virb** and the **Logitech** point clouds.

Not only the acquisition geometry but also the environment in which the surveys were conducted, influenced the results obtained. In particular, the reflective and glazed surfaces, the uniform texture of the walls and the pavement, the presence of people and moving objects such as cars and areas of dense vegetation have contributed to the noise of point clouds. In general, these aspects that characterize the urban environment do not allow a correct estimate of the matching points between the images, influencing the calculation of the alignment of the same. In order to improve the process of bundle block adjustment and facilitate the correct alignment of the images, control points have been inserted. These points, topographically measured, were also used to georeference 3D models in the UTM WGS84 32N reference system.

A limit to these low-cost mobile mapping systems is still the positioning issue. Although it was not among the purposes of this research, some tests have been carried out to assess the possibility of directly estimating the external orientation of the frames and in real-time in order to favor the automatic generation of the georeferenced 3D model. The proposed tools, **BEAtool** and **RpiBike**, allow to synchronize the various sensors between them (imaging and positioning sensors) and to include in the EXIF file the information about their orientation. However, low-cost positioning sensors, both GNSS and IMU, do not allow the acquisition of data with such level of accuracy that can be used for the correct alignment of the photogrammetric block.

In the case studies analyzed, in order to georeferencing point clouds, it was necessary to take advantage of some control points of known coordinate. This required the implementation of specific topographic surveys to achieve these measures. However, as shown in Table 3, it should be noted that the

number of points used to improve the bundle block adjustment and georeferencing the models has always been rather limited (considering the dimensions of the study areas) and the surveys campaigns for the measurements of the points required a very limited time, less than an hour. In conclusion, it is noted that point clouds obtained with these technologies are quite noisy and require subsequent filtering operations. Just because of this noise it is difficult to evaluate their consistency with LiDAR reference models. In addition, these products are often characterized by numerous holes related to shadow areas. In fact, imaging sensors have generally been placed at limited heights (from 0.70 to 1.70 m) and their field of view was obstructed by moving objects or roadside elements. However, the main purpose of this research was to get information about objects on the sides of the road infrastructure, which in fact are well described within the dense point clouds obtained (Figure 2).

4. PROCEDURES FOR 3D VISIBILITY ANALYSIS

The most popular method to analyze the visibility is to trace the line of sight (LOS) between observer and target, in order to find the potential obstruction between them (González-Jorge et al., 2016). This concept is already analyzed by some simulation models to assess whether there are obstructions between nodes interconnections on the grid (Pelechano and Malkawi 2008). However, in a 3D environment, these simulation models do not allow to perform the analysis directly on the point cloud but can be applied only to multipatch surfaces or elevation models. This research work, indeed, attempts to analyze environments represented by a three-dimensional point cloud, because this is the raw data, which does not require further processing to be analysed. Starting from these principles, many works attempted to verify the visibility directly on points clouds (Alsadik et al., 2014, Peters et al. 2015): different algorithms were proposed, but was demonstrated that they are not efficient in case of sparse and noisy point clouds and they do not take into account the dynamicity of the motion.

4.1 Available Sight Distance estimation on urban roads: preliminary tests

Preliminary tests on the estimation of the ASD explored the problems encountered in the formation of a 3D model of an urban road section used here as a case study. Sight obstructions were surveyed and included in a DSM already available in the GIS environment. Vehicle trajectories and the positioning of drivers' LOSs were first reconstructed and then used to calculate the ASD from the driver's point of view: the information was then used to generate sight profiles.

The aim here was to assess how effective GIS, numerical computing software and related tools for sight analysis were when estimating the ASD. It is worth noting that an estimation of the ASD from virtual 3D models leads to a dramatic reduction in the costs and risks involved, and sometimes the time required when compared to the direct survey of this parameter in the field. To this purpose, two algorithms were developed, which are able to operate automatically on a GIS platform and in a numerical computing environment; these algorithms have been tested and the final results compared in terms of computational effort, time, and accuracy.

The case study used for the development of the first two ASD evaluation methodologies was a section of Corso Castelfidardo in Turin, surveyed as case study for the test of the MMS mounted on the van.

The first step of the project regarded the integration of digital maps and digital surface models to build realistic DSM models. To build an initial prototype of the 3D model, a basic 2D model was generated by integrating the cartographic data (the technical map), the colored orthophoto and the DTM into a commercial GIS platform. This basic model was then integrated with objects along or near the road path through analysis of the orthophoto. Horizontal markings were added to the model using aerial images and the stereoscopic model.

Figure 3 shows how the ASD was estimated with the 3D model. The driving path, assumed to be in the center of the lane, which is discretized into several observation points (P point in Figure 3) placed at 1.1 m above the road surface in accordance with Italian standards. On the same driving path, the target points (Q_1, \dots, Q_i) are spaced with the interval "s" in front of the P point and initially located 0.10 m above the pavement surface. The Q_i points are connected by line of sight to the observation point P, following a step by step procedure that generates the sequence of lines PQ_1, PQ_2, \dots, PQ_i . The algorithm for the ASD estimation identifies the first point (Q_{i+1}), which is obscured by a sight obstruction in the DSM, and then the ASD was calculated as the difference in station between points Q_i and P. Figure 3 illustrates how the algorithm works on a few points Q_i along the trajectory of the case study investigated.

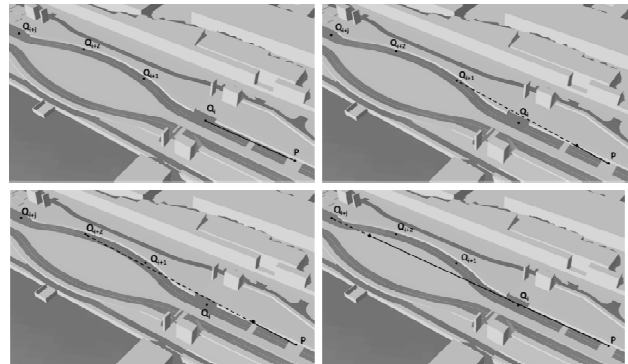


Figure 3. 3D representation of the algorithm used for estimating the ASD (the continuous line represents the visible part of the line of sight, while the dashed one is the portion blinded by the sight obstruction).

In the GIS platform, the ASD Toolbox was built ad hoc to perform the ASD analysis using the ModelBuilder® application (Figure 4). The first instruction used in the ASD Toolbox is the "Construct Sight Line", which connects the observer with all the following targets. The "Sight lines" are the outputs, which become the input of the "Line of Sight". The outputs of this second process are (a) the lines of visibility, which are continuous for the part visible to the observer, and dashed if hidden by an obstruction. Each line of sight is associated with the station of the obstacle it is connected to. The coordinates of the point where the line touches the obstruction constitute the second output of the "Line of Sight" tool. The instruction "Add XY Coordinates" returns the 3D coordinates of such points. Once the station of the last visible point has been identified, it is subtracted from the station of the observation point and the ASD is then estimated.

A similar algorithm was adopted in Matlab® using the instruction called "los2", which computes the mutual visibility between two points on a DSM (this tool will be subsequently called M_ASD1). This instruction was included in a proprietary code to manage the trajectories of the observer and the target in the DSM. It automatically generates both the "line of vision"

between the points and the graph of the surface, and also calculates the coordinates of the obstruction.

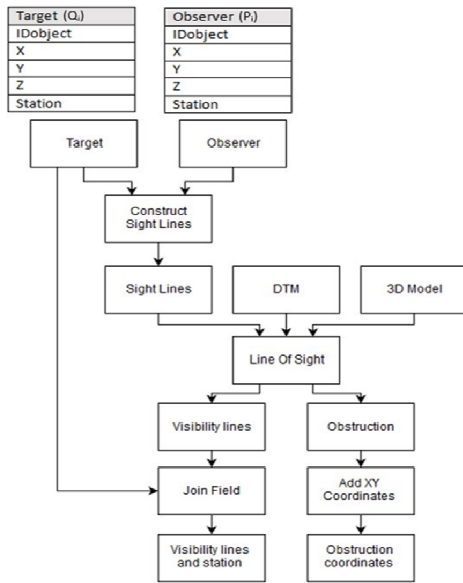


Figure 4. Workflow of the ASD Toolbox built with ModelBuilder®.

The code M_ASD1 in Figure 5 requires input data to start the process, which in this case were the DSM and the spreadsheet containing the coordinates of the points forming the trajectories of the observer and the target.

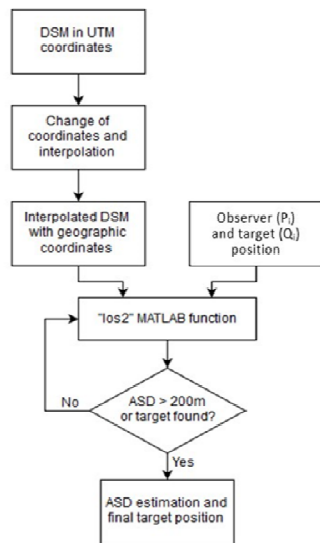


Figure 5. Workflow of the M_ASD1 tool in the numerical computing environment.

The code was designed to allow the user to select data and to immediately execute the coordinate transformation of the trajectory points. An iterative procedure performs the sight analysis for each pair of observer (P) - target (Q_i) points. The ASD was estimated by assuming a maximum distance P_{Q_i} of 200 m, which is greater than the maximum possible values of SSD for vehicles traveling below the speed limits on urban roads. If an obstruction is detected at a distance of less than 200 m, the loop stops and the ASD is calculated as the difference between the station of the last visible target and the observation point; otherwise, the value of 200 m is assigned to the ASD. This procedure was also adopted to limit the processing time.

The loop then restarts and passes to an analysis of the following observation point. At the end of the process, the system automatically generates a new spreadsheet with the ASD results.

Result and discussion. Figure 6 includes an estimate of the ASD using ArcGIS® with the target set at a height of 10 and then 30 cm, and the SSD estimated as a function of driver speed behaviour as per the Italian standard.

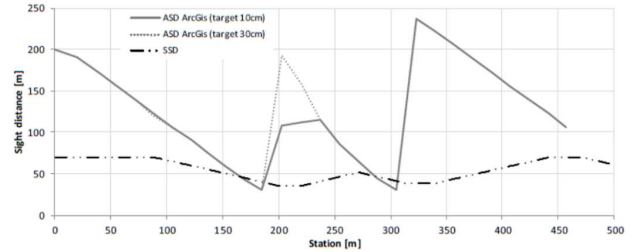


Figure 6. Comparison between SSD and ASD estimated at 10 cm and 30 cm in accordance with the ArcGIS® code.

A comparison between the SSD and the ASD confirms the limitation in driver visibility in the case of possible emergency stop manoeuvres. A comparison between the two solutions obtained for different target heights illustrates the effects of the vertical profile, which presents a significant convexity at the stations 300 – 400 m. The graph in Figure 6 confirms that at station 203 m, the farthest target set at 10 cm above the pavement surface is visible at a distance of 108 m, while when it is set at 30 cm the driver can see it at a distance of 193 m.

Figure 7 reports the results of the ASD estimated in ArcGIS® and Matlab® with the target height set at 10 cm, and the Matlab® solutions at 15, 20, and 30 cm.

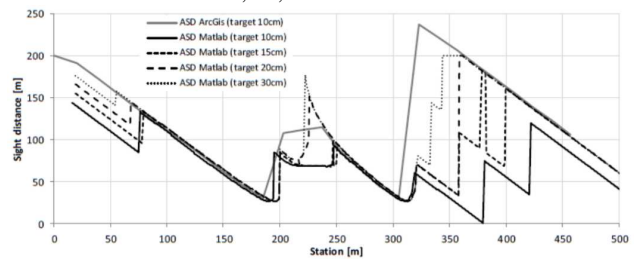


Figure 7. Comparison between ASD estimated with ArcGIS® and Matlab® at 10 cm, and the variation in Matlab® solutions at 15, 20 and 30 cm.

The graph shows that as the height increases, the ASD curves estimated with Matlab® tend to rise and become closer to the GIS solution. This is because if the target is placed at a greater height to the pavement, the probability of an intersection between the line of sight and the paved surface decreases, with results that may change in much the same way as was previously discussed for the ArcGIS® solution. Local differences visible around the station at 225 m depend on the different spacing that was adopted for the GIS (around 20 m) and the Matlab® (< 1 m) analyses.

Figure 7 highlights the discrepancies between the ArcGIS® and Matlab® solutions, which can be attributed to several factors. The DSM used in this investigation had an accuracy of 15 cm with respect to the 3D model which is 5 cm greater than the height of the target set at 10 cm. Local irregularities of the paved surface, detectable in Figure 6 between stations 200 and 400 m, also obscure the target point and lead to significant variations in ASD values. The two “line of sight” instructions are based on different algorithms, which analyzes different kind of surfaces. ArcGIS® uses the Multi-Patch geometry

(proprietary format), while Matlab® uses an unknown internal function (“los2”) that cannot be opened or controlled by the operator. It is worth noting once again that small differences between two surfaces and the trajectories of the observer and target may lead to very great differences between the two estimates.

4.2 ASD estimation on a point cloud

In order to speed up the generation of the 3D model of the urban infrastructure, to maintain the accuracy of the acquired data and, also, to improve the accuracy of the ASD estimation it was decided to evaluate the possibility of using directly the raw data extracted from the MMS surveys, the three-dimensional point cloud of the environment as input data for the ASD computation. The case study chosen to perform the analysis was, again, Corso Castelfidardo (Turin), of which it was built the dense point cloud after the van surveys. The criticalities of this route are similar to those described in the previous case, namely the parked cars on the roadside that can limit the visibility of the driver as well as the presence of various roadside objects. In addition, in the middle of this road section, the ASD is significantly restricted by an alignment inflection due to a roundabout characterized by high vegetation, which may interfere with visibility. To test the proposed methodology, it was decided to employ the point cloud realized merging the solution obtained by Garmin action-cam and webcams for its greater density with respect to the other.

The new algorithm for the ASD estimation was developed in Matlab® environment, as it is able to provide easier point cloud management and analysis as well as being more flexible. The tool will be called M_ASD2. The methodology proposed in this section is summarized in Figure 8. The position of the driver eyes and the target high are fixed respectively to 1.1m and 0.1m, such as in the previous cases. Two trajectories are provided as input data to the tools, which are parallel and are defined by one point each circa 1 m. The M_ASD2 tool also requires the point cloud as input data. The detection of the occlusion is now carried out through an iterative procedure along the rays, which connect the observer point (P) to each target point (Qi), as long as the distance between the two points does not exceed 200m. The visibility analysis is performed by checking the number of points of the 3D point cloud inside a sphere moving in a cylinder generated around the LOS (Figure 9). Verification is then carried out at various steps along the LOS, whose distance is defined as input data. In the proposed approach, an obstruction corresponds to a determined number of points of the 3D model that interrupt the sight between the observer and the obstacle that needs to be seen. As in the previous case, if an obstruction is detected at a distance of less than 200 m, the loop stops and the ASD is calculated as the difference between the station of the last visible target and the observation point; otherwise, the value of 200 m is assigned to the ASD.

Since only object larger than 0,80m can be considered obstructions, it is necessary to set a condition which defines when a cluster of points in the model can be assumed as a real obstruction, which affects the visibility. Consequently, it was taken into account the local density of the 3D model to evaluate the presence of occlusion, estimated as the number of points that are inside of the sphere with center in the LOS (190 points) and with the radius corresponding to the buffer radius (0,65m) (Figure 9). Two tests were conducted setting the distance between the spheres along the LOS at 1 m and 3 m.

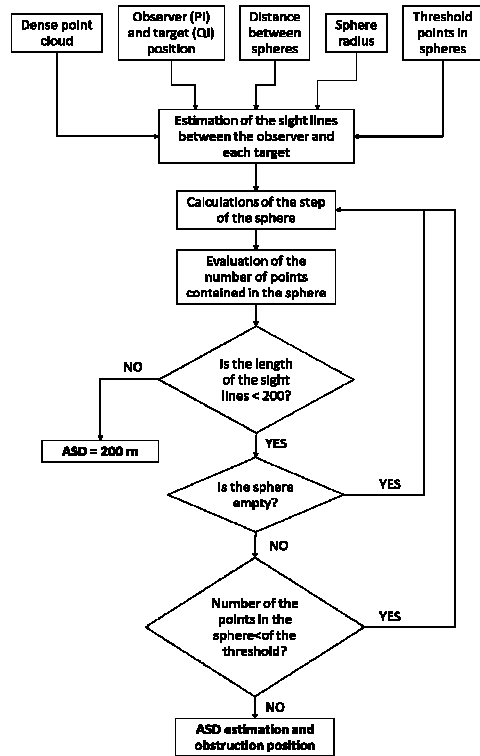


Figure 8. Workflow of the M_ASD2 tool in the numerical computing environment, which allows to compute the ASD using a 3D point cloud as input data (see Appendix C for the code).

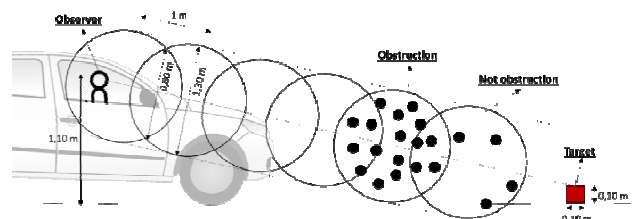


Figure 9. Representation of the buffer around the LOS. The algorithm allows you to estimate the number of points within the spheres that are placed along the cylinder.

Result and discussion. Figure 10 includes the estimate of the ASD using the M_ASD2 tool, implemented on Matlab®, with the distance between the steps of the spheres steps at 1m, while the Figure 11 is realized by setting the distance to 3m, and the SSD estimated as a function of the driver speed behaviour. The graphs were interrupted at the station 1270m, as, subsequently, the ASD is equal to 200m until the end of the road. A comparison between SSD and the ASD showed that in both cases ASD is always equal or greater than the SSD. The comparison between the two solutions obtained for different step length between the spheres shows that a discretization of the sight line in steps of 3m brings to an overestimation of the ASD, as parts of space are left out of the analysis, where, in some cases, there may be a high density of points representing an obstruction. In this case, at some station, the obstruction is not even identified and the ASD is defined equal to 200m. The test performed by setting the distance between the spheres at 1 m confirm that, the main causes of visibility obstruction are precisely the cars parked on the side of the roadway. With such a result, it is, therefore, possible to affirm that the accuracy of the ASD estimation performed by the M_ASD2 tool with a

discretization of the line of sight in steps of 1m and sphere radius of 0,65 m, is almost equivalent to the point cloud accuracy. However, it is important to take into account the noise of the input point cloud data, which can lead to an erroneous detection of an occlusion point. It is therefore essential to set an appropriate density value of the point cloud.

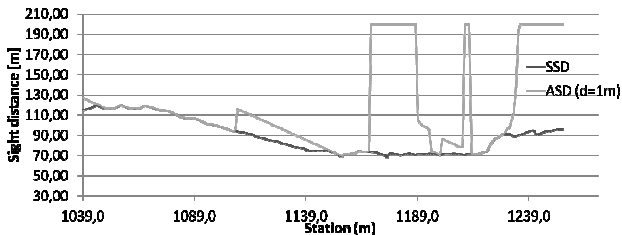


Figure 10. Comparison between ASD estimated with M_ASD2 tool setting the distance between spheres along the LOS to 1 m.

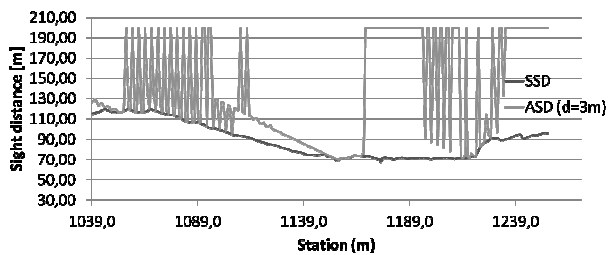


Figure 11. Comparison between ASD estimated with M_ASD2 tool setting the distance between spheres along the LOS to 3 m.

4.3 Evaluation of the complexity of indoor escape routes

From analyses on evacuation simulation models, it is evident that, despite these consider both the mechanical aspects of motion and behavioural ones, they do not take into account how the perception of the complexity of the environment, during the exodus affect the movement itself. The main aim of this research work is to propose a methodology to assess the complexity of an evacuation path, as a user passing through subjectively perceives it, and to try to quantify this characteristic, analysing a three-dimensional point cloud representation of the environment. To this purpose, the isovist method and the visibility graph approach relate the spatial properties of the environment with the spatial behavior. These approaches allow extracting several numerical indexes, which describe the properties of the corresponding space, from the point of view of the user, as it is perceived while he is moving through (Turner et al. 2001). Information that can be extracted from a single isovist, which is a polygon representing all the visible area from a certain point of view, are not sufficient to quantitatively and qualitatively describe the environment, but it is necessary to combine them together and assess their relationships to represents the variation of a certain property if isovists, within the whole environment. However, until now, most of these works were oriented on the perception of the architecture of the building or of the landscape from a static point of view, without taking into account the dynamics of motion within an environment. Benedikt, 1979 mentioned a possible temporal extension, but no examples were found in the literature of a dynamic 3D framework being analyzed through isovists. In this proposal, the navigable path is discretized in a sequence of nodes, which represent the accessible positions to the user. In a three-dimensional framework, the height of the viewpoints should correspond to the "eye-level" of the user. It has been hypothesized a distance between nodes corresponding

to a human step, which depends on his estimated speed and on the stopping sight distance needed to avoid collisions with other objects or users.

In a first step, it is considered a network of three-dimensional nodes that covers the entire environment. These are subdivided into accessible nodes, corresponding to the navigable path, at eye-level, and in inaccessible nodes, which are not part of the path. The visual interconnections between the different kind of nodes will be analyzed. This configuration allows to estimates different environment descriptors: the 3D integration index, which corresponds to the average number of turns plus one required to move in space, and the 3D connectivity index, which estimates how the visibility is influenced by the volume variation (Varoudis et al., 2014). Subsequently, 3D isovists are generated from each node of the path (at eye-level) (Figure 12), considering the three-dimensional visual angle of the user, oriented in the movement direction.

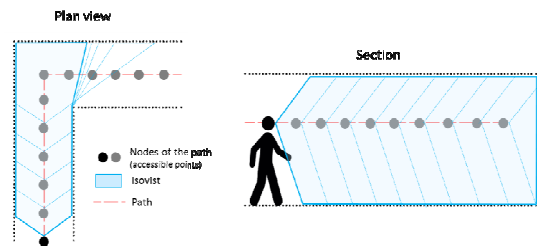


Figure 12. 3D isovist field generation.

The aim is to generate three-dimensional volumetric isovists, which would be represented as polyhedrons, from each step of the path, to evaluate how the perception of the environment varies during the movement and define which could be the most critical areas that can be encountered while traveling through it. We assume that a configuration like this allows extracting several 3D properties, as those analytically described by van Bilsen (2008), including the 3D clustering coefficient that defines the complexity of space. Besides, this configuration allows to calculate the Spatial Openness Index, as the sum of the spatial openness which characterizes each isovist along the path.

Discussion. The methodology proposed in this section of the research thesis is still on a theoretical level due to some issues that still need to be overcome.

The first issue regards the discretization of the path. The path is the most relevant input data of our model and, as mentioned before, to be correctly analyzed with our approach, needs to be discretized in a series of nodes. We assume the distance between nodes as equal to the step of a person, which is influenced by his speed, but it is necessary to verify if this level of discretization is adequate to describe the perception along the route. The dimension of the field of view of the user and the direction in which to build the isovists are also issues that need to be tackled. During the navigation along a straight path is easy to assume that the user looks in front of him, which in our configuration means that he looks in the direction of the next node, in particular in the case in which the nodes are placed only to the corners of the path. On the other hand, using a greater number of discretization nodes, considering the previous node to the one placed on the corner, it is possible that a human does not look in front of him, but also may turn his gaze in direction of the next node to that at the corner, increasing the FOV. Furthermore, the proposed methodology has not yet been put into practice and it is necessary to evaluate the possibility of generating isovists for an environment represented by a 3D point cloud and of extracting the respective numerical

descriptors. As demonstrated earlier, it is now possible to easily generate 3D point cloud representations of the environment, using image sensors mounted on common devices. In addition, the software based on the strategies of stereo matching and structure from motion allows to calculate, without any input data, except to the images, the image center positions. The acquisition centers can be assumed as correspondent to the nodes of a path. Furthermore, the above-mentioned algorithms, allow to extract the three-dimensional information from the images, by the identification and the analysis of some matching points between the frames. The position of each matched point in the image is known, therefore, it is possible to project their position in the 3D space by the collinearity equation. In this context, we can assume that the lines of sight between the image center positions and the matched points correspond to the radial of the isovists. Future activities will be focused on the implementation of this method for the isovists generation and on the evaluation of the errors made by performing this approximation and on the analysis of filtering algorithms and feature extraction techniques for the improvement of the image matching.

5. CONCLUSIONS

The aim of this research was to analyze and propose low-cost technology and methodology in order to realize 3D representation of the urban environment and use them to perform visibility analyses. The aspects examined concern the entire process that from the acquisition phase leads to the analysis of final result accuracy.

A first phase was focused on the research of instruments for data acquisition. The issue to be tackled was to find solutions able to guarantee a certain accuracy of the data, but at the same time to fulfill the requirements of portability, low-cost, speed in data acquisition and flexibility to adapt their use in complex urban contexts. Due to these devices are generally realized for amateur purposes, it has become crucial to study their characteristics, analyze their behavior and test performances in depth, before using them in surveying operations. The calibration problem was one of the addressed topics in this research, because in photogrammetry a good accuracy of the final model cannot ignore a correct calculation of the internal parameters of the camera.

The following activities involved the realization of various MMSs, each of them integrating different combination of imaging and positioning sensors. First of all it is important to plan and define the position of each device on the involved mobile platform. In order automatize the acquisition phase, to ensure the accurate data flow synchronization and limit the errors inherent the post-processing of disjointed measurement, two acquisition tools, BEAtool and the RPiBike system, were developed. Both tools were addressed to the synchronized capture of images and positioning data and to the data storage. The software were very easy-to-use and allowed to set different acquisition parameters. However, it was demonstrated that the tools had still some difficulties to maintain a constant frame rate during the data acquisition, even though these have not had any influence on the reconstruction of the model; in the future, it will then be necessary to further work on their improvement.

Many tests within the urban environment were performed in order to identify limits and potentialities of the proposed MMSs combining the use of different mobile platforms.

The experiments have highlighted some difficulties related to the use of the proposed MMSs, due in particular to the characteristics of the urban environment, with narrow streets, vegetation, in some cases even dense, in the presence of objects

and pedestrians in motion, and the high number of reflective surfaces. All this criticality affected the results, which in most cases consisted of very noisy clouds, which required filtering operations. In addition, the acquisition geometry of this type of survey, may be a limitation, as it does not respect the configuration of the ideal acquisition geometry and also affects the estimation of the internal camera parameters, with obvious consequences in the alignment of frames. It was demonstrated that an effective solution involved the acquisition of stereoscopic pairs of images.

From the case studies analyzed, has emerged a great criticality related to the georeferencing of the data, due both to the poor satellite availability and low performances of the employed positioning devices. In fact, the accuracy of the data acquired by the low-cost GNSS receivers was still too scarce and therefore a direct photogrammetry approach with this instrumentation was not achievable. However, it has been demonstrated that in order to georeference point clouds, a limited number of GCPs were needed. Moreover, the tests carried out have shown that through these low-cost photogrammetry systems can be reached accuracies appropriate for scale 1: 500 and 1: 1000 and the realized products allowed to identify also the objects along the roadside. This was an excellent result when compared to the resolution of the elevation models of urban environment that are currently used for road visibility analyses (grid greater than 5m). It was demonstrated that the proposed MMSs are an affordable solution, both economically, in terms of ease of use, even if they require the presence of an expert operator in the survey planning and data processing phase, and flexibility as they can be employed in different urban context, thanks also for their limited size, and eventually, in indoor environment, which often have characteristics and limits similar to those found in urban canyons.

Considering this aspect, future research should be oriented on the development of a methodology for the integration and merging of 3D models of outdoor and indoor environment between them, treating the urban environment as a continuous space. It is therefore necessary to find a solution to georeference the two environments in the same reference system to ensure a spatial continuity between the interior and exterior. To this purpose, it might be also useful to deepen the possible application of the dual frequency GNSS already integrated in the smartphone; this particular technology could guarantee centimeter accuracy even within urban canyons and possibly in indoor environments, if it would be available the satellite visibility. Moreover, since telecom signals are widely available in urban areas and indoors, their use for positioning, complementary to the GNSS, could be another valid solution. Indeed, the positioning functionality could be improved by the next generation mobile networks 5G, by combining all available signals into a hybrid positioning system using cloud technologies.

In the second part of this research different algorithms for visibility analysis, working both in outdoor and indoor environments, were proposed. The idea was to exploit the 3D point clouds generated with the MMSs to derive information useful to improve the safety of the individual, by knowing his motion trajectory.

The first study dealt with the estimation of the Available Sight Distance (ASD) along the road infrastructure in urban environments. An insufficient ASD from the driver point of view is generally assumed to be a contributing factor in many road crashes. In this research work, it has been proposed the use of new algorithms to estimate the ASD in 3D space with commonly used geographic and numerical analysis software.

The algorithms proposed here operated automatically, and provided an estimate of the ASD by moving potential obstacles along the centerline, assuming the driver point of view at a fixed height above the road pavement. This approach was effective and of interest since it did not require recourse to in-field direct surveys, which would involved higher costs and implicated closure to traffic.

It was demonstrated that the proposed procedure was able to correctly analyze the roadside visibility with different degrees of accuracy. In the case that the visibility analysis generates a negative result, it is given the possibility for the public administration to take action to correct these problems, allowing to increase the level of security on the various types of infrastructure. The results indicated that geographic information and numerical computing environments could have both supported sight analyses for road safety investigations. Computational and operating differences between the three approaches described were due to the accuracy levels and to the noise of the point cloud.

Future research activities will be addressed to the evaluation of the ASD in correspondence to intersections, which are always affected by higher accident frequencies than longitudinal road sections and which were excluded by this research as they require the involvement of additional factors to correctly model the dynamicity of the driver movements.

Subsequently, the research was orientated to the indoor environment. Several strategies to quantitatively assessing the complexity of a known escape route were evaluated. The proposed methodology could be easily implemented in each model for the exodus simulation, to improve the analysis of people behaviors with the respect to the crossed space.

The new approach here proposed is still on a theoretical level and needs to be validated in a real case study. Future activities will be focused on the implementation of the proposed procedure. Such a simulation based on the extraction of environment descriptors from high-resolution data should be, therefore, compared with the correspondent subjective perception in the real world.

REFERENCES

- AASHTO (2011). *Policy on geometric design of highways and streets*. American Association of State Highway and Transportation Officials, Washington, DC, 6th edition.
- Aliaga, D. G., Rosen, P. A., & Bekins, D. R. (2007). Style grammars for interactive visualization of architecture. *IEEE transactions on visualization and computer graphics*, 13(4).
- Anguelov, D., Dulong, C., Filip, D., Frueh, C., Lafon, S., Lyon, R., Weaver, J. (2010). Google street view: Capturing the world at street level. *Computer*, 43(6), 32-38.
- Bassani, M., Grasso, N., & Piras, M. (2015). 3D GIS based evaluation of the available sight distance to assess safety of urban roads. *The International Archives of Photogrammetry, Remote Sensing and Spatial Information Sciences*, 40(3), 137.
- Benedikt, M. L. (1979). To take hold of space: isovists and isovist fields. *Environment and Planning B: Planning and design*, 6(1), 47-65.
- Dabove, P., & Manzano, A. M. (2014). GPS & GLONASS mass-market receivers: positioning performances and peculiarities. *Sensors*, 14(12), 22159-22179.
- Goesele M, Curless B, Seitz SM (2006) Multi-view stereo revisited. In: Proc. CVPR 2006, pp 2402-2409.
- González-Jorge, H., Díaz-Vilariño, L., Lorenzo, H., & Arias, P. (2016). Evaluation of driver visibility from mobile lidar data and weather conditions. *International Archives of the Photogrammetry, Remote Sensing & Spatial Information Sciences*, 41.
- Haala, N., & Rothermel, M. (2015). Image-based 3D Data Capture in Urban Scenarios. *Proc. Photogrammetric Week 2015*, 119-130.
- Haala, N., Peter, M., Cefalu, A., & Kremer, J. (2008, October). Mobile lidar mapping for urban data capture. In *Proceedings of the 14th International Conference on Virtual Systems and Multimedia, Limassol, Cyprus* (Vol. 2025, p. 95100).
- Hartley, R., & Zisserman, A. (2003). *Multiple view geometry in computer vision*. Cambridge university press.
- Hartmann, W., Havlena, M., & Schindler, K. (2016). Recent developments in large-scale tie-point matching. *ISPRS Journal of Photogrammetry and Remote Sensing*, 115, 47-62.
- Kukko, A., Kaartinen, H., Hyypää, J., & Chen, Y. (2012). Multiplatform mobile laser scanning: Usability and performance. *Sensors*, 12(9), 11712-11733.
- Ministero delle Infrastrutture e dei Trasporti (2001). *Norme Funzionali e Geometriche per la Costruzione delle Strade*. Decreto Ministeriale No. 6792, Roma, Italy (in Italian).
- Pelechano, N., & Malkawi, A. (2008). Evacuation simulation models: Challenges in modeling high rise building evacuation with cellular automata approaches. *Automation in construction*, 17(4), 377-385.
- Peters, R.; Ledoux, H.; Biljecki, F. Visibility analysis in a point cloud based on the medial axis transform. In Proceedings of the Eurographics Workshop on Urban Data Modelling and Visualisation 2015, Delft, The Netherlands, 23 November 2015; pp. 7-12.
- Remondino, F., & El-Hakim, S. (2006). Image-based 3D modelling: a review. *The Photogrammetric Record*, 21(115), 269-291.
- Remondino, F., & Rizzi, A. (2010). Reality-based 3D documentation of natural and cultural heritage sites—techniques, problems, and examples. *Applied Geomatics*, 2(3), 85-100.
- Schwarz, K. P., & El-Sheimy, N. (2004). Mobile mapping systems—state of the art and future trends. *International Archives of Photogrammetry, Remote Sensing and Spatial Information Sciences*, 35(Part B), 10.
- Sirmacek, B., Shen, Y., Lindenbergh, R. C., Diakite, A. A., & Zlatanova, S. (2016). Comparison of Zeb1 and Leica C10 indoor laser scanning point clouds. *ISPRS Annals of the Photogrammetry, Remote Sensing and Spatial Information Sciences*, 3.
- Turner, A., Doxa, M., O'sullivan, D., & Penn, A. (2001). From isovists to visibility graphs: a methodology for the analysis of architectural space. *Environment and Planning B: Planning and design*, 28(1), 103-121.
- Van Bilsen, A. (2008). *Mathematical explorations in urban and regional design* (Doctoral dissertation, TU Delft, Delft University of Technology).
- Weinmann, M. (2016). Reconstruction and analysis of 3d scenes. *Springer International Publishing, Cham*. doi, 10, 978-3.
- Varoudis, T., & Psarra, S. (2014). Beyond two dimensions: architecture through three dimensional visibility graph analysis. *The Journal of Space Syntax*, 5(1), 91-108.



c/o CIRGEO, Centro Interdipartimentale di Ricerca di Geomatica - Università degli Studi di Padova
Viale dell'Università 16, 35020 Legnaro (PD)
Prof. Antonio Vettore tel. 049-8272688
e-mail antonio.vettore@unipd.it

con il supporto di



ISBN 978-88-942926-6-4

Luglio 2019